DEVELOPMENT OF IN-SITU STRESS MEASUREMENT TECHNIQUES
FOR DEEP DRILLHOLES

A DISSERTATION
SUBMITTED TO THE DEPARTMENT OF GEOPHYSICS
AND THE COMMITTEE ON GRADUATE STUDIES
OF STANFORD UNIVERSITY
IN PARTIAL FULFILLMENT OF THE REQUIREMENTS
FOR THE DEGREE OF
DOCTOR OF PHILOSOPHY

By

Colleen Barton
August, 1988

ABSTRACT

New techniques to measure in-situ stress at great depth in the earth's crust have been developed. The first method utilizes data recorded with the acoustic borehole televiewer (BHTV). The BHTV provides excellent data for the detection and measurement of stress-induced wellbore breakouts, natural fractures, and lithologic features that intersect the drillhole. It can also be used to gain engineering information on borehole size and stability. A system to digitize analog BHTV data was developed to quantify measurements of specific borehole features such as wellbore breakouts, and natural fractures and to generate depth profiles of other borehole data such as borehole caliper and formation reflectivity. A comprehensive set of digital display and analysis routines were designed and implemented for this purpose. Three case studies of the application of some of these routines to specific geophysical problems are included.

In the first study analog televiewer data from the Fenton Geothermal well EE-3 in New Mexico were digitized and interactively processed for detection and analysis of azimuth and shape of stress-induced breakouts occurring in the well at depths of about 2.9 - 3.5 km. A statistical analysis of the measured breakout azimuths yields a well resolved orientation of least horizontal principal stress of 119°, consistent with least principal stress data from the Rio Grande Rift. As the magnitude of the least horizontal compressive stress, S_{hmin}, in EE-3 is known from hydraulic fracturing, we present a new method in which S_{hmin} and data on breakout width are used to estimate the magnitude of the maximum horizontal principal stress.

The orientation, distribution and apparent aperture of natural fractures intersecting the Cajon Pass research well were determined in the second study through analysis of BHTV data over the interval 1829 to 2115 meters. Large open fractures have shallow inclinations and tend to be aligned striking roughly $N15^oE$. There is no apparent relationship between these fractures and the current stress state, as measured by the analysis of wellbore breakouts and hydraulic fracturing experiments in the Cajon Pass well and as observed in other studies in the region. Temperature anomalies due to fluid flow into the well detected during a long-term permeability experiment occur at several of these fractures. Compressional, shear

and Stoneley guided wave velocities are within the expected range for crystalline rocks and elastic-wave anomalies are associated with the larger fractures. Stoneley wave coherence is reduced where the fractures are hydraulically conductive.

BHTV data recorded during Leg 104 of the Ocean Drilling Program expedition to the Norwegian Sea was analyzed for borehole caliper over a 470 m interval where the standard caliper log was unsuccessful in recording borehole size. These data, recorded under hostile logging conditions at sea exemplify the need for digital correction and enhancement before data correction can be performed.

Section II presents the analysis of the horizontal particle motion of borehole guided waves from three-component Vertical Seismic Profile (VSP) data recorded from three experiments. The polarization directions of the guided waves are consistent with the direction of horizontal principal stress determined independently. It is suggested that stress-induced velocity anisotropy in the rock adjacent to the borehole appears to cause antisymmetric flexural guided modes to be polarized in the direction of the maximum horizontal principal stress. Thus, analysis of the horizontal particle motion of borehole guided waves appears to represent a new method for determining the orientation of horizontal principal stresses.

OVERVIEW

"The measurement of in-situ stress at depth is one of the most important goals of scientific drilling programs. Nevertheless, stress measurements at great depth have not yet been accomplished and we face many important technological and scientific challenges to make them."

M.D. Zoback, 1987

Knowledge of the ambient stress field is important for elucidating understanding of tectonic processes. A number of methods are currently used to determine in-situ stress orientation and magnitude at depth. These methods include the analysis of induced hydraulic fractures, wellbore breakouts, fault slip data, earthquake focal mechanisms and overcoring in deep mines. Each method has its own drawback and limitations (see review by Zoback and Zoback, 1988). Although useful for determining stress orientation and relative magnitude, fault slip data and earthquake focal mechanisms are not always located at sites of interest. Stress-induced wellbore breakouts are a natural phenomena that occur in response to unequal horizontal principal stress that have become important as indicators of the direction of horizontal principal stresses (e.g. Bell and Gough, 1979; Zoback et al., 1985; Hickman, et al., 1985; Plumb and Cox, 1986) and as discussed below can also be used to constrain stress magnitude. Breakouts and as such their occurrence depends on the initial stress state. Hydraulic fracture data, on the other hand, can provide both in-situ stress orientation and magnitude information at specified locations, but it is often quite difficult and expensive to employ the method at great depth.

The difficulties in making stress measurements at great depths not only include the obvious problems imposed by the high pressures and temperatures encountered, but problems such as the degradation of hole shape due to the presence of breakouts. If breakouts are severe enough, they make utilization of traditional methodologies such as hydraulic fracturing nearly impossible.

This thesis describes new techniques to measure in-situ stress in deep drillholes and discusses their application in specific case studies. Part I discusses the development and application of a digital system for the acquisition and analysis of borehole televiewer (BHTV) data. Although the quantification of stress measurements was the primary motivation for the development of the analysis system, it has opened new possibilities for the analysis of a variety of phenomena that can be acquired from the BHTV images.

Measurement of the orientation, distribution, and apparent width of natural fractures intersecting the well are perhaps the most useful by-products of the development of this system. Part II discusses a new stress measurement technique utilizing Vertical Seismic Profile (VSP) data. The analysis of the horizontal particle motion of borehole guided waves from three-component VSPs show that polarization directions are consistent with the direction of horizontal principal stress determined independently. Stress-induced velocity anisotropy in the rock adjacent to the borehole appears to cause antisymmetric flexural guided modes to be polarized in the direction of the maximum horizontal principal stress. The analysis of the horizontal particle motion of borehole guided waves appears to represent a new method for determining the orientation of horizontal principal stresses.

Acknowledgements

The thesis that follows was drawn largely from concepts of Mark D. Zoback, my advisor, whose timely move from the U.S.G.S. to the Stanford geophysics faculty four years ago coincided with the focusing of my research interests on the study of crustal stress. Since I arrived at Stanford, Professor Zoback's ideas and insights have facilitated a very productive three and a half years of research in the development of stress measurement techniques at depth in the earth's crust.

The sponsors of this research include the seventeen members of the Stanford Rock Physics and Borehole Geophysics Project (SRB) that support the ongoing efforts of research in our group. The interaction with consortium members has been important to the progress of this research. This not only includes helpful scientific discussions but also collaboration in field efforts and in securing the release of industry data. I would specifically like to thank Aaron Seriff and Jacque Leveille at Shell Development Co. for the extensive and beneficial discussions on the topic of borehole guided waves. Thanks also to Amoco Oil Co. and the Gas Research Institute vis the MIT/ERL for supplying VSP data recorded in the Oklahoma test well, to Elf Aquitane Production for the VSP data from the Paris Basin, and to Arco Resources Technology, Western Geophysical and J. Richter for supplying the VSP data recorded in the Cajon Pass Scientific Drillhole. The USGS Tectonophysics Branch, the USGS Water Resource Division, Los Alamos National Labs, Shell Oil, Inc., and Woodward-Clyde Consultants have supplied BHTV and companion data from a variety of geological environments. I would like to extend my appreciation to Roger Anderson and the Borehole Research Group at the Lamont-Doherty Geological Observatory for their efforts in the numerous cooperative projects which have made available thousands of meters of BHTV and log data from both the oceanic and continental crust.

The Stanford SEP seismic data routines SEPLIB have been used extensively to process and plot the VSP data and I would like to thank all of the authors of this software for making it available. Thanks also to Terrasciences, Inc. for their generous donation of their log analysis package Terralog to the SRB project which was used to display and correlate log data.

The JOIDES organization supported my research over much of my time in the Ph.D. program at Stanford. Their interest in and support of the development of televiewer imaging for shipboard use was fundamental to the software efforts described in this

TABLE OF CONTENTS

SECTION I

The Development of a Digital Processing System for Borehole Televiewer Data and the Application to In-Situ Stress Measurements

Chapter 1: Digital BHTV Data Analysis System

Chapter 2: Quantitative Analysis of BHTV Data: Application to the Measurement
of In-Situ Stress

Study 1: In-Situ Stress Orientation and Magnitude at the Fenton
Geothermal Site, New Mexico Determined from
Wellbore Breakouts

Study 2: Analysis of Macroscopic fractures in the Cajon Pass Scientific
Drillhole Over the Interval 1829 - 2115 meters

Study 3: Analysis of BHTV Log Data for Borehole Caliper: ODP Site
642E— Outer Voring Plateau

SECTION II

Determination of In-Situ Stress from the Polarization of Borehole
Guided Waves in Vertical Seismic Profiling

List of Tables

List of Illustrations

Section I

Section II

SECTION I
CHAPTER 1: INTERACTIVE IMAGE ANALYSIS OF
BOREHOLE TELEVIEWER DATA

"The ability of scientists to visualize complex data, computations, and simulations is absolutely essential to insure the integrity of analyses, to provoke insights and to communicate those insights with others"

NSF Panel Report on Visualization in Scientific Computing, 1986

Introduction

The borehole televiewer is an ultrasonic well-logging tool useful for measuring the orientation and distribution of fractures, the orientation and width of stress-induced wellbore breakouts and imaging lithostratigraphic features. The analog televiewer, originally designed by Mobil Oil, Inc. (Zemanek, 1970), contains a rotating transducer that emits an acoustic pulse at a rate of 1800 times a second. Figure 1a is a schematic diagram of the acoustic mechanism of the televiewer tool. The 1.4 Mhz transducer rotates three revolutions per second and moves vertically up a borehole at a speed of 2.5 cm/s. The transducer diameter is about 0.5 inches however the emitted sound is focused to a narrow beam of about 3° due to the high frequency. Ultrasonic seismograms are transmitted through a standard wireline logging cable and recorded on videotape. In the standard field operation the data are channeled into a 3-axis oscilloscope where the horizontal sweep is the scan of the rotating transducer around the borehole, the vertical sweep is the rise of the tool in the borehole and the intensity is modulated by the reflected energy from the borehole wall. The oscilloscope then produces an unwrapped 360° grey scale image of about 5 feet of the borehole wall. Although the resolution is completely dependent upon hole size and logging speed typically the televiewer will provide horizontal resolution of a few millimeters and a one centimeter vertical resolution in an 12 inch borehole. A fluxgate magnetometer within the tool fires at each crossing of magnetic north making it possible to orient the data. The "north pulse" is recorded on one of the two audio channels of the video recorder. Depth is also encoded analog on the remaining audio track of the video recorder. The BHTV "log" is constructed from Polaroid photographs taken of successive oscilloscope screens as the tool progresses uphole during field logging. Each 3x5 photograph is then assembled into a composite log.
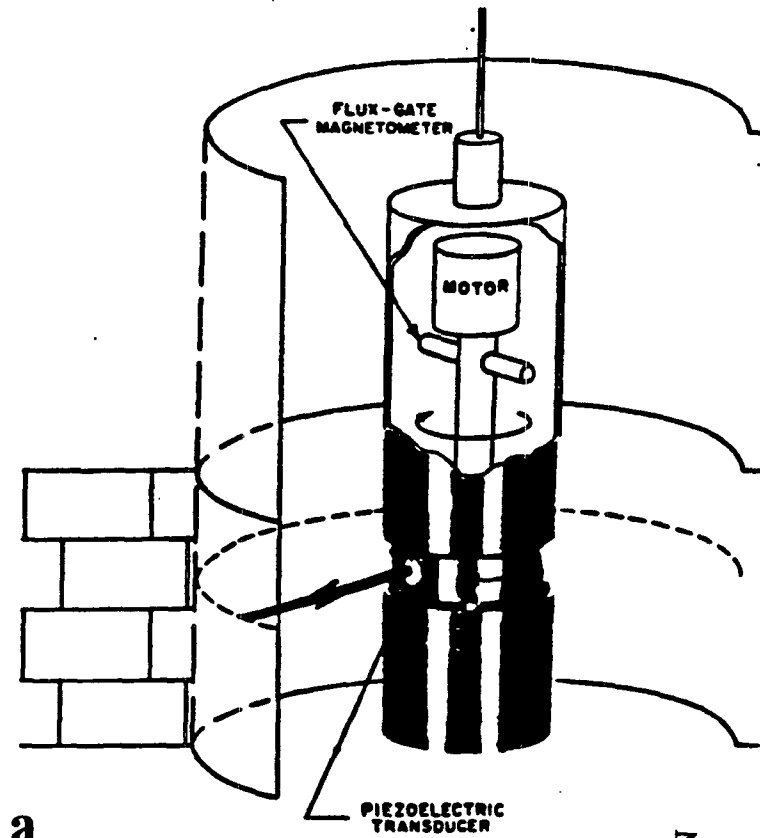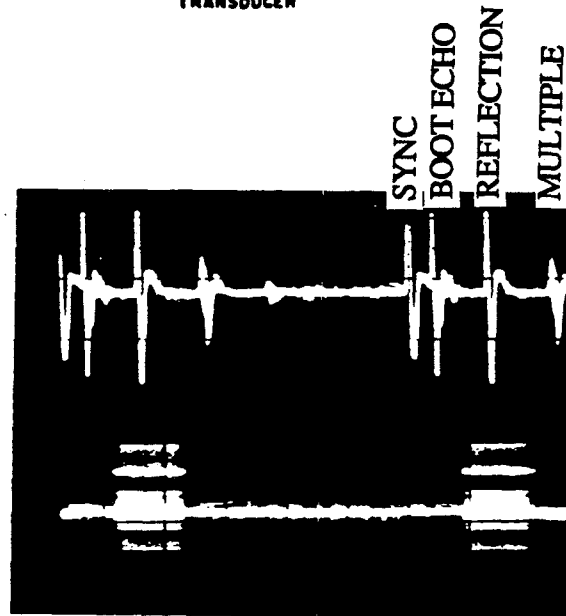
Figure 1. a) Schematic diagram of the acoustic mechanism of the borehole televiewer, b) The analog wavetrain of the televiewer signal.

The analog televiewer tool has not undergone any major design changes since it was first introduced to geophysical logging in 1970. Interpretation of the photographic log has been limited to estimations of gross structure from the reflected image. The primary use of televiewer data had been to determine the orientation of fractures in granitic rocks, analyses which involved tedious and inaccurate measurements. No capability existed in the analog data to correct the measured orientations of planar features for the effects of off-center tools or elliptical boreholes, conditions which can lead to substantial measurement error. With the rising use of wellbore breakouts to determine in-situ stress televiewer data has become increasingly important. Digitizing and digital processing of the analog televiewer data has opened a new dimension in the interpretation of BHTV data, most significantly, the precise measurement and display of the travel time of the reflected pulse. Assuming a known mud velocity along the raypath for the source and reflected pulses the two-way travel time can be converted to distance to give the detailed topography of the borehole wall. Another advantage to digital data is that it can be enhanced and corrected for geometric effects. Finally, it is possible to project borehole features in a variety of ways to an optimal view and to make systematic quantitative measurements quickly and accurately.

Data Acquisition

Digitization of the standard analog data results in the dual measurement of the acoustic reflectivity of the borehole wall and the ultrasonic travel time of the imaging pulse at a spatial resolution well above conventional logging tools. The software used to digitize the analog signal has been designed for a Masscomp 5600 microcompter and utilizes the C programming language. The analog to digital (ADC) processor on this system utilizes programmable clocks triggered by the source pulse. The sampling rate used for digitization is usually 1 μsec however the sample rate can be adjusted to suit the variability of the data. The analog wavetrain (Figure 1b), comprised of a source pulse, an echo from the pressurized housing around the transducer, the reflection from the borehole wall and multiple reflections, are transformed to a simple square wave through a sample and hold circuit before it is fed into the ADC. The north pulse is merged with the main signal through a ramp circuit triggered by the horizontal sweep which adds a large negative value to the signal as a marker of each north crossing. Figure 2 shows a

schematic of the ADC processing. The gated waveform is windowed and sampled generally for 100 μsec. The ability to vary the delay time and digitization window length provide an important flexibility in the range of data that can be digitally captured. The digitization algorithm then measures the peak amplitude and associated travel time through a binary search of the square wave.

BOREHOLE TELEVIEWER
DIGITAL DATA ACQUISITION SYSTEM
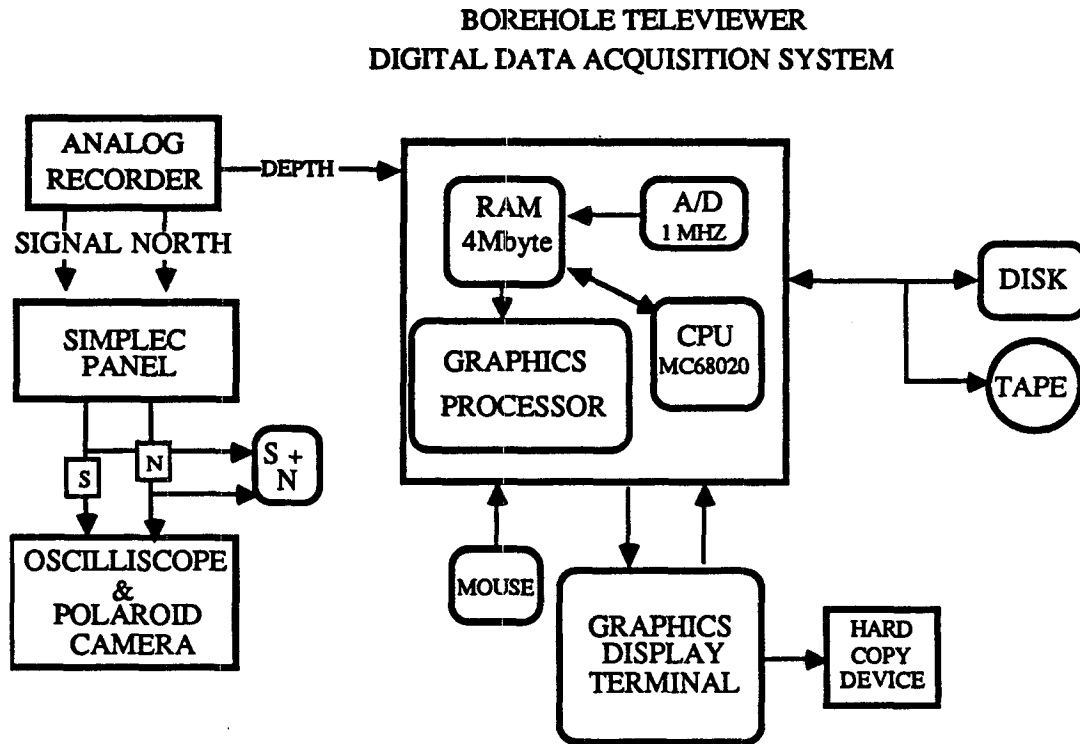
Figure 2. Schematic diagram of the ADC processing for televiewer data acquisition

At a data rate of about 1800 waveforms per second the data reduction must proceed in approximately 0.5 ms per pulse firing. Maintaining this data acquisition rate required code optimization and strategic buffer swapping for data intake. The system's ADC has 12 bit resolution with a data acquisition rate of 2.16 Mbits/s. Digital data can be acquired in real time over an extended depth limited only by disk storage capacity. The starting and ending depths are entered into a data header and depth values are stretched to span the digitized interval.

An extensible header format has been designed for the data to catalogue information pertinent to the specific well site and the data acquisition settings used to identify the data and properly scale it. Table I summarizes header specifications used in this system.

Table I

Data Attribute	Definition
Well Name	Well identification used as title for graphics output
Well Location	Well location used as title for graphics output
Mag Dec	Magnetic declination at site in degrees east of north
Marker	Azimuth correction for data collected in marker mode
Deviation	Borehole deviation in degrees
Max Depth	Bottom depth of digitized interval
Min Depth	Top depth of digitized interval
Tool Spec	Calibration adjustment
Fluid Vel	Velocity of the borehole fluid during logging
Ddelay	Time delay for reflection from borehole wall in μs
Window	Sampling window length in μs
Samples	Number of samples digitized for each pulse
Max TT	Maximum recorded travel time
Max AMP	Maximum Recorded amplitude of the reflected pulse
Min TT	Minimum recorded travel time
Min AMP	Minimum recorded amplitude of the reflected pulse
Cutoff TT	Array of histogram equalization bins for travel time
Cutoff AMP	Array of histogram equalization bins for travel time
Scans	Total number of scans in data file

To convert the travel time values to the true borehole radius the correct dimension of the televiewer tool, T_r, the fluid velocity, V_f, and the calibration constant, C, for the logging run must be known. The calibration constant is obtained through calibration tests in a specially designed tank before each logging run (G. Shamir and D. Moos, personal communication). The conversion used to compute borehole radius is:

$$R= (T_i + D - 16)/2 * V_f + T_s \tag{1}$$

where T_i is the two way travel time and D is the digitizing delay time. For each tool there is a calibration adjustment, T_s and $T_s = V_f * C + T_r$. The 16 μs is a correction recommended by the manufacturer to compensate for the lag between the source firing and the initiation of the sync pulse. Routines have been implemented to quickly adjust header values and to add or delete header information as required. Facilities are also available to quickly inspect header and data values without plotting.

Digital televiewers have recently been designed that contain downhole processors to reduce the received signal to a peak amplitude and associated travel time before digital transmission (Hinz and Schepers, 1985; Schlumberger, 1986). Generally the horizontal resolution of the data is reduced by about one half of that of the analog tools in the digital tools, however precision is gained by elimination of noise problems such as the analog signal degradation by the cable. The marker pulse at magnetic north and depth readings are encoded automatically in the data recorded by the digital tools. The tilt of the tool is monitored by two inclinometers and an accelerometer provides continuous data on tool speed. The software and analysis techniques described below developed to analyze and interpret BHTV data are completely general to any digital televiewer data set.

Interactive Processing

A sophisticated software package has been designed for the analysis of BHTV data. The system utilizes various two- and three-dimensional displays of the borehole radius and acoustic reflectivity and allows the user to make quantitative measurements of borehole features such as breakouts, fracture orientation and apparent aperture, and lithologic features. The display and analysis software has been implemented on a Masscomp 5600 computer and on a Macintosh II personal computer. Both versions are designed with a main driver for standard data handling and graphics displays which are shared by modular routines for specific analyses and computations. Documentation of the software is included as Appendix A to this thesis. The programs provide an integrated workstation for analyzing borehole shape and features where images of BHTV data are displayed in false color on a graphics screen and are manipulated by graphics mouse and keyboard commands. Menu driven commands and analysis operations provide an ease of use factor to the software. Tens of meters of borehole wall image can

be rapidly viewed by scrolling through the data within a graphics window. Images can be enlarged to the full resolution of the screen and scrolled to search for fine features. Alternatively larger sections of the well can be displayed at the scale of standard logs. The values of the scales, units and grid intervals can be modified interactively during program execution. Several windows of data may be displayed concurrently for comparison. Menu operated window management provides easy access to the various views the user is interpreting.
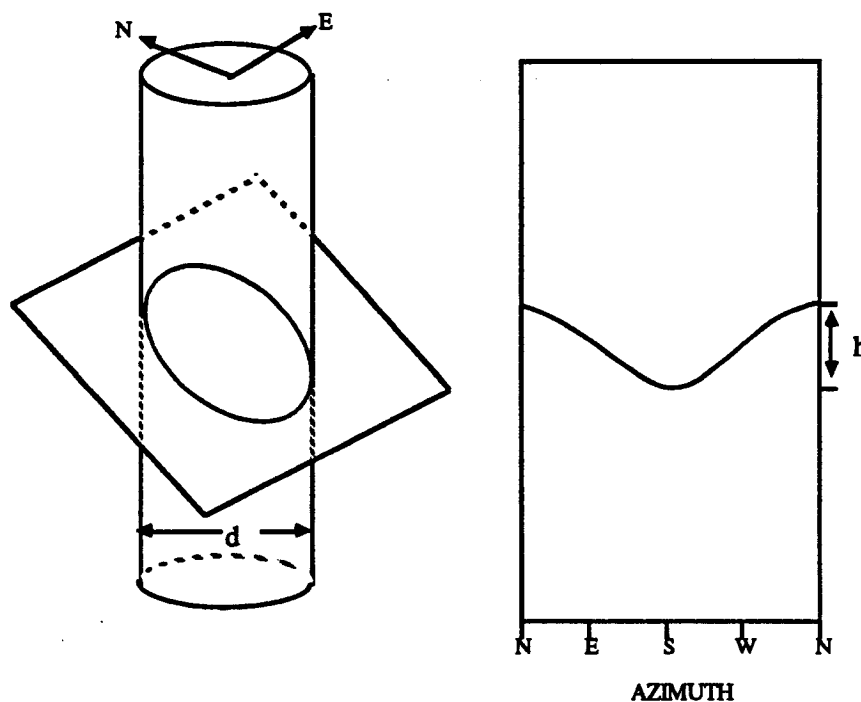
Figure 3. Intersection of a plane with a cylinder and the effective sinusoidal curve on the 2-D unwrapped cylindrical surface (after Zemanek, 1970).

Since BHTV data is multidimensional, both reflectivity and borehole radius are usually plotted with depth as unwrapped 360° images of the borehole wall. Planar features that intersect the borehole appear on the unwrapped 360° view as sinusoids (Figure 3, from Zemanek, et al., 1970). In Figure 4, nearly vertical fractures that strike about 180° are associated with low reflectivity values and large values of borehole radius. Interpretation of BHTV data involves the display of different borehole features in an optimal geometry so that they can be viewed and most accurately measured. The cylindrical geometry of the data is best represented by polar cross sections of the data scans or isometric cylindrical projections (Figure 5). Intervals of the data may be
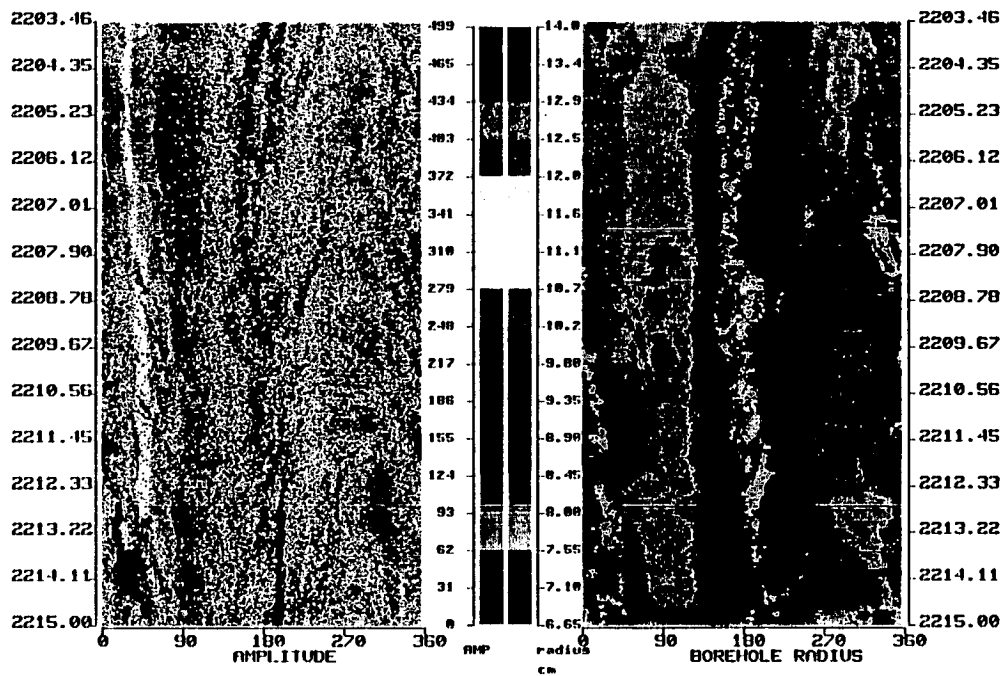
Figure 4. Standard unwrapped 360° images of the borehole wall. Vertical axis is depth, horizontal axis is azimuth, and color represents the amplitude of the reflected pulse (left panel) or the borehole radius (right panel).

selected from the 2-D unwrapped image and plotted in either polar or cylindrical projection. The radius of the cylinder is modulated by the borehole radius value at each pulse providing a true scale reconstructed image of the borehole wall. Scrolling of the data in polar cross section allows a rapid view of borehole shape changes with depth. Three dimensional wire frame cylindrical projections of the data show fine detail of the borehole wall not visible in conventional 2-D displays. Figure 5 shows a two meter interval over a hydraulic fracture in well G2 located in the Nevada Test Site. Fine scale bedding features are visible as are fine fractures dipping at 45°. The cylindrical projection may be scrolled vertically to view the reconstructed image with depth or horizontally to rotate the image 360° degrees. The surface of the cylindrical or polar projections can be color modulated by amplitude values in their spatial position for a composite image of the data. Figure 6 shows the effect of the amplitude values plotted in its correct spatial position at the borehole wall over a cross-bedded interval in a well located in the Gulf Coast.

The software maps the data values to a false color palette. Data may be represented either by a linear color scale or an enhanced color scale which performs histogram equalization of color over the range of values in the data. Histogram equalization generates an image that utilizes the available brightness levels equally and produces a display of higher color contrast which can accentuate features not visible in a linear scale. As shown in Figure 7, due to the extreme variability in data, value ranges and data quality, these two color maps do not provide the optimum display for interpretation in all cases. For this reason an additional feature was implemented that allows the palette hues to be interactively manipulated to expand or reduce the color range as needed for optimum enhancement. The same image over an eleven foot section of a Gulf Coast well in Figure 7 shows the effects of histogram equalization. The left image has a linear color distribution and the right image has an equalized color map. Histogram equalization has been an extremely useful method to enhance details of the borehole wall for the majority of BHTV data analyzed. The images can also be displayed in grey scale which can be a more intuitive interpretive tool using simple light to dark grey shades to indicate increasing values in the data.

STANFORD ROCK AND BORELHOLE GEOPHYSICS PROJECT
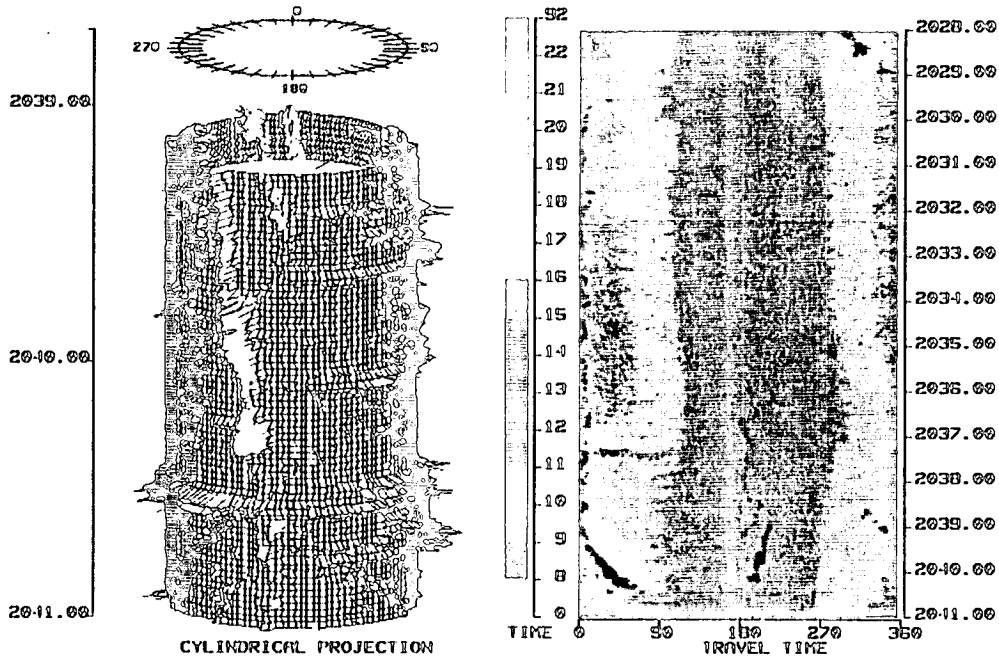
Figure 5. Left panel shows a cylindrical projection of a two foot interval of the G2 well located in the Nevada Test Site showing an induced hydrofracture and fine scale features not visible in the standard views. Travel time is used to modulate the radius of the cylinder to show the topography of the borehole. Right panel is the standard 0° - 360° unwrapped view of the travel time of the reflected pulse.
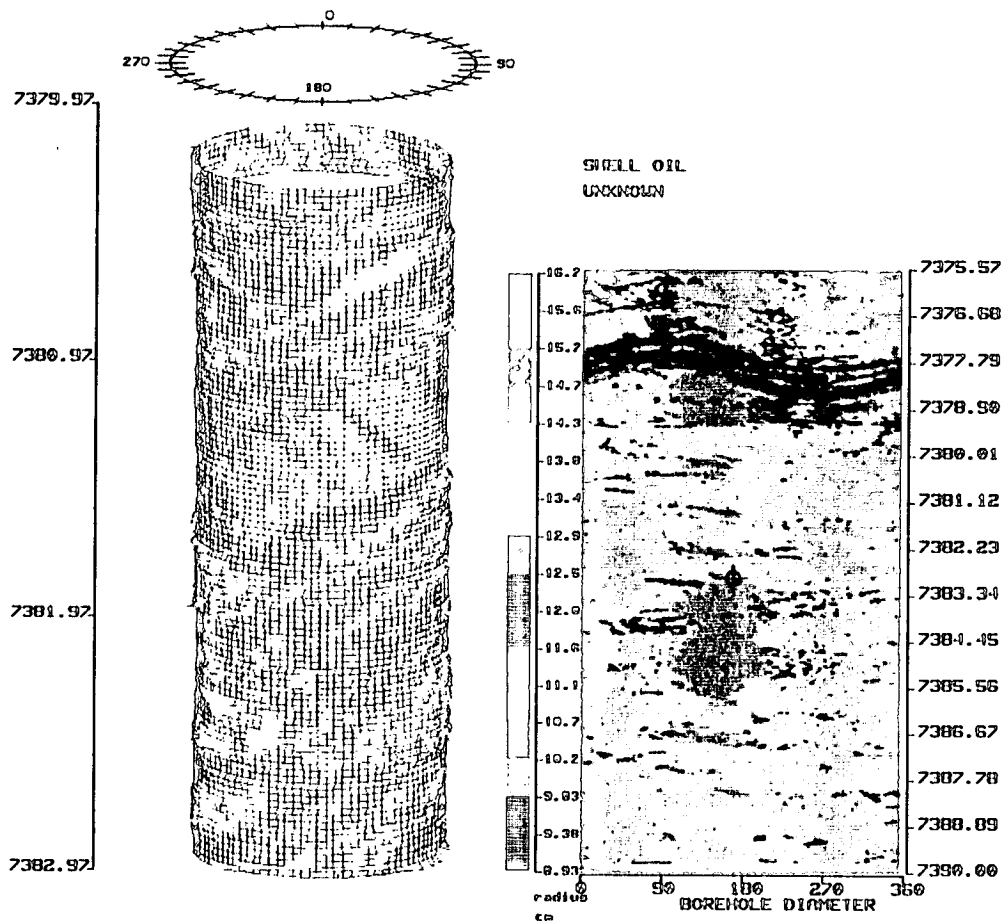
Figure 6. Left panel is a cylindrical projection of a three foot interval of a Gulf Coast well where reflectivity values have been plotted in their correct position at the borehole wall. The alternating bands of color represent cross-bedding in the sandstone/ shale lithology.
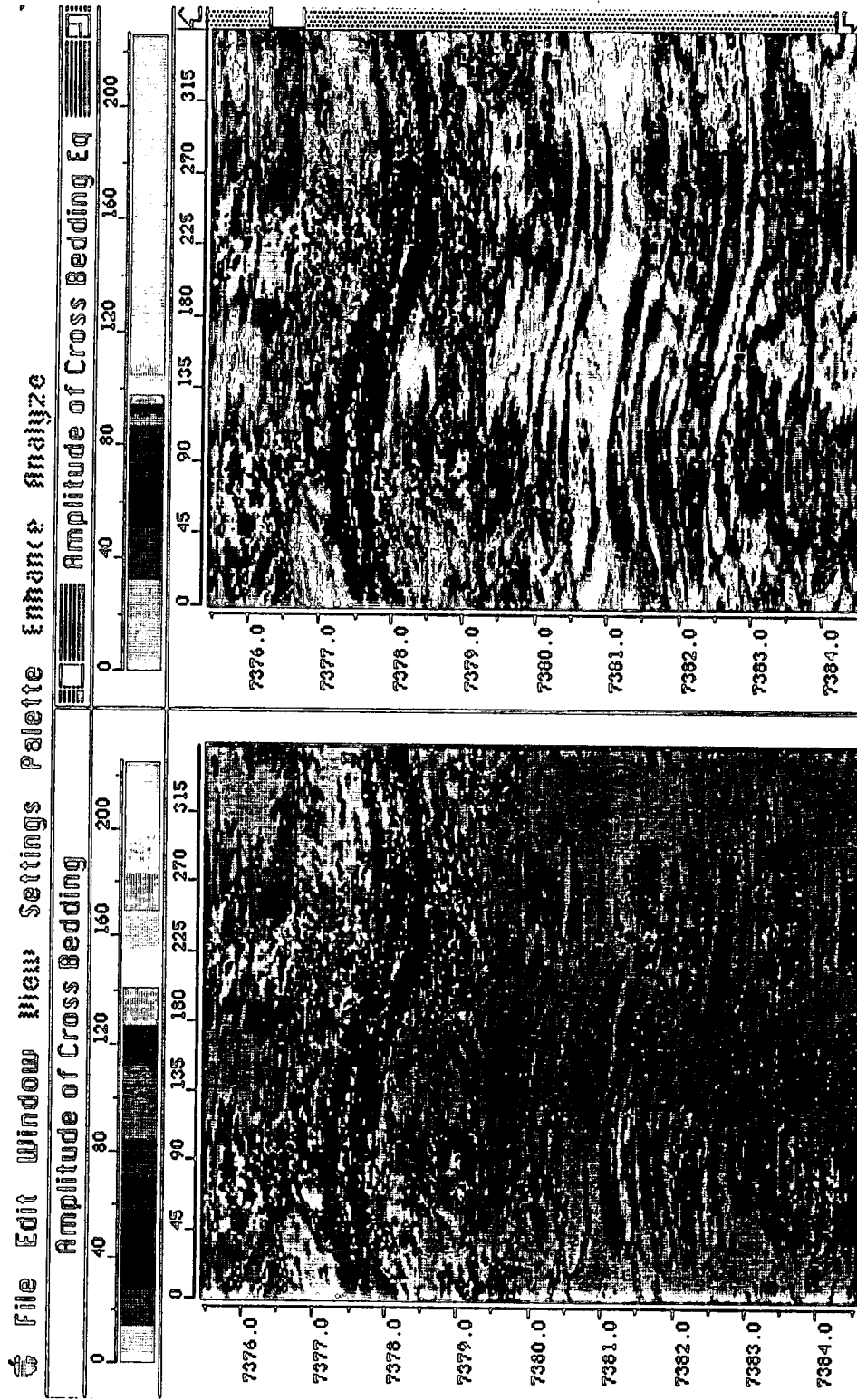
Figure 7. An example of the effects of histogram equalization. The left display shows the standard linear color distribution and the right panel the equalized color distribution. Note that the details of the cross-bedding are enhanced at depth 7380.5 feet using the equalized color scale.

Correction and Image Enhancement of BHTV Data

Standard Processing

Unfavorable logging conditions are a pervasive aspect of BHTV data acquisition. As with other image data there is a need to pre-process and edit data prior to interpretation to avoid erroneous conclusions and the masking of subtile features. This is particularly important where automatic fitting or feature analysis routines are implemented. The analog data acquisition onto video tape is very sensitive to human error as well as to poor borehole conditions. The mis-synchronization of recorder operation and winch operation can lead to missing or repeat log sections. When logging at sea ships heave is often not entirely mechanically compensated and data recorded at ocean drilling sites often show repetition of logged features. In addition, the tool may "stick" in the borehole for several rotations of the acoustic transducer then rapidly slip uphole creating a characteristic blocky image (Figure 8).

An interactive visual editing of the digital data has been implemented in the BHTV system to allow the user to delete data that should not be included in an interpretation. Figure 8 shows the application of this interactive editing on data collected at Hole 504B in the East Pacific Rise. The blocky intervals in the left image of unedited data correspond to repeat scanlines due to ships heave; the right image of edited data reveals an interval of stress-induced wellbore breakouts that cannot be distinguished on the unedited image.

Perhaps one of the most fundamental difficulties with BHTV data is random noise. Digitization of the analog signal amounts simply to the translation of a voltage inscribed onto the videotape into a number by the ADC. Spurious voltage surges can interfere with the threshold detection of the ADC clocks and result in anomalous spikes in the data. Scattering of energy due to the sampling geometry is a second major source of noise. As discussed below, the optimum raypath geometry consists of a centralized tool in a circular borehole where each incident pulse has normal reflection to the tool. Non-normal incidence of a stray pulse from a rough surface can create complex raypaths and multiple reflections which translate to anomalously high travel times and incorrect reflectivity values.

A median filter is used to mitigate these types of noise in the data. A median filter

- 14 -

ODP Hole 504B
East Pacific Rise
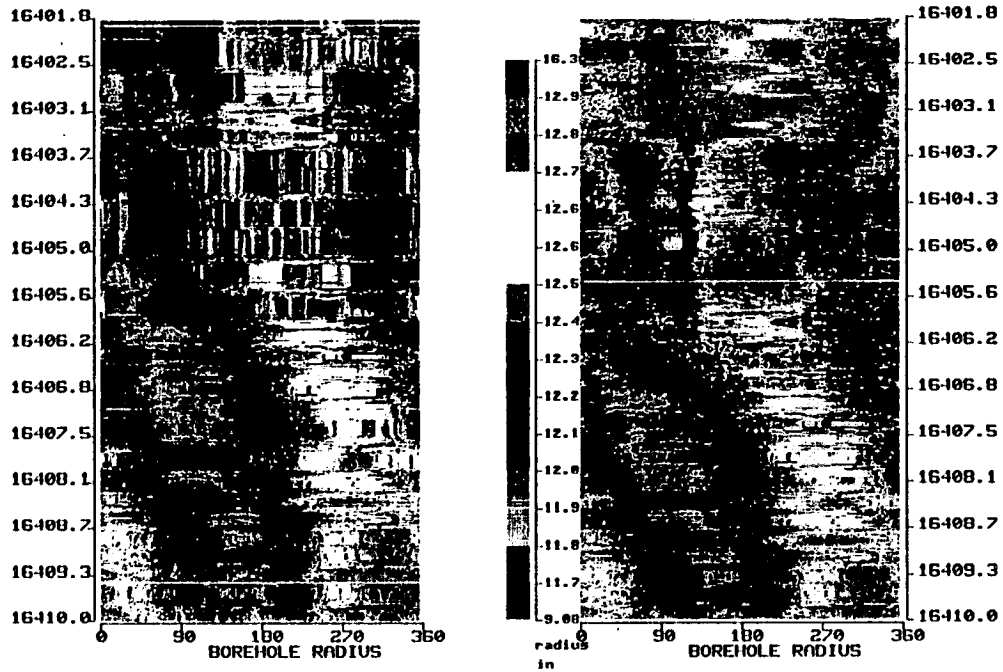
Figure 8. Left panel shows unedited BHTV data recorded in HOLE 642E located in the East Pacific Rise, right panel shows the results of visual data editing where breakouts are now visible in the data centered at azimuths 100º and 280º between depths 16,406 and 16,401 feet.

- 15 -

Cajon Pass
California
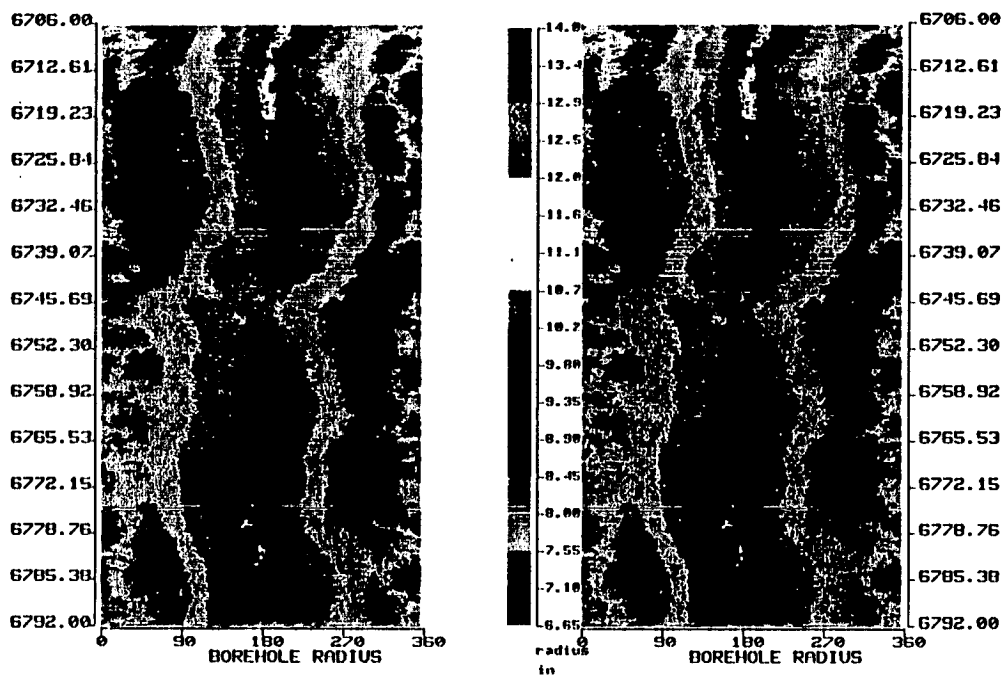
Figure 9. The right panel shows unfiltered data from the Cajon Pass well and the left panel shows the results of the application of a median filter. Note that the majority of the specks in the right panel have been removed in the left panel.

was selected among the myriad of smoothing operations in image processing because it is a smoothing in which the edges in an image are maintained. In median filtering a template is slid along the scans of data and the center value of the template is given the median value of all the values covered by the template. This type of filter is particularly good for removing impulse-like data because the pixels corresponding to noise spikes in their neighborhood are replaced by the most typical pixel in that neighborhood. A horizontal, three pixel template was determined to be the most appropriate for pre-processing BHTV data because it provides sufficient filtering while having the advantage of being the fastest type of computational sort for large image files (Richards,1986). Figure 9 shows the effects of a median filter on noisy data from the Cajon Pass well where the left panel has been filtered.

Low pass filtering and subtractive smoothing (high pass filtering) routines have been implemented as an aid in the detection of fine scale features. As is the case with the median filter these filters are horizontal and 1-D. In subtractive smoothing the data are low-pass filtered to attenuate all of the high frequency features, such as edges and lines, then the smoothed image is subtracted from its original resulting in a difference image which has only edges and lines substantially remaining. The enhanced definition of the cross bedding at depth 7380.5 ft in a Gulf Coast well (upper plot of Figure 10) is apparent when compared to the original data (lower plot of Figure 10).

Data intervals can also be plotted as a cross plot of amplitude (x axis) versus distance (y axis) to look for anomalous relationships in the two variables that could indicate the presence of a particular borehole feature or the need to make a geometric correction to to the data. There are expected relationships between reflectivity and travel time in the borehole, for example, low amplitude values and high travel time values within fracture zones, anomalous relationships such as high travel time and high amplitude isolated in a cross plot such as the upper plot in Figure 11 are the result of anomalies in the data. These plots can be used to interactively determine intervals of problematic data such as the off-center effects characteristic of the low travel time high amplitude cluster in Figure 11. After correction for off-center effects the cross plot shows a normal distribution of data (Figure 11, lower plot).
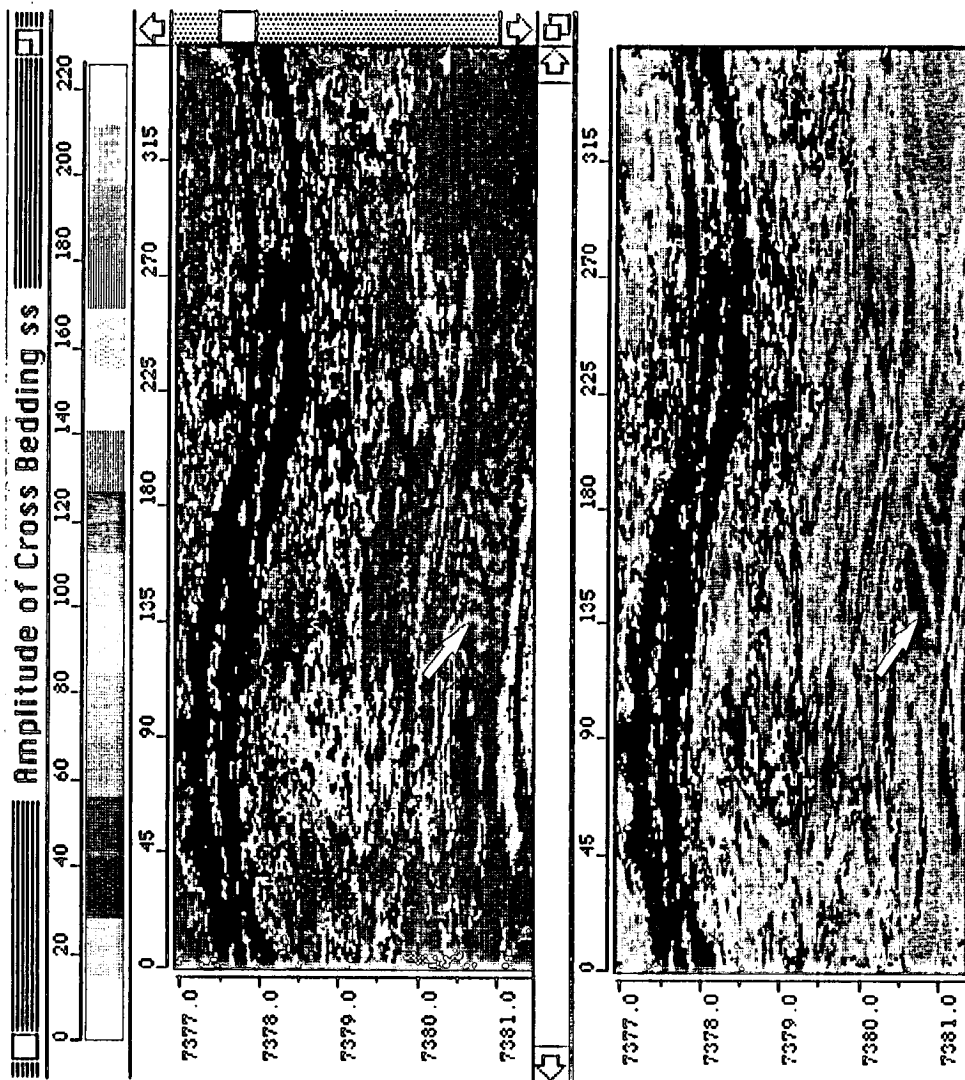
Figure 10. Bottom panel shows raw image data over a cross bedded interval from a Gulf Coast well. The top panel shows the results of subtractive smoothing. In the top panel enhanced texture appears in the cross beds at depth 7380.5 feet.
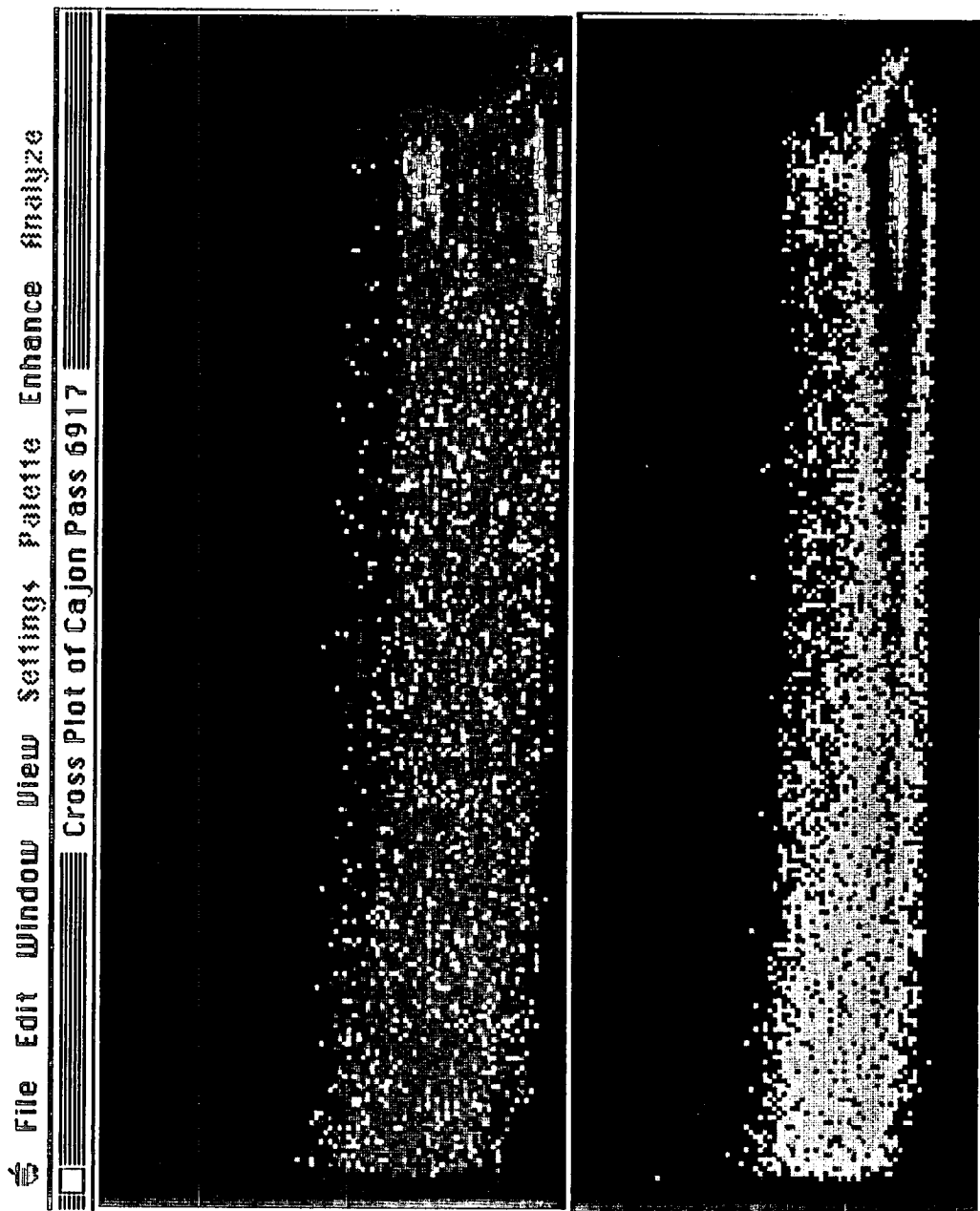
Figure 11. Cross plots of amplitude (x axis) and travel time (y axis) used to isolate anomalous features in the data. The upper plot represents data collected with an off-centered tool and the lower plot showing a more typical relationship between amplitude and travel time represents the data data interval after correction for off-center tool effects.

Geometric Corrections

Prior to the analysis and interpretation of BHTV data any distortions in the data due to signal noise or improper tool geometry must be corrected. The borehole televiewer is designed to acquire data with the tool vertically positioned in a vertical borehole. Bowspring centralizers are strung above and below the tool to stabilize the tool in the center of the borehole. Ideally the tool should be centrally located in a circular borehole. In reality, this optimum geometry is often not achieved. The possible raypaths for the BHTV pulse launched from the transducer are shown in Figure 12 (after Georgi, 1985). When the tool is significantly off-center in a circular drillhole vertical bands of missing data result from the non-normal incidence of the pulse at the borehole wall and subsequent deflection of the returned signal away from the transducer. An example of this phenomena is shown in Figure 39 below. A significant source of error in the interpretation of BHTV data can arise from the apparent location of borehole features

CIRCULAR BOREHOLE

CENTERED TOOL   OFF-CENTER TOOL

ELLIPTICAL BOREHOLE

CENTERED TOOL   OFF-CENTERED TOOL
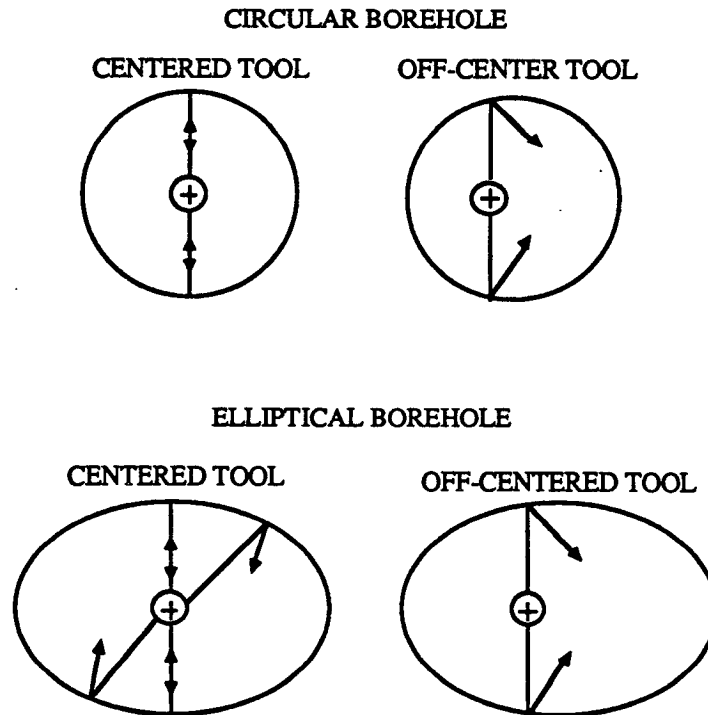
Figure 12. The possible raypaths for the BHTV pulse for circular and elliptical boreholes with centralized and off-centered tools (after Georgi, 1985).

from an non centered tool which has the effect of "moving" features to incorrect positions on the borehole wall. These effects can lead to miscalculated orientations of planar features as well as incorrect azimuths of features such as wellbore breakouts. The effects of elliptical boreholes is also a source of error in the measurement of planar features. This error is dependent upon the orientation of the ellipse and dip direction. If the long axis of the ellipse is coincident with the dip direction the dip is overestimated; if the long axis is perpendicular to the dip direction it is underestimated. (Georgi, 1986). Off-center tools in an elliptical borehole presents another, more complicated, geometric problem and the potential loss of a larger percentage of the returned reflection (Lysne, 1986).

Geometric corrections for decentralized tools in circular or elliptical boreholes are made using routines which find the true center of the borehole then calculate the corrected azimuth and radius for each reflected pulse. In the case of an off-center tool in a circular borehole the correction can be made by a relatively simple forward model. In an ideal circular borehole the point on the circumference with the minimum radial distance to the tool defines the tool position. In general borehole features complicate this ideal scheme and instead, an iterative search for the center is used to determine the true center. The minimum radius, r_{min}, is used to initially define the center of the borehole (Figure 13).
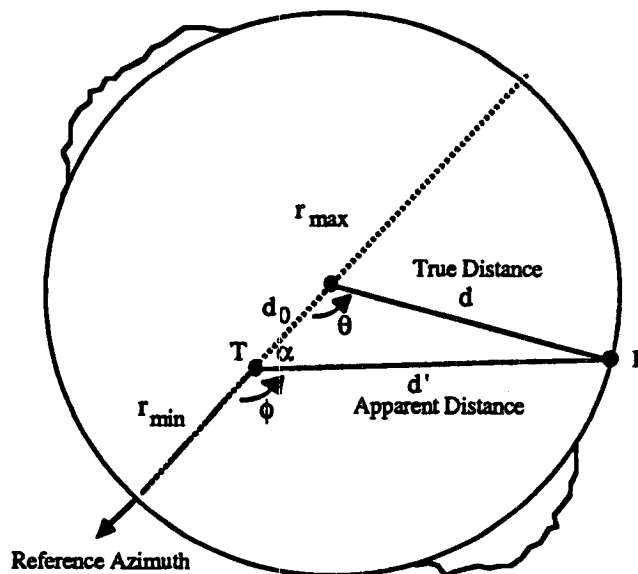
Figure 13. Geometry of the correction of BHTV data for the effects of an off-centered tool in a circular borehole.

Here d' is the recorded distance from the tool to the point P, d is the true distance from the center of the borehole to the point P, ϕ is the angle from the reference azimuth to the point P. The maximum radius, r_{max}, is taken as the diameter at the azimuth ϕ minus r_{min}. The distance the tool is offset from the true center, d_0, is simply $(r_{max} - r_{min})/2.0$. With this initial guess of the center of the borehole the radial distance, d, and angle to true center, θ, are computed for each pulse through:

$$d^2 = (d' - d_0 \cos \alpha)^2 + d_0 \sin^2\alpha \qquad (2)$$

$$\theta_0 = -(\phi + \pi/2) + \cos^{-1}(d_0 \sin \alpha) \qquad (3)$$

where $\alpha = \pi - \phi$ (see geometry in Figure 13)

The upper left plot of Figure 14 displays the borehole radius in polar cross section, the lower plot in cartesian cross section and the upper right plot as a histogram in a single window for the user to evaluate potential off-center problems. The bimodal distribution of the histogram of the borehole radius, in blue, and the curvature of the uncorrected cartesian cross section indicate this data is from an off-centered tool in a circular borehole. The application of this algorithm to data recorded with an off-centered tool in a circular borehole will be discussed below.

The initial estimate for the tool position is accurate only for featureless circular boreholes. To determine the correct center for circular boreholes where features with respect to tool location may result in a minimum radius that has no relationship to the true center, the new positions are used to iteratively determine the center of the borehole until the routine converges to the true center. When the difference between the current iteration and the previous iteration, δd_0, is zero the routine has converged. For most data sets convergence to the true center of the borehole occurs within 3 or 4 iterations. Figure 15 show successive iteration of the algorithm for two separate scans of BHTV data where the original data is plotted in black and the corrected data is plotted in red. The center point of both the original and corrected data is show by the crosshairs. For extremely variable data, where adjacent travel time values vary more than 35%, stability in finding the true center is achieved by evaluating successive d_0 values. The smallest value of d_0 within a given number of iterations was found to provide the best estimate of the true borehole center. Once the borehole center and radial distances are calculated for each pulse the routine interpolates the amplitude values to their correct spatial position.
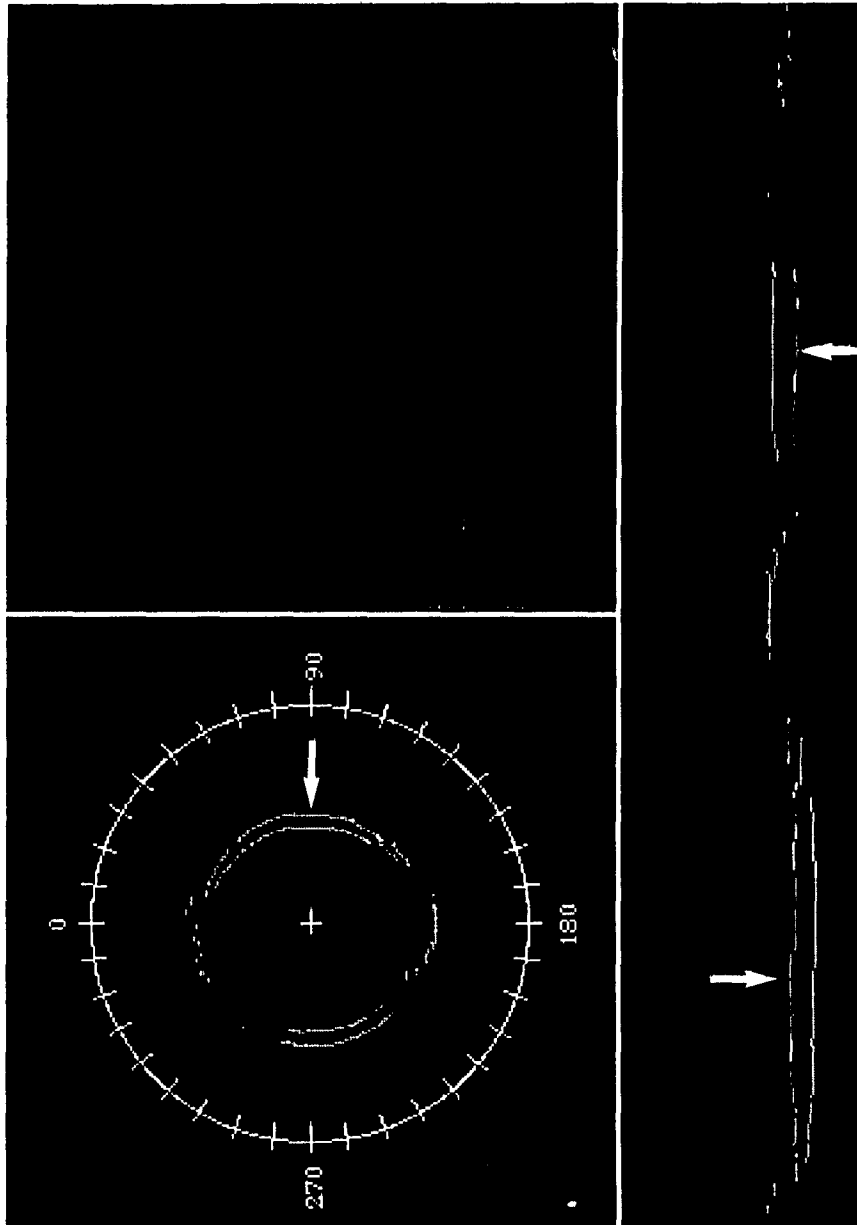
Figure 14. Workstation screen showing the interactive data correction of borehole geometric effects. Upper left polar plot shows original data scan and corrected (white arrows) scan of data. Histograms of the original travel time data (blue) and the corrected data (red) are shown in the upper right plot. The lower plot represents the original data and the corrected data (white arrow) in cartesian coordinates where the x axis is azimuth and the y axis is radius.
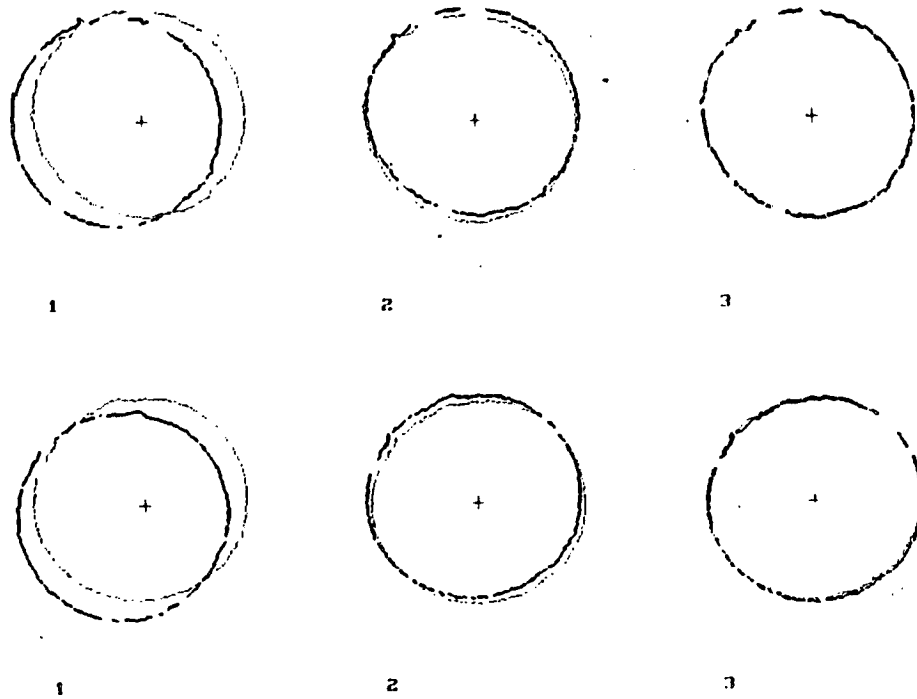
Figure 15. Iterative search for the true center in BHTV data recorded in an off-centered circular hole. The black scans represents the original data and the red scans the corrected data and the numbers correspond to the iteration number. Cross hairs mark the center for both original and corrected data.

In the more complicated case of an off-center tool in an elliptical borehole a Marquardt inversion is used to determine the tool distance and azimuth from the borehole center (after Lysne, 1986). This technique was found to successfully correct the data, however, field data recorded in an elliptical borehole with an off axis tool are rare and synthetic data had to be generated to test this algorithm. Figure 16 shows the geometry for this case where again d_0 is the radial distance of the tool from the center of the borehole, θ_0 is the angular distance of the tool from the reference azimuth, P is the position of the reflected pulse, d' is the recorded distance between the tool and the point P and θ' the azimuth of point P from the tool position. ϕ is the coordinate rotation between the recorded (primed) and the true (unprimed) coordinate systems and a and b are the major and minor axes of the ellipse.
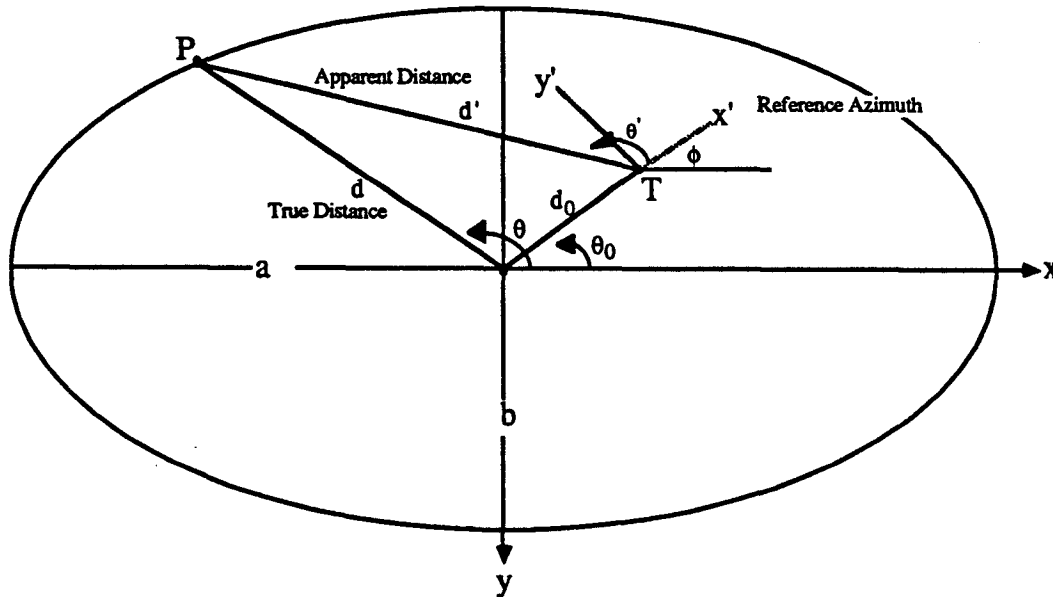
Figure 16. Geometry of an off-center tool in an elliptical borehole (after Lysne, 1987).

The inversion scheme sets up a forward model with:

$$d'= -d_0 b^2\cos \theta_0 \cos(\theta_0+\phi)+a^2 \sin \theta_0 \sin(\theta'+\phi))+ \qquad (4)$$
$$ab[d_0^2\sin^2(\theta_0-\theta'-\phi)+b^2\cos^2(\theta'+\phi)+a^2\sin^2(\theta'+\phi)]^{1/2}/b^2\cos^2(\theta'+\phi)+a^2\sin^2(\theta'+\phi))$$

Twenty equally spaced data points are extracted from a scan of data to build the data space for the inversion. Initial guesses of the parameters that define an array **p**

namely a,b, d_0, θ_0 and ϕ are determined; a and b through a simple max/min search of the data points, d_0 is set initially to $(a-b)/2$, θ_0 to 45° and ϕ at 30°.

The Marquardt (1963) algorithm minimizes the least squared error:

$$\Psi^2 = \| e - d' \| \tag{5}$$

by a simultaneous adjustment of the parameters of p

With $D_{ij} = \left(\dfrac{\delta d'_i}{\delta p'_j}\right)_{\theta i'}$

$$A = D^T D \tag{6}$$

$$g = D^T(e - d') \tag{7}$$

$$\delta p = (A + \lambda I)^{-1} g \tag{8}$$

where δp is the iterative change in the parameters p, λ is a number that changes with each iteration and I is the identity matrix. The algorithm approaches the steepest descents method of solving non-linear least squares problem for large λ and a Taylor expansion technique at small λ. Once convergence to the parameters p which fit the data values is reached these parameters are used to compute the new azimuth, θ, and radius, d, for each pulse. Convergence to the true center is typically reached within 6 iterations. Finally the amplitude data are interpolated to their correct spatial position at the borehole wall.

It was noted by Lysne (1986) that this inversion technique is unstable where the tool was off-center by less than 10% of the nominal borehole radius, in other words, as the tool approaches the center of an elliptical borehole the off-center direction becomes less unique. This was found to be the case when this algorithm was applied to field data where the tool was not sufficiently off axis in an elliptical borehole. As mentioned above, an appropriate data set recorded with a significantly off-centered tool in an elliptical borehole was not readily available. In order to test this routine on field data a section of data from the Cajon Pass well where wellbore breakouts are present was used to synthesize test data. The original field data was used as input to the forward model and forced to lie along an off-centered axis. The success of this algorithm applied to the synthetic data is shown in polar cross section in Figure 17 where the polar projection plotted in black is the synthetic data and the projection plotted in red is the corrected data. Again the crosshairs mark the center for both the original and corrected data. Note that this correction modifies both the azimuth and shape of the breakouts, features that are important to stress measurements.
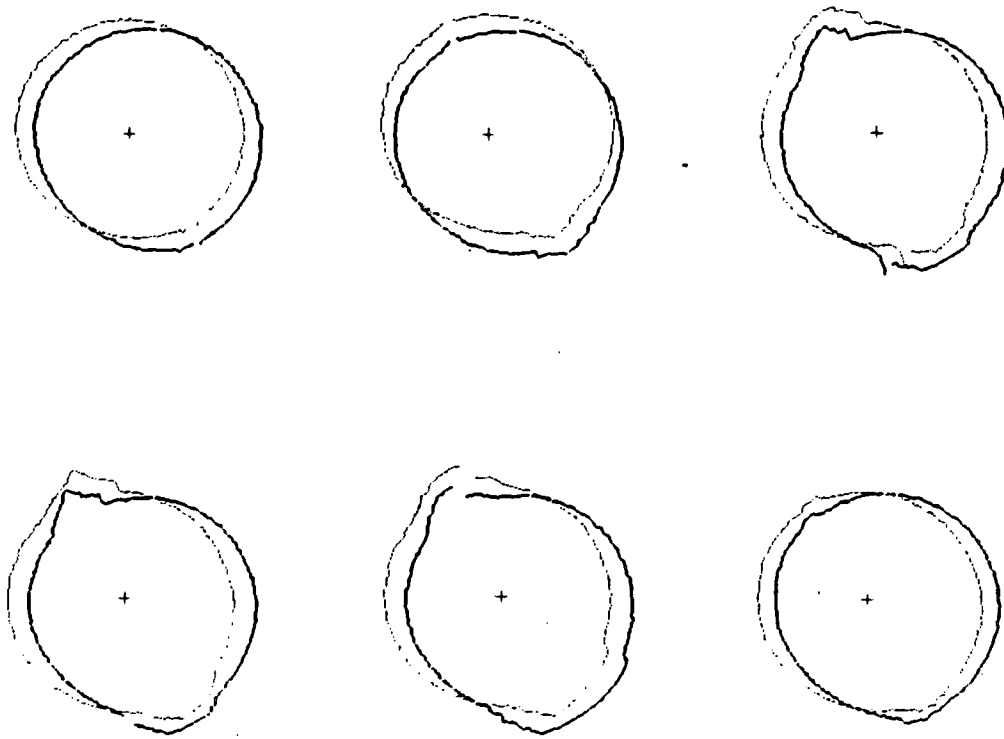
Figure 17. Polar cross sections are sample scans of the synthetic data (black) and data corrected of the effects of an off-center tool in an elliptical borehole (red). The cross hairs mark the center position for each scan.

Image and Data Processing

Borehole Shape

A detailed analysis of the digital data can be performed over a logged interval with this system to precisely measure borehole shape with depth. This routine was specifically developed for the analysis of wellbore breakouts (Barton, et al, 1988; Shamir et al., 1988) however, the algorithm can also be used to determine the precise azimuth of induced hydrofractures or other borehole features. Figure 18 is a conceptual drawing of the development of a breakout (see theoretical shapes in Zoback, et al., 1985) along with a plot of field data from the Cajon Pass well which demonstrates the picking technique. The sign convention for stress is positive compression. The greater travel time within the breakout defines the characteristic breakout shape. θ_b is the angle of breakout initiation with respect to S_{Hmax}. Several superimposed scans of travel time data (representing a

BREAKOUT DEVELOPMENT   BHTV FIELD DATA
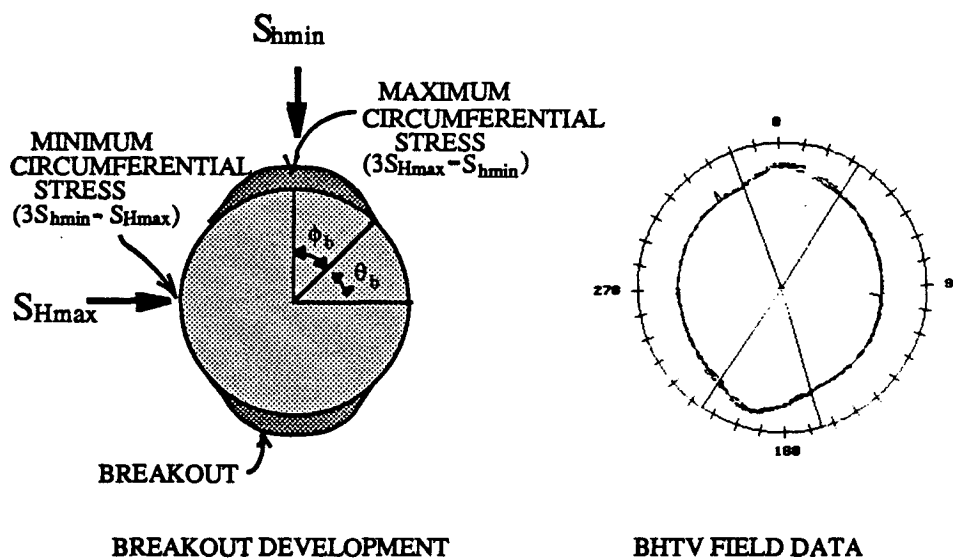
Figure 18. Schematic representation of the breakout process showing the angle of breakout initiation ϕ_b. Also shown is BHTV data over a breakout interval where polar cross sections delineate the breakout shape. The radial lines indicate the picks of breakout width. Breakout azimuth is the bisector of this angle.

vertical distance of several cm in the well) are plotted in polar cross section to allow measurement of breakout azimuth and minimum breakout width.

The minimum width of a breakout is a function of the initial failure of the borehole wall upon breakout formation and erosional effects on the initial shape of the breakout, such as fluid circulation or tool trips. Superimposing scans was found to be preferable to averaging scans in order to preserve the minimum width of the breakout over the vertical interval. The data are corrected for tool position and magnetic declination before plotting. The objectives of this analysis are to obtain precise breakout azimuths and the minimum breakout width and to utilize all of the recorded data. Figure 19 shows the systematic process of the data analysis where a 360° unwrapped view of the data interval is plotted in the right panel and successive polar cross sections of the borehole are plotted in the left panel. The user visually picks the breakout widths using a graphics mouse. Where there are continuous reflections from the broken out sections, as in the example in Figure 19, the breakout width is easily determined. The breakout width for each interval is picked interactively and stored in a data base for later statistical reduction. In the data analysis, the two sides of a breakout are picked independently. The two radial lines in Figure 19 represent the picked angle of the breakout width, the breakout azimuth bisects this angle. Breakout azimuth should coincide with the direction of least horizontal principal stress; breakout width is important for estimation of stress magnitude as discussed below.

Fracture Analysis

The primary use of BHTV data since it became operational in geophysical logging has been the measurement of the orientation and distribution of planar features in a drillhole. As mentioned, planar features that intersect the borehole appear on the unwrapped 360° view as sinusoids (see Figure 3). These sinusoids are often discontinuous for fine scale fractures and they can show very complex patterns at points where several fractures intersect or where fractures are not perfectly planar. At least three fractures intersect at depth 5135.5 ft in Figure 20. The circular features in Figure 21 are interpreted as curved fracture planes that enter and exit the borehole. The steeply dipping fracture at depth 149.2 m appears to merge with a shallow fracture above. It is important
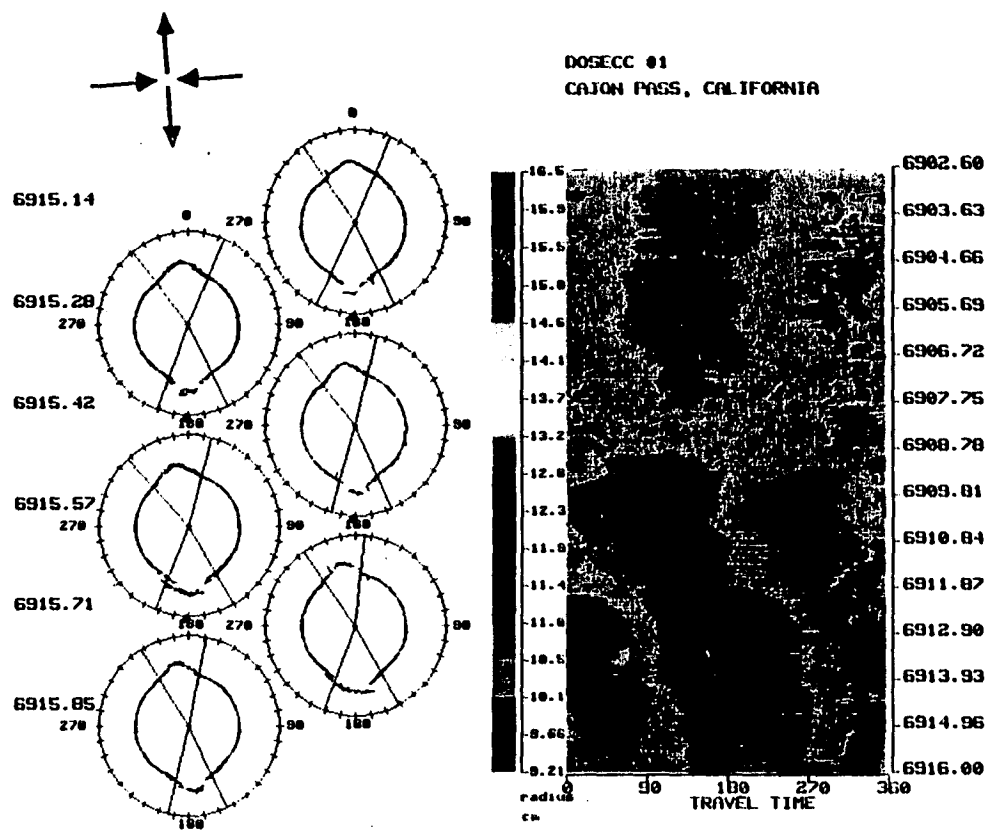
Figure 19. The right panel is an unwrapped 360° view of borehole radius over a 14 foot interval of breakouts in the Cajon Pass well. The left panel shows the interactive analysis of breakout azimuth and width for this data.
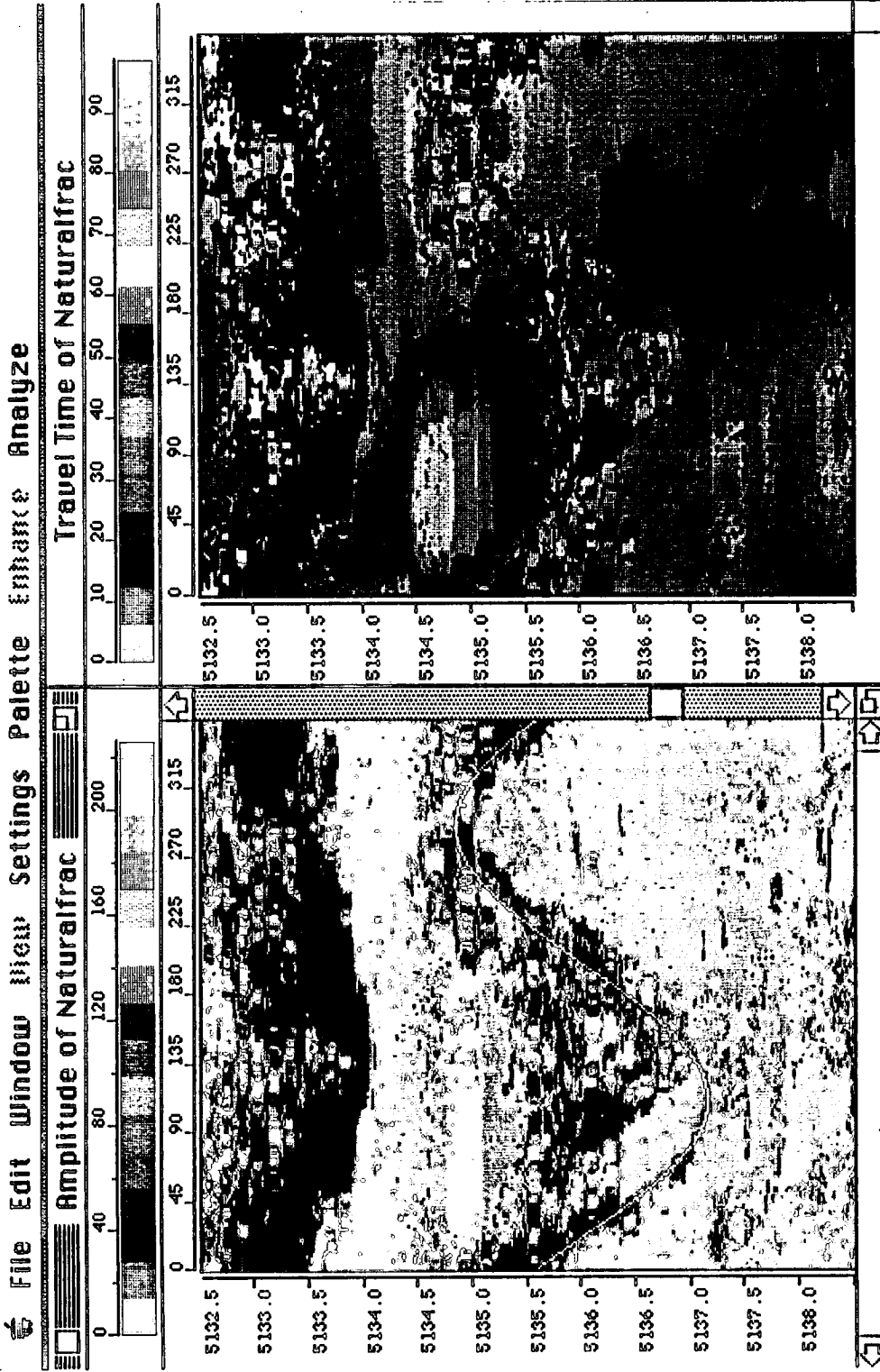
Figure 20. Intersecting fractures at depth 5135.5 feet in the Auburn Geothermal well, New York. White curve represents the interactive fit to a steeply dipping fracture.
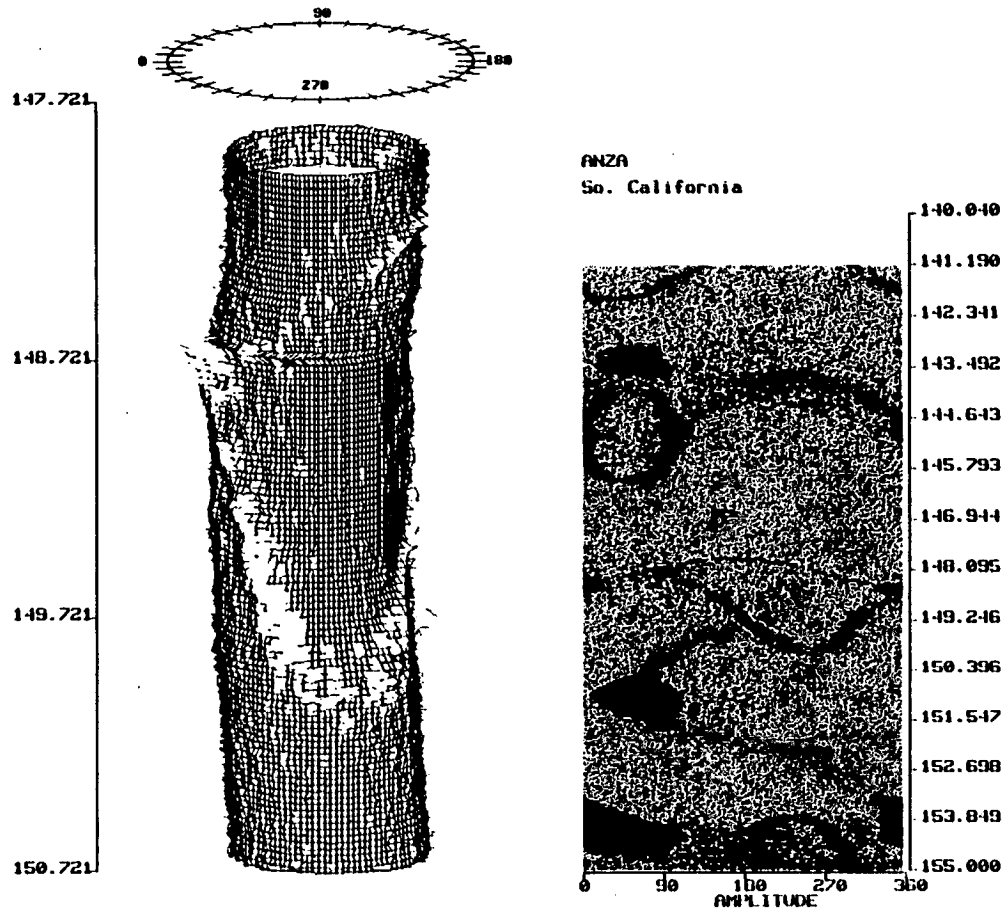
Figure 21. An example of a complex fracture zone where fractures are not perfectly planar in the Anza Well located in southern California.

in these cases to use the various enhancement techniques discussed above to best resolve the trace of the fracture before measuring its orientation. Because of the flexibility designed into the interactive analysis system different enhancement techniques can be explored until the optimum resolution of the fracture of interest is achieved before determining the fracture orientation.

The BHTV image of a fracture surface can be extremely irregular due in part to the true topography of the surface, the limits of the resolution of the transducer and to multiple reflections from within the fracture surfaces. Because the eye can often perform the best least squares fit to a curve within a complex network of fractures an interactive routine was implemented to measure the amplitude and phase of the sinusoid (Figure 20). The graphics mouse is used to drag an adjustable curve over the imaged fracture; up and down mouse movements controlling the amplitude of the sinusoid and left to right movements its phase. With the amplitude and phase of the sinusoid picked the strike of the plane is simply $90^o - \phi$ where ϕ is the minimum of the sinusoid. The dip angle, α is $\tan^{-1}$ h/d where h is the peak to trough amplitude and d the borehole diameter (see Figure 3). Interpreting fracture orientations using this interactive method reduces the possibility of errors from improperly fit sinusoids that can occur with other methods. It also aids in the detection of fracture planes not readily visible in the data. For example, in Figure 20 the trace of the steeply dipping fracture below the intersecting fractures at 5135.5 feet is not initially apparent; however placement of the flexible sinusoid reveals the fracture trace well below the intersection of the three fractures.

Fracture distribution and qualitative size can be determined through the systematic analysis of cylindrical wire frame projections of the data at a scale which preserves the correct aspect ratio (Figure 22). Three 3-D "core" images at 120° orientation over the same one meter interval are used to examine fine scale features in data that are not visible in the standard 2-D unwrapped view. Interactive graphics picks of feature depths and qualitative size are made creating a data base of fracture distribution that can be used to correlate with other log data. This technique is discussed more fully below where it has been applied to data from the Cajon Pass scientific well.

Alteration zones that characteristically surround a fracture are susceptible to damage in the harsh borehole environment. There is initial destruction of the fracture zone at its intersection with the drillhole by the drill bit followed by erosion from fluid flow, reamer tools and logging tool trips. This, combined with the limited distance range of the BHTV transducer means that fracture aperture as preserved in the BHTV log is at best an upper
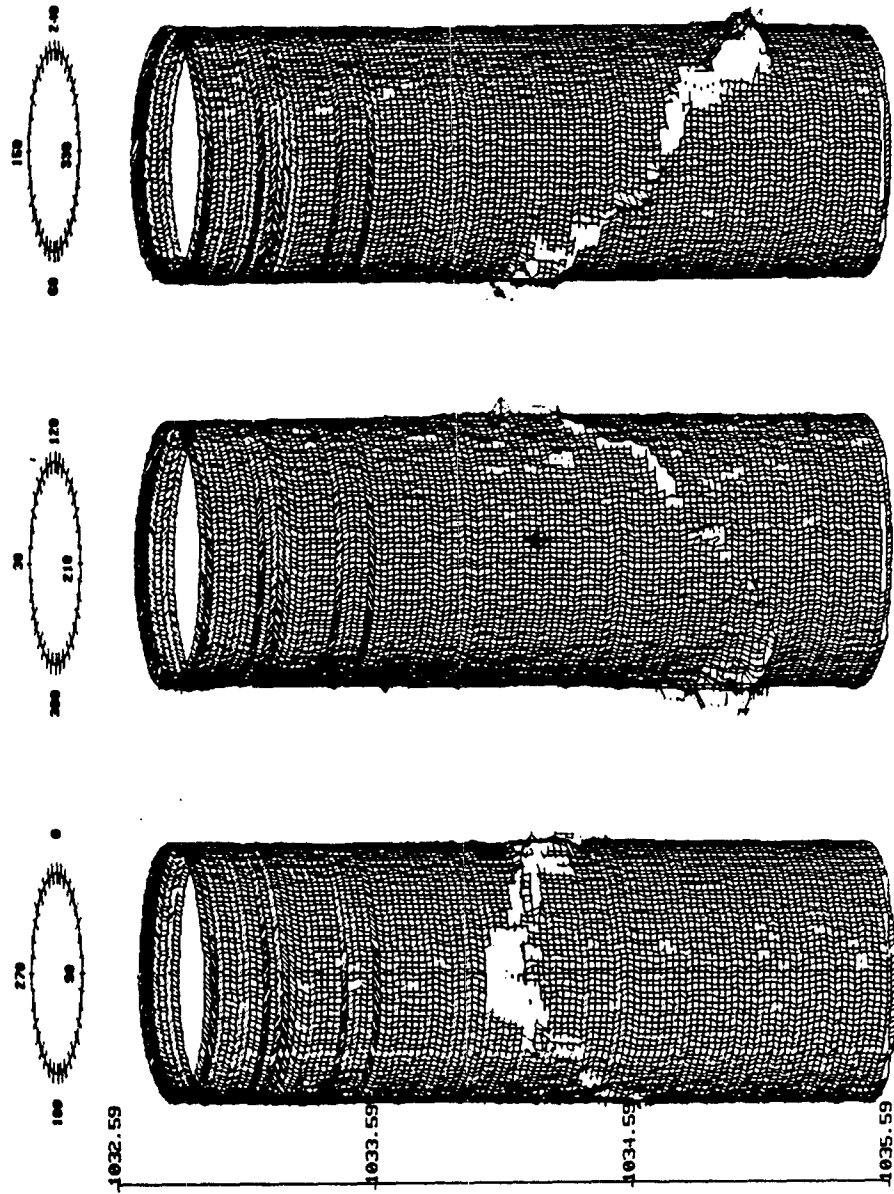
Figure 22. Cylindrical projections in three 120° views of a fracture from HOLE 753B in Atlantis fracture zone.

bound to the true aperture of the fracture at some distance away from the borehole. To a first order however, an estimate of true fracture aperture can be made using digital BHTV data. Plots of topographic cross sections through fractures generally show sloped fracture edges which break up as the acoustic energy is lost into the fracture zone (c.f. Figure 23, sections 1, 2 and 7). The detection of fracture topography is somewhat dependent upon the tool gain setting used during logging being better preserved at higher gain. The term "apparent fracture aperture" is used in this text to describe the minimum width of fractures as they appear in BHTV data.

Measurements of apparent fracture aperture can be made in two ways. Both methods require the prior measurement of the orientation of the fracture plane to correct for apparent dip. With the amplitude and phase of the sinusoid determined, the wire frame "core" image can be rotated into the plane of the fracture and the fracture width can be measured on the rotated image. Figure 24 shows the curve fit to a zone of small fractures in the Cajon Pass well and Figure 25 the rotation of the core image into the fracture plane. Measurements of apparent fracture aperture can be made across the fracture gap in this image. An alternative method for measuring apparent fracture aperture utilizes the unwrapped 360° views of BHTV data (Figure 23). Cross sections constructed normal to the sinusoid are plotted at several points along the fracture in the left image. The user can interactively pick the apparent aperture from these cross section. The red horizontal lines in Figure 23 indicate the pick of fracture aperture. Multiple measurements across the fracture give a more accurate estimate of fracture aperture.
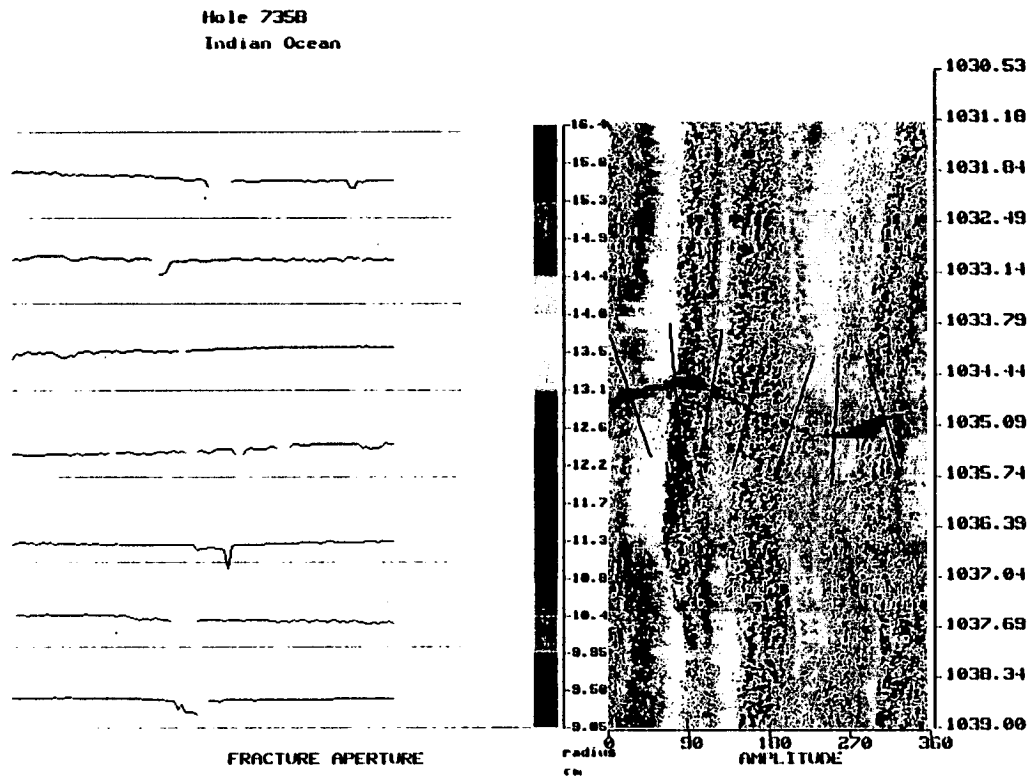
Figure 23. Right panel show the reflectivity over a 9 meter interval of ODP Hole 735B in the Atlantis Fracture Zone. Left profiles are cross sections of the fracture showing the apparent fracture aperture.
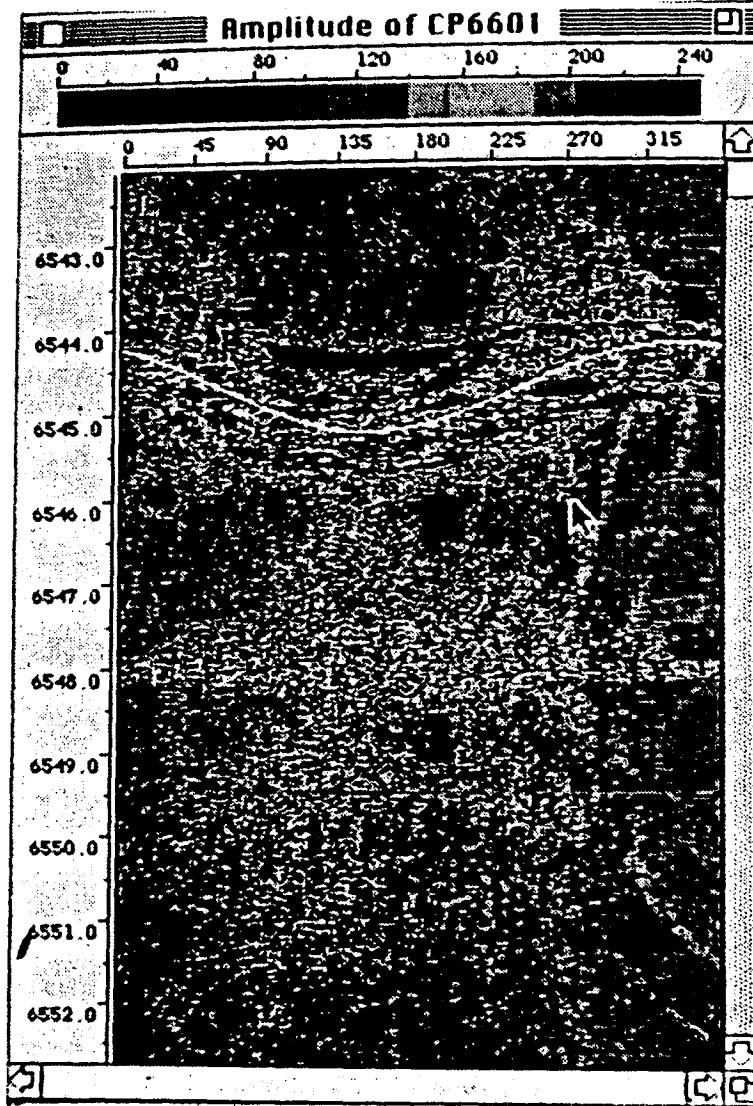
Figure 24. Interactive fit of a flexible sinusoid to a shallow dipping fracture at depth 6544 feet in the Cajon Pass well.

Figure 25. Rotation of the "core" image of the fracture of Figure 24 into the plane of the fracture to permit measurement of fracture with corrected for apparent dip.

Caliper Analysis

    The system generates "logs" of variations in downhole parameters that can be
quantified by the BHTV such as caliper, wellbore ellipticity and formation reflectivity.
These logs may be correlated with full waveform, resistivity and other diagnostic logs.
Digital televiewer data provides geophysical logging with extremely fine scale caliper
information. Caliper tools usually have two to four mechanical arms that measure the
borehole diameter with depth whereas the BHTV log has several hundred "arms" and
provide data at a scale that is 15 times finer than the standard caliper log. A routine was
developed to provide caliper log data from the digital BHTV scan. The algorithm
performs a fit of an ellipse to the data by taking a running derivative of neighboring
pulses to find the maxima and minima that define the major and minor axes of and
ellipse. This routine also preserves the orientation of the principal axes of the ellipse and
is substantially faster than a least squares approach. Figure 26a shows the fit to an ellipse
for a scan of data from the Cajon Pass well where data is continuous across the breakout
interval and Figure 26b shows data from a geothermal well in Auburn, New York where
the acoustic energy has been lost across the breakout interval. In both cases the routine
can approximate the elliptical shape of the borehole and preserve the orientation of the
major and minor axes. The algorithm performs well over these small intervals of missing
data (e.g. breakouts), however, it is not robust for poor quality data where more than
one quadrant of continuous data pulses are missing. Figure 27 shows the log data
created from the caliper analysis of an interval of the Auburn Geothermal well from 4823
to 4835 feet. The "logs" include the major, a, and minor, b, axes of the elliptical fit to the
data, the percent eccentricity, defined as $\frac{a-b}{(a+b)/2}$, and the orientation of the major axis of
the ellipse with depth. Caliper information in this form can be easily correlated with other
log data. The major axis of the ellipse in many cases corresponds to the direction of
minimum horizontal principal stress and in such a log provides a rapid method for the
analysis of breakout orientation with depth (c.f. the cluster of points at azimuths 0° and
180° in track 4, Figure 27). Also computed are the borehole volume useful for
calibrating other logging tools like the Schlumberger spectral analysis tool. The rightmost
profile represents the average reflectivity value over this depth interval as discussed
below.

Cajon Pass
California
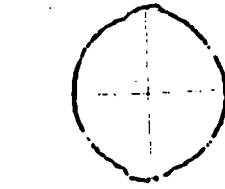
64.27
56.52

64.67
54.92

AUBURN GEOTHERMAL WELL
AUBURN, NEW YORK

87.37
60.87

85.02
81.02

Figure 26. Polar cross sections of BHTV data with a fit to an ellipse (red) for the measurement of borehole caliper; a) represents data with continuous reflections across a breakout and b) data where the signal is not returned from the breakout and the data are discontinuous.
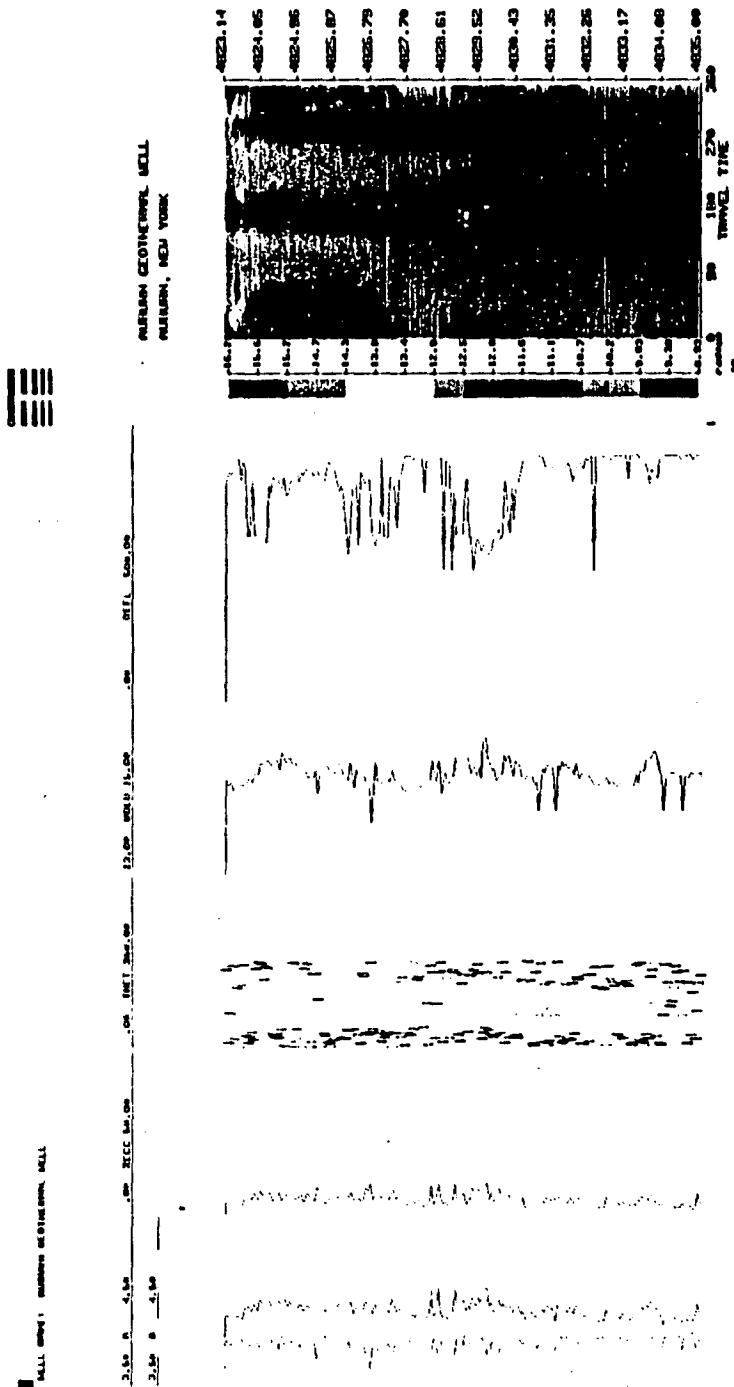
Figure 27. "Log" data produced from the BHTV image. Plotted in track 1 are the a and b axes of the elliptical fit, track 2 shows the eccentricity, track 3 the orientation of the ellipse, track 4 the borehole volume, and track 5 the reflectivity profile.

Acoustic Reflectivity

The piezoelectric transducer of the BHTV is a thin circular disk; for conditions of perfect cylindrical geometry the disk surface and the observation plane are parallel. Assuming a Fresnel approximation, the radiation pattern can be modeled as the spatial Fourier transform of the transducer pattern (Castleman, 1979) where the displacement at the point (x_i, y_i) on the borehole wall is (after Rubel, et. al, 1986):

$$U_i(x_i, y_i) = 2 \left| \frac{J_1 (\pi\tau/\tau_0)}{\pi\tau/\tau_0} \right| \qquad (9)$$

where J_1 is a Bessel function of the first order, $\tau = \sqrt{x_i^2 + y_i^2}$ and $\tau_0 = \dfrac{\lambda d}{a}$ and where a is the transducer diameter, λ the wavelength and d the distance to the borehole wall. For a given transducer, as the beam width at the borehole wall increases, the resolution decreases. Assuming the reflected waves from the borehole wall are generated as secondary point sources distributed over the reflector area, the pattern of the reflected beam is calculated in the same way as the incident beam and is similar to the width of the incident beam.

Acoustic reflectivity of the borehole wall as measured by the BHTV tool has incorporated the effects of the impedance contrast from various rock types and the borehole fluid along with the effects of scattering of the energy from irregularities in the borehole wall. Because the true reflection amplitude is proportional to the reflection coefficient at the borehole wall plus an unknown variation in amplitude due to scattering (the angle between the beam and the reflecting surface), no quantitative value of the reflectivity can be associated with a particular lithology. Because of the combined effects however, the BHTV image of the amplitude of the reflected energy often shows more detail than does the surface topography. This is particularly true for logged intervals of sedimentary rock where rock properties vary over small distances. A 3D wireframe image with reflectivity values superimposed in color has become an important interpretative tool. Figure 6 shows a cylindrical projection of a two foot interval through a cross-bedded sequence in a Gulf Coast well. The reflectivity values have been superimposed on the topographic reconstruction of the core and show more variability than the corresponding travel time image indicating that the impedance contrast over

this interval exceeds the small variations in the travel time due to the differential erosion of the interbedded sand and shale.

To determine the reflectivity value to represent a given depth interval a histogram of the amplitude values is computed for each scan. A single scan in the BHTV data has values that represent the reflectivity of unperturbed rock as well as reflectivity values associated with structural or erosional features (fractures, tool reamer marks). To sample only the intact rock a user determined cutoff reflectivity value is used above which histogram bins will be used to compute the mode value of the amplitude for each data scan as a single representative value. Figure 28 shows the results of this statistical approach to an interval containing the contact between a basement marble formation and an overlying sandstone unit at 5049.7 ft in the Auburn Well, New York. The marble has a very different reflectivity character that the overlying sediment and the contact can be more easily picked in the "log" plot than in the image itself. Another use of the reflectivity data is to plot the reflectivity values as a log plot for correlation with companion log data. Presented in Figure 27 was the reflectivity profile over a zone of breakouts in the Auburn Geothermal Well in New York, depth correlated with the BHTV image over the same interval 4823 to 4835 ft. Sharp decreases in reflectivity track the breakout zones exactly and the decrease is proportional to the width of the breakout. Reflectivity logs have proven to be quite useful for correlation with other log data to isolate borehole features such as breakouts and fractures. Using reflectivity logs generated from the analysis of BHTV data Zoback and Moos (1988) found that low reflectivity values correlate with breakout zones in the Moodus Research Well in New York state and that reflectivity profiles used in conjunction with the BHTV caliper log are useful for discriminating between natural through going fractures and wellbore breakouts. A sharp low reflectivity response associated with a strong kick in the eccentricity log characterizes a natural fracture whereas low reflectivity values over a finite length of the borehole associated with a consistent azimuth of the major elliptical axis generally represents breakout zones.
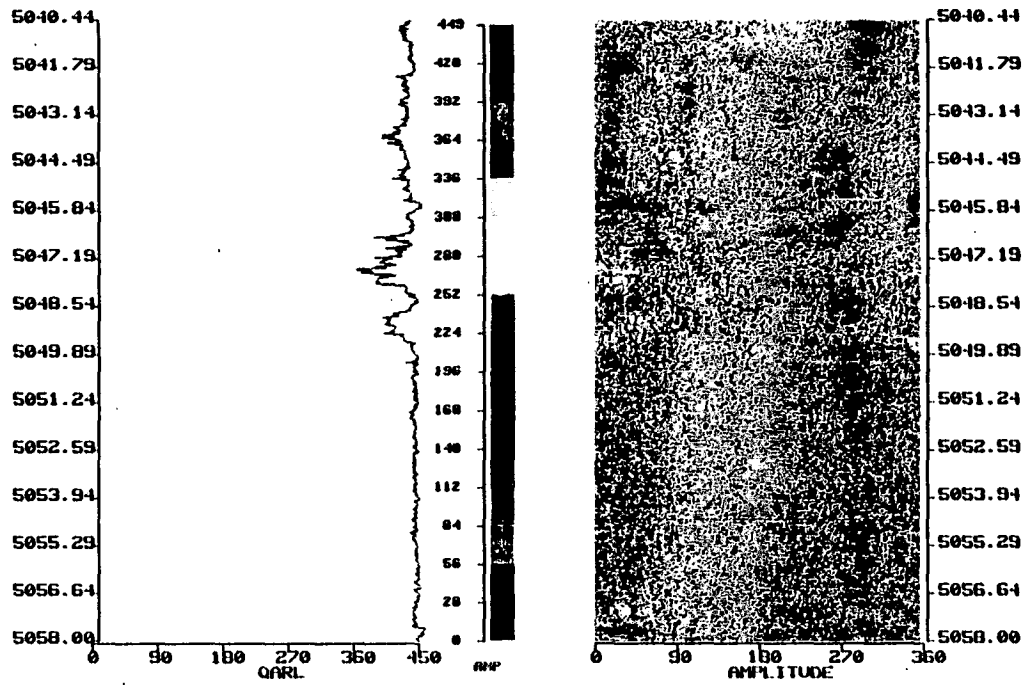
Figure 28. Log plot of reflectivity values over the contact between the basement marble formation and the Potsdam sandstone from data recorded in the Auburn Geothermal Well, New York.

Comparison of BHTV and FMS Data

A recently developed borehole imaging tool, the Formation Microscanner (FMS) (Ekstrum, et al., 1987) has standard dipmeter capabilities and is equipped with four orthogonal 8 X 20 cm pads containing twenty-seven 5 mm diameter buttons which make contact with the borehole wall and measure the formation resistivity. The resistivity values measured at discrete points provide a vertical image as strips of the borehole wall (see Figure 29). The vertical and horizontal resolution of the FMS is 2.5 mm with a lateral span of 7 cm. The image coverage of the tool is completely dependent on borehole size. A single pass through a 30 cm diameter borehole will generally cover 30% of the total borehole azimuth. Repeated passes of the tool can often be used to form a composite image with greater azimuthal coverage. Grey scale images are generated in which the gray level at each pixel represents the current density at that point.

The FMS responds to conductivity changes in the formation surrounding the borehole, and is specifically sensitive to the presence of fractures and microcracks in their varying degree of alteration. The depth of penetration of the resistivity probe is on the order of a few centimeters and the FMS tool responds to variations in rock properties such as porosity or pore chemistry that the BHTV is not capable of detecting. The resolution of the FMS exceeds that of the BHTV and can be used to map fine scale features such as foliation planes and finely interbedded intervals with depth.

The horizontal resolution of the FMS is comparable to the horizontal resolution of the BHTV, however, the vertical resolution of the FMS generally exceeds that of the BHTV by 7:1 depending on the speed of logging. A linear interpolation of the BHTV data can be used to generate an expanded image that can be directly compared to the FMS data. Analysis of the two images in this way provides vertical verification for the BHTV data and permits filling in of the azimuthal gaps in the FMS data. A vertical linear interpolation routine was developed for the BHTV data where adjacent points are iteratively calculated through nearest neighbor resampling:

$$P(i,j') = j' \, P(i,j+1) + (1-j') \, P(i,j) \tag{10}$$

until the appropriate scale of the FMS data is reached. This resampling was found to preserve the correct image geometry and brightness level.
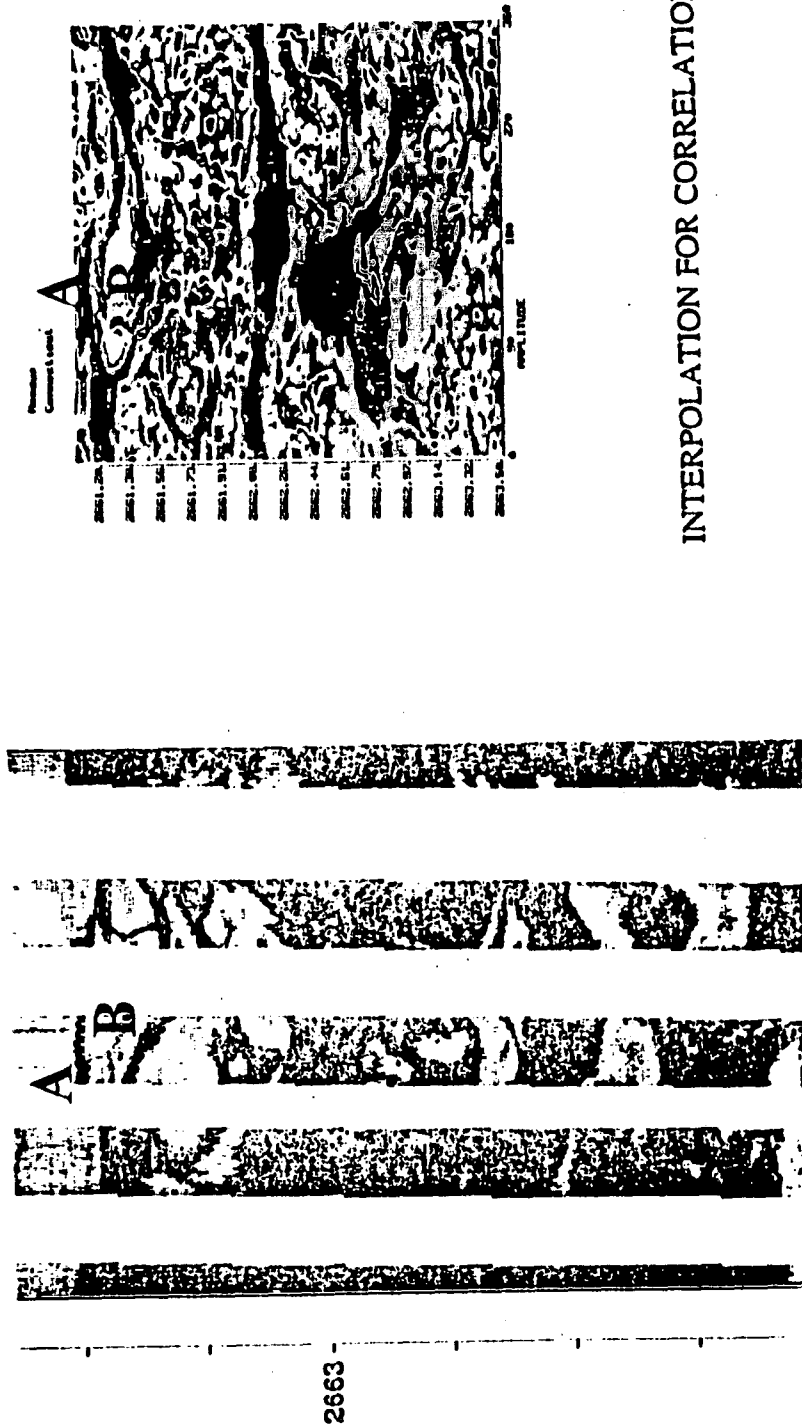
Figure 29. Comparison of FMS (left) and interpolated BHTV data (right). Fractures (A) and variations in rock properties (B) correlate well between the data sets.

Figure 29 shows a comparison of BHTV reflectivity data expanded to the scale of the FMS from data collected in a well located in Moodus Connecticut. Although the black features marked "A" in the FMS data of this figure are disconnected by missing azimuthal data, the corresponding feature can be easily seen in the BHTV data. Grey scale variation in the FMS data , "B", can also be correlated to reflectivity variations in the BHTV data. The lower section of available paper logs of the FMS data recorded in the Moodus well are unfortunately of too poor quality to discern the fracture at 2662.08 in the BHTV image. With digital FMS data it would be possible to constrain the interpolation of the BHTV data to information over the same interval from the FMS tool and to generate a composite image.

Correlation of BHTV Data with Standard Logs

Log interpretation has long been the basis for discriminating changes in lithology, fluid content of pore space, structural horizons and general physical properties of rock both for industry exploration and scientific research. Geophysical logs that are generally recorded in a freshly drilled well include the caliper, natural gamma, spectral natural gamma (from which K, U, and Th concentrations can be determined), induction resistivity, neutron porosity, gamma-gamma density, and sonic travel-time. Correlation of these logs and extracted core provides an ideal set of information for the measurement of physical properties of rock with depth.

BHTV data provides information at about 0.3 inch intervals whereas typical logging produces a data point for every 6 inches of wellbore. For this reason, analog BHTV images are commonly photo-reduced to the scale of log data (5" = 100') before correlations can be made. As mentioned above interpretation of analog BHTV images usually involves overlays and tedious drafting. Digital data provides several advantages over analog data for this type of coarse scale interpretation of BHTV data and for correlation with standard logs. The first is the simplicity of scaling with a minimal loss of information. The second advantage is in the ease of constructing an interpreted BHTV log. In a coarse scale analysis only the large scale features such as breakout intervals or through-going fractures are required for interpretation. The location of these features can be plotted in black and white plots of amplitude and borehole radius where black represents a feature and all other variations in the data have been suppressed into a white background (Figure 30, right profiles). To achieve this effect an interactive plotting

routine was developed to produce BHTV data decimated to the log scale of 5"=100'
where a user specified threshold of reflectivity is used below which all reflectivity pixels
will be black and above which reflectivity pixels will be white. Similarly, a radius
threshold is used above which pixels will be black and below which they will be white.
Adjustment of these thresholds to an optimum level produces an interpreted BHTV
image. Fractures may also be interactively picked and the interpreted sinusoids plotted.
Figure 30 shows standard logs over the interval 9600 to 9800 feet recorded in the Cajon
Pass well with the corresponding digitally interpreted section of BHTV data. Major
features include wellbore breakouts represented by discontinuous black zones at 180°
azimuths and fractures. Fractures often do not have a continuous trace in BHTV data and
can be elusive at this minute scale, however, they represent all of the features in these
reduced logs excluding breakouts. The reflectivity log over this interval shows far more
detail then the log of borehole radius primarily due to scattering effects over breakouts
and fractures in the reflectivity logs.

A preliminary interpretation of this interval was performed by F. Paillet (written
communication, 1988). The continuous interval of wellbore breakouts below depth 9800
ft is evident on the caliper log (Figure 30, track 4, curve 1) and the elongation of the
borehole is very pronounced in the x-y caliper log (Figure 30, track 1, curves 1 and 2).
The fracture zone just below depth 9700 has caused a marked decrease in both the LLS
and LLD resistivity curves (Figure 30, track 2, curves 1 and 2) however this zone has a
minimal effect on the neutron porosity logs (Figure 30, track 4, curves 2 and 3). Severe
breakouts at 9665 ft cause an anomaly in the caliper (Figure 30, track 4, curve 1) and
density logs (Figure 30, track 3, curve 3). Between 9600 and 9650 ft breakouts are
interrupted by small fractures; breakouts often terminate at the intersection of a fracture.
It is interesting to compare the digital interpretation of BHTV logs with an interpretation
made from the black and white Polaroid field logs by a scientist who is very familiar with
BHTV data and very experienced in log interpretation. In addition, this particular
"expert" has artistic talents useful to this sort of data reduction. Figure 31, an
interpretation of BHTV data over the interval 9,350 to 10,350 feet in the Cajon Pass
well, was sketched by F. Paillet (written communication, 1988). Thick lines represent
the interpreted trace of larger fractures visible in the analog records and thin lines the
trace of smaller fractures. Breakouts are again represented by vertical black bands.
Figure 32 is the digital counterpart to this interpretation over the same depth interval.The
location of fractures on the digital section compares well with the individual fracture
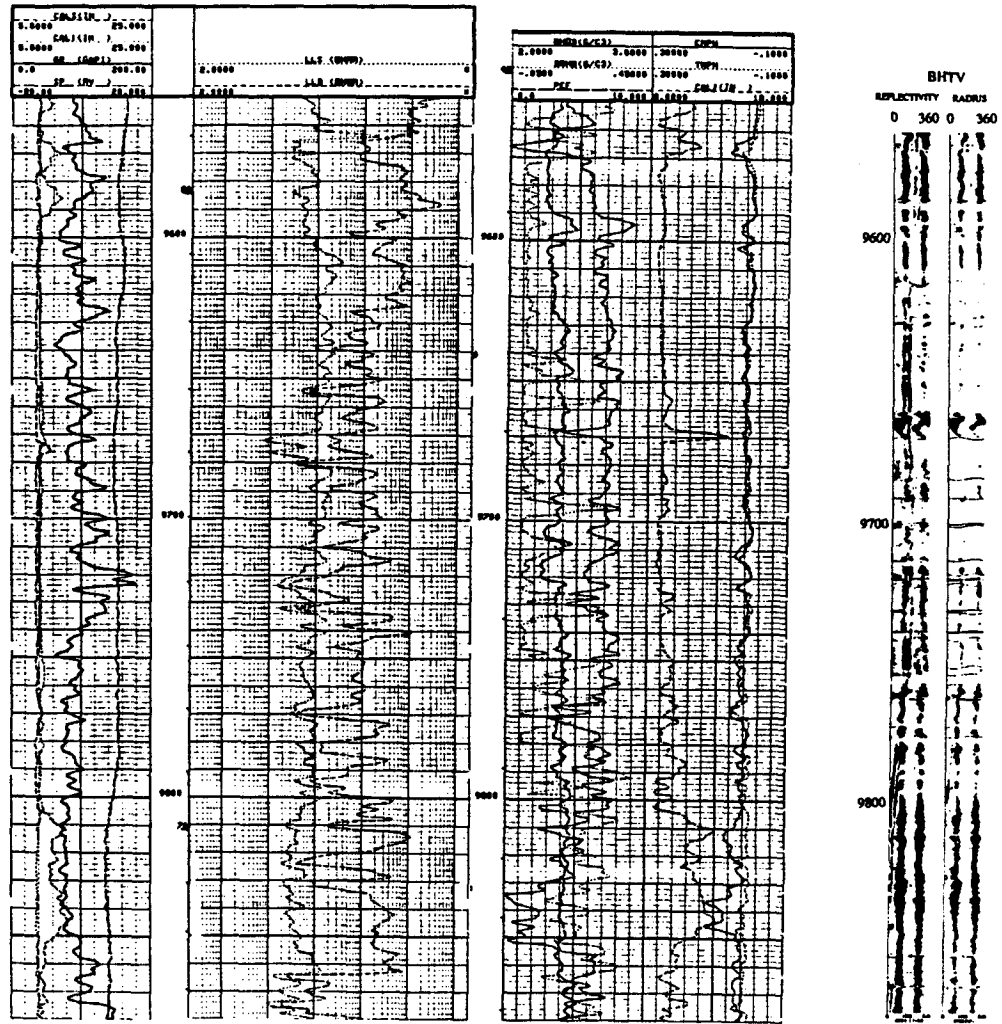
Figure 30. Standard Schlumberger logs over the interval 9600 to 9800 meters in the Cajon Pass well correlated with BHTV data recorded over the same interval.
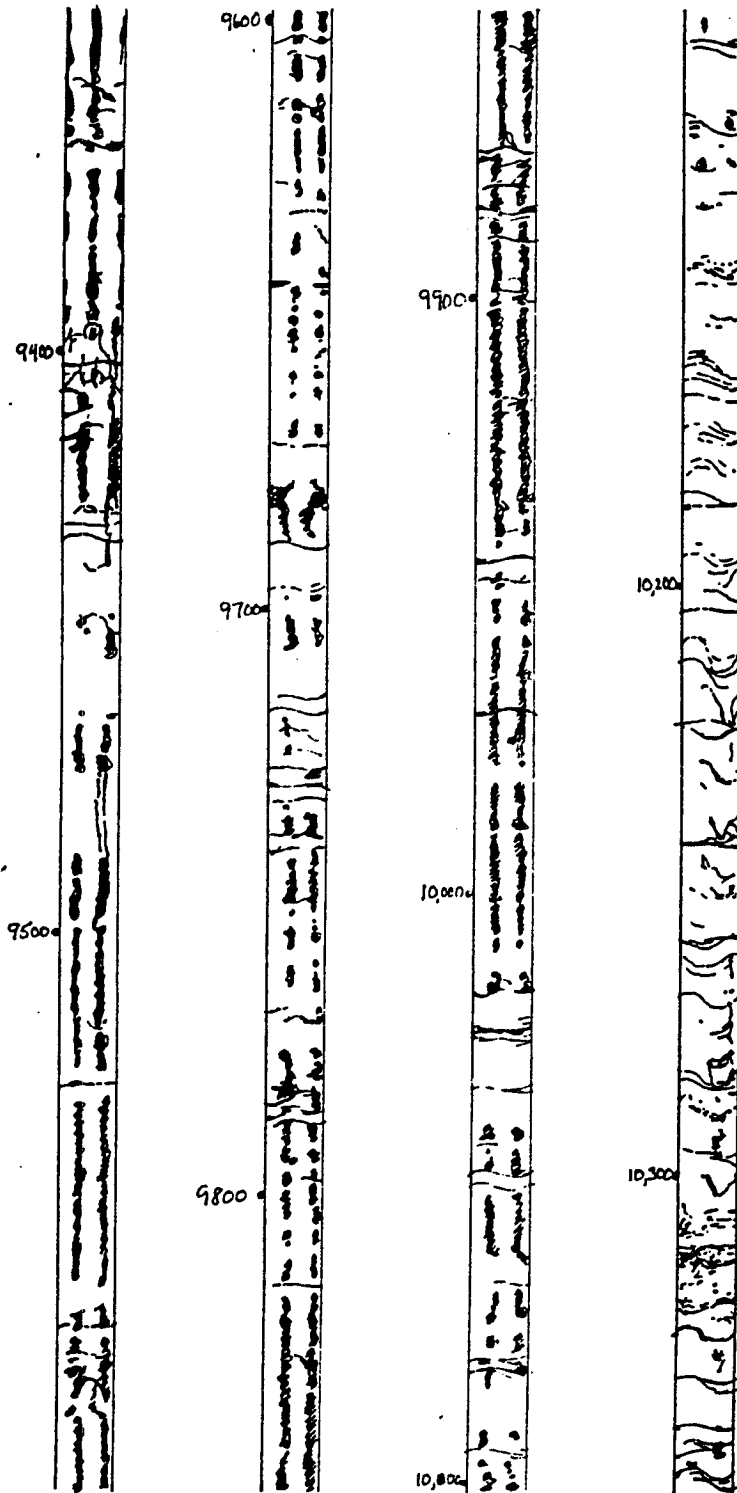
Figure 31. Manual interpretation of BHTV field logs over the interval 9,300 - 10,300 feet in the Cajon Pass well.

picks in the manually interpreted section. Breakouts reduce with good precision and correlate very well with the manually interpreted section. The most logical use of the digital interpretation is to provide an easily generated, accurate base plot either for further computer based interpretation or manual interpretation. Scientists that lack substantial experience with interpreting BHTV data or general log interpretation (or artistic capabilities) can produce more reliable interpretations with the help of the digital BHTV system.

CAJON PASS DIGITAL BHTV ANALYSIS
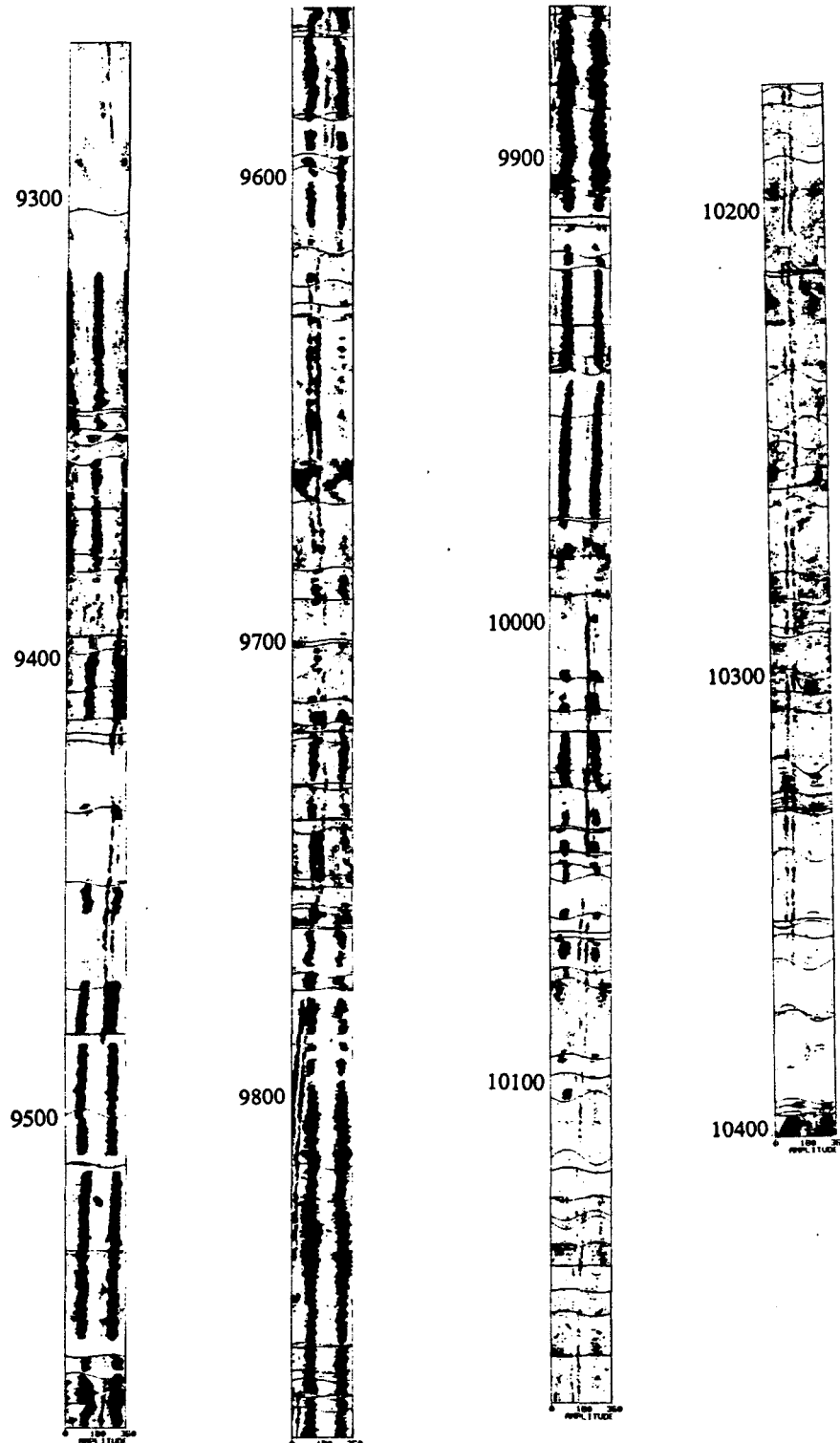
Figure 32. Digital interpretation of BHTV data over the interval 9,300 - 10,300 feet in the Cajon Pass well.

Animation of BHTV Data

Digital BHTV data from an interval of the Cajon Pass well has been transformed
to a video movie to explore the potential of animation for data interpretation. The
animation shows a core-like reconstruction of the BHTV data at various depth of interest
in the well where features such as fractures and breakouts are examined. Image frames
are expanded to an appropriate scale and slowly rotated to observe a feature's 3D
expression. The first step in animation, referred to as modeling, involves translating the
data into cylindrical geometry, similar to that used for the wireframe images of Figures 4
and 5, where the radius value is used to modulate the radius of the cylinder and the
amplitude of the reflectivity is used as the surface color value. Coordinates of the
cylindrical projection become center points of a connected mesh of irregular polygons.
The next step in the animation process is rendering, where each of the polygon elements
in 3D space are mapped to a 2D space (the video screen), and where coloring and
shading is performed. Shading each polygon involves calculating the surface normal
from a fixed light source to determine the color saturation and brightness. The polygon
surfaces are also textured and highlighted during rendering. The final steps in the
rendering process are smoothing of the polygon edges by interpolation and an accounting
of hidden surfaces that may be blocked by other surfaces in the line of sight of the
perspective view.

The BHTV animation was generated at 30 frames per second. Each scanline of
data contains about 420 points in the Cajon Pass data and each frame contains about 75
data scans resulting in approximately 63,000 polygons per animation frame. A test tape
was generated for successive data frames over the depth interval 1829 m to 2114 m in the
Cajon Pass well in which three 120° views of the data were rendered on each frame in
order to isolate interesting depth intervals and to choreograph the motion that would best
display each feature (zooming, rotations, etc). Over 7000 separate frames were required
to produce the final animation with a computer time cost of about 58 CPU hours on an
Allient, Inc. supercomputer.

Figures 33 through 35 show representative frames from the animation. The
broad, flat topography of a breakout at 1869 m is shown in Figure 33. A wide natural
fracture dipping at about 45° is shown in Figure 34 and Figure 35 represents the BHTV
image over the interval of a borehole diameter size change from $8\frac{1}{2}$ to $6\frac{1}{2}$ inches. The

resolution of these images greatly exceeds that possible with other media. The computer rendering of the data at such a fine scale shows detail that cannot be achieved with wire frame projections. This new technology also provides a powerful means to produce data in a format that can be easily interpreted by scientists and the non-scientific community. This animation work was done in conjunction with the N.S.F. National Center for Supercomputer Applications in Champaign, Il.
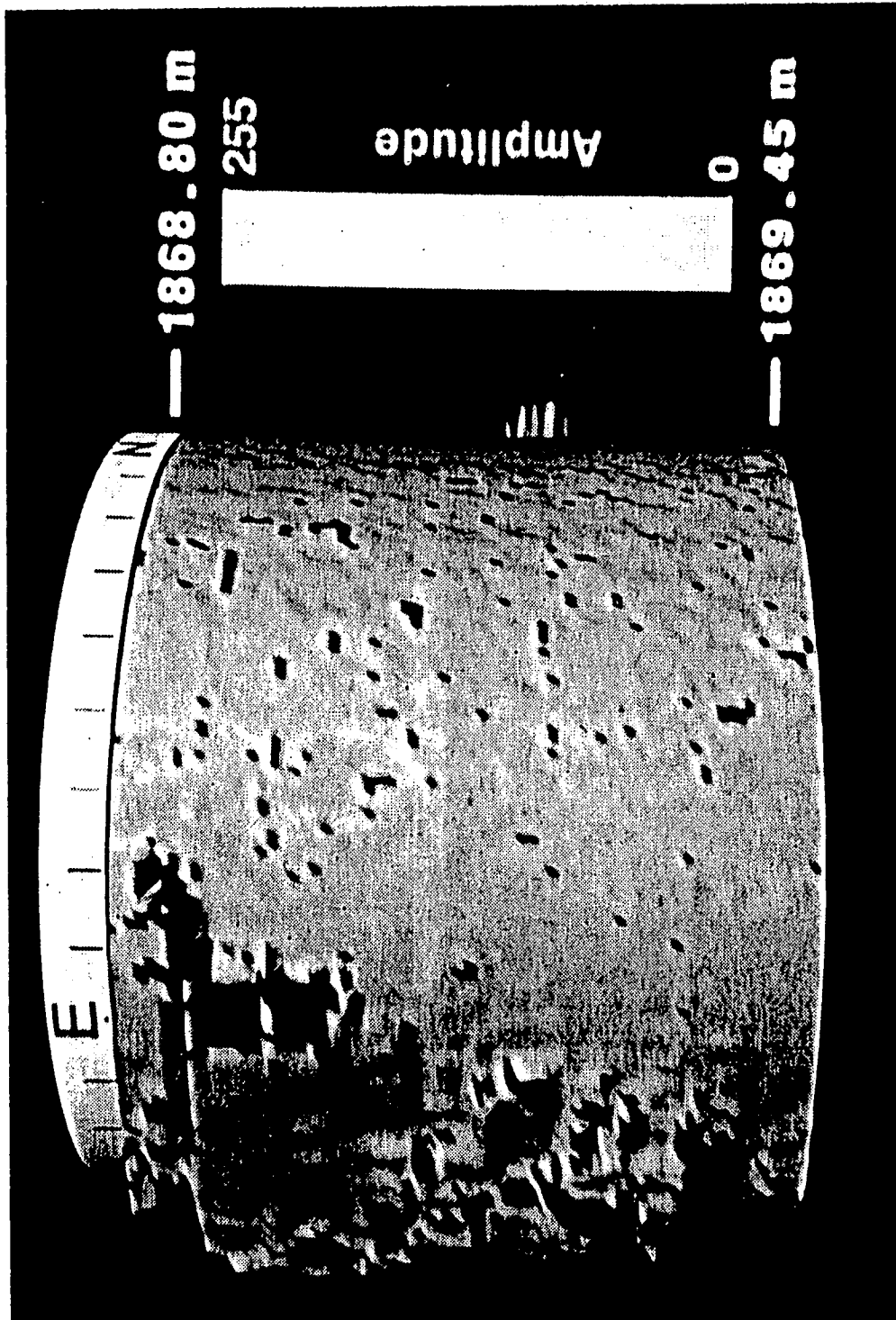
Figure 33. Rendered frame of BHTV data over a breakout interval in the Cajon Pass well
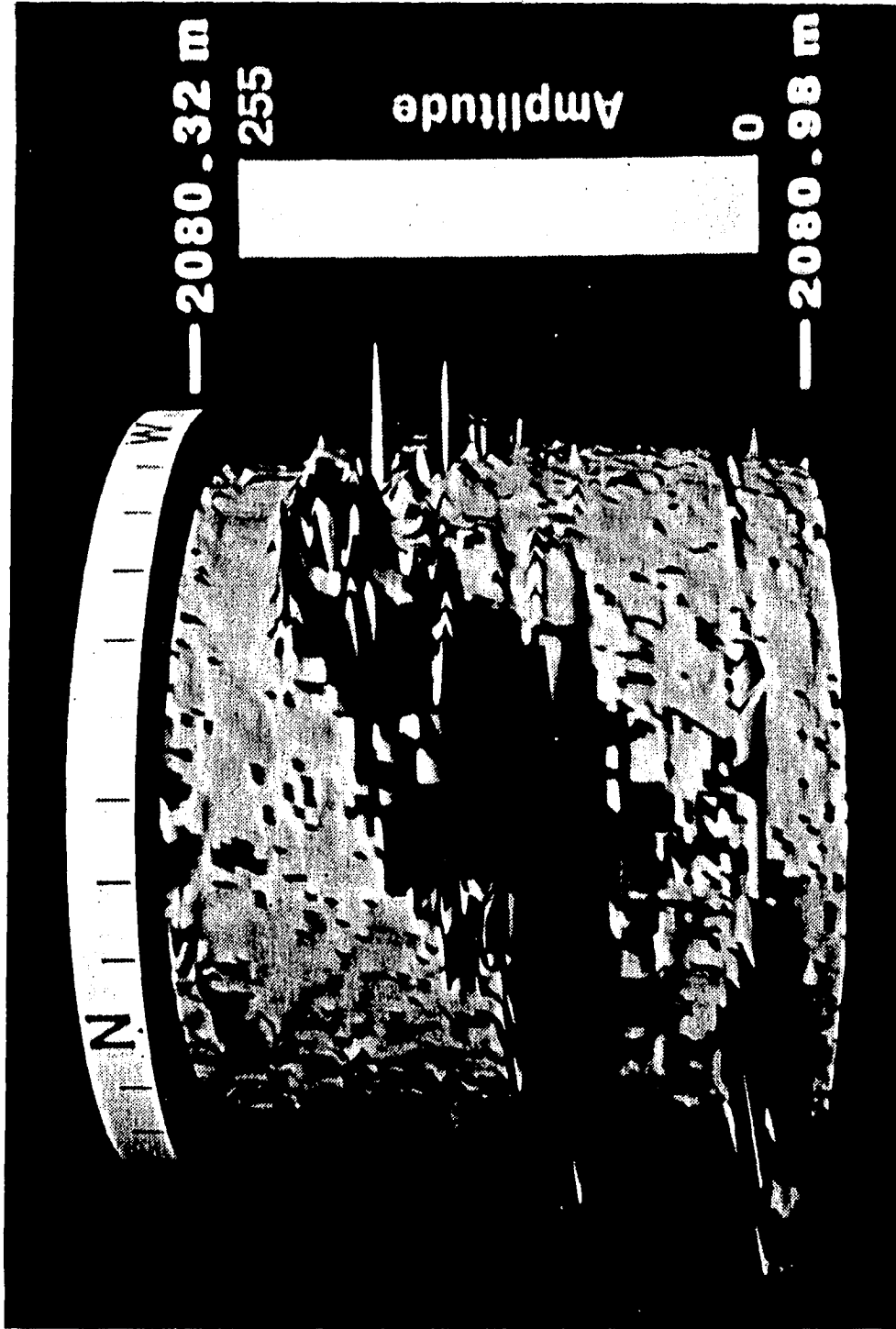
Figure 34. Rendered frame of BHTV data over a fracture interval in the Cajon Pass well
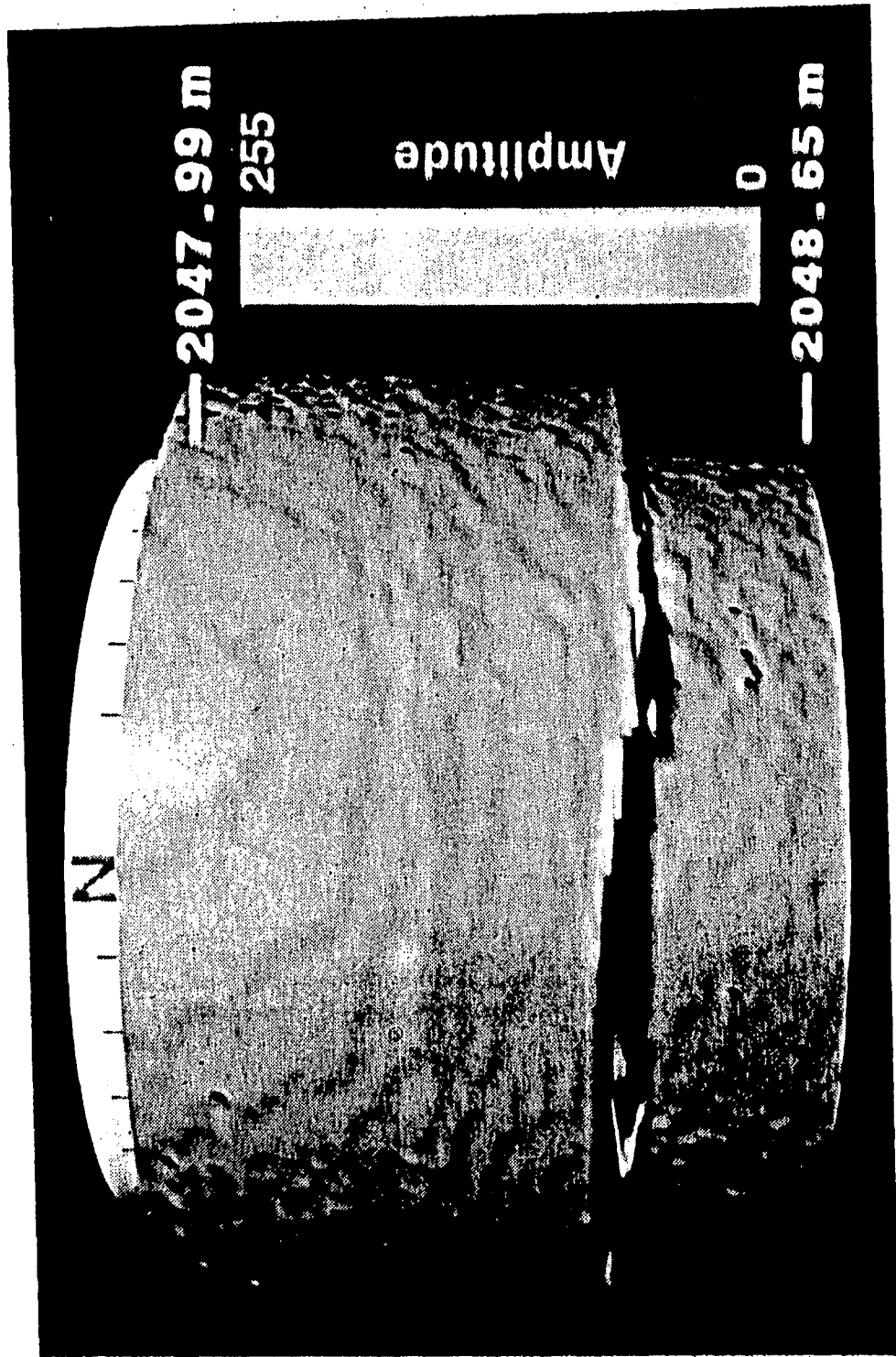
Figure 35. Rendered frame of BHTV data over an interval with a change in borehole size in the Cajon Pass well.

CHAPTER 2: QUANTITATIVE ANALYSIS OF BHTV DATA —
APPLICATION TO THE MEASUREMENT OF IN-SITU STRESS

In-Situ Stress Orientation and Magnitude at the Fenton
Geothermal Site, New Mexico Determined From Wellbore Breakouts

Introduction

Stress-induced wellbore breakouts have become important as indicators of the
direction of horizontal principal stresses (e.g. Bell and Gough, 1979; Hickman, et al.,
1985; Plumb and Cox, 1986). Their mechanism of formation was first discussed by
Gough and Bell (1981) and later expanded upon by Zoback et al., (1985). Breakouts
are the result of localized shear failure around a borehole in response to horizontal
compression. This compression creates spalling in symmetric zones around the
borehole at the azimuth of least horizontal principal stress where the circumferential
compressive stress is greatest. Correlation of breakout data with independent stress
measurements has demonstrated that breakouts give reliable stress orientations of the
upper crust (Zoback and Zoback, 1988).

The acoustic borehole televiewer provides excellent data for the detection and
measurement of stress-induced wellbore breakouts. Analog televiewer data from the
Fenton Geothermal well EE-3 in New Mexico were digitized and interactively
processed for detection and analysis of azimuth and shape of stress-induced breakouts
occurring in the well at depths of about 2.9 - 3.5 km. A statistical analysis of the
measured breakout azimuths yields a well resolved orientation of least horizontal
principal stress of 119°, consistent with least principal stress data from the Rio
Grande Rift. As the magnitude of the least horizontal compressive stress, S_{hmin}, in
EE-3 is known from hydraulic fracturing, a new method is presented in which S_{hmin}
and data on breakout width are used to estimate the magnitude of the maximum
horizontal principal stress.

Site Location and Stress History

The Fenton Geothermal well is drilled 4018 m into the Precambrian basement underlying the 1.1 to 1.4 m.y. tuffs and the Mesozoic and Paleozoic sediments of the Jemez Mountains in north central New Mexico (Figure 36). Situated on the western boundary of the Rio Grande rift, data collected at the Fenton Geothermal well provide stress information for a complex, tectonically active region. Figure 37, taken from Ankeny et al., 1986 is a schematic structural cross section in the vicinity of the Fenton EE-3 well. The Rio Grande rift is an intraplate rift that trends NNE from south central New Mexico to central Colorado (Chapin and Cather, 1981). The rift has a central depression partially filled with sediments that is bordered by mountains. It is bounded by the Great Plains and Southern Rocky Mountains to the east and by the Colorado Plateau and Basin and Range to the west. Rifting in this region began with extension between 25 and 29 m.y. ago. It is geologically active today, characterized by high heat flow, high seismicity, vertical crustal movements, recent volcanism, shallow magma bodies and a thin lithosphere (Golombek, 1983; Cordell, 1978; Smith and Bailey, 1966; Doell et al.,1968; Olsen et. al, 1986). Orientation of spreading of the Rio Grande rift has been E-W since the beginning of rifting (31 m.y.). Concomitant WSW extension occurred outside the Rio Grande Rift in New Mexico and the rest of the southwest U.S. during late Oligocene and early Miocene but structural data from within the rift indicates predominantly E-W extension. In the Fenton region, mid-Tertiary dykes trend parallel to the structural grain of the rift which indicates that the preexisting structural grain has controlled spreading of the rift.

Four stress provinces have been delineated in this region based on compilations of paleo and contemporary stress orientation data by Aldrich and Laughlin (1984) and Aldrich et al. (1986). The criteria used to define three time boundaries for the stress orientation data are: (1) a 32 m.y. boundary coincident with the earliest rifting, (2) a 20 m.y. boundary, the midpoint of the early Miocene lull in volcanism which coincides with the change in style of regional extension in southern Arizona from "thin-skinned" to "ductile" Basin and Range style (Eaton, 1979), and (3) a 5 m.y. boundary which marks the beginning of the contemporary stress field. Figure 38, taken from the 0 to 5 m.y. map of Aldrich and Laughlin (1986), shows
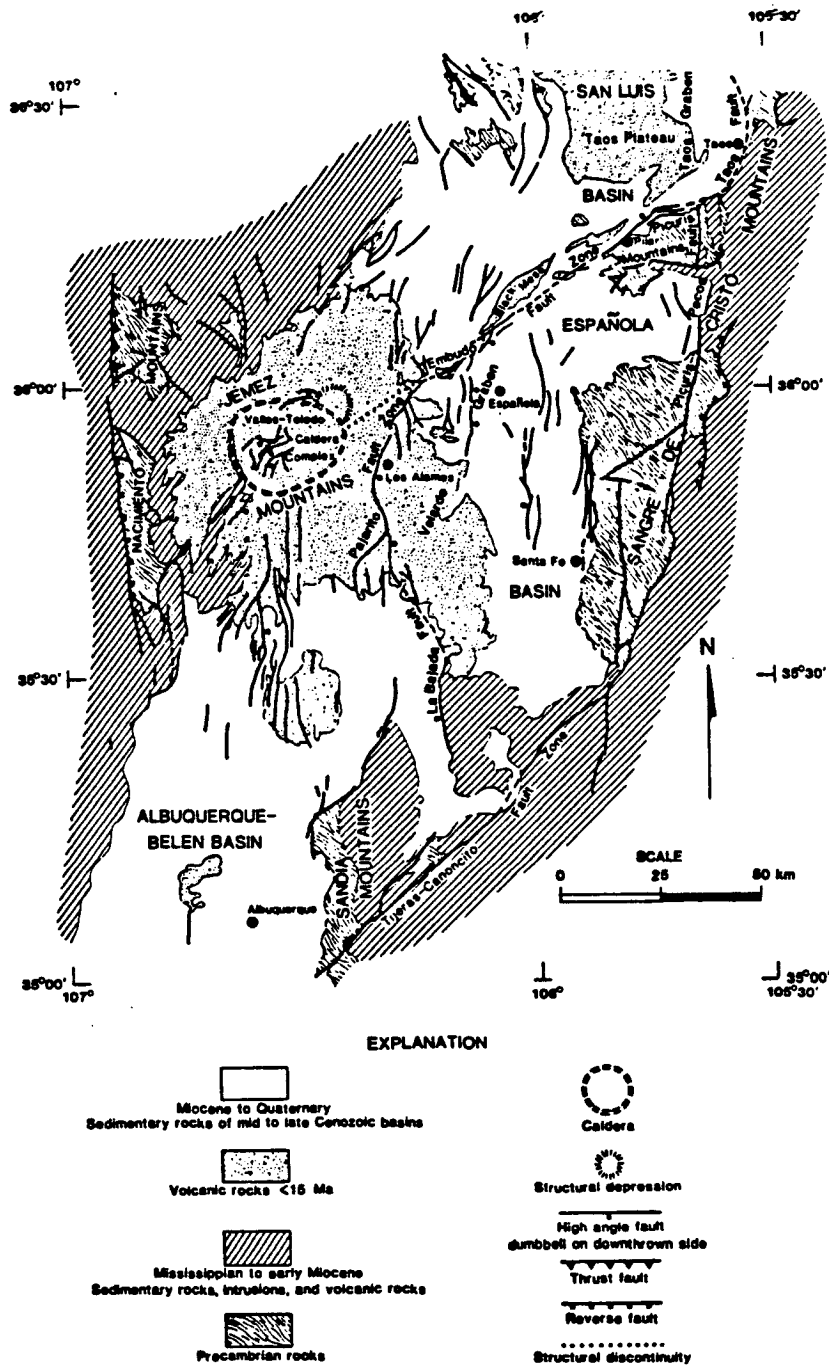
Figure 36. Site geologic map of the Rio Grande rift showing the location of the Valles-Toledo caldera, the Jemez Mountains and the Fenton well. From Aldrich et. al., 1986.
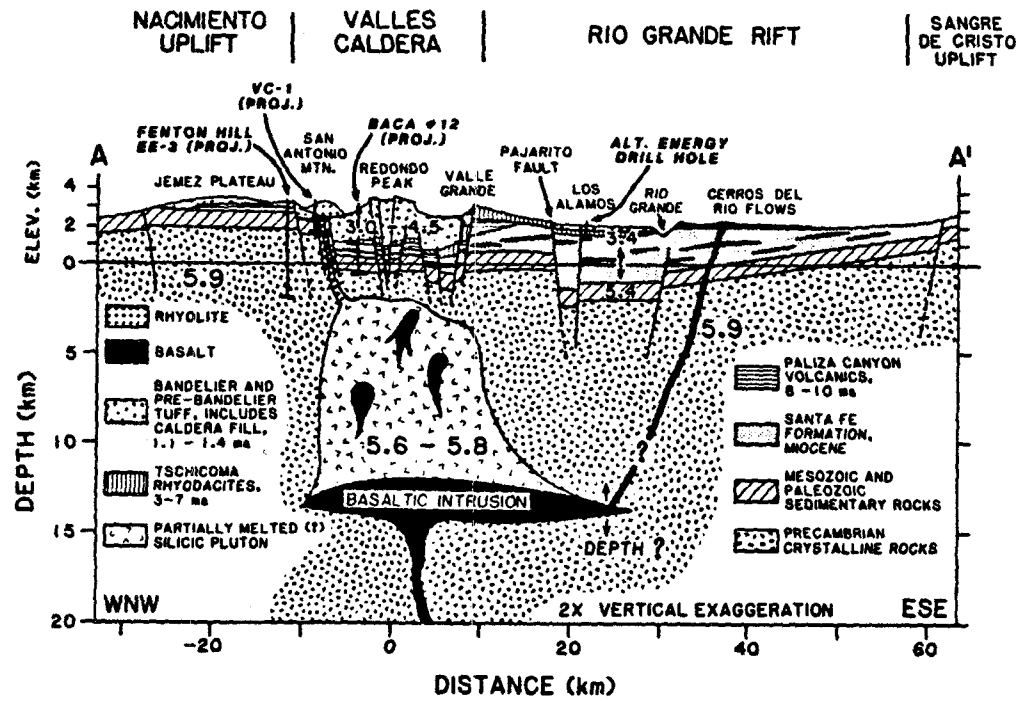
Figure 37. Structural cross section through the Rio Grande rift. From Ankeny et al., 1986.

stress trajectories for the direction of least horizontal principal stress compiled from the alignment of cinder cones, fault data, structural relationships, as well as hydraulic fracture and breakout data. The contemporary stress province boundaries are sharp with 90° changes in less than 30 km. The four provinces are: (1) a uniform NNE-SSW oriented least horizontal principal stress east of Taos, New Mexico, consistent with the Southern Great Plains stress regime; (2) NNE to NE oriented least horizontal principal stress characteristic of the Colorado Plateau west of the Rio Grande Rift; (3) between the Rio Grande rift and the Colorado Plateau is a NE-trending transition zone which corresponds in position with the Jemez lineament. Least horizontal principal stress orientations vary considerably within this zone but generally average NW-SE (at right angles to the stress indicators of the Colorado Plateau interior); (4) the bounding portion of the Basin and Range least horizontal principal stress is E-W making a stress pattern similar to that of the Wasatch front rather than the remainder of the Basin and Range province where least horizontal principal stress is WNW-ESE.

The extensional stress field has existed for roughly 31 m.y. The precise timing of stress change is complicated by faulting and block rotations. Paleostress measurements from radiometrically dated dykes located in NewMexico give regional extension beginning 32 m.y. in New Mexico (earlier to south) (Aldrich et al., 1986). This orientation was maintained through the mid-Tertiary. Between 15 and 7 m.y. regional extension rotated clockwise 45° to WNW-ESE or E-W (its present orientation). This rotation may not have occurred simultaneously across entire Basin and Range. In Nye County, Nevada, a shift to north-trending normal faulting beginning 17 m.y. implies a rotation in the direction of extension (Ekren et al., 1968). Zoback and Thompson (1978) bracket rotation of least horizontal principal stress between 15 and 6 m.y. in the northern Basin and Range based on a change in the trend of the ranges in the northern Basin and Range at 10 m.y., on the orientation of dyke intrusions, and on large vertical offsets across ENE-trending range front faults. Eaton (1979) suggests a timing between 11 and 7 m.y. across the entire southwest. Zoback et al. (1981) state the rotation occurred at approximately 10 m.y. synchronously over a broad region. Paleomagnetic evidence from volcanic rocks in the Jemez Mountains indicate a 15° clockwise rotation whereas paleomagnetic data to the east indicates counterclockwise rotation of the same magnitude (Brown and Golombek, 1986). The timing for the onset rotation is 5 m.y. Differential rotation is
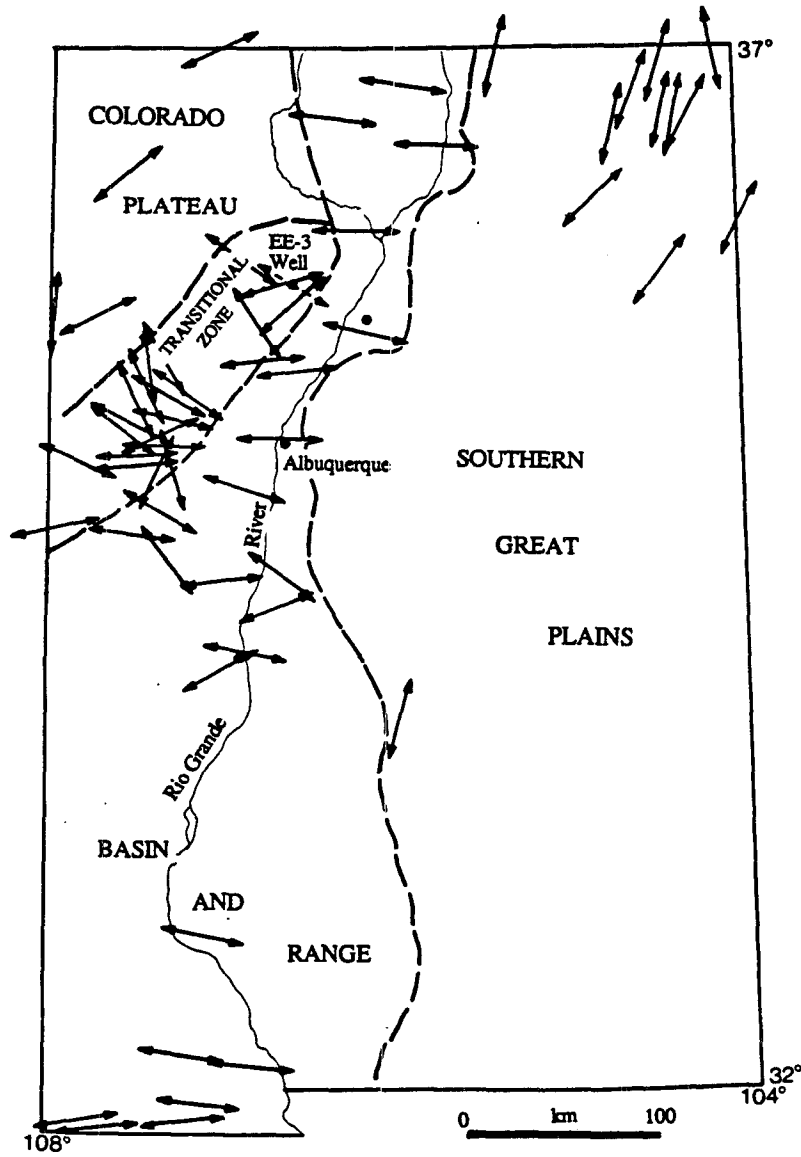
Figure 38. Trajectories of least horizontal principal stress and boundaries of stress provinces defined for the Rio Grande rift region by Aldrich et al., 1986.

about 4 per million years. These results support left-lateral strike-slip movement along the rift as the likely driving mechanism for counter clockwise rotation of the basin.

The Fenton Geothermal well is drilled 4018 m into the Precambrian basement underlying 1500 meters of 1.1 - 1.4 m.y. tuffs and Mesozoic and Paleozoic sediments of the Jemez Mountains. The well is located within the transition zone between the Colorado Plateau and the Rio Grande rift (Zoback and Zoback, 1980, 1987). Within this transition zone, in-situ stress indicators show variation in the direction of ambient horizontal compressive stresses (Figure 38, after Aldrich et al., 1986).

Data Acquisition and Analysis

The televiewer logging in the Fenton EE-3 geothermal well was completed in January, 1986 by the Denver U.S.G.S. Water Resources Division (A. Hess and R. Hodges, pers. comm.). An analog, high temperature televiewer tool with a 10.2 cm diameter and 1.4 MHz acoustic transducer was used to image the borehole wall over a 798 m depth interval. Two separate sections of this interval were logged; the lower from depth 3627 m to 3432 m and the upper interval from 2896 m to 2829 m producing a total of 262 meters of data. The log was run at a rate of 10 cm/s producing an image with a scan line every 4 cm. The data are fair to poor quality, because the tool was off-center in the slightly inclined wellbore and temperatures in this well are approximately 325° C at 4.5 km depth resulting in an extremely difficult environment for televiewer operation.

A detailed analysis of the digital data was performed to precisely measure borehole shape with depth. The data were median filtered and corrected for off center effects before the analysis. The data were corrected for tool position and magnetic declination before plotting. 12 cm long intervals of the Fenton well were evaluated through the interactive graphics routine. Figure 39 shows an interval of the EE-3 data from 11,849 to 11,900 feet. The data are somewhat difficult to interpret because of the black continuous vertical bands centered at azimuths 20° and 260°. These bands of missing data are the result of a non-centralized tool which causes non-normal incidence of the pulse at the borehole wall and subsequent deflection of the returned signal away from the transducer (Georgi, 1985). Superimposed on these bands are
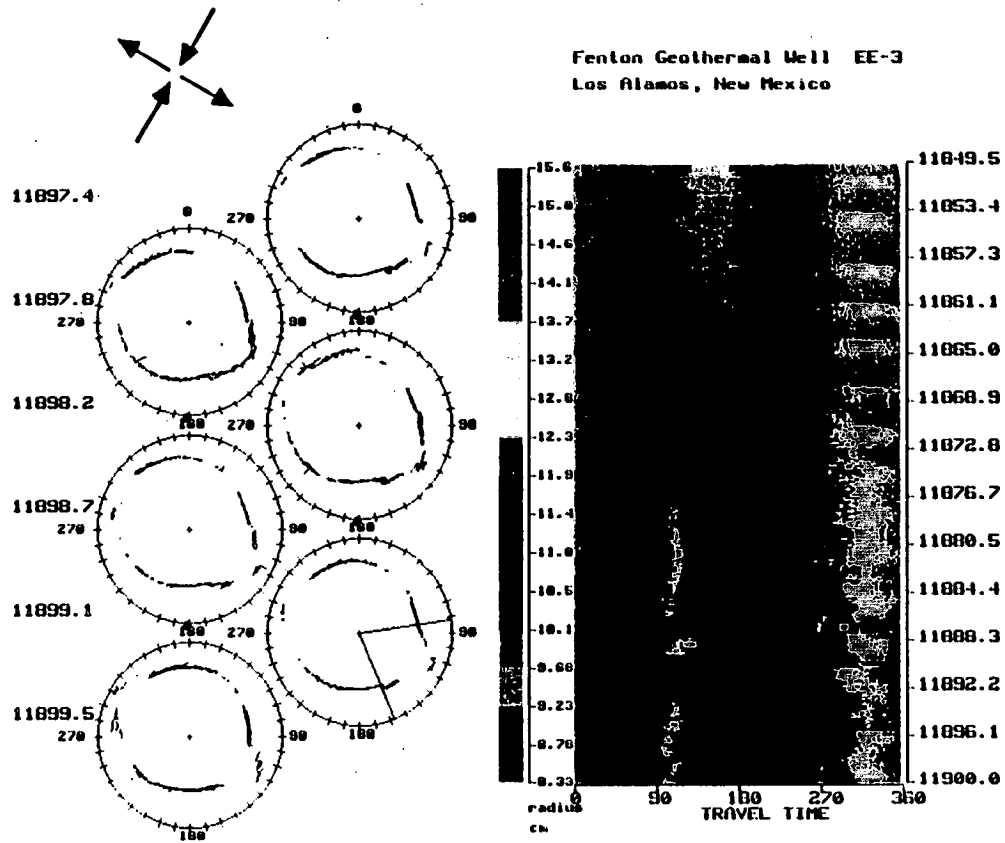
Figure 39. Display of interactive graphics routine used to analyze televiewer data. Left panel shows polar cross sections of 12 cm intervals of the borehole wall. Right panel is travel time of the reflected pulse with depth.

discontinuous bands of wellbore breakouts where high radius values indicate acoustic returns from within the breakouts. In the left panel are polar cross sections of the data that show the characteristic shape of the breakouts. Where high quality data were recorded, it was possible to measure the azimuth and the width of breakout intervals. Over some intervals it was only possible to pick the breakout width on the northwest side of the borehole due to the missing data between azimuths 80° and 120°. The two radial lines represent the picked angle of the breakout width and the breakout azimuth bisects this angle. Breakout azimuth gives the direction of least horizontal principal stress. As discussed below, breakout width is important for estimation of stress magnitude.
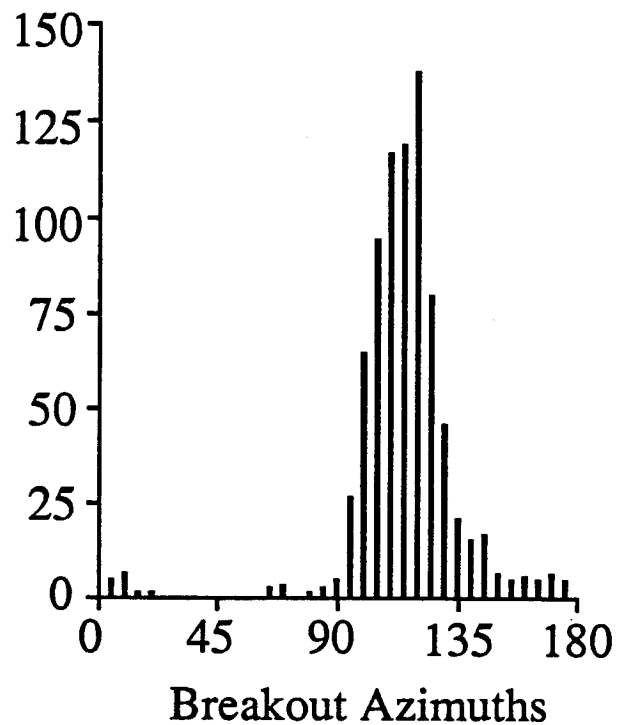
Figure 40. Histogram of breakout azimuths over a 262 meter interval in the EE-e well of the Fenton Geothermal Field.

In the interactive analysis, the two sides of a breakout were picked independently and entered into a data base. 928 separate breakout azimuths and 644 breakout widths were measured in the analysis of the Fenton data. The histogram of

Figure 40 presents the results of the statistical analysis of the breakout azimuths. Over the 262 meters where breakouts were observed in this well the predominant direction is ESE. The data were statistically reduced to obtain the mean direction of least principal horizontal stress after a method developed by Mardia (1972). Mardia's statistical technique determines the mean direction, the circular variance, a measure of the dispersion about the mean and the standard deviation. The breakout azimuths were grouped into 5° intervals in the range of 0° to 180° with group midpoints at 2.5^O, 7.5^O, 12.5^O, etc. The frequencies (number of breakouts) of all breakout azimuths within each 5° interval were summed to determine the interval frequency f_i. The mean directions in Cartesian coordinates C and S are:

$$C = 1/n \ \Sigma \ f_i \ \cos 2\theta \tag{11}$$

$$S = 1/n \ \Sigma \ f_i \ \sin 2\theta \tag{12}$$

where $n = \Sigma f_i$ is the population size. The magnitude of the resultant vector R is:

$$R = (C^2 + S^2)^{1/2} \tag{13}$$

R is a measure of the concentration of the data about the mean direction. The mean direction of the resultant vector θ is:

$$\theta = \frac{1}{2}(180 + \tan^{-1} \ S/C) \tag{14}$$

The circular variance in the range $(0^O, 360^O)$ is:

$$V_o = 1 - R \tag{15}$$

The circular variance in the range $(0^O, 180^O)$ is:

$$V = 1 - (1 - V_o)^{1/4} \tag{16}$$

The standard deviation, σ, of the resultant vector in radians is

$$\sigma = (-2 \log_e (1 - V))^{1/2} / \mathcal{L} \tag{17}$$

where $L = 2$. The mean direction is 119°, and the standard deviation 11°. The orientation of least horizontal principal stress of N119°E in this study is similar to principal horizontal stress indicators of the Basin and Range and Rio Grande Rift and not aligned with stress indicators located in the Colorado Plateau to the northwest (Aldrich and Laughlin, 1984). The orientation obtained in this study is significantly different from the N70°E orientation of least horizontal stress obtained from poorly resolved data obtained with hydrofracture methods at the Fenton site (see measurement #64, Aldrich and Laughlin, 1984).

Stress Magnitude Analysis

The occurrence of wellbore breakouts may be used to fully determine the in situ stress state. Failure of the borehole wall is the result of a stress concentration due to unequal far field horizontal principal stresses. At the borehole wall, remote stresses are translated to radial and circumferential principal stress components in polar coordinates and become functions of r, the radius from the center of the borehole, and θ, the angle with the maximum horizontal stress. The borehole stress field is completely described by normal stresses acting in the horizontal plane, σ_r and σ_θ and the vertical stress, σ_z. The effective stress components in the vicinity of a circular hole are given by Kirsch (1898) and by Jaeger and Cook (1979) as:

$$\sigma_\theta = \frac{1}{2}(\sigma_1+\sigma_3)(1+\frac{a^2}{r^2}) - \frac{1}{2}(\sigma_1-\sigma_3)(1+\frac{3a^4}{r^4}\cos2\theta) - \Delta P_w\frac{a^2}{r^2} \tag{18}$$

$$\sigma_r = \frac{1}{2}(\sigma_1+\sigma_3)(1-\frac{a^2}{r^2}) + \frac{1}{2}(\sigma_1-\sigma_3)(1+\frac{4a^2}{r^2}+\frac{3a^4}{r^4}\cos2\theta) - \Delta P_w\frac{a^2}{r^2} \tag{19}$$

$$\sigma_{r\theta} = -\frac{1}{2}(\sigma_1-\sigma_3)(1+\frac{a^2}{r^2}) - (\frac{3a^4}{r^4}\cos2\theta)\sin2\theta \tag{20}$$

$$\sigma_z = \rho g z - 2v\frac{a^2}{r^2}(\sigma_1-\sigma_3)\cos2\theta + \Delta P_w\frac{a^2}{r^2} \tag{21}$$

where σ_1 is the maximum and σ_3 the minimum effective horizontal principal stress, a is the borehole radius, r is the radial distance from the center of the borehole, v is

Poisson's ratio, and ΔP_w is the difference between the formation pore pressure and borehole fluid pressure.

At the borehole wall, the radial and shear stresses are zero and the stress field is defined by the circumferential and vertical stresses:

$$\sigma_\theta = (\sigma_1 + \sigma_3) - 2(\sigma_1 - \sigma_3) \cos 2\theta - \Delta P_w \qquad (22)$$

$$\sigma_z = \rho g z - 2\nu(\sigma_1 - \sigma_3) \cos 2\theta + \Delta P_w \qquad (23)$$

Under conditions of unequal horizontal principal stresses, the circumferential stress has its maximum value at $\theta = \pi/2$ where:

$$\sigma_{\theta=\pi/2} = 3S_{Hmax} - S_{hmin} - 2P_p \qquad (24)$$

and its minimum at $\theta = 0$ where:

$$\sigma_{\theta=0} = 3S_{hmin} - S_{Hmax} - 2P_p \qquad (25)$$

where S_{Hmax} and S_{hmin} are the principal horizontal stresses, P_p is the pore pressure and the conversion from effective to principal stress $\sigma_1 = S_{Hmax} - P_p$ has been used.
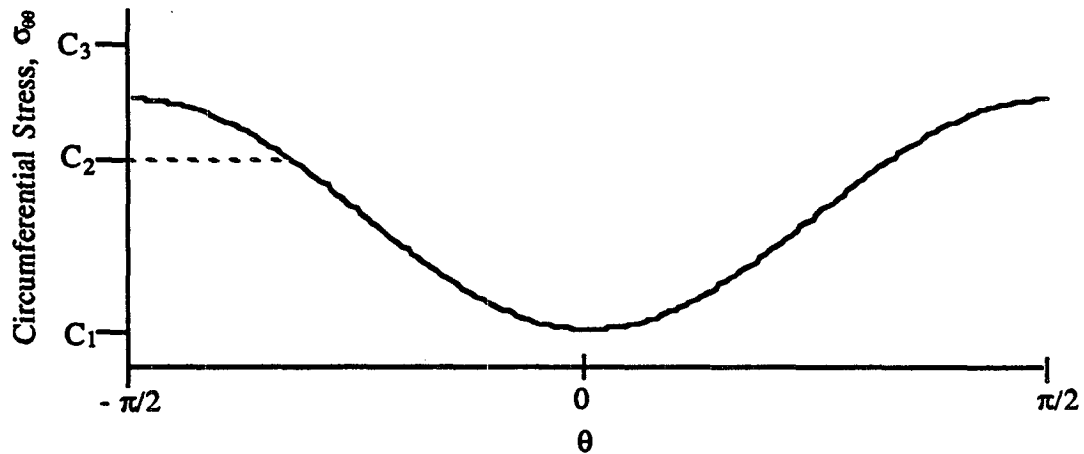
Figure 41. The variation in circumferential stress, σ_θ, with angle θ from S_{Hmax} for arbitrary values of S_{Hmax} and S_{hmin}.

The variation of circumferential stress as a function of azimuth is shown in Figure 41 for nominal values of S_{Hmax} and S_{hmin}. In Figure 18, θ_b is the angle of breakout initiation with respect to S_{Hmax} and ϕ_b is the half width of the breakout ($\phi_b = \pi/2 - \theta_b$). Usually breakouts occur if the uniaxial compressive strength of the rock is exceed by the concentrated circumferential stress. If the uniaxial compressive
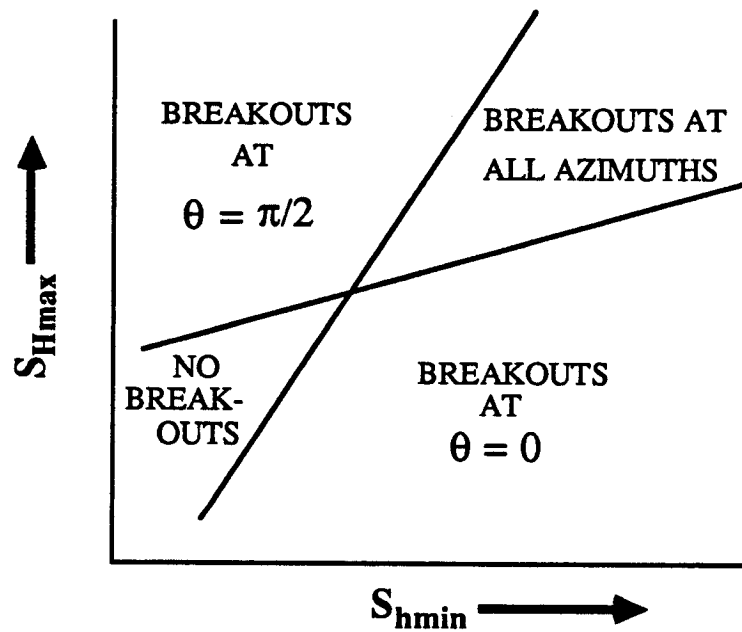
Figure 42. Possible fields of breakout occurrence in horizontal principal stress space. Curves are constructed using the equality of equations 24 and 25 to the unconfined compressive rock strength, C_0. The region Breakouts at $\theta = 0$ is physically impossible as it requires the minimum principal stress to be greater than the maximum principal stress.

strength of the rock is sufficiently high, as at C_3, the strength exceeds the concentrated circumferential stress and no breakouts occur. However, when the strength of the intact rock is exceeded by the concentrated stress, as at C_2, the rock will fail in a restricted section of the borehole (see dashed line in Figure 41). If the rock is sufficiently weak, as at C_1, failure could occur at all azimuths. With information regarding the unconfined compressive strength of the rock it is straightforward to define regions in horizontal principal stress space where breakouts will and will not occur (Figure 42). The shallow curve in Figure 42 is constructed

using the equation 24 in the relation $3S_{Hmax} - S_{Hmax} - 2P_p = C_0$ and the steep curve using equation 25 in the relation $3S_{Hmax} - S_{Hmax} - 2P_p = C_0$. These curves are calculated assuming conditions of hydrostatic pore pressure.

In-situ principal stress differences in the crust can be further constrained by assuming that the ratio of shear to normal stress on pre-existing faults does not exceed the frictional strength of the faults. In terms of principal stresses, the ratio of maximum to minimum effective principal stress is related to the coefficient of friction, μ, by:

$$\frac{\sigma_1}{\sigma_3} = \frac{S_1 - P_p}{S_3 - P_p} = (\sqrt{(\mu^2 + 1)} + \mu)^2 \qquad (26)$$

(Jaeger and Cook, 1979). Using Anderson's (1951) classification of faults the principal stresses are: $S_3 = S_{Hmax}$ and $S_1 = S_v$ in a normal faulting environment; $S_3 = S_{hmin}$ and $S_1 = S_{Hmax}$ and in a strike-slip environment; and $S_3 = S_v$ and $S_1 = S_{Hmax}$ in a thrust fault environment. Where S_{Hmax} and S_{hmin} are the horizontal principal stresses and S_v is the lithostatic load. Using reasonable values for μ of $0.6 < \mu < 1.0$ (Byerlee, 1978) bounds may be placed on the values of in-situ horizontal principal stresses in each fault regime (see also Sibson, 1985; Brace and Kohlstadt, 1980; Zoback and Healy, 1984).

Figure 43 indicates the domain of permissible values of minimum and maximum horizontal principal stress for each of the faulting modes where the frictional limit is calculated using equation 26 and hydrostatic pore pressure is assumed. Figure 44 shows the superposition of these two constraints on the magnitude of horizontal principal stresses for the EE-3 well at the depth where breakouts are observed. If the Fenton region is considered extensional, normal fault mechanics would prevail and the possible values for maximum and minimum principal stress would be bound by the shaded region within the normal faulting triangle.

Seismicity studies at the Fenton site, which indicate extensional as well as strike-slip earthquake focal mechanisms, can be used to provide an independent estimate of S_{Hmax} (Fehler, et al., 1986; Dey, 1986). The use of focal mechanisms to determine stress assumes a uniform stress field and that traction on the fault plane is parallel to the slip direction (A. Michael, 1987). The coexistence of strike-slip and
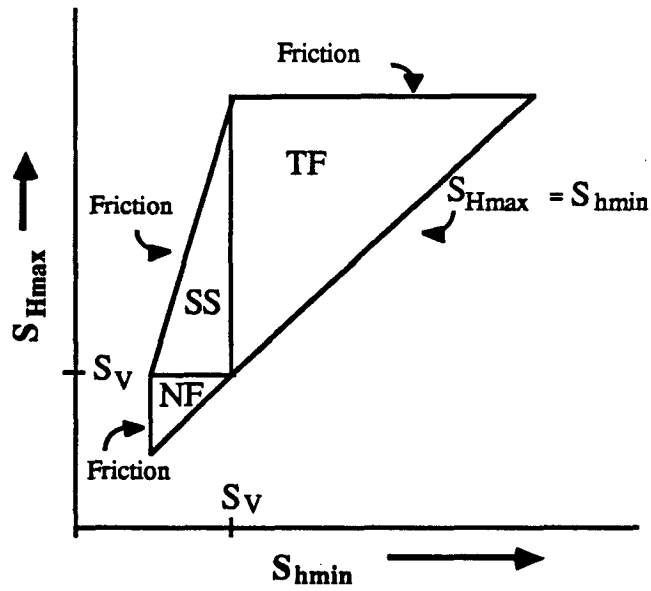
Figure 43. Possible values of maximum and minimum horizontal principal stress defined through a frictional analysis and faulting equilibrium theory.
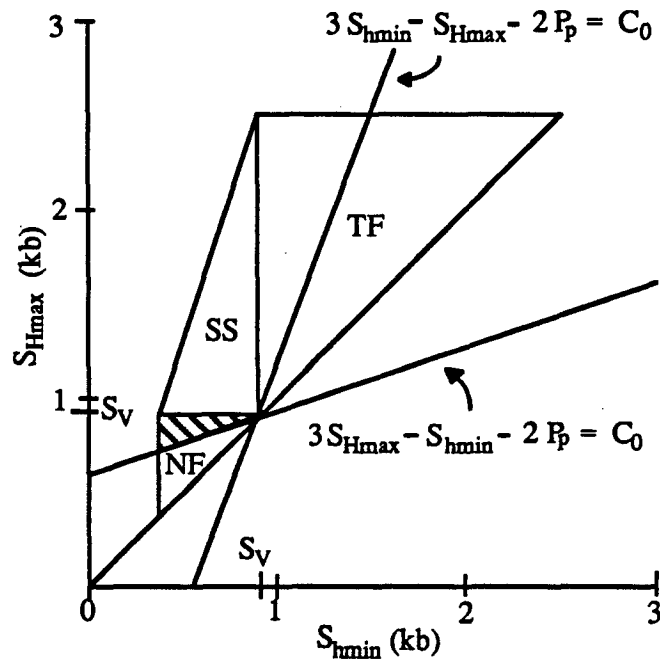
Figure 44. Superposition of the theoretical fields shown in Figures 42 and 43 constructed for the depth 3.5 km at the EE-3 well.

normal fault focal mechanisms implies that S_1 and S_2 interchange at the site and the difference between intermediate and maximum principal stress may be small (Wright, 1976; Angelier, 1979). Assuming a value of $\mu = 0.6$ and hydrostatic pore pressure (which is appropriate for the EE-3 well) suggests that S_{hmin} is about $0.6\,S_V$ (equation 26) and that S_{Hmax} is approximately equal to S_V. Figure 45 is the stress profile for the EE-3 well. Published estimates of S_{hmin} from hydraulic fracture experiments in this well and companion wells at the Fenton site (solid squares) are quite consistent with the theoretical value of $0.6S_V$ (Murphy, 1976; Burns, 1984).
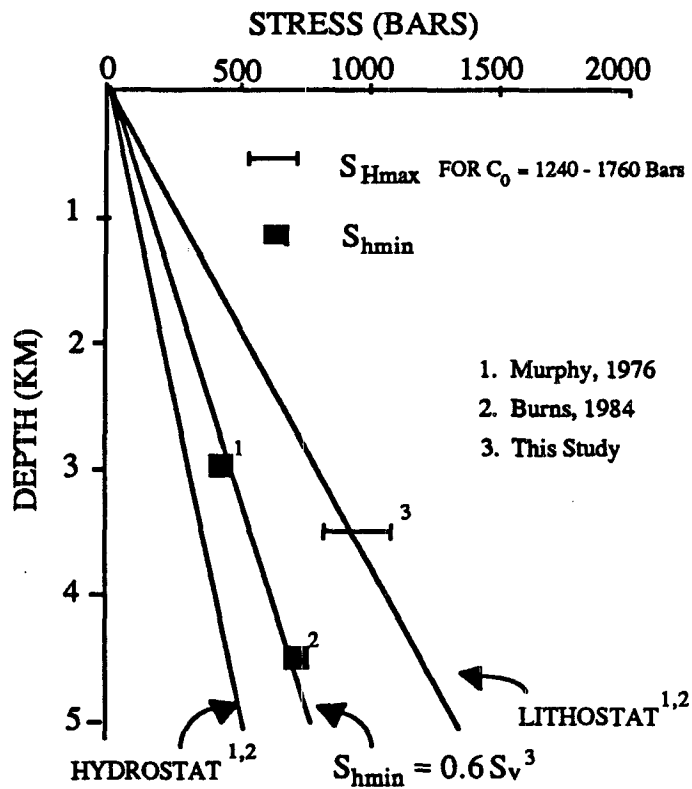
Figure 45. Stress state for EE-3 well Fenton geothermal well. The pore pressure is assumed to be hydrostatic at bars/km and the vertical stress increases at a rate of 265 bars/km. Theoretical S_{hmin} curve is 145 bars/km which fits the measured data points (solid squares) quite well. Solid horizontal bar is the range of S_{Hmax} calculated from breakout width for $C_0 = 1240$ to 1760 bars.

With knowledge of C_0, S_{hmin} and breakout width the magnitude of maximum horizontal principal stress can be estimated by the breakout analysis. After the initial failure of the borehole wall upon breakout formation the circumferential

stress decreases preventing widening of the breakouts. Thus, with time breakouts will deepen but do not widen (Zheng, written communication; Mastin, 1984; Zoback et al., 1985). Aside from erosional effects on the initial shape of the breakout, such as fluid circulation or tool trips the angle ϕ_b, should remain fairly constant. Using breakout geometry to determine stress magnitude was found be limited by the time dependent failure processes that deepen the breakout (Zoback et al., 1986). Utilizing only breakout width in this method avoids the problem of the time dependent growth of breakouts in depth.

At the borehole wall, the circumferential stress is given by equation 22 above. It may be assumed that at the maximum angle of breakout initiation, ϕ_b, the circumferential stress is just equal to the unconfined compressive rock strength, C_o.

$$C_o = \sigma_\theta = (\sigma_1 + \sigma_3) - 2(\sigma_1 - \sigma_3) \cos 2\theta - \Delta P_w \qquad (27)$$

Converting from effective to principal stresses, using the effective stress law, $\sigma_1 = S_{Hmax} - \alpha P_p$ where α is assumed to be 1 for brittle failure of intact rock (Nur, 1971), we have:

$$S_{Hmax} = \frac{(C_o + \Delta P_w + 2P_p)}{(1 - 2\cos 2\theta)} - S_{hmin} \frac{(1 + 2\cos 2\theta)}{(1 - 2\cos 2\theta)} \qquad (28)$$

The width distribution of breakouts was determined over a 262 meter interval in the EE-3 well through the interactive graphics algorithm developed to analyze detailed borehole shape. The resulting histogram of breakout widths is shown in Figure 46. Using all of the measured breakout widths the mean width over this interval is 38°. Laboratory data from strength tests on core samples from the Fenton well indicate a range of values for C_o between 1240 and 1760 bars (T. Dey, personal communication). The corresponding range of maximum horizontal principal stress magnitudes is 880 to 1080 bars (Figure 45, solid bar). The magnitude of S_{Hmax} in this calculation has a nonlinear dependence on breakout width. Using the standard deviation in breakout width over the range of values for C_o from 1240 to 1760 bars the error estimates are approximately ± 50 and ±150 bars respectively.

The analysis of breakout widths in the Fenton well substantially constrains the value of maximum horizontal principal stress. The area above the S_{hmin} curve and below the lithostat (Figure 45) is the domain maximum horizontal principal stress in

the normal faulting environment and that above the lithostatic curve is the domain of strike-slip faulting. The range of horizontal stress magnitudes determined from the breakout data are very close to lithostatic stresses in agreement with these observations. Observed seismicity in the Fenton region has not been successfully explained in terms of simple extension. Two types of fault plane solutions or focal mechanisms can be inferred from our analysis of breakout data. Both types are limited to the stress state $S1 = S2 > S3$; $SHmax = Sv > Shmin$. The first is normal faulting on NNE-striking planes and the second is strike-slip faulting on NNW-SSE- and NE-SW-striking planes. Focal mechanisms from either of these cases may be expected in the Fenton region.
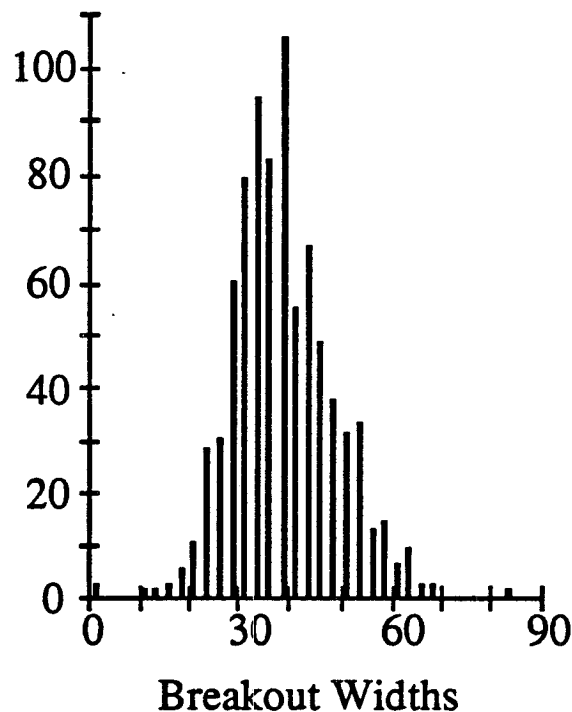
Figure 46. Histogram of breakout widths for the EE-3 well Fenton Geothermal Site

Thus, the independently determined values for C_0 and $Shmin$, the analysis of breakout widths in the Fenton well constrains the value of maximum horizontal principal stress to be approximately Sv, just as was predicted above from the occurrence of both strike-slip and extensional earthquakes in response to fluid

injection at Fenton Hill (Fahler, 1986). The Fenton well has been the site of extensive research and available information on the minimum horizontal principal stress and on rock strength made the site an excellent test of the calculation of stress magnitude using the angle of breakout initiation.

This detailed analysis of borehole shape using televiewer data recorded in the Fenton well has provided a well resolved orientation of the horizontal principal stresses that agrees with other observation of the stress state at the Fenton site. The magnitude of the maximum horizontal compressive stress constrained by these data is consistent with the occurrence of both strike-slip and normal faulting focal mechanisms at this site. The analysis of breakout width may be a promising technique to estimate stress magnitude in drillholes where other techniques are not useful.

Analysis of Macroscopic fractures in the Cajon Pass Scientific Drillhole
Over the Interval 1829 - 2115 meters

Introduction

The properties of crystalline rock masses are profoundly affected by the presence of fractures. Permeability (e.g. Brace, 1980), seismic velocities (e.g. Nur and Simmons, 1969; Stierman and Kovach, 1979; Moos and Zoback, 1982) and seismic anisotropy (Nur, 1969; Crampin, 1980) are often controlled by fracturing. Fractures provide permeable pathways for fluids which further affect rock properties by chemical alteration of the surrounding rock mass. The relative importance of fractures in controlling rock properties depends on the fracture density and orientation, as well as the hydraulic and elastic characteristics of the fractures themselves.

The Cajon Pass research well, located in southern California approximately 2 km east of the San Andreas Fault near San Bernadino (Figure 47, after Zoback et al., 1988), reached a total depth of 2115 m at the end of the first phase of experimentation. The borehole diameter above depth 1829 is significantly larger than the 30.5 cm bit size resulting in lower quality BHTV data in the uppermost section of the borehole. Data collected in the interval from 1829 to 2115 m is of excellent quality, however, and revealed numerous zones of wellbore spalling (Shamir et al., 1988) as well as a number of fractures intersecting the borehole. Full waveform sonic logs were also recorded over this interval, from which compressional, shear and Stoneley wave velocities were calculated. A long-term permeability study was carried out to measure the transmissivity of the open-hole interval (Coyle and Zoback, 1988) and continuous temperature (Lachenbruch and Sass, 1988) and fluid conductivity (Kharaka, 1988) logs were also obtained while fluid was flowing into the borehole. The combined data provides a unique opportunity to study fracture orientations and properties near the San Andreas fault.
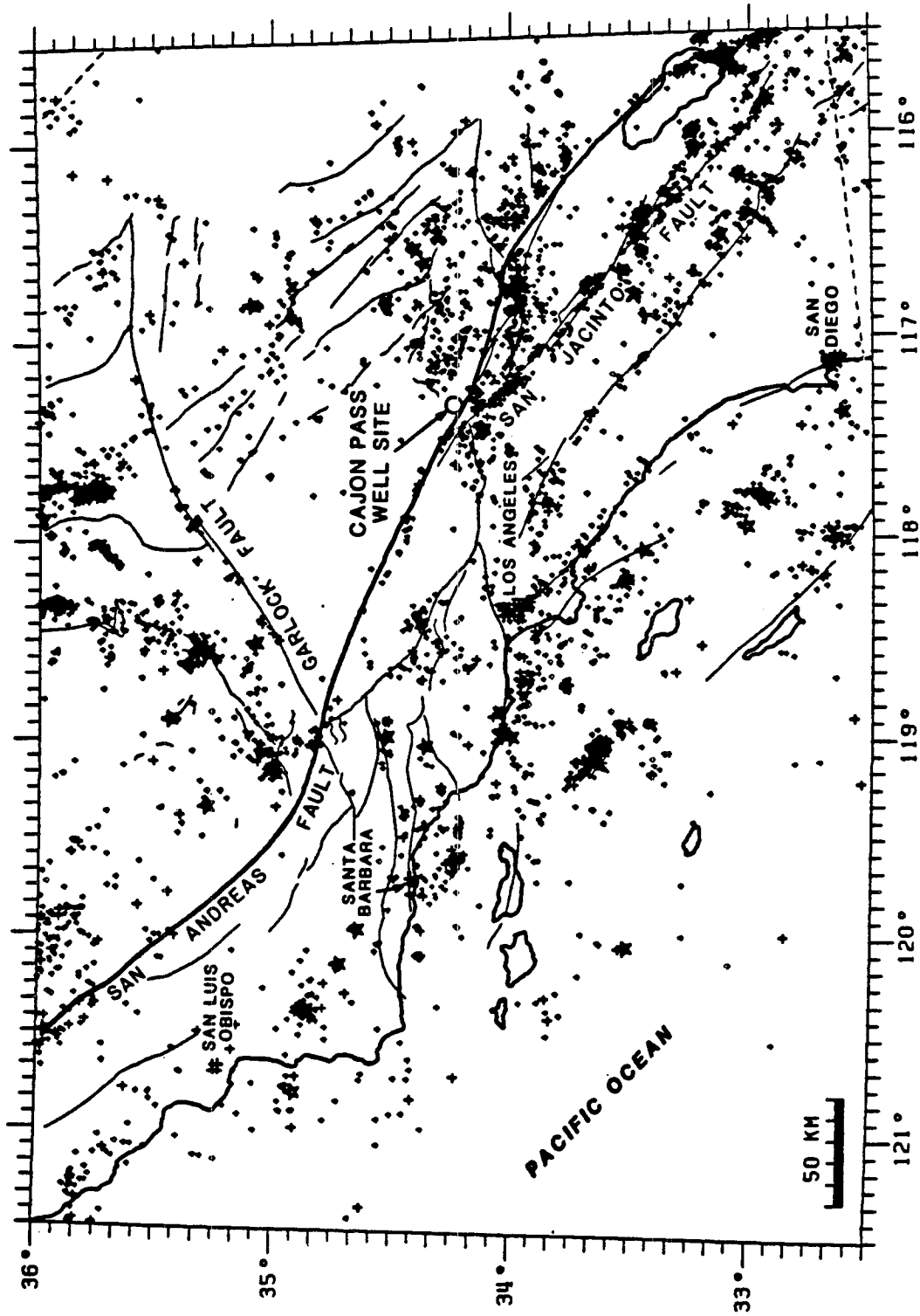
Figure 47. Site location map of the Cajon Pass scientific drillhole (after Zoback et al, 1988).

Fracture Analysis from BHTV Images

Digital BHTV data acquired in the Cajon Pass well from 2114 m to 1829 m were analyzed to determine the characteristics of natural fractures intersecting the drillhole. Two separate analyses of the natural fracture population were performed. The first determined the distribution of all measurable fractures and planar features in the data as a function of depth and the second determined the orientation and apparent aperture of continuous through-going fractures greater than about 1 cm in width. The data were median filtered before analysis to eliminate the characteristic noise that result from the analog to digital conversion and from anomalous multiple arrivals. In this study we have discriminated between planar features according to apparent width, that is, the gap measured by the televiewer, across a planar fracture as it intersects the borehole. A variety of factors including the mechanical erosion of the fracture surface and the geometry of the acoustic reflection of the BHTV signal, which is controlled by the transducer beam width and the size of the feature, preclude the measurement of true fracture aperture away from the borehole.

In the first analysis fracture distribution and qualitative size were determined through the analysis of cylindrical wire frame projections of the data to a scale which preserves the correct aspect ratio. This reconstruction of the topography of the borehole emphasizes fine scale features that may not be visible on conventional displays of reflectivity or borehole radius. It also aids in discriminating between two or more intersecting fractures and isolating fractures from other borehole features such as breakouts. The cylindrical projection in Figure 48 shows a fracture at 2076 m depth which dips about 45° as it intersects a smaller aperture, subhorizontal fracture.

Planar features were grouped by apparent aperture into three categories based on relative size. The apparent width is the minimum fracture width observed in cross sections of the fracture plane where correction for the apparent dip of the fracture has been made. Many fine scale features are interpreted as foliation based on their similarity to low angle, fine scale features visible in core. Larger features may be fracture zones or faults that have been in-filled with debris. A total of 365 features were identified from the BHTV images and profiles of the fracture density with depth for the three size categories are shown in Figure 49. No trend in fracture density with depth is observed for any scale of the fractures. The identified fractures are combined
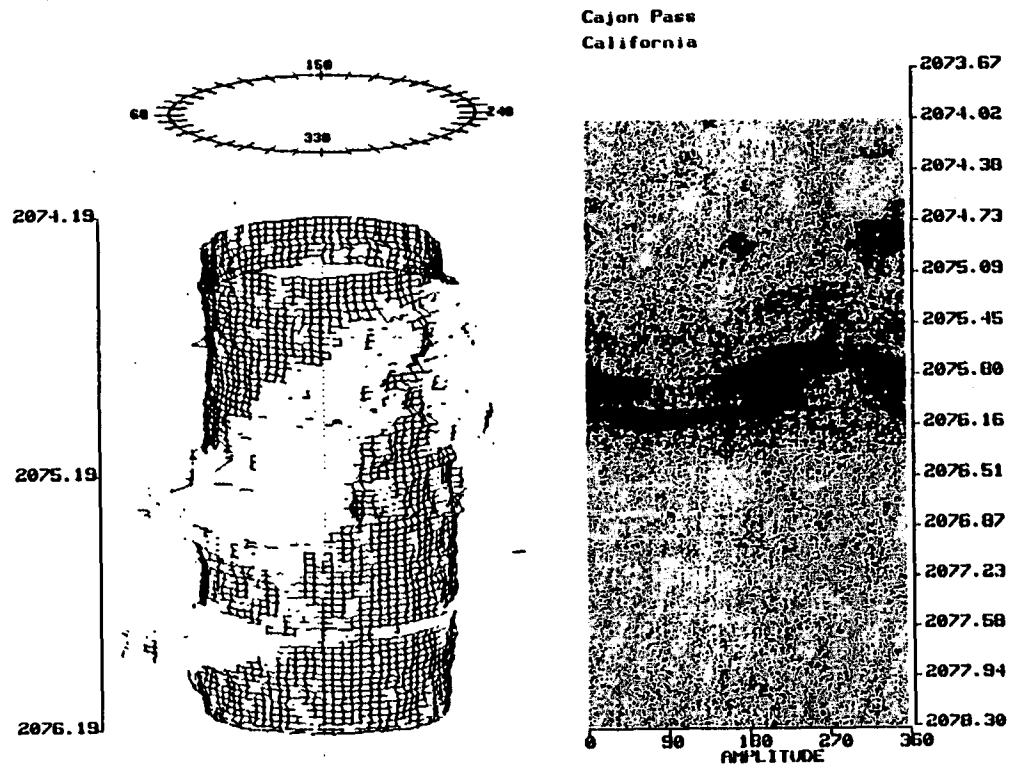
Figure 48. 1a) Standard unwrapped 360° plot of the amplitude of the reflected acoustic pulse (left panel) and the borehole radius (right panel) over the fracture at depth 2076. b) Perspective view of a 1 meter interval in the Cajon Pass well, surrounding a large fracture at 2076 m. Fracture geometry can be resolved on this true vertical scale image. The large dipping fracture is cross cut by a smaller sub-horizontal feature.

to show the fracture density per meter correlated with lithology and sonic data in the second profile of Figure 50. Aside from the interval from 1940 to 1960 m of stress-induced wellbore breakouts (Shamir et al., 1988), which contain only a few observable fractures, the total fracture population shows no trend in size or distribution with depth over the logged interval. These results are in contrast with a fracture analysis from an Illinois drillhole where fracture density and hydraulic conductivity decrease with depth (Haimson and Doe, 1983). Fracture studies of ten wells located in the western Mojave Desert just west of the Cajon Pass well by Seeburger and Zoback (1982) found only a slight decrease of fracture density with depth for most wells studied. They found some wells to have a uniform fracture density distribution while others showed concentrations of fractures at various depths as is the case in the Cajon Pass well.
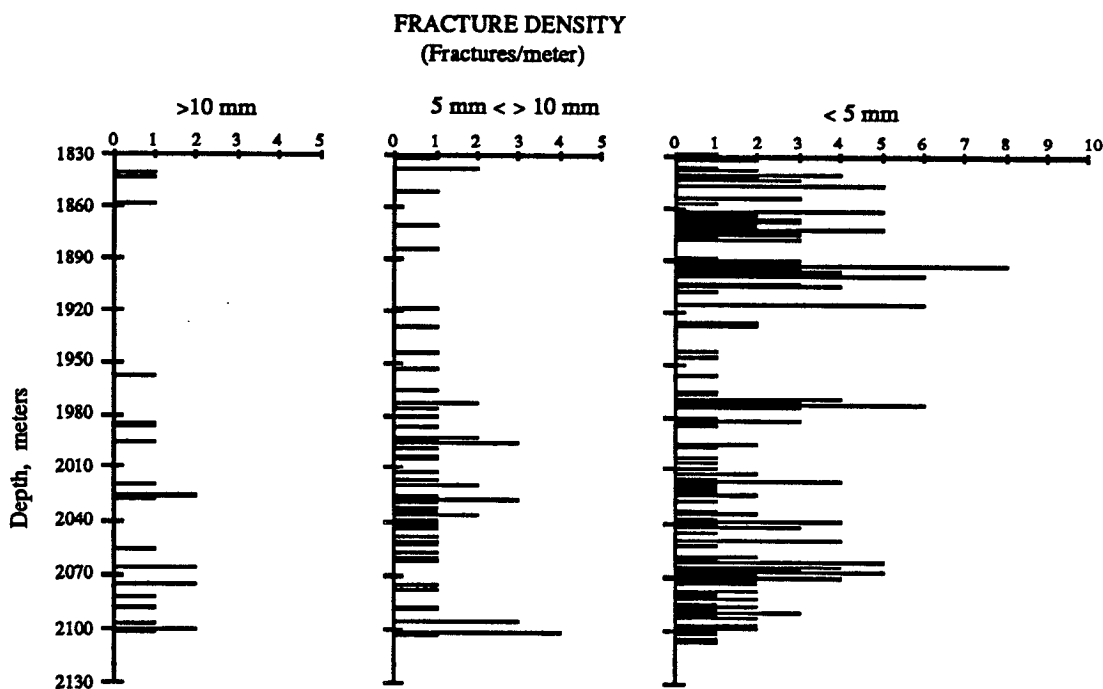
Figure 49. Fracture density with depth in the Cajon Pass well for three size categories of fractures.
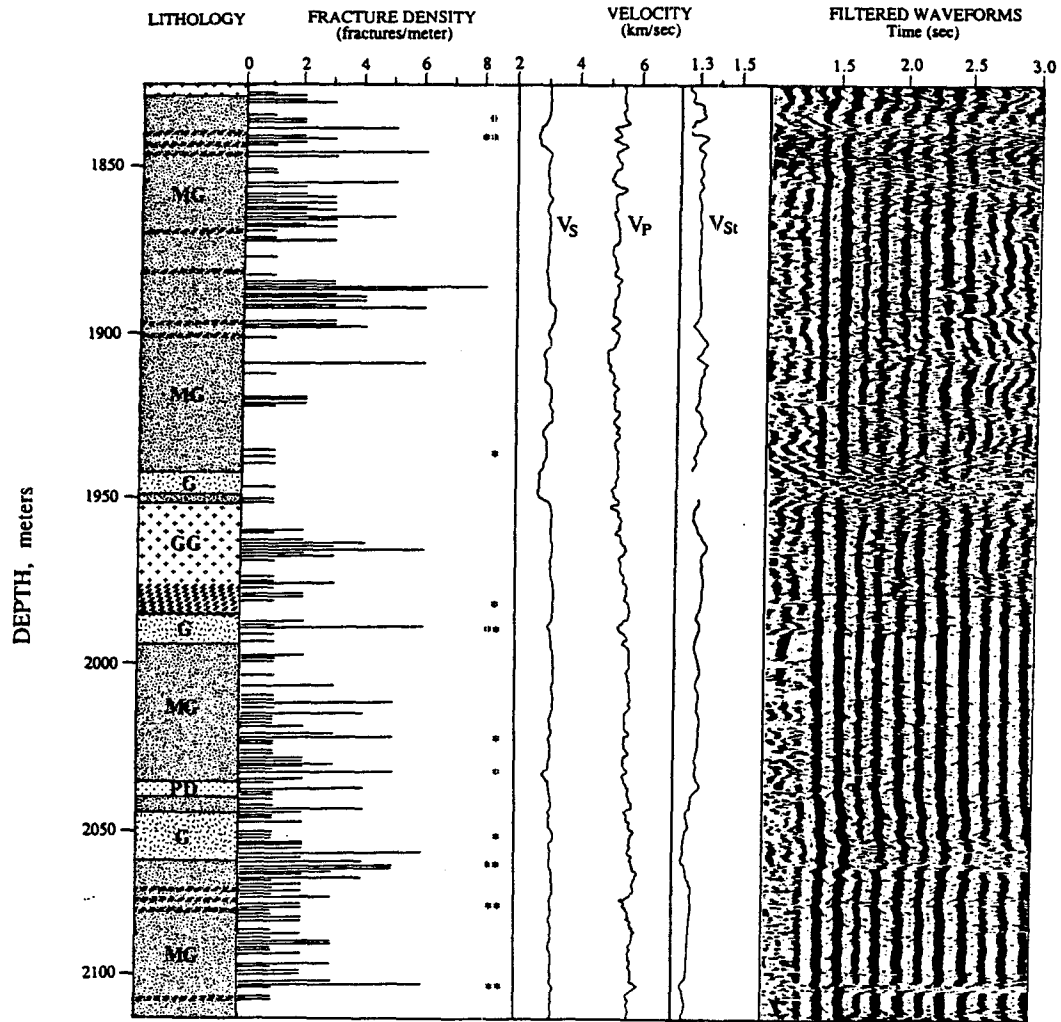
Figure 50. Lithology, fracture density, apparent aperture, sonic velocities and filtered sonic waveforms over the interval 1829 to 2115 in the Cajon Pass research well. A simple count of fracture density (on the left) is poorly correlated with the sonic arrival times displayed on the right. By weighting the fractures by their apparent aperture, a much stronger correlation is observed.

The apparent width of a fracture in BHTV images is probably larger then its true aperture. The rock surrounding a fracture may be weaker due to chemical alteration and preferentially broken by the destructive drilling process. It is likely then that the aperture of a fracture at the intersection of the borehole is greater then its aperture away from the borehole. Repeated pipe trips into and out of the hole and fluid circulation further increase the apparent fracture width at the borehole wall.

Figure 51a shows cross-sections for the fracture at depth 2076 m where the plane of the fracture has been determined and the cross-sectional profiles are corrected for apparent dip of the fracture. These sections were constructed at azimuth intervals of 60° around the borehole. Many fractures imaged by the BHTV do not have abrupt breaks at their boundary with the intact rock — instead, that boundary is often sloped in cross-section (c.f. Figure 51a 90° profile). Detailed cross-sections through the fracture image can be used to measure its minimum apparent width. Through the evaluation of several fracture cross sections an average apparent fracture width is determined. Figure 51b shows cross sections over about 0.75 meters of smaller aperture fractures at 1995 m.

Where fractures are open along the extent of their intersection with the borehole to the resolution of the BHTV imaging, apparent fracture aperture could be measured. The double asterisks in the second profile of Figure 50 correspond to zones where the fracture width per meter is greater than 10 cm; the single asterisks to zones with fracture width between 5 and 10 cm. The remaining intervals have nominal apparent aperture per meter. In several intervals with a high frequency of fractures the cumulative width per meter is quite low. However, where the apparent aperture per meter is large there are usually a large number of fractures. Although mechanisms acting to close fractures would be expected to reduce the number of open fractures with increasing depth, the data do not show this trend.

Only those through-going planar features that are open to an apparent width greater than 1 cm can be analyzed for orientation, substantially reducing the number of fractures where orientation can be determined. Fractures that intersect the borehole appear as sinusoids on unwrapped 360° views of reflectivity and borehole diameter (see Figure 3 and Figure 48). These sinusoids are often discontinuous for fine scale fractures and they can show very complex patterns at points where several fractures intersect or where fractures are not perfectly planar. For this reason automatic curve fitting routines cannot be used and interactive graphics are required to fit the

Fracture Cross Sections
Depth 2076 meters

Fracture Cross Sections
Depth 1995 meters

30°

90°

150°

210°

270°

330°

30°

90°

150°

210°

270°

330°
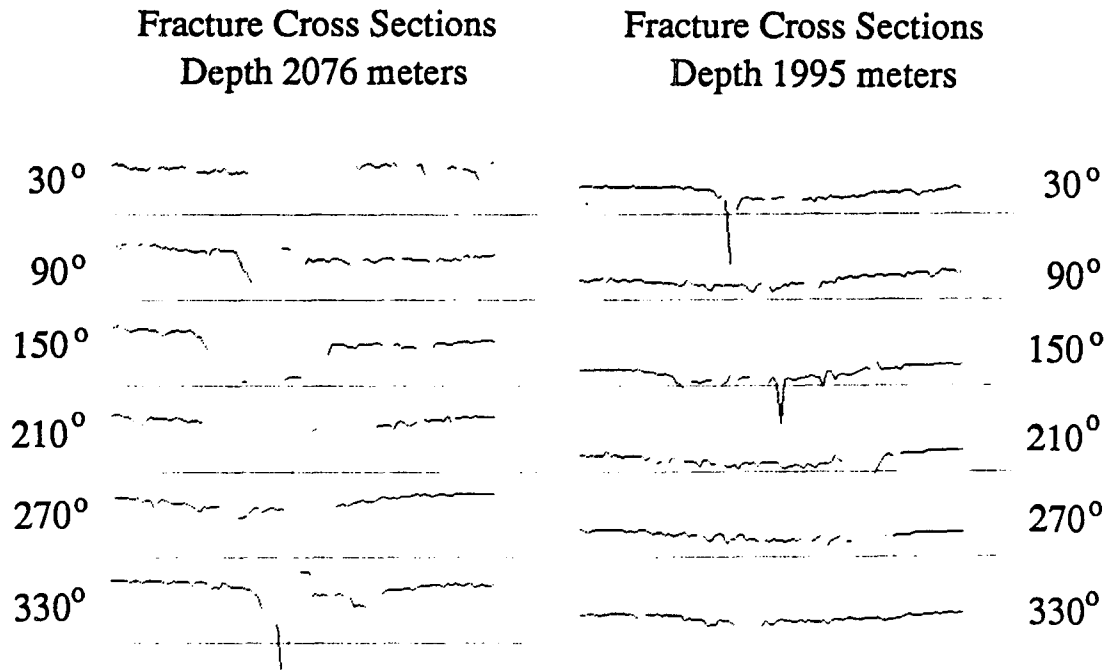
Figure 51. a) Cross sections across fracture at depth 2076 m where apparent aperture is approximately 26 cm. Sections are constructed normal to the fracture sinusoid at spacing of 50° azimuth and corrected for apparent dip.b) Cross sections across a 0.75 m fracture zone at depth 1995 m where individual fractures are less than 5 cm. Sections are constructed normal to the fracture sinusoid at a 60° azimuth spacing and corrected for apparent dip.

sinusoidal shapes. To measure fracture orientation the amplitude and phase of a best fit sinusoidal shape to the fracture are found using a graphics mouse with the standard 360° display of the image. The dip angle of the fracture plane is then the inverse tangent of the ratio of the fracture height to the borehole diameter. The dip direction is the direction of the lowest point on the sinusoid, and the strike is 90° to the dip direction.

Fracture orientations are shown in the Schmidt diagrams in Figure 52. Small circles in Figure 52 represent the poles of fractures with apparent widths between 1 and 5 cm, and large circles the poles of fractures over 5 cm. Although there is substantial scatter in fractures orientations the majority of large fractures strike north northeast, with moderately shallow dips to the northwest. No trend in fracture orientation was observed with depth.

The orientation of maximum horizontal principal stress at the Cajon Pass site is N73°E based on breakout data (Shamir et. al, 1988) and hydraulic fracturing experiments (Zoback and Healy, 1988). Stress magnitude measurements indicate a normal faulting stress regime at shallow depth in the Cajon Pass well. Fractures developed under this ambient stress field would be expected to have east northeast orientations. Thus, there appears to be no obvious relationship between the orientations of fractures over the interval 1829 to 2115 m and the current stress field. There is no evidence that Mode I extension (see Engelder, 1982) prevails at this depth nor are these fractures easily interpreted as shear features.
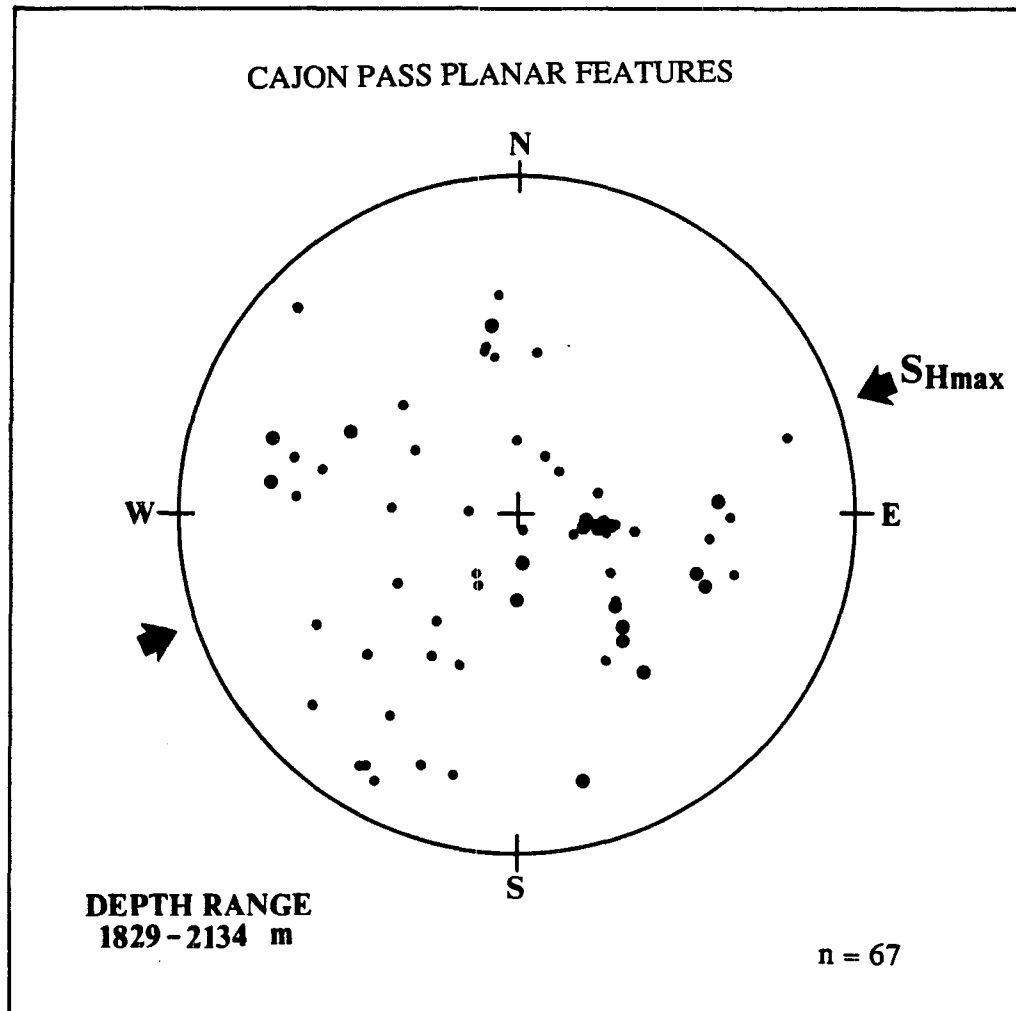
Figure 52. Lower hemisphere equal area projections of the poles to fracture surfaces in the interval 1829 to 2115 m in the Cajon Pass research well. Large fractures are shown as larger symbols. Although the smaller features have random orientations, a cluster of large fractures is present striking N15°E, dipping 30° west.

Correlation of Natural Fractures with Other Data

Fractures and Lithology

Core analysis over this interval was completed by Silver and James (unpublished data) and the simplified lithology is shown in the first profile in Figure 50. The major units are mafic granite (MG), granitic gneiss (GG), and younger intrusions of granite (G). The diagonal symbol represents zones of migmatites or highly foliated rock. A pegmatite dike (PD) intersects the well at 2040 m. Over the interval 1850 to 1950 m the mafic granite includes several migmatite zones which appear to separate alternating intervals of high and low fracture frequency. The interval 1940 to 1960 m corresponds to a zone of extremely wide breakouts; it is not possible to determine if the low density of fractures over this interval is real or a function of the image quality. Below 2000 m there is uniform fracture distribution although the interval includes several migmatite zones. From 1950 to 2000 m the gneissic granite and overlying and underlying migmatites have a relatively high fracture density with very low measurable aperture. This relationship is attributed to the abundant measurement of foliation planes in the BHTV analysis.

Sonic Velocities and Fracturing

At the time of this analysis comprehensive geophysical logs were not available, however, the Cajon Pass experiment has provided an ideal set of complementary data for the analysis of the acoustic waveform response to fluid-filled fractures. The complete BHTV log and the digital analysis of fracture geometry were used in conjunction with the full waveform sonic data to determine the response to fractures (Barton and Moos, 1988). Figure 43 shows velocities correlated with fracture densities and apertures for the interval 1829 to 2115 m in the Cajon Pass well. Velocities are relatively constant over this interval (Vp 5.5 to 6.0; Vs 3.0 to 3.3 km/s). Vp/Vs is about 1.75. Several low velocity zones occur at 1835-1845 m, 1940-1960 m (Vs only), and at 1995, 2076, and 2040 m. Some of these have high

Vp/Vs; all have decreased mean coherence. Stoneley velocities are about 1.3 km/s in the 26-cm hole above 2045 m, and 1.25 km/s in the 20-cm hole below. Low Stoneley coherence occurs at 1840, 2026, 2045, 2065, 2076 and 2102 m, and 1940-1960 m. Some of these are associated with lower Stoneley velocities.

Note that there is little apparent relationship between fracture density and sonic velocity. A much greater correlation exists between the velocities and the apparent apertures determined from the BHTV logs. Each of the intervals listed above contains fractures with measurable apertures, ranging more than 25 cm (2102 m) to somewhat less than 10 cm (2026 m). The correlation of these features with thermal and other anomalies is summarized in Table II and discussed in greater detail below. Several zones are the site of wellbore elongation due to the presence of breakouts (Shamir, et al., 1988). The Stoneley velocity is accordingly more variable over these zones precluding the identification of individual fractures within the breakout zones. In one instance (1940-1960 m) the shear velocity decreases, resulting in an increase in Vp/Vs.

Previous research has demonstrated a relationship between Stoneley wave amplitude and permeability (Paillet, 1980; Burnes, et.al, 1988). The amplitude of the Stoneley wave is particularly sensitive to the presence of hydraulically conductive fractures intersecting the borehole wall (Paillet and White, 1982; Rosenbaum, 1974), but it is also affected by variations in the borehole diameter and the seismic properties of the rock. Shear head waves will also show a response to fluid filled fractures where energy is scattered by the fracture intersecting the wellbore.

Field experiments with full waveform sonic tools show that the effect of fractures on velocities is complicated. Moos and Zoback (1983) demonstrated that fractures in crystalline rock can reduce velocities; where that effect is a consequence of both increased microscopic fracturing and alteration, the ratio Vp/Vs increases. Goldberg et al. (1984) observed decreases in Vp and Vs, and no change in the ratio, within fractured intervals in limestone. They did not observe any correlation between Stoneley wave amplitude and vertical fractures. Paillet and White (1982) showed that Stoneley wave amplitude is roughly proportional to total fracture aperture, however, Paillet (1983) compared different acoustic methods for estimating fracture permeability, and found that, with the exception of the Stoneley mode, amplitude reductions for the principle borehole modes do not necessarily correlate with hydraulic properties of the fractures. Hardin et al. (1987) observed that although the

effects are strongly frequency dependent, Stoneley wave amplitude reduction is positively correlated with fracture transmissivity determined by flow tests.

Correlation of Natural Fractures with Conductivity Logs

Data from a series of precision temperature logs (Lachenbruch and Sass, 1988), an electrical conductivity log of the borehole fluid (Kharaka, 1988) and measurements of the concentration of fluorescene dye used to tag the drilling fluid before initiation of a fluid drawdown test can be used to determine the origin of the fluid being drawn into the well. The four temperature profiles recorded between May 14th and September 30th shown in Figure 53 (after Lachenbruch and Sass, 1988) compared to the aperture data over the same interval. Fluid flowing into the well within a narrow zone will offset the temperature profile, giving an anomalously low thermal gradient at the fracture. For example, the gradient minimum at 2076 m correlates with a major fracture observed in the BHTV image which has a measured aperture of 26.6 cm (Figure 44a). This fracture correlates exactly with a change in fluid conductivity gradient (Kharaka, 1988) and a drilling break where the penetration speed of the drill bit was suddenly accelerated (Silver, written comm.). Fluorescene concentrations in fluids below 2076 m are equal to those of the original drill fluid, implying no influx of formation water below that depth. Note, however, that the fracture series at 1995 m (Figure 44b) has a cumulative aperture of 20.9 cm over 1 m, but no associated temperature anomaly. Additional fractures delineated in the BHTV log that also correlate with minima in the thermal gradient occur at 1840, 1940, 2026, and 2065 m. Thus many of the large natural fractures that intersect the Cajon Pass drillhole have an expression in the temperature logs, suggesting that they are hydraulically conductive. Fractures under about 5 cm do not appear to have significant hydraulic conductivity.
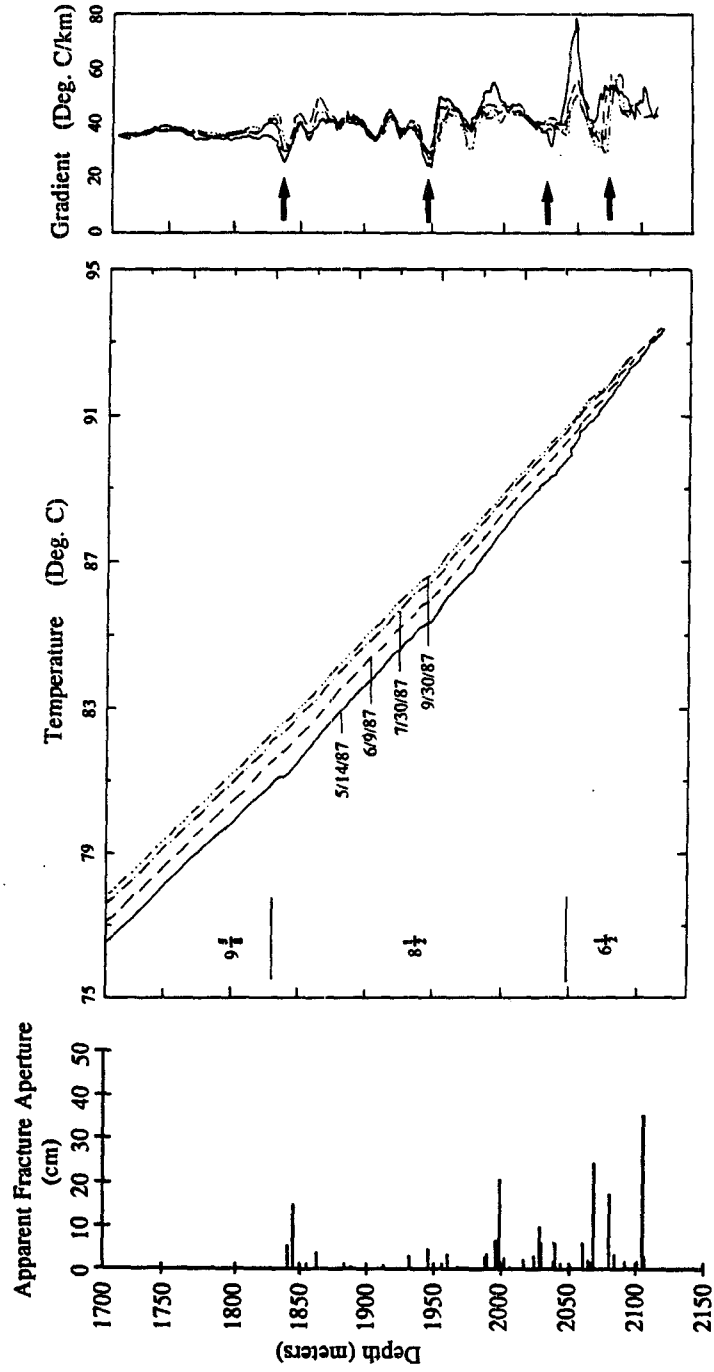
Figure 53. Temperature profiles over the interval 1829 to 2115 m in the Cajon Pass Well run between 5/14/87 and 9/30/87 (after Lachenbruch et al., 1988).

Discussion

Table II presents the results of fracture aperture and sonic wave analyses of all of the major features observed in the Cajon Pass well from 1829 to 2115 m. Also shown are the other anomalies associated with these fractures. Anomalies not associated with fractures (such as those due to the change in hole size at 2046 m) are not shown. Note that all of the fractures with Stoneley anomalies also have thermal gradient minima, except that at 2102 m; the possible presence of a Stoneley anomaly is obscured for the fracture within the breakouts at 1940. Drilling breaks were seen at three fractures. All of the fractures had some anomalous refracted (P and S) wave response, although again the lack of response at 1940 m may be due to the breakouts.

Table II

CAJON PASS FRACTURE COMPARISON

DEPTH meters	Fracture Aperture	Stoneley Wave	Refracted Waves	Fluid ** Conductivity	Drilling Break	Temperature
1841	13.5	v/c	v/c	X	X	X
1940	4.6	***	***	X		X
1995	20.9		v/c			
2026	11.7	c	v	X?	X	X*
2065	31.8	c	c			X
2076	26.6	c	v/c	X		X
2101	34.3	v/c	c	−	X	?

v=velocity change
c=coherence change
* Temperature anomaly appears on 5/14 temperature profile only (Lachenbruch and Sass, 1988)
** Depths are approximate (Y. Kharaka, 1988)
*** Elastic properties obscured by severe breakouts

In this study a reduction in Stoneley wave coherence is seen at fractures which by other indications appear to be permeable. This is not unreasonable as the mechanism proposed for Stoneley wave amplitude reduction (scattering, reflections, etc.) would also reduce coherence. The relationship between Stoneley wave coherence and fractures is generally supported by these data, except for the interval 1992-1996 m. A cross section across this fracture zone was presented in Figure 44b where a series of thin parallel fractures span approximately 0.75 m in the borehole.

Compressional and shear velocities are lower within the fractured interval, but Vp/Vs is unchanged. The waveforms are distorted due to the reduced coherence of the arrivals, although the Stoneley wave arrival is unaffected. For the large fracture at 2076 m the Stoneley wave is strongly attenuated. The refracted arrivals are also less coherent, although in this case the velocities are unchanged. Both temperature and fluid conductivity are affected at this depth. The aperture of the fracture at 2076 is 26.6 cm, only slightly greater than the 20.9 cm cumulative aperture over the fracture zone at 1995 m (Figure 44a). Although the zone at 1995 shows no evidence of hydraulic conductivity, the velocities and coherence of refracted waves are lower, suggesting that these fractures are mechanically weak.

The data shown in Table II indicate that the fracture at 2076 m is not the only permeable fracture. However, not all of the measurably open fractures contribute to the total permeability. Based on the Stoneley response the most conductive fractures are at 1840 and 2076 m. One inconsistency in these data is the apparently high permeability of the fracture at 2102 m which based on the constant fluorescene concentration below 2076 m has not contributed any fluid. The only explanation of these observations is that this fracture has no connectivity to a fluid source.

Conclusions

The orientation, distribution and aperture of natural fractures intersecting the Cajon Pass research well were determined through analysis of borehole televiewer (BHTV) data. More than 300 planar features have been observed in borehole televiewer data over the interval 1829 to 2115 m in the Cajon Pass well. Most of these are probably foliation planes. Large open fractures have shallow inclinations and tend to be aligned striking roughly N30°E. There is no apparent relationship between these fractures and the current stress state, as observed in other studies. Temperature anomalies due to fluid flow into the well detected during a long-term permeability experiment occur at several of these fractures. Compressional, shear and Stoneley guided wave velocities are within the expected range. The relationship between fracturing and sonic velocities is clearer if the fracture apertures rather than simply the density of natural fractures, are used. Indications of enhanced permeability are associated with many of the larger features. These are also

characterized by reductions in Stoneley wave coherence, in agreement with theoretical studies.

Analysis of BHTV Log Data for Borehole Caliper at
ODP Site 642E — Outer Voring Plateau

Introduction

One of the main objectives of the Ocean Drilling Program is to explore the
geology of the ocean crust and increase our understanding of the formation and
development of the deep ocean basins. This initiative involves drilling exploratory
research wells at target oceanic sites. The drillship Resolution (BP/SEDCO 451) is
used to perform the the drilling operations at each site and as a base for scientific
experimentation. On Leg 104 of its mission the Resolution visited the Outer Voring
Plateau located in the Norwegian Sea midway between Iceland and the Norwegian
coast (Figure 54, from the Init. Rept ODP Leg 104, Eldholm, et al., 1987). Eight
holes were drilled at three sites during leg 104; the deepest site 642 was located at the
inner part of a prominent wedge of dipping reflectors on the Outer Voring Plateau
(Figure 55). Reflector "K" was the specific target depth for drilling on this leg. The
continental margin off Norway is a relatively young geological feature and as such is
particularly well suited for investigating events occurring during the late rifting and
early seafloor spreading evolutionary stage of a passive continental margin.
Geophysical surveys off Norway have revealed buried features on the lower
continental slope that appear to be closely related to the breakup of a continent and the
earliest history of sea-floor spreading, however, no consensus as to the nature and
crustal composition of these features had been reached before drilling at the ODP Leg
104 site. The results of experiments conducted during this expedition below reflector
"K" indicate a transition from rift to drift phase, whereas the material above this
horizon was likely emplaced later, during the North Atlantic Thulean volcanic surge in
the lower Eocene (53-56 m.a.) (Eldholm et al, 1987).

Over 906.8 m of material beneath about 320 m of sediment cover were cored
on the landward side of the Voring Plateau Escarpment. The basement lithologic units
encountered in this drillhole are an upper and lower volcanic series differentiated on
the basis of structure, texture, mineralogy and geochemistry (Init. Rept. ODP Leg
104). Both the upper series (337 to 1086.5 mbsf) and the lower series (1086.5 to
1229.4 mbsf) consist of cyclic repetitions of volcaniclastic sediments and basalt
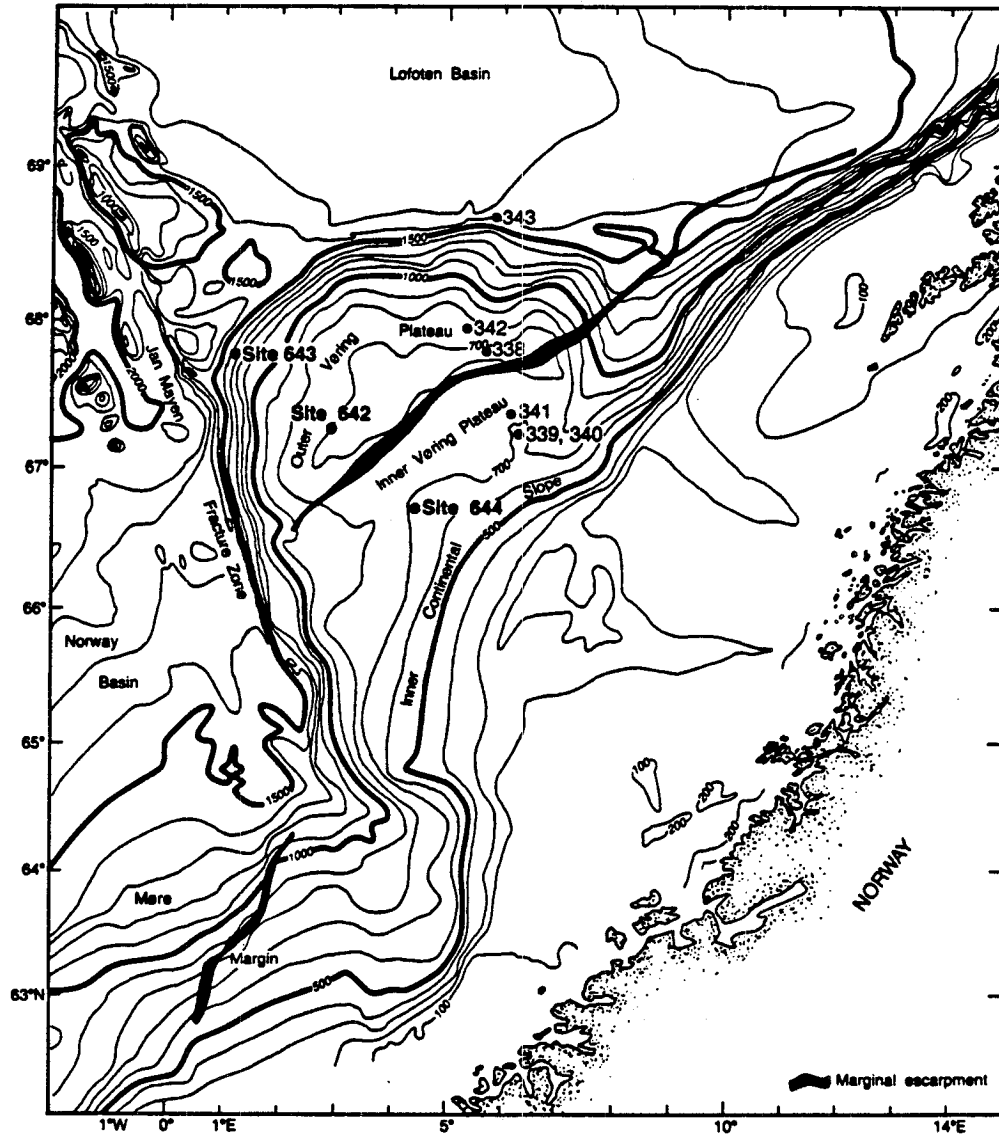
Figure 54. Site location for ODP Hole 642E in the Outer Voring Plateau (after Eldholm et al., 1987)
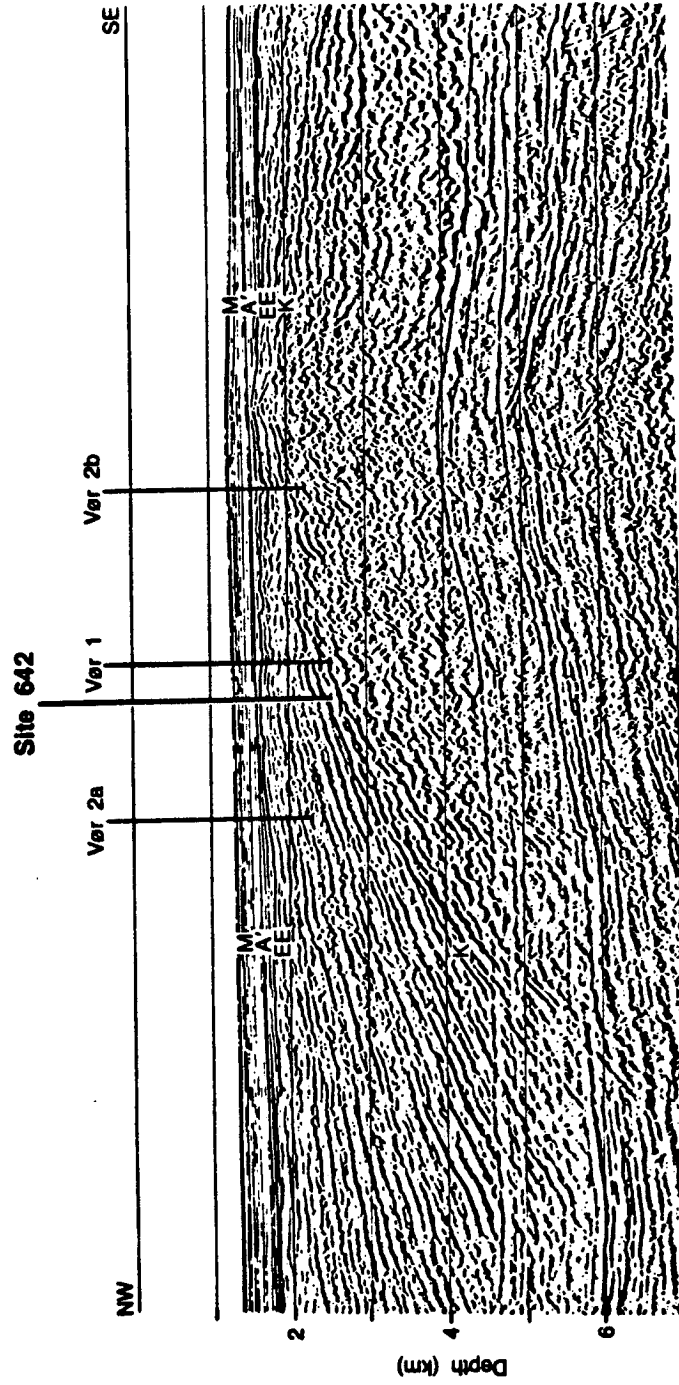
Figure 55. Reflection profile showing dipping reflectors in the vicinity of ODP site 642E.

flows. Both series were further subdivided into groups according to grain size. The upper and lower series are also distinguished by the nature of the volcaniclastic sediments that are interlayered with the basalt flows. Throughout the drilled section the basalts are usually brecciated at the tops of the flow sequences.

During Leg 104 a complete suite of standard Schlumberger logs was recorded in Hole 642E. These included caliper, natural gamma, spectral natural gamma, induction resistivity, neutron porosity, gamma-gamma density, and sonic travel-time (picked during logging). Figure 56 gives the extent of the logged interval for each logging tool run in Hole 642E and the simplified sketch of the lithologic column as defined by petrographic analysis of the core (from Summary and Conclusions, Leg 104 Initial Report, Eldholm, et al., 1987).

The BHTV log was run as a specialty log on this cruise in an attempt to fulfil the ODP objective for measuring in-situ stress in the oceanic crust. The log was planned to transect the entire cored interval of basalt however because of mechanical complications only a portion of the drillhole was logged. Due to the failure of one of the centralizer bow springs the BHTV tool was extremely off-center in the drillhole. Ships heave was another adverse component to data collection as was the failure of the electronic depth encoder in the logging cabin. Lack of ships time to properly run the log was an additional factor and the majority of the log was run at about ten times the speed of a typical BHTV log.

All of the standard log measurements were good except for the caliper log. The lack of variability in the caliper data indicates that the caliper arm was not functioning properly rendering it useless for correlation with other logs. This study makes use of the caliper potential of the BHTV logging tool in an attempt to recover viable caliper data needed for the complete analysis of other logs such as sonic waveforms. In addition, careful correction and examination of the data for borehole shape has provided information on in-situ stress at the site.
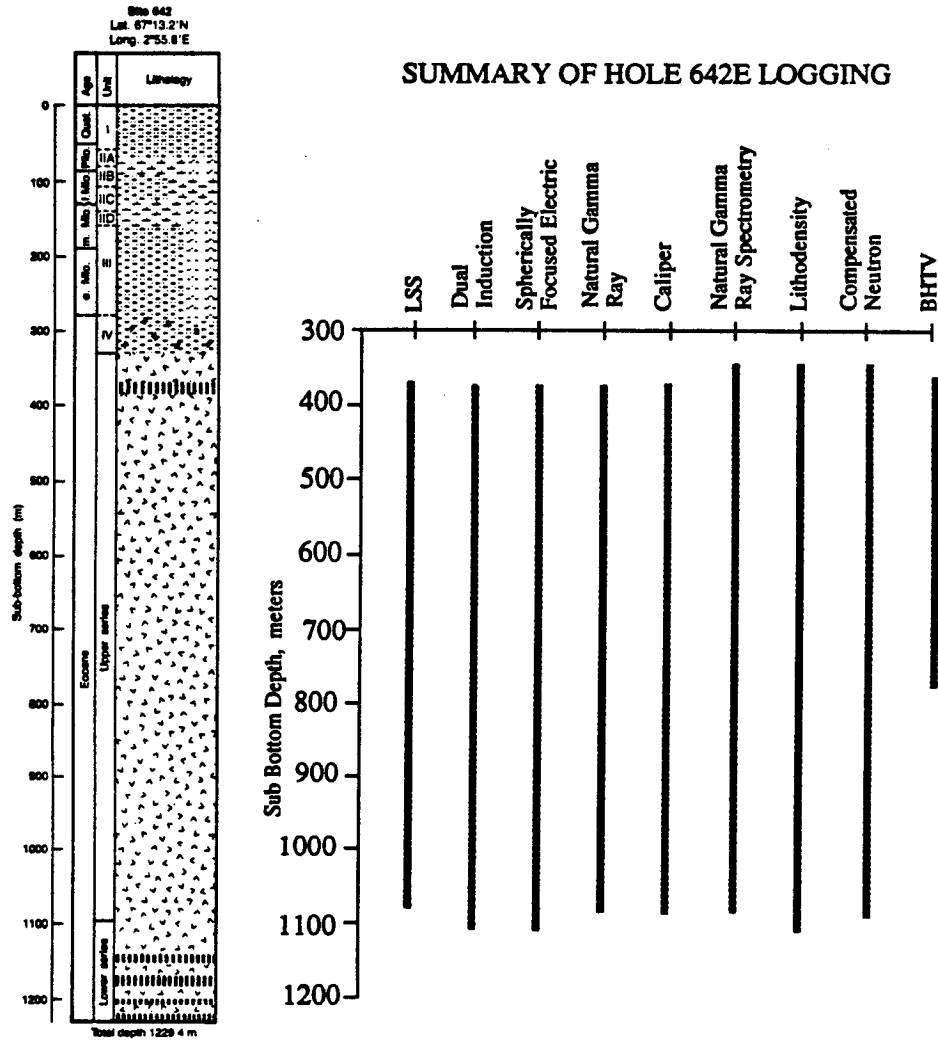
Figure 56. Extent of the logged interval for each of the logs run in Hole 642E along with a simplified lithologic column.

Caliper Analysis and Results

The BHTV data were recorded in August, 1985. 140 meters of data were recorded at the standard logging speed of 2.5 cm/sec and approximately 470 meters at approximately 25 cm/sec. Rough seas prevailed during the recording requiring substantial editing of the digitized data prior to interpretation. Polar cross sections of the digital data indicated that the tool was off center in a circular borehole and data were processed to determine the correct tool position. Figures 57 and 58 show the effects of the off center correction for this data set where the uncorrected data is plotted with depth in Figure 57 and the corrected data in Figure 58. The data were also median filtered before analysis.

The data recorded at the separate logging speeds were analyzed separately. The 2.45 cm/sec speed interval was recorded in the lower section of the well and the 8.5 cm/sec interval begins at about 2090 m to the top of casing at 1619 m. This interval transects a portion of the upper series of basalt flows. The water depth is 1289 m.

The results of the caliper analysis are shown in Figure 59 plotted with other standard log data. The major axes of an elliptical fit to the data (Figure 59, track 1, curve 1) ranges between 10.6 to 12.0 cm. The minor axes (Figure 59, track 1, curve 2) range between 9.4 and 10.6 cm. There is an increase in borehole diameter at approximately 1933 m. The eccentricity (Figure 59, track 2, curve 1) range is 5 to 20% over the logged interval. It must be emphasized that the reported depths are only estimates of the true depth of the sonde as the depth encoder had malfunctioned and depths were taken from logging cable markers. The companion logs plotted for correlation with the BHTV derived caliper data in Figure 59 are the natural gamma (Figure 59, track 3, curve 1), the deep induction and spherically focused resistivity logs (track 4, curves 1 and 2), the neutron porosity (Figure 59, track 5, curve 1), the density log (Figure 59, track 5, curve 2) and the formation compressional and shear wave velocities (Figure 59, track 6, curves 1 and 2) measured from full waveform acoustic logs (Barton et al., 1988). There is a gradual decrease in both resistivity measurements and in the compressional and shear velocities below 1933 m as well as a gradual increase in natural gamma content. The increase in borehole diameter
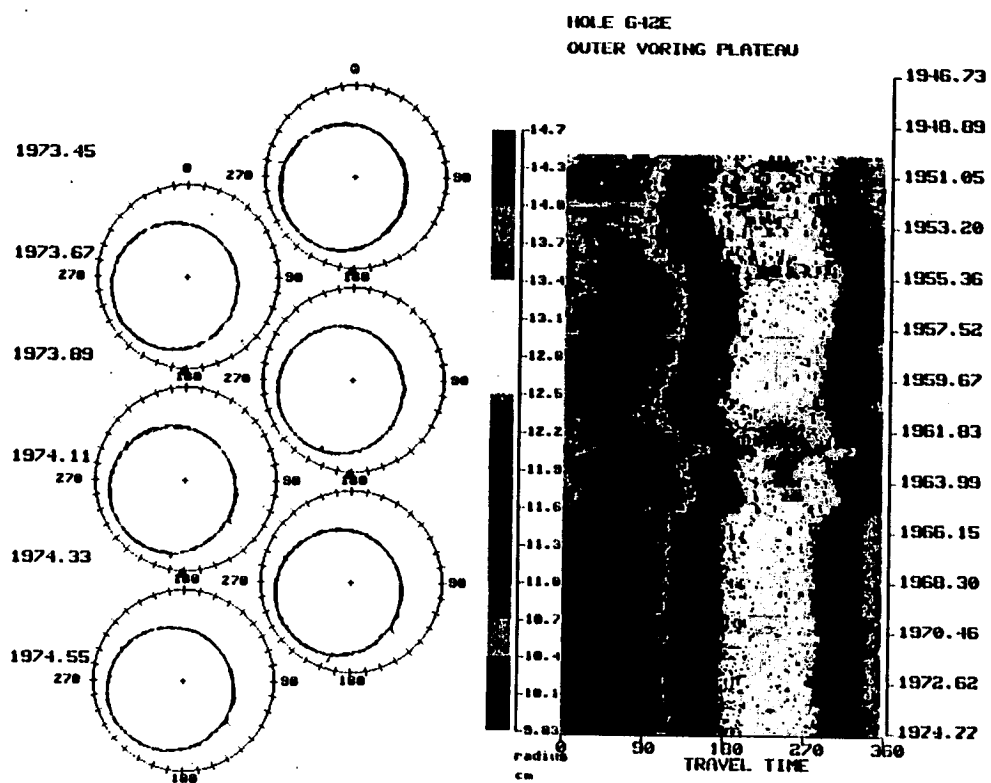
Figure 57. Polar cross sections (left panel) of data recorded in Hole 642E and corresponding BHTV image (right panel) where data has not been corrected for off center effects
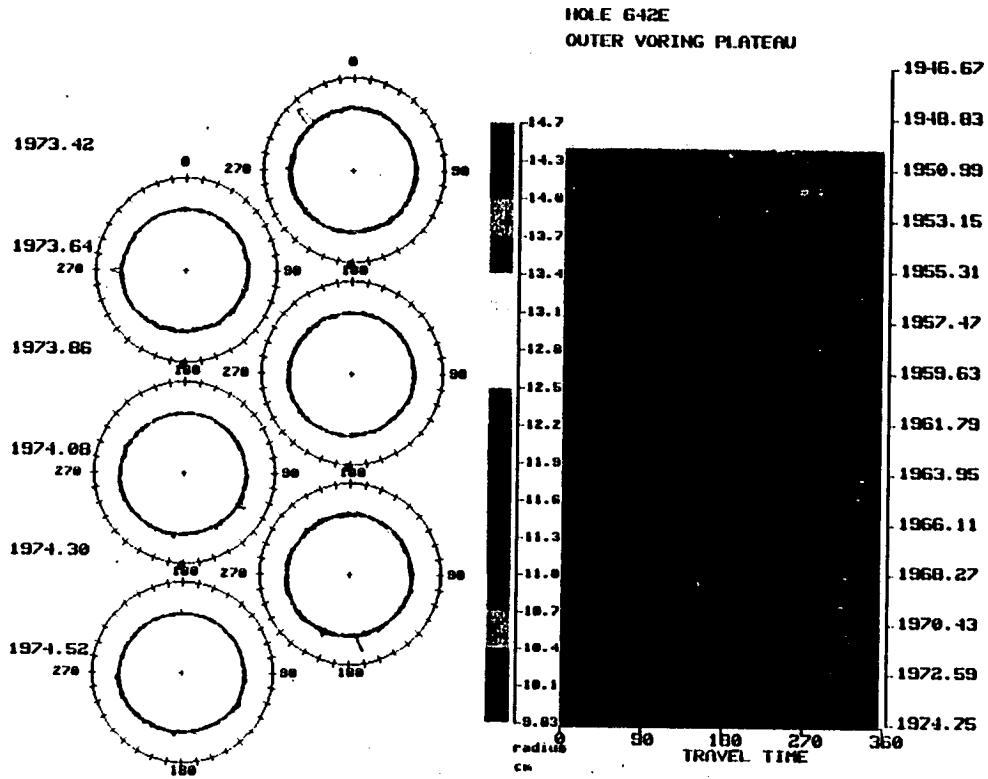
Figure 58. Polar cross sections (left panel) of data recorded in Hole 642E and corresponding BHTV image (right panel) where data has been corrected for off-center effects.
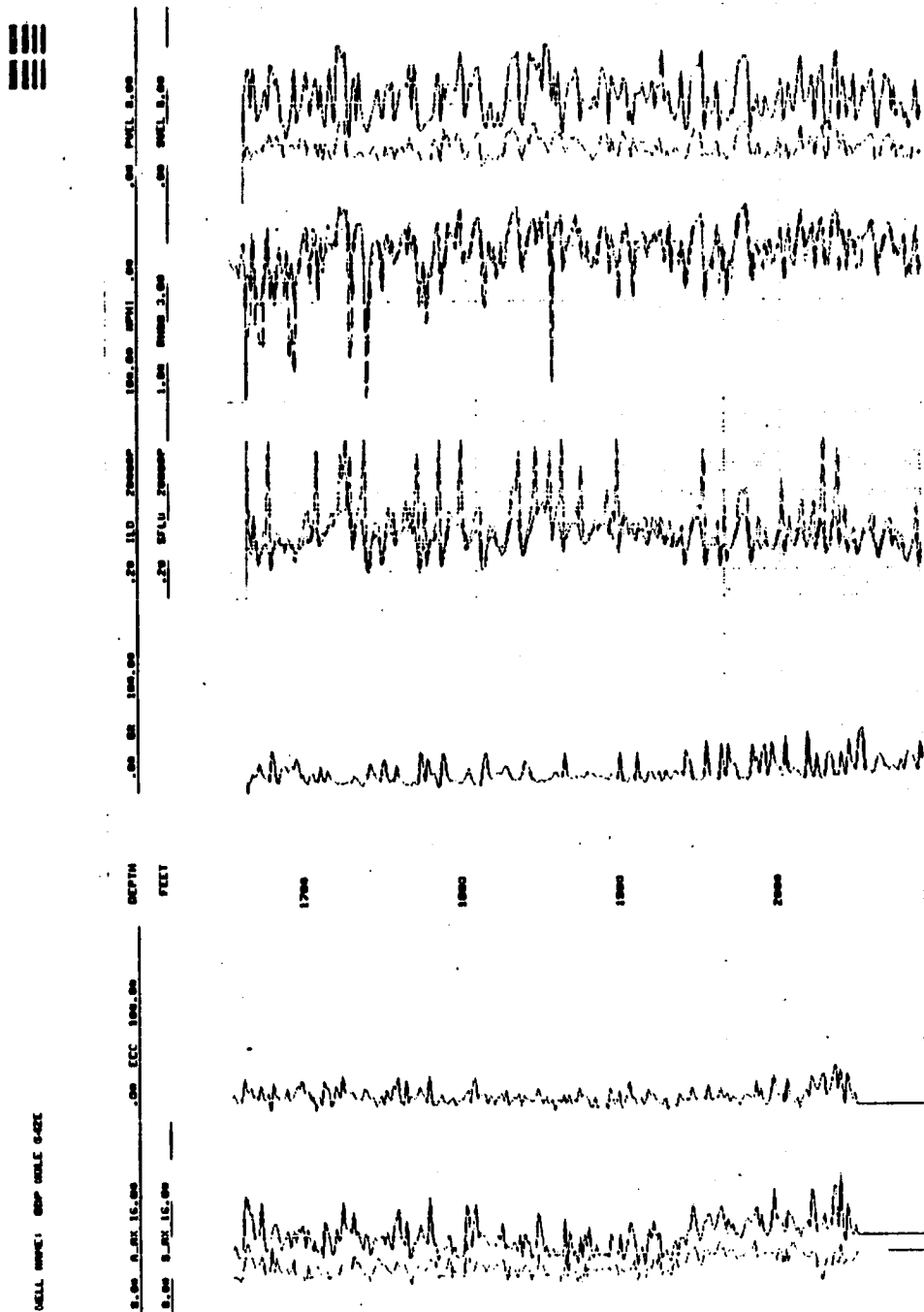
Figure 59. Caliper log results for data recorded in Hole 642E over the interval 1619 to 2090 m correlated with standard logs.
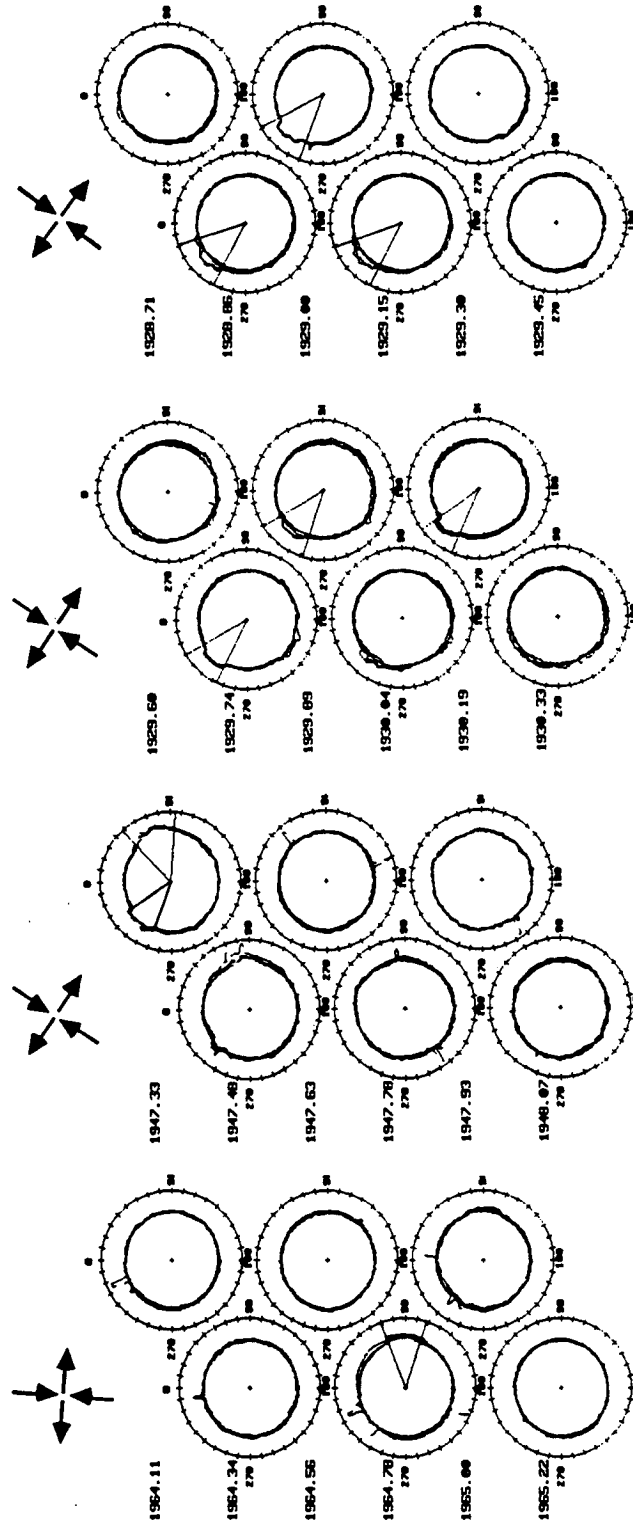
Figure 60. Polar cross sections of possible wellbore breakout zones in Hole 642E located in the Outer Voring Plateau. Arrows indicate the direction of the deviatoric stresses with inward positive compression.

determined from the BHTV data is relatively abrupt at depth 1933. As mentioned, the upper series of basalt flows is divided into three groups, the top subdivision, measured from the rig floor, is from 1612 m to 1896 m, the second group from 1896 to 2088 m and the third from 2088 m to reflector "K" at 2376 m. The change in response of the logs at depth 1933 m can be associated with the boundary between Group I and Group II basalts of the Upper Series of flows.

The corrected data were analyzed for detailed borehole shape to detect evidence of wellbore breakouts. The lower section logged, analyzed over 5 cm intervals, does include zones that may be interpreted as breakouts. Polar cross section through three of these zones are shown in Figure 60. The breakouts are generally very wide over these intervals where the distribution of orientations has a peak at about 124° (Figure 61) corresponding to a direction of maximum horizontal principal stress of N34E^O. These observations must be interpreted with extreme uncertainty due to the very low number of observations (n=25) and the quality of the data. The exact depth location in the well is unknown due to the mechanical failures mentioned above. A mean direction of N124^{O}E for the least horizontal principal stress at the 642E site was computed for this data with a standard deviation of 19.8^O
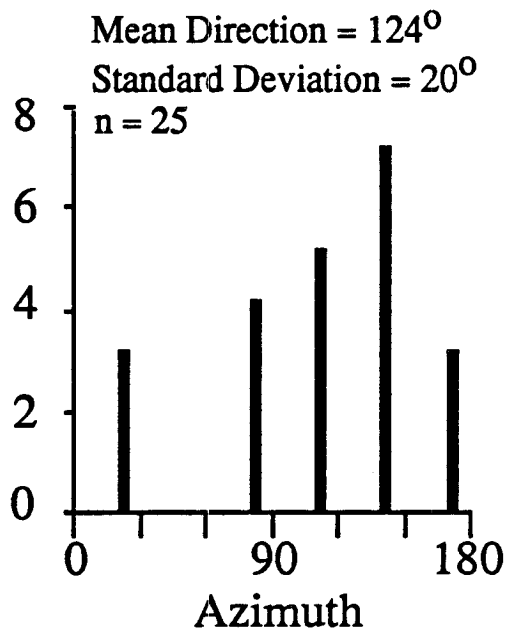
Figure 61. Histogram of breakout azimuths for Hole 642E located in the Outer Voring Plateau.

Discussion

The direction of the maximum horizontal compression of N34°E determined from the analysis of wellbore breakouts in Hole 642E is parallel to the strike of the Voring Plateau Escarpment (Figure 54). Figure 54 shows the bathymetry in the vicinity of the Outer Voring Plateau. Site 642E, is surrounded by sharp topographic gradients of about 1000 m in 400 km. There is some evidence from the southern Atlantic coast of North America that the topography of the continental margin can effect the regional stresses. Figure 62 shows a portion of the world stress map that includes the location of ODP Site 642E. Aside from two stress indicators near the southern coast of Norway the regional stress data indicate a southeasterly direction for S_{Hmax}. The orientation of maximum horizontal principal stress at this site obtained through the breakout analysis appears to be uncorrelated with other stress measurements in this region.

Although the Outer Voring Plateau incorporates passive margin tectonics there is active seismicity in this region. Figure 63 from Sleep et al. (1988, after Husebye et al., 1978) shows the seismicity pattern of Fennoscandia which defines a seismic zone along the Norwegian coast. The single focal mechanism available for this region represents an earthquake swarm in Meloy, Norway and shows pure normal faulting with tension parallel to the Norwegian coast. Modeling of passive margin stress and rheology has been undertaken by Sleep et al., 1988 and Stein et al., 1988) in order to explain the observed seismicity in the passive margin of eastern Canada and elsewhere. The distribution of seismic events there implicates the reactivation of faults created during continental rifting as the source of the seismic activity. Seismic data also shows focal mechanism variations across the passive margin in the Baffin Bay area suggesting a spatially varying stress field (Stein et al., 1988). In contrast to conventional explanations which favor intraplate stresses acting at this margin, these authors indicate that deglaciation is in part the cause of the earthquakes.

Deglaciation gives rise to flexural stresses generated by the removal of ice sheets loading the continental shelf. From the analysis of available data from the eastern Canadian margin, deglaciated margins are better correlated with the larger passive margin earthquakes. Earthquakes are not well correlated with regions of large sediment loads but are well correlated with deglaciated regions. The variation in stress

mechanisms across the margins can be explained by the deglaciation models of Sleep et al. (1988) and Stein et al. (1988). In addition to the stress effects of flexure, continental margin spreading stresses are present due to the lower density of continental crust than that of the mantle which causes the continental crust to spread out over the oceanic lithosphere (Sleep et al., 1988). This phenomena results in tensional stresses on the continent which become compressional in the oceanic lithosphere. The available seismic data and the data analyzed in this study may fit a model of a tensional to compressional stress change from the Norwegian coast seaward to the Outer Voring Plateau.

Modeling the stresses in the vicinity of Hole 642E using an appropriate flexural model and rheology could provide the necessary constraints to interpret the results of this analysis of wellbore breakouts. Further stress measurements in the vicinity of Site 642E are also necessary to determine if this stress measurement is effected by deglaciation, local topography or if the data are too poor to resolve the true stress field.
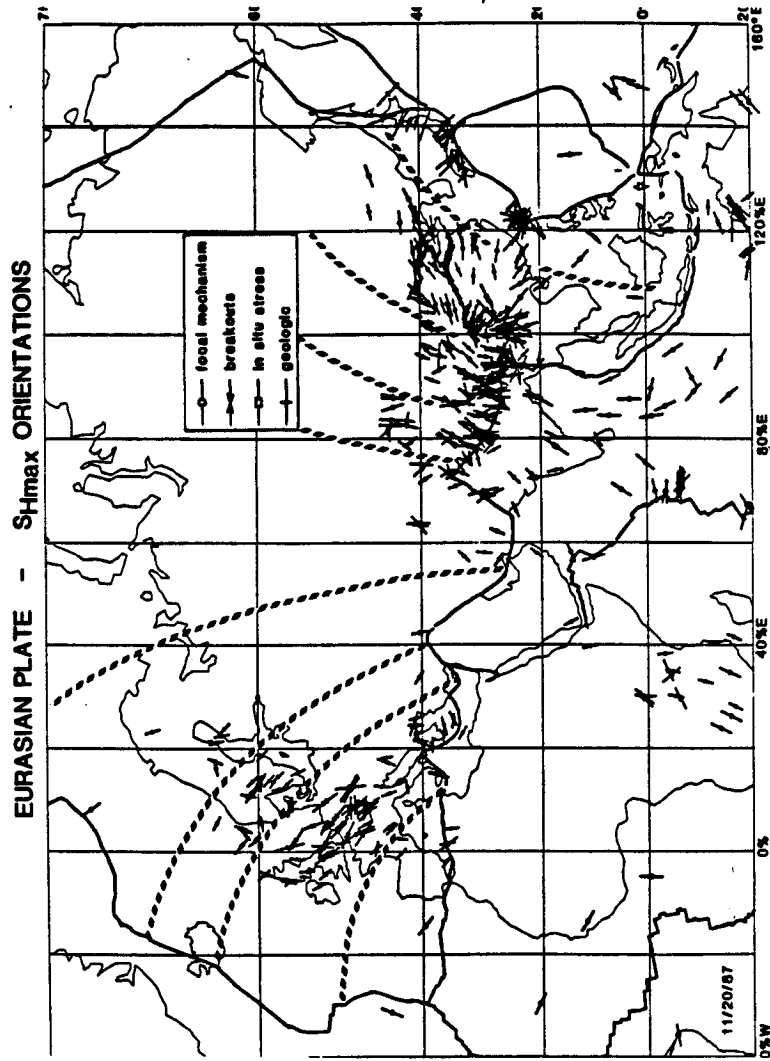
Figure 62. A portion of the world stress map (from Zoback and Zoback, 1988) in the region of ODP site 642E.
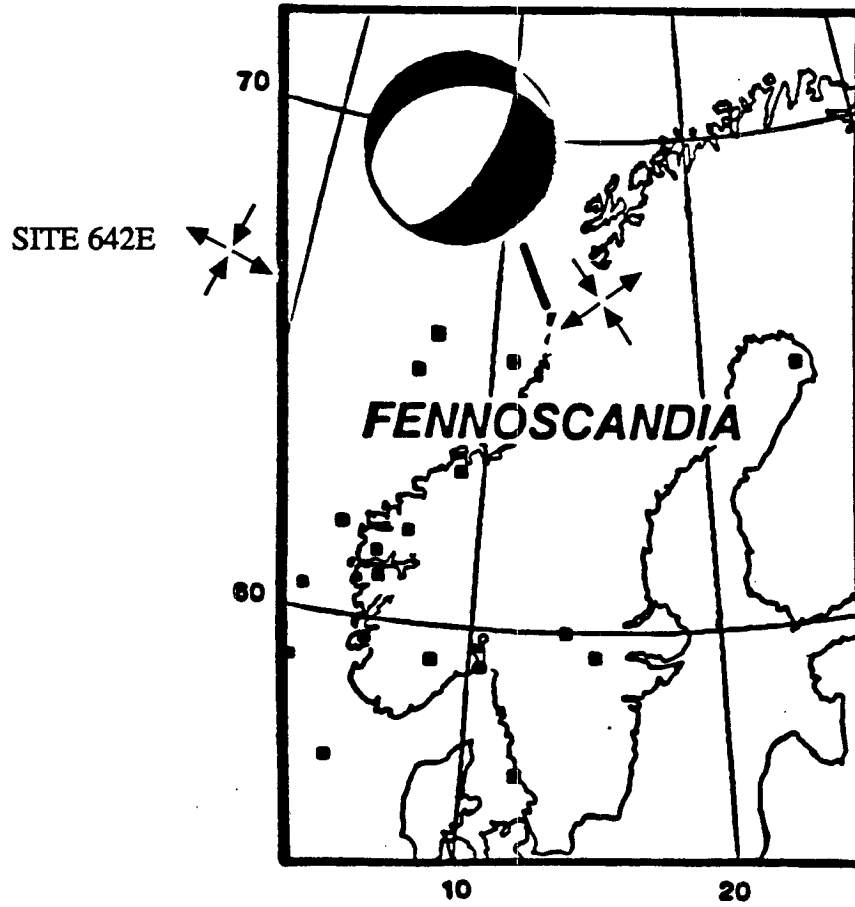
Figure 63. Seismicity off the Norwegian coast (after Sleep et al. 1987 and Husebye et al., 1978). Deviatoric stresses are shown for Site 642E and for the coast of Norway.

SECTION II

Determination of In-Situ Stress from the Polarization of Borehole Guided Waves
in Vertical Seismic Profiling

*"Every truth passes through three stages before it is recognized.
In the first it is ridiculed, in the second it is opposed, in the third
it is regarded as self-evident."*
Arthur Schopenhauer   (1788-1860)

CHAPTER 1: BACKGROUND

Introduction

This section describes a new technique for determination of the orientation of
horizontal principal stresses based on the horizontal particle motion of borehole
guided waves recorded during vertical seismic profiling (VSP) experiments. Among
the advantages of this method are the ability to obtain stress information at great
depth, the ability to make stress measurements in cased wells, and the broad
availability of VSP data. In a typical VSP experiment three-component seismometers
provide simultaneous measurement of vertical and horizontal wave fields, resulting in
the capability of determining the directional dependence of velocity and particle
motion of seismic waves as they propagate.

In recent years there has been considerable interest in seismic velocity
anisotropy detected in VSP experiments. In general, there are three possible causes of
velocity anisotropy. It may be intrinsic anisotropy due to rock composition such as
the velocity anisotropy of the upper mantle observed in teleseismic data (Newmann,
1930; Byerly, 1938; Herin, 1969; Solomon, 1972; McEvilly, 1964; Brune, 1969). A
second cause of velocity anisotropy is due to the ambient stress field (Nur, 1971;
Crampin, 1977; and Crampin et al., 1980). Stress-induced velocity anisotropy refers
simply to changes in stress that cause changes in crack width and consequently in
wave velocity. Given measurements of wave velocity in stressed materials it should
be possible to infer the stresses that produce the observed values. The use of velocity
anisotropy for determining stress changes in the shallow crust was explored

theoretically by Nur (1971) and by Crampin et al. (1980, 1978). These analyses specifically relate the distribution of microcracks to changes in effective elastic moduli due to stress. Experimental measurements of stress induced velocity anisotropy are not extensive but do confirm theoretical predictions (Nur, 1969; Nur and Simmons, 1969a; Stesky, 1985). Field experiments to determine in-situ stress by measuring seismic velocity have been attempted. In-situ measurements have shown considerable variability in the magnitude of the velocity dependence (Reasenberg and Aki, 1974; Gladwin and Stacy, 1973, Liu, et al., 1985). A third possible cause of velocity anisotropy, in the specific case of VSP experiments, is related to the perturbation of the ambient stress field by the existence of the borehole. The borehole stress distribution can be modeled as the effect of a stress concentration created by a hole in an infinite elastic plate (e.g. G. Kirsch, 1898). This concentration of stress may affect the velocity of wave propagation near the borehole wall. Because the wavelengths of the compressional, shear and guided waves in the VSP are on the order of ten times the borehole diameter, the velocity anisotropy detected from the analysis of borehole seismic waves probably relates to far field effects. However, the amplification of non-hydrostatic tectonic stress due to the stress concentration around boreholes may provide an additional stress heterogeneity factor that is superimposed upon the ambient stress field.

Velocity anisotropy studies utilizing three-dimensional VSP data generally consider compressional and shear wave velocity as a function of the azimuth of ray propagation (Gal'perin, 1971; Crampin 1983; DiSiena, et al. 1984; Gaiser et al.1984). Wavemode polarization analyses of VSP data have been restricted primarily to body waves to determine seismometer orientation (DiSiena, et al., 1984). Gaiser et al. (1984) compared compressional wave polarizations to ray theoretical models to measure velocity anisotropy. Stephen (1981, 1984) analyzed VSP data recorded in the ocean crust and found evidence of anisotropy from horizontally polarized shear waves. In this study, we focus on polarizations of borehole guided waves to determine if the polarization directions are consistent with theories developed for isotropic rock (White, 1962 and Cheng and Toksoz, 1984) or if they are affected by stress-induced velocity anisotropy.

Intrinsic Anisotropy

Materials with intrinsic velocity anisotropy have effective elastic constants that are arranged in the form of the crystalline symmetry (Crampin, 1977). Aligned crystalline anisotropy unquestionably exists on a small scale within the earth (Crampin, 1975). For example, many materials are known to have layered structures in which sheets of relatively tightly bound atoms are stacked in a repetitive sequence, with weaker binding forces between the layers. In these structures, material properties vary with the direction of measurement. On a larger scale, anisotropy is often the result of the existence of planar structures or foliation, commonly referred to gneissic fabric. This inherent rock fabric has two modes of origin (Balsley and Buddington, 1960). The first is due to magmatic flow structures formed as the result of the preferred orientation of inequidimensional crystals in the early stages of crystallization and subsequent overgrowth. Another mode of formation of gneissic fabric is deformation in the solid state with plastic flow at high temperature accompanied by recrystallization of the minerals. Large scale anisotropy may also be the result of the stratification of sediments where thin layers of material with different elastic properties cause anisotropic behavior. Although the existence of anisotropic fabric and anisotropic layering is well documented in outcrop and thin section analysis, it is difficult to determine the presence of seismic anisotropy on a larger scale because of the limitations in the sensitivity of the seismic recording equipment. In order to discriminate between anomalous behavior due to material anisotropy and behavior due to a local inhomogeneity the anisotropic anomaly must be relatively pronounced.

In anisotropic materials both body and surface waves have anomalous wave propagation behavior relative to waves traveling in isotropic materials. Wave propagation in anisotropic material follows Huygen's principle for isotropic material except the ray paths and wavefronts are no longer orthogonal. Wave propagation anomalies exist in recorded travel times, in seismic velocities, in the relationship between P, SV, and SH waves, in body wave amplitudes, in surface wave dispersion and in polarization directions (Crampin, 1975, 1977). Except along directions of crystal symmetry, the three body waves in an anisotropic material have independent velocities and particle motions (Crampin, 1970). In addition to the variation in dispersion with direction, anomalous surface wave behavior in

anisotropic material includes the coupling of the elliptical Rayleigh wave motion with the transverse Love wave.

Anomalies in both body and surface wave propagation behavior have been used to explore the large scale composition of the earth's crust. Brune (1969) differentiated seven basic crustal types using the measured dispersion from long period Love and Rayleigh waves. In another study using teleseismic data by Herrin (1969), a map of the lateral variations in compressional wave velocity of the upper mantle below North America was produced using seismic delay time variations. More recently, Crampin and King (1977) used the polarizations of surface waves to detect anisotropy in the upper mantle beneath Eurasia.

Stress-Induced Velocity Anisotropy

The dependence of velocity on stress is well documented from both in-situ investigations (Reasenberg and Aki, 1974; Gladwin and Stacy, 1973, Stierman, et al. 1979) and laboratory measurements (Birch, 1960, 1961; Nur and Simmons, 1969b). Laboratory studies on sedimentary and crystalline rocks of the velocity variation with pressure show a decaying exponential increase in velocity with confining pressure over the range 0 to 30 MPa (Carmichael, 1982; Nur, 1969). Typical laboratory data from sediments (data from Carmichael, 1982) and granites (Nur, unpublished data) are shown in Figure 1 with a multivariate fit to the measurements of the form (Stierman, et al., 1979):

$$V = a - b\, e^{-c\, P} + k\, P \tag{1}$$

In crystalline rocks the sensitivity of compressional and shear velocity to pressure in the range below 30 MPa is generally attributed to the closure of microcracks (Nur and Simmons, 1969b). The important question addressed in laboratory and in-situ studies is whether the changes in the elastic moduli associated with crack closure are sufficient to account for the observed changes in velocity. Nur (1969) and Nur and Simmons (1969) determined the fractional pressure dependence of compressional and shear velocity for granite to be 10^{-4} /MPa under saturated conditions. Measurements made by Stesky (1985) to determine the stress sensitivity of velocity to fracture characteristics on a variety of rock types show the highest stress sensitivity to

be approximately 2.5×10^{-3}/MPa for metabasalts which have a relatively low crack porosity. This value was seen to decrease rapidly with increasing pressure. For rocks with a higher crack porosity, for example granites and marbles, there is less stress sensitivity, with a range between 10^{-4} to 10^{-3}/MPa. All of these laboratory values decrease with increasing saturation.

In-situ velocities depend on stress state, fracture spacing, fracture roughness, and degree of saturation. Compressional velocity measurements performed over time by Liu, et al. (1985) clearly show that different arrival times correspond to the vertical joints and horizontal cracks in a granite quarry. Time dependent velocity changes measured in this study were found to correlate with variations in tidal strain. Because of the effects of joints and fractures, in-situ velocities are generally found to be lower than velocities measured in the laboratory. Many authors have found a correlation between this velocity difference from lab and in-situ measurements with fracture
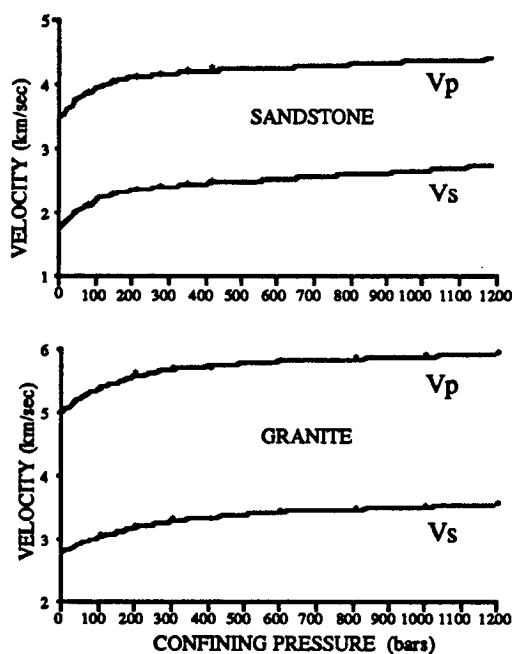
Figure 1. Laboratory measurements of velocity versus confining pressure for granites and sandstones with a multivariate fit to the data points.

frequency (Stierman & Kovach, 1979; King, et al, 1978; Stephanson et al. 1979; Sjogren et al., 1979; Moos and Zoback, 1983). In-situ measurements have also shown considerable variability in the magnitude of velocity dependence. Reasenberg

and Aki (1974) calculate a stress sensitivity $[(1/Vp) \, \partial Vp/\partial P]$ of 2.0×10^{-2}/MPa by monitoring Rayleigh waves generated in a granite quarry. This value is much higher than that found in laboratory measurements and in other field experiments. Malin and Leary (1981) conducted airgun experiments to model the near surface behavior of the
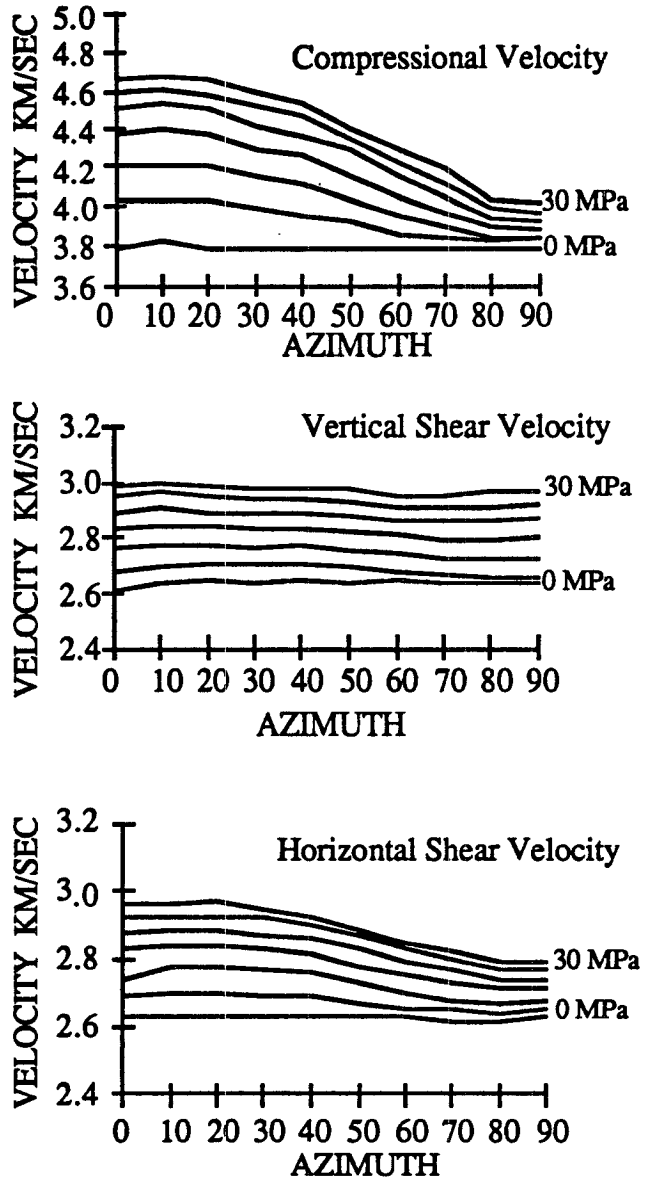
Figure 2. Experimental data from Nur and Simmons (1969) for the Barre granite of compressional and shear velocity measurements with respect to angle of maximum compression at increasing values of uniaxial compression.

crust and found a pressure dependence of 10^{-3} /MPa at a depth of 0.5 km and 10^{-4}/MPa at 2 km. Gladwin and Stacy (1973) found an in-situ stress sensitivity for compressional velocity of approximately 10^{-4} /MPa in granite. The differences in these field experiments may be due to the presence or absence of large joints and fractures.

An estimate of the sensitivity of particle velocity and displacement to stress direction can be made using data from laboratory experimentation of Nur and Simmons (1969) where the dependence of compressional and shear velocity on stress direction at uniaxial pressures from 0 to 30 MPa was studied (Figure 2). At any given orientation of applied stress, velocity increases with increasing pressure indicating a typical decaying exponential behavior. In addition, the data show distinctly higher velocity in the direction of applied stress than in the orthogonal direction. For compressional and horizontal shear velocity the magnitude of this difference increases significantly with increasing confining pressure. Vertical shear velocity is less sensitive to stress direction than either horizontal shear or compressional velocity.

Theoretical curves were constructed from Nur and Simmon's laboratory data of the velocity/pressure relationship at various azimuths from maximum compression using multiple regression to find a decaying exponential form to fit the measurements. The curves at the 10° azimuth intervals of the laboratory measurements are presented in Figure 3. The percent anisotropy with increasing stress ratio at the borehole wall was calculated from these theoretical curves and equation (5) assuming a strike-slip stress state (where $S_3 = S_{hmin}$ and $S_1 = S_{Hmax}$) and the results are plotted in Figure 4. As an example, a hydrostatic pore pressure of 10 MPa, and values of $S_{Hmax} = 30$ MPa, $S_{hmin} = 10$ MPa and $S_v = 17$ MPa were used to compute the percent anisotropy (defined as $1-V_{min}/V_{max}$ x 100). The results of this computation indicate that for pressures below 30 MPa we should expect the compressional velocity anisotropy in granite due to the borehole stress concentration be about 15% and that horizontal shear velocity anisotropy will be approximately 9%. For comparison, under no stress conditions material may have intrinsic anisotropy which is dependent on rock type and crack porosity (Nur, 1969). Measured values of intrinsic anisotropy are less than 1% for granites and as high as 27% for slate (Brace, 1965).
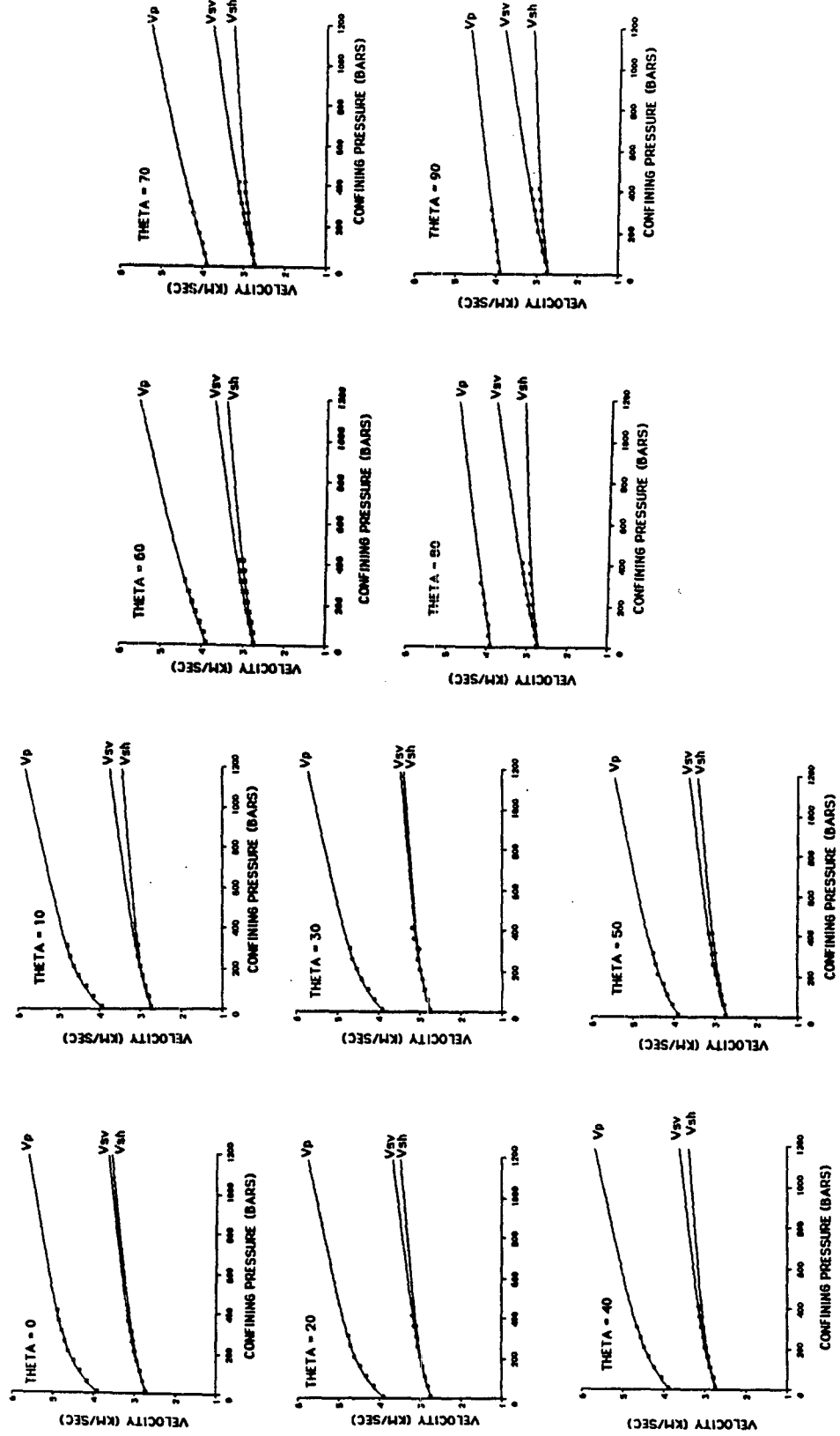
Figure 3. Family of velocity versus pressure calculated to fit the data of Nur and Simmons (1969) for each 10° azimuth from the direction of maximum stress.
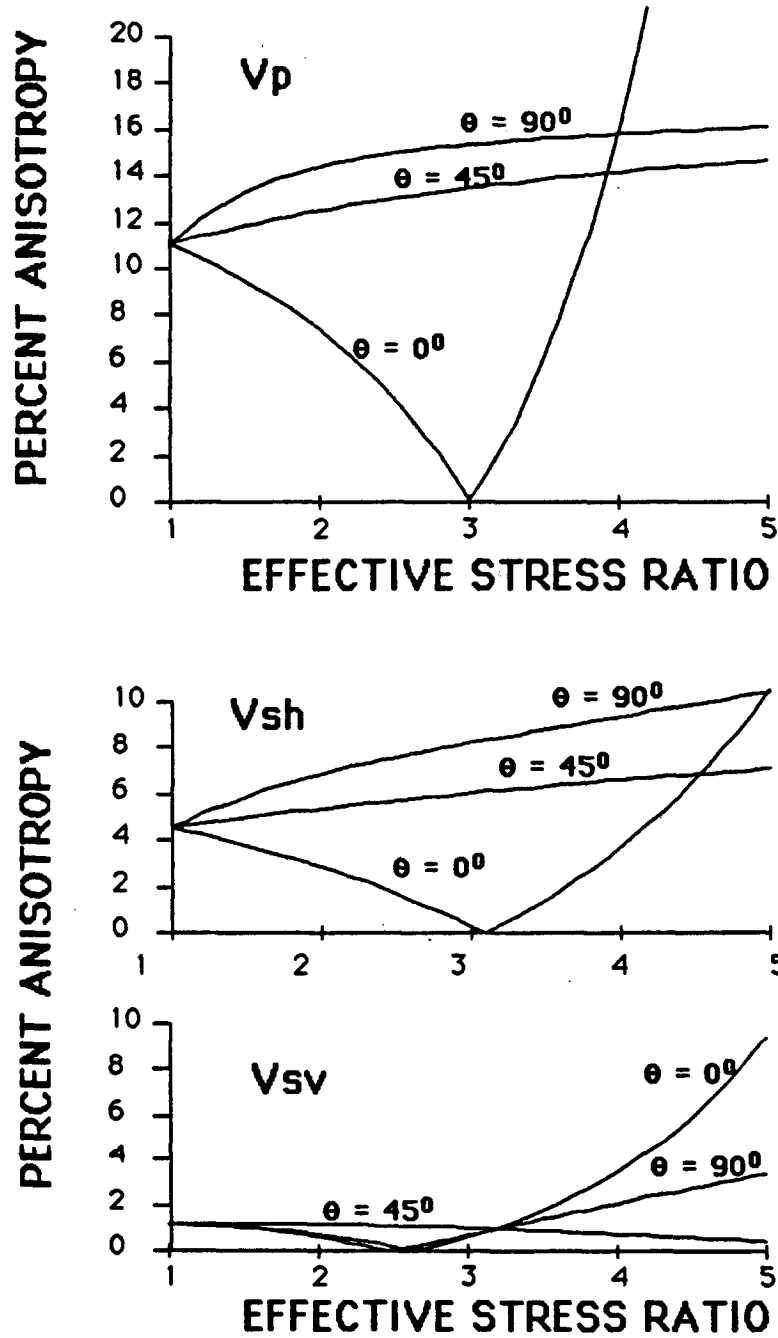
Figure 4. Percent anisotropy with increasing effective stress ratio for compressional, horizontal shear and vertical shear velocity constructed using equation 5 and the curves of Figure 2.

Borehole Stress Distribution

The borehole stress distribution can be modeled as the effect of a stress concentration created by a hole within an infinite elastic plate. This concentration of stress will affect the velocity of wave propagation at the borehole wall. Remote stresses are translated to radial and circumferential principal stress components in polar coordinates and become functions of r, the radius from the center of the hole and θ, the angle with the maximum horizontal stress (Figure 5). The borehole stress field is completely described by normal stresses acting in the horizontal plane, σ_r, σ_θ,

Borehole Stress Distribution
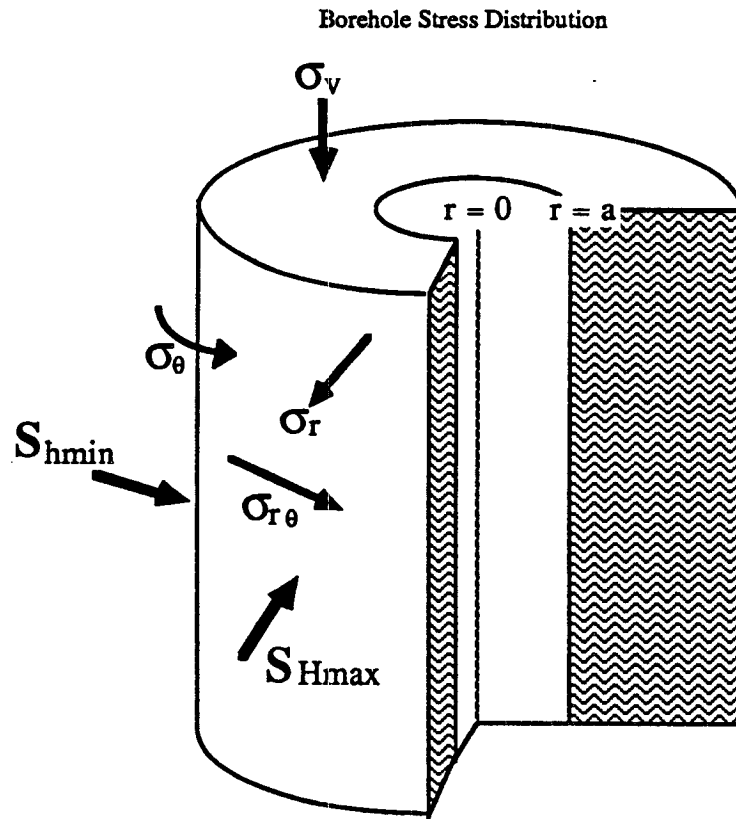
Figure 5. Borehole stress distribution. Far field stresses S_{Hmax} and S_{hmin} are translated to local stresses, σ_r, $\sigma_{r\theta}$, σ_θ at the borehole wall (r=a) and surrounding formation.

and $\sigma_{r\theta}$ and the vertical stress, σ_z. The effective stress components in the vicinity of a circular hole were given in Part I, Chapter 1 of this thesis, page 67, after Kirsch (1898) and Jaeger and Cook (1979).

The principal stress trajectories that exist under uniaxial stress conditions in the near field around the borehole can be computed from equations 1-4 and are shown in Figure 6 for nominal values of maximum and minimum horizontal principal stress. The directions of the maximum local principal stress trajectories align with the direction of maximum horizontal far field stress and are deflected around the borehole. Away from the borehole, radial stresses parallel to the applied stress are maximum at $r/a = 1.5$ and those perpendicular to the applied stress are maximum at $r/a=1.15$. The radial stresses decay to negligible values within three borehole radii. Circumferential stress is maximum at $r=a$ parallel to the applied stress and minimum at $r=a$ in the orthogonal direction. Circumferential stresses approach the value of the far field stress within three borehole radii in the direction perpendicular to the applied stress and within one borehole radius parallel to the applied stress.

PRINCIPAL STRESS TRAJECTORIES
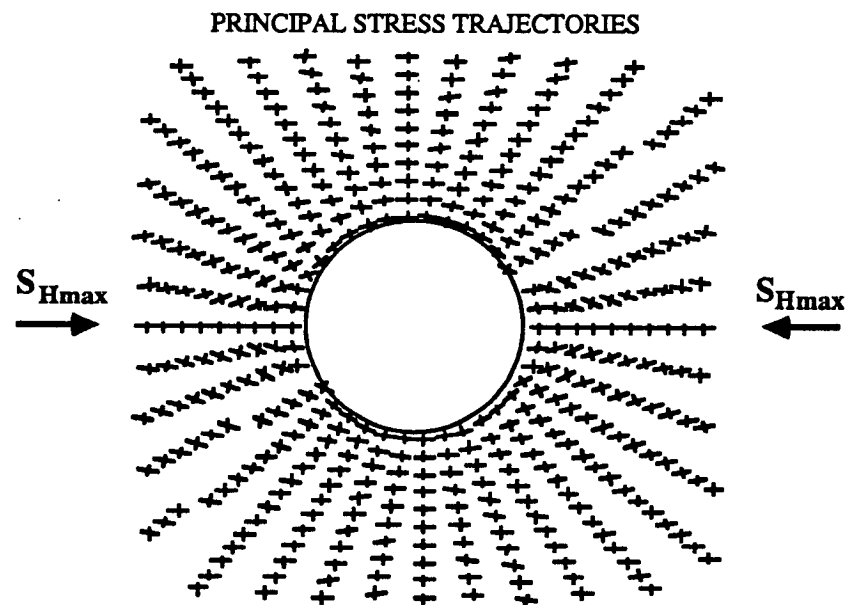
Figure 6. Principal stress trajectories computed using equations 1 - 3 for nominal values of the far field stresses. Heavy tick is the maximum and the light tick the minimum local principal stress.

At the borehole wall, equations (1-4) reduce to only one normal component, σ_θ Assuming $\Delta P_w = 0$ the radial and shear stresses are zero and the stress field is defined by the circumferential and vertical stresses.

$$\sigma_\theta = (S_{Hmax} + S_{hmin} - 2Pp) - 2(S_{Hmax} - S_{hmin}) \cos 2\theta \qquad (2)$$
$$\sigma_z = \rho gz - 2\nu (S_{Hmax} - S_{hmin}) \cos 2\theta \qquad (3)$$

Under conditions where a borehole is drilled into a medium of unequal horizontal principal stresses, the circumferential stress at the borehole wall, in terms of the far field total principal stresses, is:

$$\sigma_\theta = (S_{Hmax} + S_{hmin} - 2Pp) - 2(S_{Hmax} - S_{hmin}) \cos 2\theta \qquad (4)$$

where θ is the angle from S_{Hmax} and Pp is the formation pore pressure. The circumferential stress has its maximum value at $\theta = 90^o$, and its minimum at $\theta = 0^o$. The difference between these two extreme values of circumferential stress can produce a four-fold magnification of the far field stress difference at the borehole wall, where the VSP geophone records particle motion, $\sigma_{\theta = 0^o} - \sigma_{\theta = 90^o} = 4(S_{Hmax} - S_{hmin})$. For example, maximum and minimum horizontal principal stresses of 35 and 20 MPa produce a difference of 60 MPa between maximum and minimum circumferential hoop stress at the borehole wall measured from $\theta = 0^o$ to $\theta = 90^o$. Thus, even relatively nominal differences in the magnitude of horizontal principal stresses may cause a large stress heterogeneity and suggest that the polarization angle may follow the stress trajectories around the hole. However, if the borehole guided waves are sensitive only to the far field stress, polarization directions at all geophone azimuths should have an orientation in the direction of S_{Hmax}. The scatter in the data analyzed in this study prohibit discrimination between far field and local stress effects. Scatter in the data may also result from differences in the velocity sensitivity to stress for a certain lithologic layer, from different fracture characteristics, or from poor geophone coupling.

Borehole Guided Waves

Wave propagation in cylindrical boreholes is extremely complex due to the presence of head waves, trapped fluid modes, and surface waves. Typically, in the acoustic well logging environment the received pulses consist of overlapping combinations of these waves. The compressional head wave which arrives first is generally well resolved, but later energy is often difficult to interpret (Schoenberg, et. al., 1981). The trapped modes are dispersive which significantly complicates data interpretation.

The formal modal solution to isotropic, elastic-wave propagation in a fluid filled borehole was presented by Roever et al. (1974). The symmetric modes have been discussed in considerable detail by Biot (1952). The lowest order symmetric, circumferential mode exists over all frequencies. At low frequencies the axial phase and group velocity of these modes approach the tube wave velocity. At higher frequency, the phase and group velocities approach the velocity of Stoneley waves at the solid-fluid interface. Higher order symmetric modes extend from a cutoff frequency where the phase and group velocity equals the formation shear velocity to infinite frequency where the phase and group velocity equals the Rayleigh wave velocity. These modes are referred to as normal modes.

A higher order antisymmetric circumferential mode, the flexural wave, also exists over all frequencies. The phase and group velocities of the flexural wave are bracketed between the formation shear velocity at low frequency and the Stoneley wave velocity at higher frequency (Roever et al., 1974). In the low-frequency limit this mode describes a simple bending of the fluid-filled borehole. From an analytic expansion for the pressure response in a borehole Roever et al. (1974) found that higher circumferential modes are observed when both the source and detector are located off the borehole axis. These higher order modes may be present in VSP data recorded in standard experimental configurations.

The nature of the excitation of the higher order flexural mode is not well understood at this time. However, theory indicates that an incident body wave will generate a non-symmetric response in the borehole. If the material is cylindrically symmetric the initial asymmetry will be maintained, and a downhole receiver will see a particle motion polarized in the direction of the incident particle motion. Where

stress anisotropy generates preferred directions for particle motion not associated with the source direction, the initial polarized mode will decompose into modes polarized in the preferred directions defined by the stress field. Alternatively, the flexural mode may be the result of conversion from an initial mode with particle motion determined by the incident wave, at an inhomogeneity in the borehole wall. In either case it is likely that the VSP records substantial mixed-mode wave propagation behavior (J. Leveille, per. comm).

Determining which guided wave mode is recorded on a particular VSP record is difficult. The normal modes or pseudo-Rayleigh waves have very high cutoff frequencies (7 to 15 kHz) below which these modes cannot exist. Thus, in the frequency range of the VSP (0 to 100 Hz), the normal modes or pseudo-Rayleigh waves are not related to the particle motion behavior observed in this study. The remaining guided wave modes however, do not have diagnostic frequency spectra.The long wavelength limit of the Stoneley mode, usually between 10 and 60 Hz does appear at VSP frequencies. The frequency range of the flexural mode is similar and also lies within the recording frequency of the VSP.

The Stoneley wave is a high amplitude, low frequency type of borehole surface wave propagates along the axis of the borehole at phase velocities that are less than both the shear velocity of the formation and the acoustic velocity of the fluid (Figure 7a). The propagation characteristics of the Stoneley mode in boreholes are well understood for the isotropic case (White, 1962 and Cheng and Toksoz, 1984). Their amplitude decays exponentially away from the fluid/rock interface. The particle motion of the Stoneley wave is prograde elliptical with the major axis of the ellipse parallel to the axis of the borehole. Isotropic theory constrains particle displacement to radial motion in the horizontal plane. This behavior would be represented by a straight line particle velocity path along one of the horizontal geophones recording the radial field. The other horizontal geophone would have a zero response recording the tangential field. Isotropic theory also implies that at all geophone positions the orientation of the particle motion would be in the radial plane defined by the tool azimuth and the center of the borehole. Thus, for isotropic rock, Stoneley wave particle displacement is purely radial in the horizontal plane thus precluding the possibility of azimuthally polarized displacement for the Stoneley mode (Leveille and Seriff, 1988; L. Nicoletis, 1988).

For flexural modes, the radial motions at opposite points on the circumference move in phase opposition; consequently the boundaries execute a flexing motion (Figure 7b). In isotropic conditions, the azimuthally varying modes have particle velocity fields with r, θ, and z components. Flexural modes are again high amplitude, low frequency phenomena with no geometrical spreading. In the isotropic case, the particle motion behavior would be represented by a linear particle motion
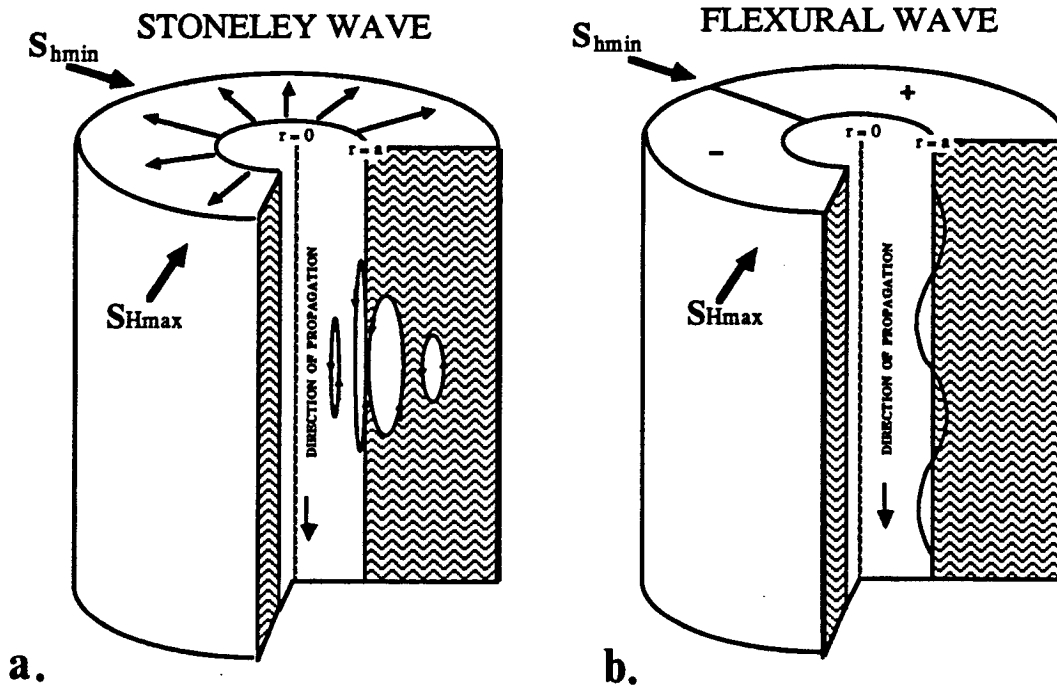
Figure 7. Sketch of the theoretical propagation and displacement characteristics of the borehole Stoneley wave (left) ant the flexural wave (right).

path in the horizontal plane. At various positions of the geophone the particle motion would be polarized in the direction of hole flexure.

In addition to the wavemode velocities the relative amplitudes of the modes on the three component records should provide a mechanism for discriminating between the flexural and Stoneley modes. The ellipticity of the particle motion of the Stoneley mode is a function of borehole radius and frequency in both the fluid and in the formation (Cheng and Toksoz, 1984). In the fluid, the axial (vertical) particle motion of the Stoneley mode is very much larger that the radial particle motion. At the fluid rock interface the ellipticity of the particle motion in the fluid diminishes with decreasing frequency. At low frequency the major axis of the ellipse changes from

axial (vertical) to the radial direction across the fluid rock interface. Radial displacements are continuous across this boundary and the particle motion in the formation become circular. The response of the flexural mode would be stronger on the horizontal than the vertical geophone components. For this reason examining vertical to horizontal amplitude differences over the guided wave arrivals may be important as evidence of the existence of flexural waves.

The stress concentration around a borehole can significantly amplify intrinsic velocity anisotropy. Even with modest differences in the magnitude of principal horizontal stresses, describing the propagation characteristics of borehole guided waves with the isotropic, homogeneous, elastic theory may be overly simplified due to stress-induced anisotropy. Again, due to the propagation wavelengths in VSP experiments it is not possible to discriminate between local effects on the elastic moduli of the material around the borehole from the effects of far field stresses.

CHAPTER 2: ANALYSIS OF VSP DATA FOR POLARIZATION DIRECTIONS

Measurement of Polarization Angle

The horizontal particle motions of the guided waves were analyzed in three sets of field data. The polarization angle of the guided wave particle motion can be determined by horizontal particle motion plots, or hodograms, constructed from the two horizontal geophone records. Assuming the geophone elements are oriented along cartesian X-Y-Z axes with Z vertical, the hodogram plot of the response created when the guided wave activates the two horizontal elements will define the direction of particle velocity in the horizontal plane.

The orientation of horizontal particle motion is determined using hodograms of the windowed guided wave arrival on the horizontal geophone elements. In the seismometers used to record the data analyzed in this study one of the horizontal transducers (e.g. X) lies in the plane of a locking arm that pushes the sonde against the side of the hole and the other is at right angles to that plane (e.g. Y). Figure 8a shows a set of seismograms for a typical three-component set of field data. The trace labeled Z is the seismogram recorded with the vertical component and the traces labeled X and Y are the seismograms recorded with the horizontal components of the VSP tool. The horizontal records have been normalized to a common value to preserve relative amplitude ratios for these plots. Figure 8b is a hodogram of the horizontal particle motion of the borehole guided wave over the time interval indicated "G" on the X and Y traces in Figure 8a. It is apparent in Figure 8b that the horizontal particle motion is elliptical. The time window used to construct the hodogram must be sufficient to capture repeated wavelengths of the guided wave which typically has frequencies of 10 to 60 hertz. The angle between the dashed line in Figure 8b and the X axis represents the polarization angle of the guided wave with respect to the reference coordinates. The direction of maximum particle velocity over the sampled wavelengths is taken as the azimuth of guided wave particle motion and this azimuth is referenced to the X-Y coordinate system.
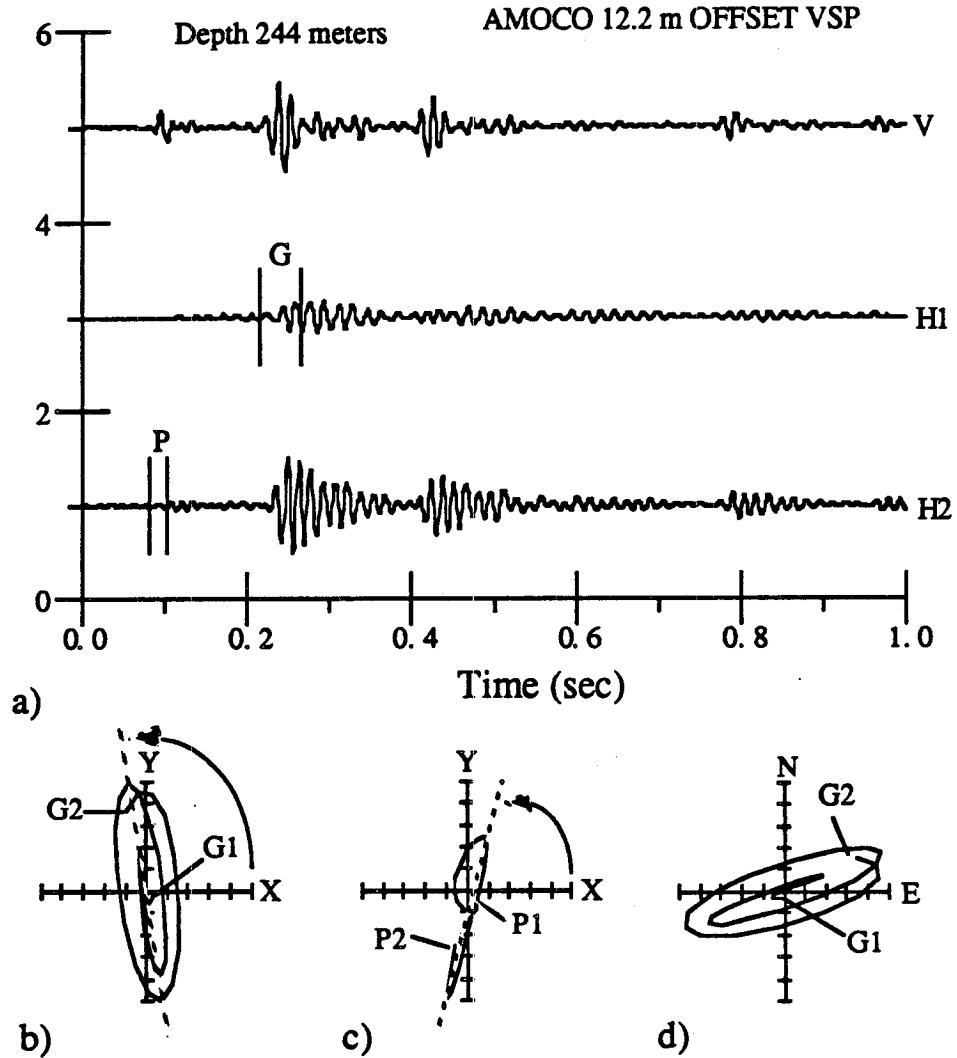
Figure 8a) The time series for typical three component VSP data (offset 12.2 m) at depth 244 meters showing windowed guided wave arrival "G" and the windowed compressional wave arrival "P" on the horizontal X and Y components. b) The corresponding particle velocity plots of the windowed guided wave arrival between G1 at 0.215 and G2 at 0.269 sec of the traces shown in 1a; c) the windowed compressional arrival traces between P1 at 0.076 and P2 at 0.100 sec of the traces shown in 1a; and d) the guided wave arrival corrected to north.

In order to reference the guided wave polarization angle to north the azimuth of the seismometer sonde must be determined. This can be accomplished with the assumption of linear polarization of the compressional arrival in the direction of propagation (White, 1964; Hardage, 1983; DiSiena, et al., 1984; Gaiser et al., 1984). To determine the tool orientation the compressional arrival is windowed on the horizontal X and Y traces (Figure 8a). The orientation of maximum energy over this window is taken as the source azimuth with respect to the reference coordinates. Figure 8c is the hodogram of the compressional first motion generated from the windowed portion of the X, Y traces labeled "P" in Figure 8a. The angle of the linear polarization of the compressional wave in the reference coordinate system can usually be determined without ambiguity. The straight dashed line in Figure 8c indicates the direction of first motion of the compressional wave and hence the direction of the source with respect to the tool. The difference between this angle and the polarization angle of the guided wave particle motion represents the azimuth of the guided wave polarization with respect to the source. A final correction is then made for the angle between the reference coordinates and the known compass location of the source. The hodogram of Figure 8d represents the oriented guided wave particle motion for the set of field traces shown in Figure 8a.

Results

Three-component VSP data have been analyzed from 1) two separate experiments in the same well located in Oklahoma, 2) a well located in the Paris basin, and 3) in the Cajon Pass scientific drillhole, located in southern California. The two sets of data recorded in the Oklahoma test well, owned by Amoco Oil Company, intersect 282 meters of a sandstone/shale lithology. The two VSP's recorded in this well differ in geometry and instrumentation; both experiments used a Vibroseis source and were recorded at a sampling rate of 1 ms. The source location for both experiments was due north of the wellbore.

The VSP tool used in the first experiment, recorded in the Amoco well by Seismograph Services Corporation, was their "K-tool". The guided wave energy in this data set is responsible for the prominent downgoing and upgoing events in Figure 9a, the depth profile of the vertical component. The same gain value was used to plot each component profile to preserve the relative amplitude information. The offset was
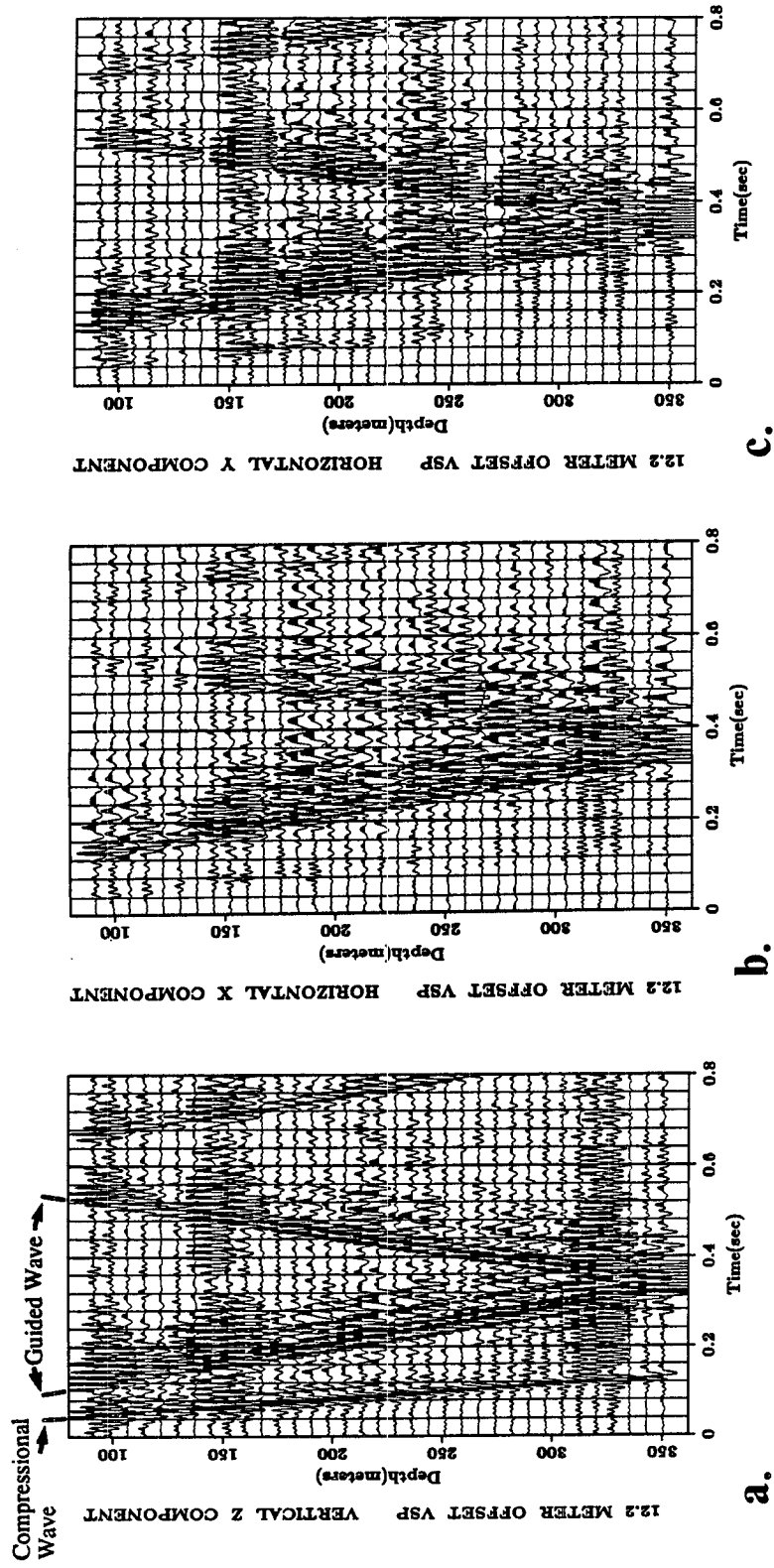
Figure 9. a) VSP profile of the vertical component profile for the 12.2 m offset data set recorded in the Amoco test well for the depth interval 3050 m to 1510 m. b) the horizontal X and c) the horizontal Y component profiles for the 12.2 m offset data.

12.2 m and the sonde spacing interval 7.62 m. The data were recorded before the borehole was cased. Compressional velocity was measured at 3,050 m/sec and the guided wave at 1,510 m/sec. This data set was analyzed below depth 91.5 m where the guided wave mode was well separated from the body wave arrivals. The limits of the time window used around the compressional and guided wave arrivals to compute the orientation of maximum displacement are indicated.

Figure 8a shows the three-component records for depth 244 m from the data shown in Figure 9 where the vertical and horizontal records are plotted at the same amplitude scale. The compressional arrival is identified as the first break at about 0.1 sec and the onset of the guided wave arrival is at 0.24 sec. Figures 9b and 9c are the horizontal X and Y component profiles for this data set . The guided wave is again the prominent event on these profiles due to the near offset geometry of the experiment. The maximum vertical amplitude of the windowed portion of the guided wave arrival is 7.9×10^7 whereas the maximum amplitude of the H1 and H2 components are 2.8 $X \ 10^7$ and 8.4×10^7 respectively over the same window (Figure 8a). A Fourier analysis of the data was performed to establish the overall frequency response of each of the three geophone elements. A severely mismatched frequency response between the two horizontal components or the vertical to horizontal components could effect the detection of a particular wavemode on that geophone element. The amplitude spectra of Figure 10 are the vertical (top), H1 (middle) and H2 (bottom) traces from depth 244 m. The frequency content and peak response are well matched among the three geophone elements. Several sets of the horizontal records show a very low signal to noise ratio. Particle motion plots of the guided wave arrival as well as the compressional wave arrival in these records are poorly oriented (c.f. depths 334 m and 108 m). Traces indicating low signal to noise ratio in Figure 9 and were excluded from the analysis.

A borehole televiewer log recorded in the Amoco well has been examined to consider the general hole conditions. The televiewer image is nearly featureless through most of the logged interval suggesting that the analysis of the VSP data has not been perturbed by geometric effects of the borehole. Near the bottom of the borehole the conditions are less pristine and fine fractures are observed (Figure 11).
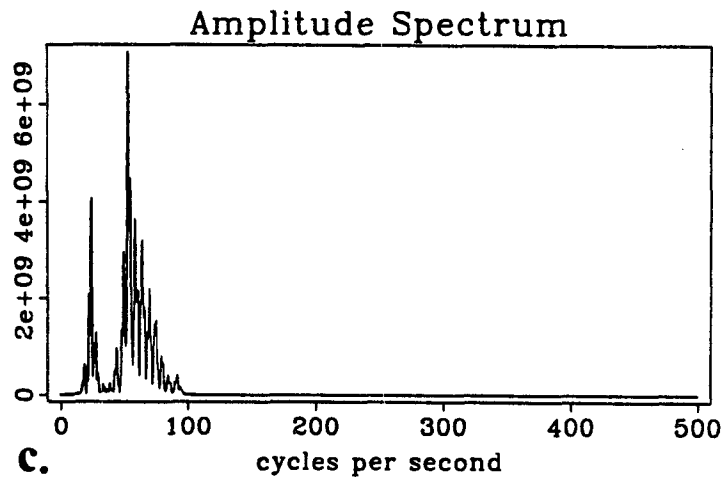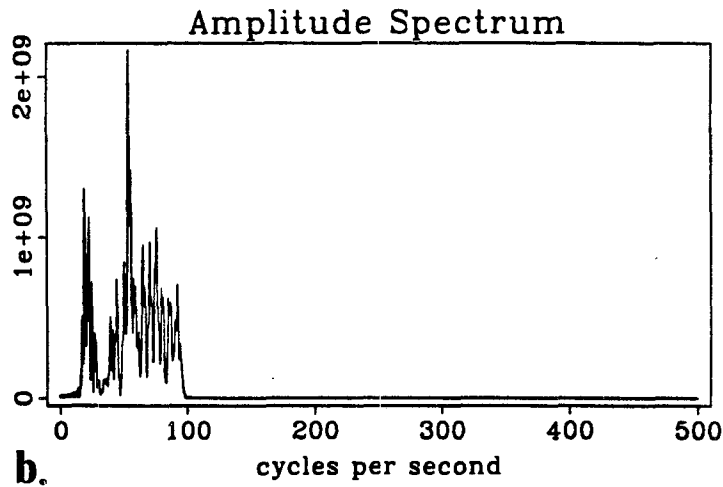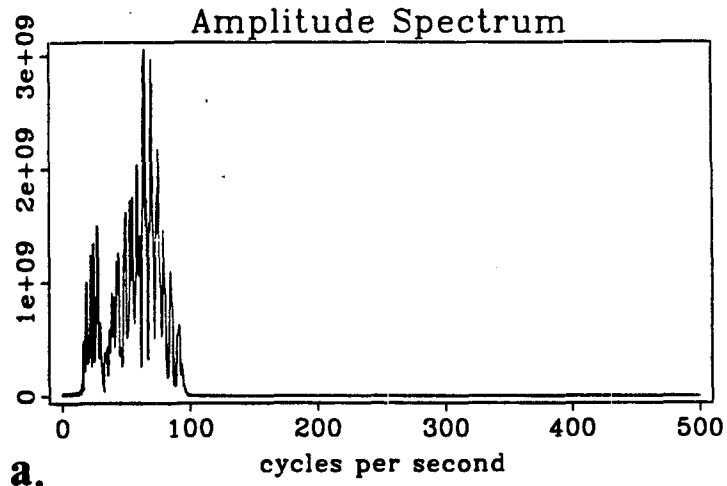
Figure 10a) Amplitude spectra for the vertical b) H1 and c) H2 geophone elements for the time series at depth 244 m in the Amoco test well 12.2 m offset data.
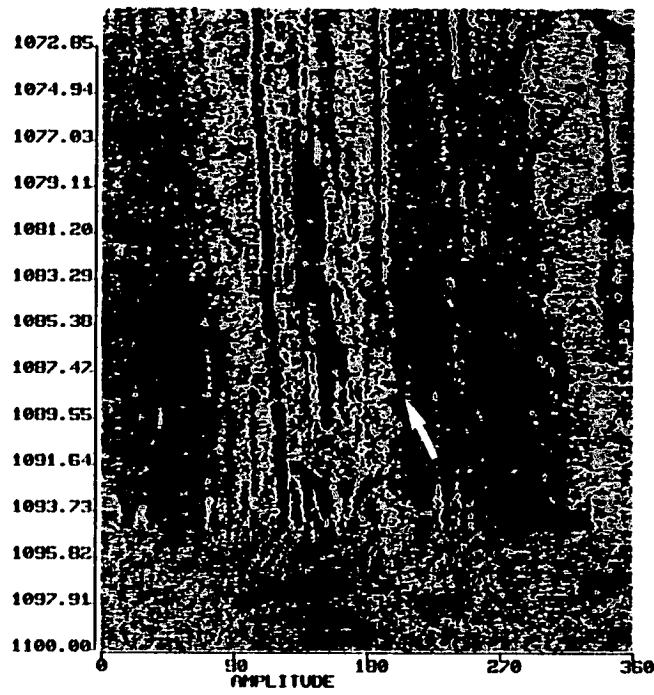
Figure 11. Borehole televiewer log from the Amoco Test well showing fine scale fractures at depth 1091 ft oriented N70°E.

Figure 12a shows the individual azimuths of the guided wave particle motion (heavy tick) measured at multiple depths in the Amoco test well on a single plan view. It is immediately apparent that the polarization azimuths are not directed radially outward from the center of the borehole as would be expected for a Stoneley wave traveling in isotropic material. Figure 12b shows a histogram of the distribution of polarization azimuths for the first data set indicating a peak of the measured polarization angle at about N65^{O}E.

These results are in good agreement with the direction of regional maximum horizontal stress in the area of Oklahoma based on independent stress measurements (Zoback and Zoback, 1988). Although no formal experiment to measure the stress magnitude at depth was performed in this drillhole, it had been pressurized to induce fractures before televiewer logging (T.J. Taylor, pers. comm). Assuming these cracks formed parallel to the maximum horizontal stress (Hubbert and Willis, 1957) their azimuth at approximately N70^{O}E is in agreement with the orientation of maximum compression determined from the guided wave polarization.

As it is possible that the guided wave polarization is affected by the stress concentration around the borehole, the theoretical stress trajectories that exist around a circular hole under uniaxial stress are shown in Figure 12c. These trajectories were constructed through the solution of the well known equations that describe the stress components in the vicinity of a circular hole (Equations 1 - 3) with S_{Hmax} at an azimuth of N70^{O}E. This diagram shows the agreement between the measured azimuth of guided wave polarization and computed stress trajectories although it is not possible to distinguish between particle motion response to the ambient stress field or to the borehole stress state. Regardless, it is clear that the measured particle motion is not radial and that it is generally in the direction of maximum horizontal compression.

A second set of three-component data recorded in the Amoco test well were analyzed as an additional test of this concept. The data were recorded after the hole was cased at a larger offset and with a different geophone tool, the CGG "Geolock-H" model. Profiles of the vertical and two horizontal geophone recordings in this experiment are presented in Figure 13. Again, the same gain value was used to plot each component profile to preserve the relative amplitude information. The offset in this experiment was 48.8 m and the measurements were made over essentially the
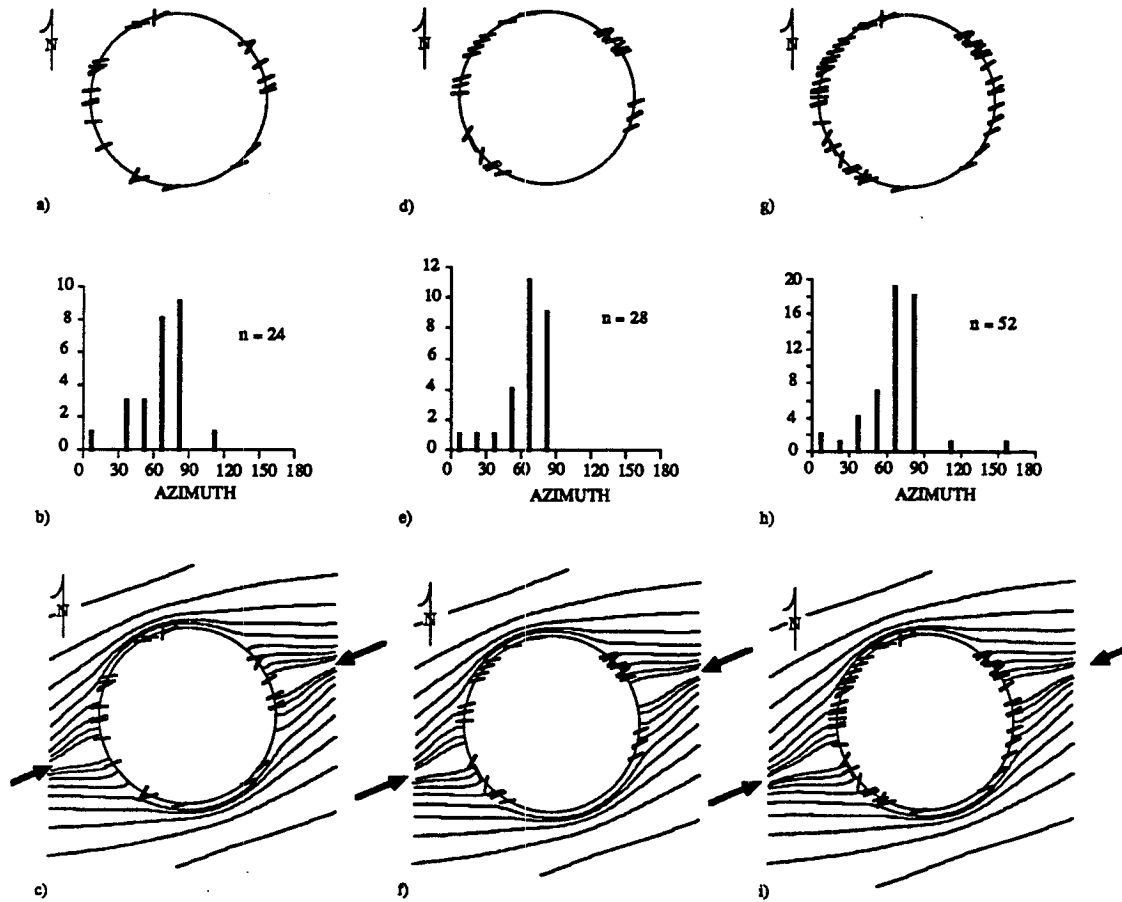
Figure 12. a) The orientation of the guided wave particle motion at multiple depths in the Amoco well. b) Histogram of the azimuth of guided wave particle motion for the 12.2 m offset data. c) the theoretical stress trajectories computed for S_{Hmax} at N70°E. d). the orientation of guided wave particle motion for the 48.8 meter offset VSP experiment at multiple depth in the Amoco well. e) Histogram of the azimuth of guided wave particle motion for the 48.8 m data. f) the theoretical stress trajectories computed for S_{Hmax} at N70°E. g) orientation of guided wave particle motion for combined data sets in the Amoco well. h) Histogram of the azimuth of guided wave particle motion for the combined data. i) theoretical stress trajectories computed for S_{Hmax} at N70°E.

same depth interval. The increased offset in this experiment resulted in better developed compressional wave energy (Figure 13a). The guided wave energy is, however, less well developed than that of the 12.2 m offset experiment and the shot configuration resulted in less time separation between the two modes at shallower depths. For this reason only the records shot below depth 198 m were used in this analysis. The limits of the time window used around the compressional and guided wave arrivals to compute the orientation of maximum displacement are indicated in Figure 13a.

Typical traces for the second set of data recorded in the Amoco well are shown in Figure 14a with the vertical to horizontal amplitudes matched. The maximum vertical amplitude over the windowed portion of the guided wave arrival shown is 2.3×10^{11} and the maximum H1 and H2 component amplitudes over this window are 4.8×10^{11} and 5.0×10^{11} respectively. The frequency response of the three geophone elements for depth 335 m indicates that all elements have the same dynamic range between 50 and 175 Hz and individual peaks are well matched (Figure 15).

The orientation of the observed azimuth of guided wave particle motion at each depth is drawn in Figure 12d. Figure 12e shows the statistical distribution of the polarization azimuths as a histogram where the peak is about N70°E, consistent with the results obtained from the 12.2 m offset data and again with the known direction of horizontal principal stress in the locality of the well. Figure 12f shows the variation of these directions from the theoretical stress trajectories computed for a maximum horizontal stress at N70°E. Again, the guided wave particle motion is polarized in the direction of maximum horizontal compression exhibiting both radial and transverse displacement.

In Figure 12g the measured azimuths from the guided wave particle motions for both data sets are combined for comparison. The statistical distribution of the combined data is shown in Figure 12h and the computed mean direction is N68°E. The standard deviation for the combined data is 9.7°. Figure 12i shows the theoretical stress trajectories computed for far field stress at N70°E. Figure 12i demonstrate the consistency between these two separate experiments and the independence of factors as the seismic sonde, the offset and azimuth of the source, and whether or not the hole is cased.

Figure 13. a) VSP profile of the vertical component for the 48.8 m offset data set recorded in the Amoco test well for the depth interval 3050 m to 1510 m. b) the horizontal X and c) the horizontal Y component profiles for the 48.8 m offset data.
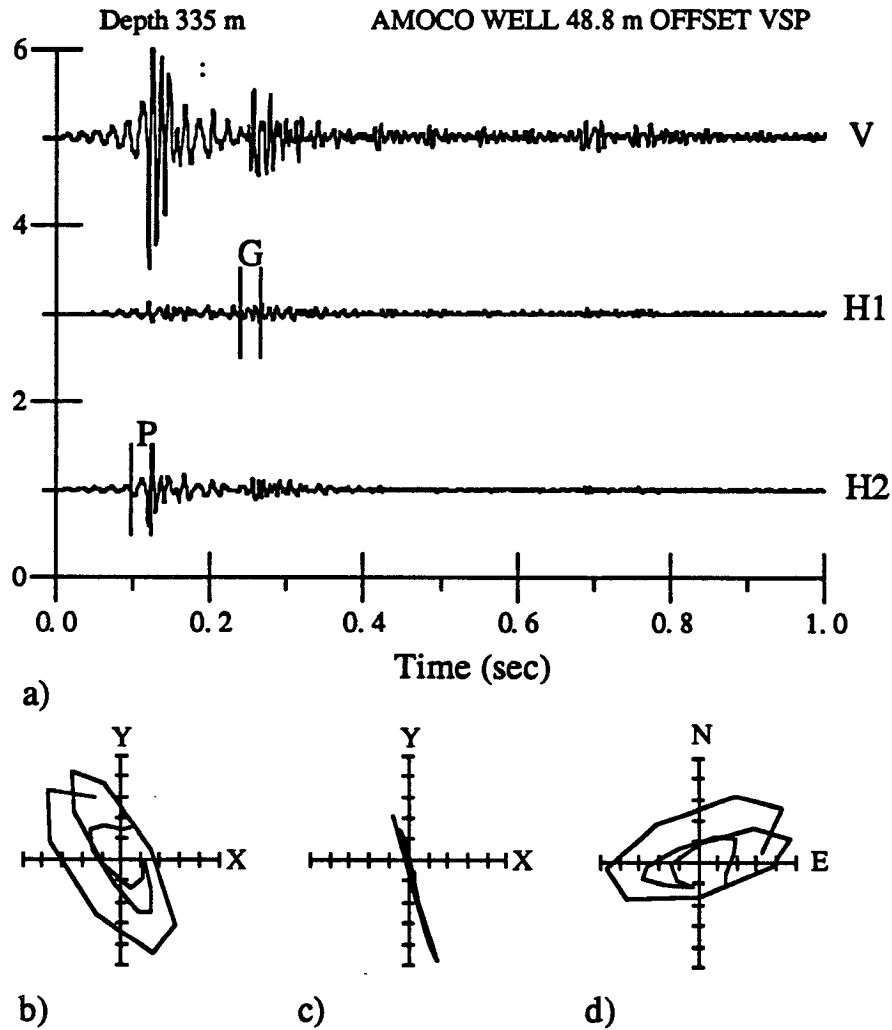
Figure 14. a) Times series from depth 335 m in the Amoco test well recorded in 48.8 m offset data showing windowed guided wave arrival "G" and the windowed compressional wave arrival "P" on the horizontal X and Y components. b) The corresponding particle velocity plots of the windowed guided wave arrival between 0.241 and 0.246 sec of the traces shown in 1a; c) the windowed compressional arrival traces between 0.100 and 0.123 sec of the traces shown in 1a; and d) the guided wave arrival corrected to north.
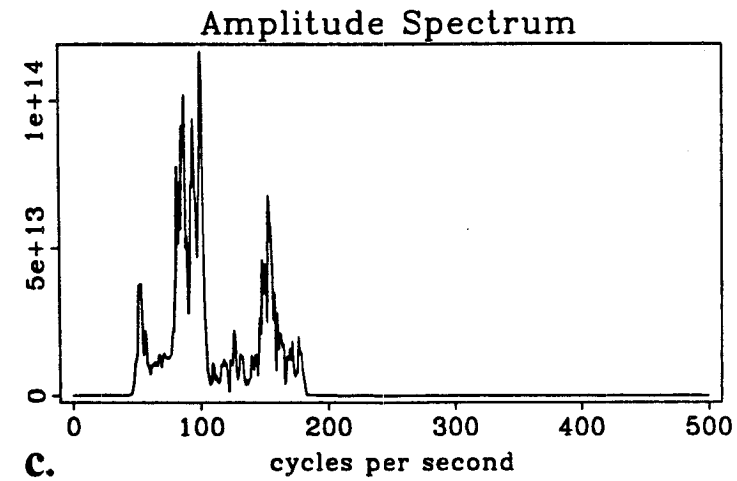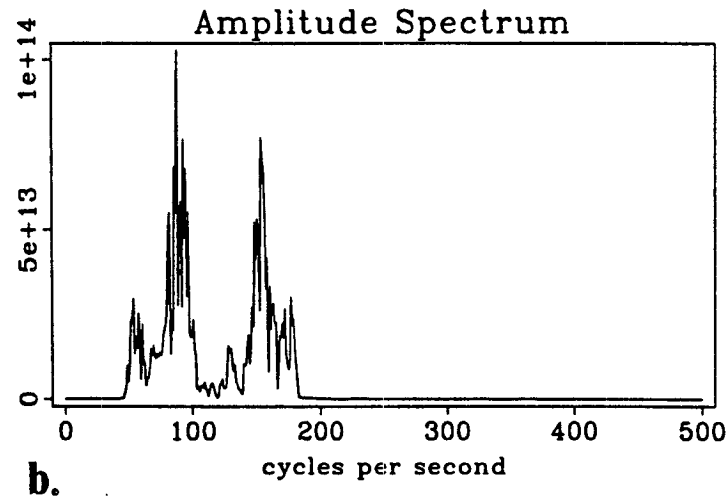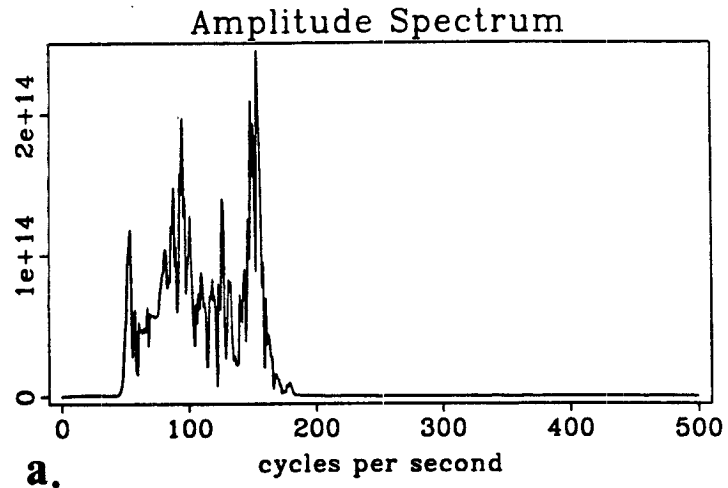
Figure 15. a) Amplitude spectra for the vertical b) H1 and c) H2 geophone elements for the time series at depth 355 m in the Amoco test well 48.8 m offset data.

Data obtained from ELF Aquitaine was recorded in a cased well located in the Paris Basin which transects 960 meters of a sandstone/shale sequence. This data consists of two sets of three-component records, one at zero offset (Figure 16) and the other at a 262 m offset (Figure 17). The same gain factors were used to plot these profiles. The limits of the time window used around the compressional and guided wave arrivals to compute the orientation of maximum displacement are indicated. These data were recorded at 15 meter shot spacings. The VSP tool used in the experiment was the CGG-"Geolock " and the sampling rate is 2 ms. Each source was fired for one receiver position. To make optimum use of the data the far offset shot records were used to compute the tool azimuth and the zero offset records were used to determine the orientation of the guided wave particle motion. The far offset source was located at an azimuth of 182°. Typical traces for Elf data are shown in Figure 18a again with the vertical to horizontal amplitudes matched. The compressional arrival is identified as the first break at about 0.55 sec and the onset of the guided wave arrival is at 0.24 sec. Compressional velocities are 4100 m/s.

After the compressional wave arrival, two separate modes are visible in the horizontal records of the Elf data (Figure 18b, mode 1 and mode 2). The first arrival at 1.18 sec propagates at a velocity of 2360 m/s and the second arrival at 1.37 sec propagates at at 1540 m/s. As discussed above, guided wave modes propagate over a range of velocities and frequencies. It may be possible, however, to use the velocities of separate modes to determine which guided wave mode has been excited in a particular experiment. In the Elf data for example, the first clear arrival after the dissipation of the compressional wave energy, has a velocity of 2360 m/s, a value greater than theoretically possible for the propagation of a Stoneley mode. This velocity is very near a typical formation shear velocity for clastics with a compressional velocity of 4100 m/s (for a Poisson's ratio of about 0.2)which fits the expected values for the propagation of flexural waves. (Seriff, per. com.). The second mode has a velocity of 1540 m/s which is close to the borehole fluid velocity and typical of the borehole Stoneley mode. In the particle motion analysis of this data, both modes have similar eccentricities and polarization directions.

In additional to using the velocities to characterize the wave type the amplitude information my also be diagnostic. The maximum amplitude of the vertical component over the windowed guided wave arrival at 3.9×10^7 is compared to that of the H1 and H2 components at 1.2×10^8 and 1.3×10^8. The greater relative amplitude
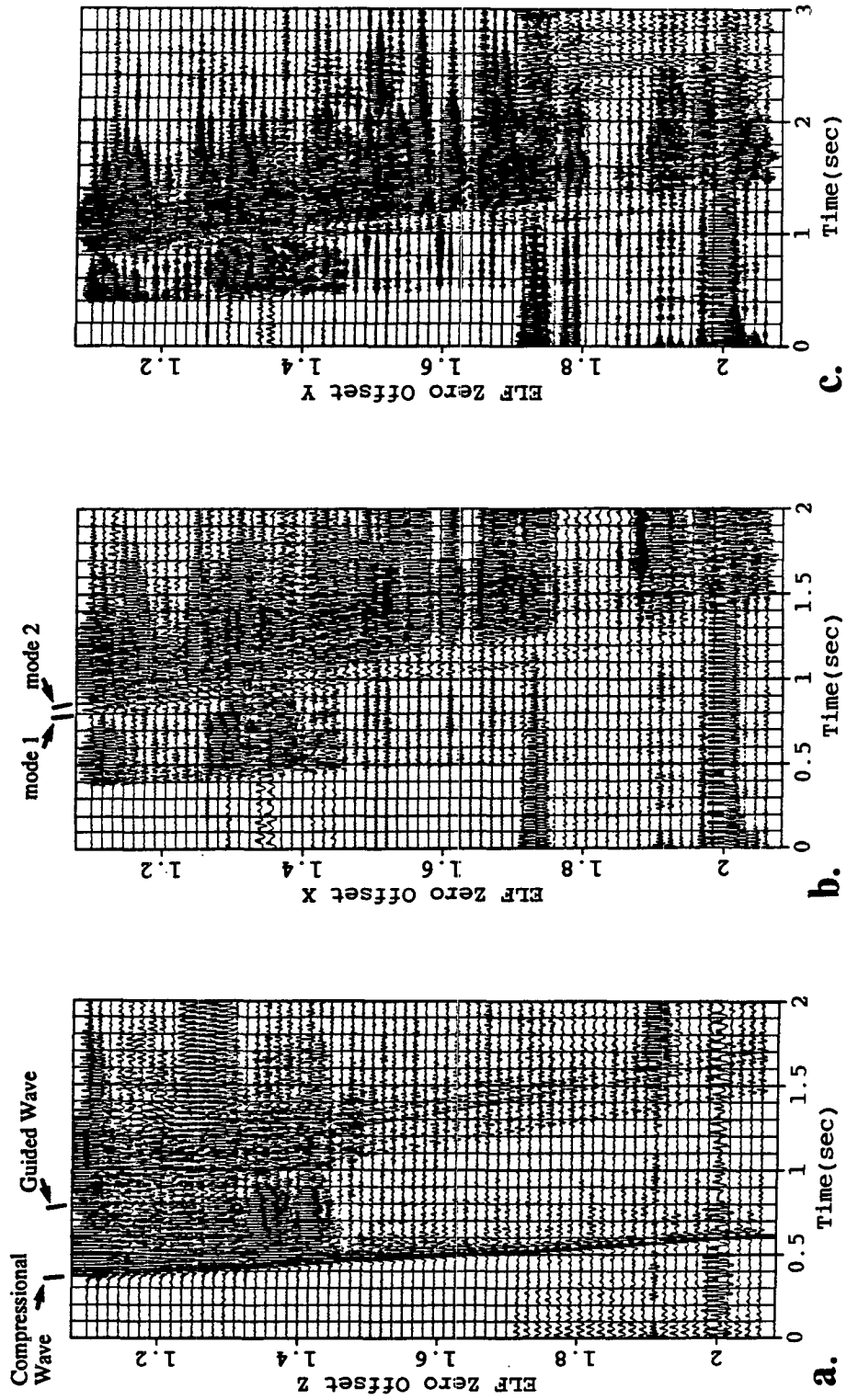
Figure 16. a) VSP profile of the vertical component for the zero offset ELF data set recorded in the Paris basin for the depth interval 1100 m to 2060 m. The window limits around the guided wave arrivals used in the analysis are indicated. b) the horizontal X and c) the horizontal Y components for the zero offset data.

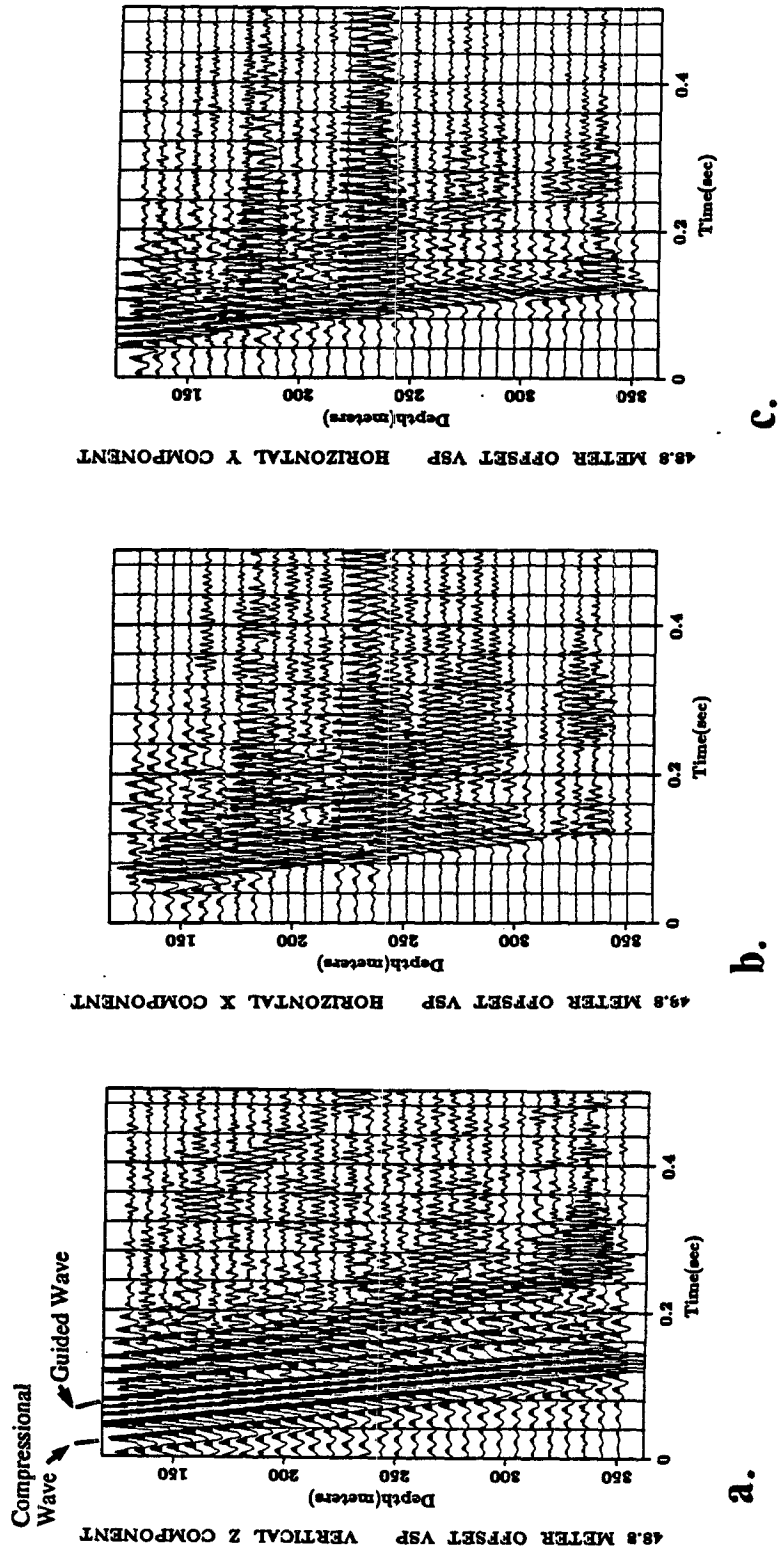Figure 17. a) VSP profile of the vertical component for the 262 m offset ELF data set recorded in the Paris basin for the depth interval 1100 m to 2060 m. The window limits around the compressional wave arrivals used in the analysis are indicated. b) the horizontal X and c) the horizontal Y component profiles for the 262 m offset data.
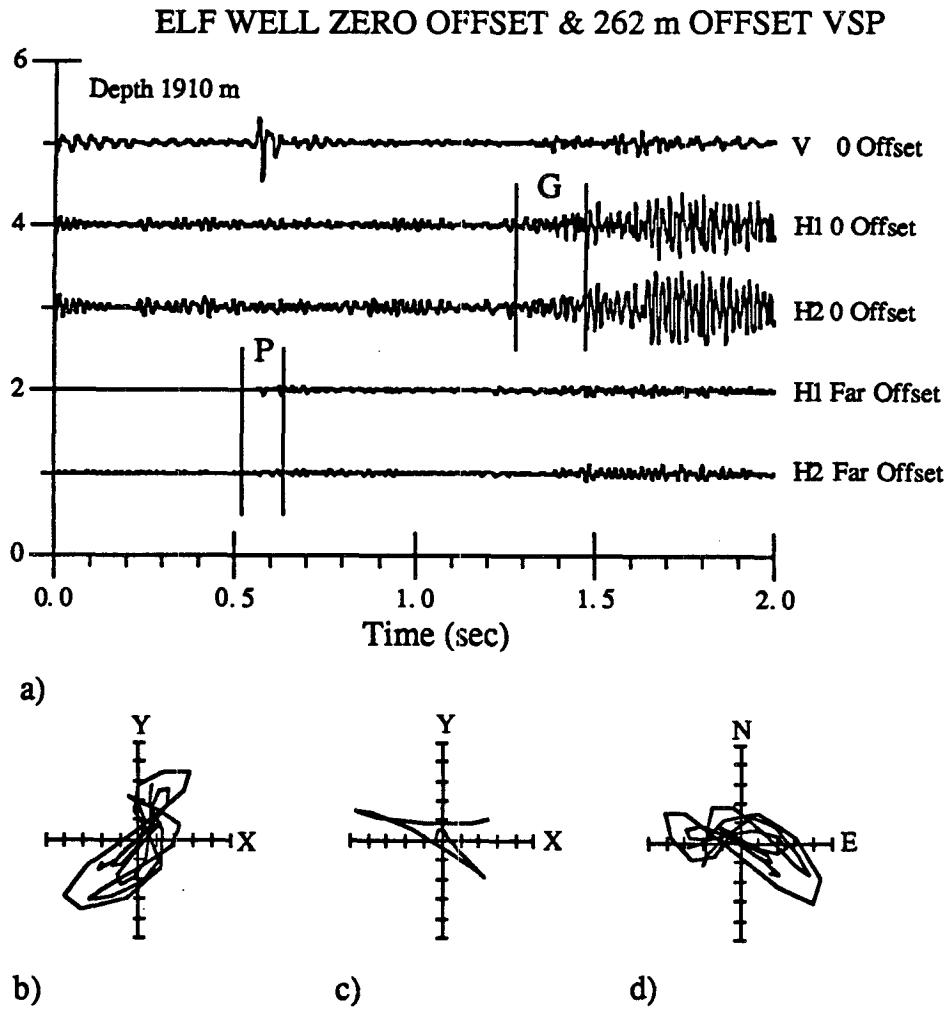
Figure 18. a) Times series from depth 1910 m in the Elf well showing windowed guided wave arrival "G" and the windowed compressional wave arrival "P" on the horizontal X and Y components. b) The corresponding particle velocity plots of the windowed guided wave arrival between 1.336 and 1.432 sec of the traces shown in 1a; c) the windowed compressional arrival traces between 0.522 and 0.580 sec of the traces shown in 1a; and d) the guided wave arrival corrected to north.

response of the guided wave energy on the horizontal components is evidence that this mode is in fact flexural wave energy. The results of the spectral analysis for the zero offset traces at depth 1910 m in the elf well are show the the frequency range is again well matched between the elements (Figure 19).

65 traces from depth 2060 m to 1100 m covering 960 meters were analyzed. Figure 20a shows the individual azimuths of the faster mode guided wave particle motion (heavy tick) measured at multiple depths in the ELF well on a single plan view. As with the Amoco data, it is immediately apparent that the polarization azimuths are not directed radially outward from the center of the borehole but have both radial and tangential displacement components. Figure 20b shows a histogram of the distribution of polarization azimuths for the ELF data indicating a peak of the measured polarization angle at about N50°W. These results are in good agreement with the direction of regional maximum horizontal stress in the locality of the well (Froidevaux, 1980) Also shown in Figure 20c are the theoretical stress trajectories that exist around a circular hole under uniaxial stress constructed through the solution of the borehole stress equations at an azimuth of N50°W.

The Cajon pass scientific drillhole is located in southern California approximately 4.3 km northeast of the San Andreas Fault (Figure 47, Section I, from Zoback et al., 1988). The drillhole transects 300 meters of sediments overlying felsic and mafic granites and gneisses. VSP data were recorded in the Cajon Pass drillhole after the first phase of drilling over the interval 300 to 1800 meters. These data were analyzed to determine the relationship of the guided wave particle motion to the orientation of horizontal principal stress in the well measured from wellbore breakouts (Shamir, et al., 1988). The geometry of the VSP experiment utilized a LRS 1300 (Litton Resources) receiver and an experimental source the ARCO ARIS[R] source (Rector, 1988). The ARIS[R] source is an angled weight drop device providing directional energy in an orthogonal pattern (front, back, left and right) for each geophone position and correspondingly four sets of records are generated for each geophone position. The source position was due south of the well. The geophone tool was oriented during the recording of the upper 1120 meters of the logged interval using a gyro device strung with the geophone tool.

This upper section of the data from 300 to 1420 meters (Figure 21) represents the data from the left source shot recorded using a gyroscope attached to the geophone. The tool spacing for the upper interval was 20 m. The non-gyro data was

Figure 19. a) Amplitude spectra for the vertical b) H1 and c) H2 geophone elements for the time series at depth 1910 m in the Elf well.
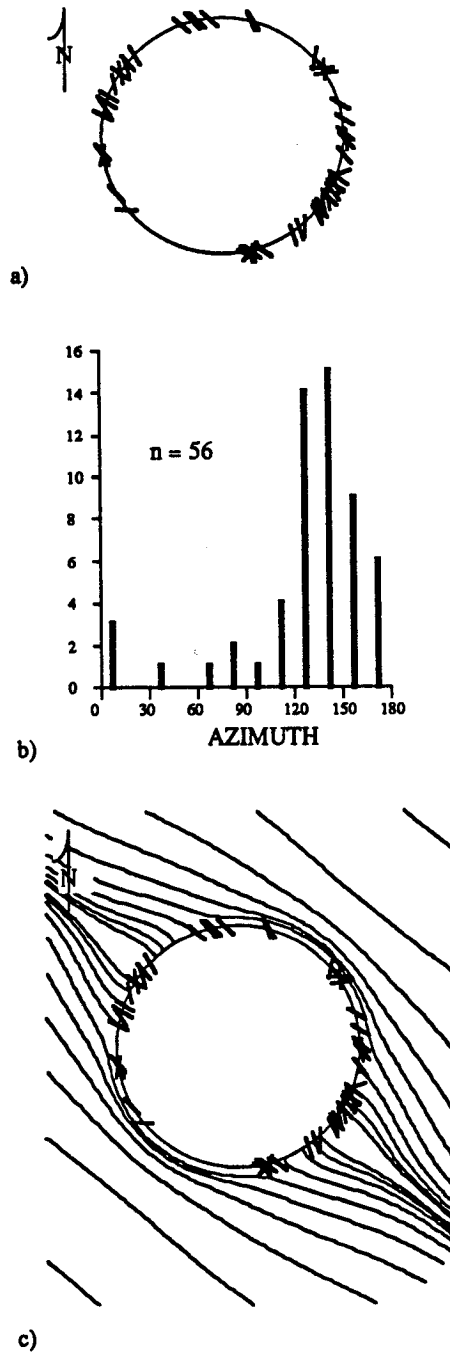
Figure 20. a) Orientation of the guided wave particle motion for the ELF data at multiple depths b) Histogram of the azimuth of guided wave particle motion for the ELF data c) the theoretical stress trajectories computed for S_{Hmax} at N50°W.
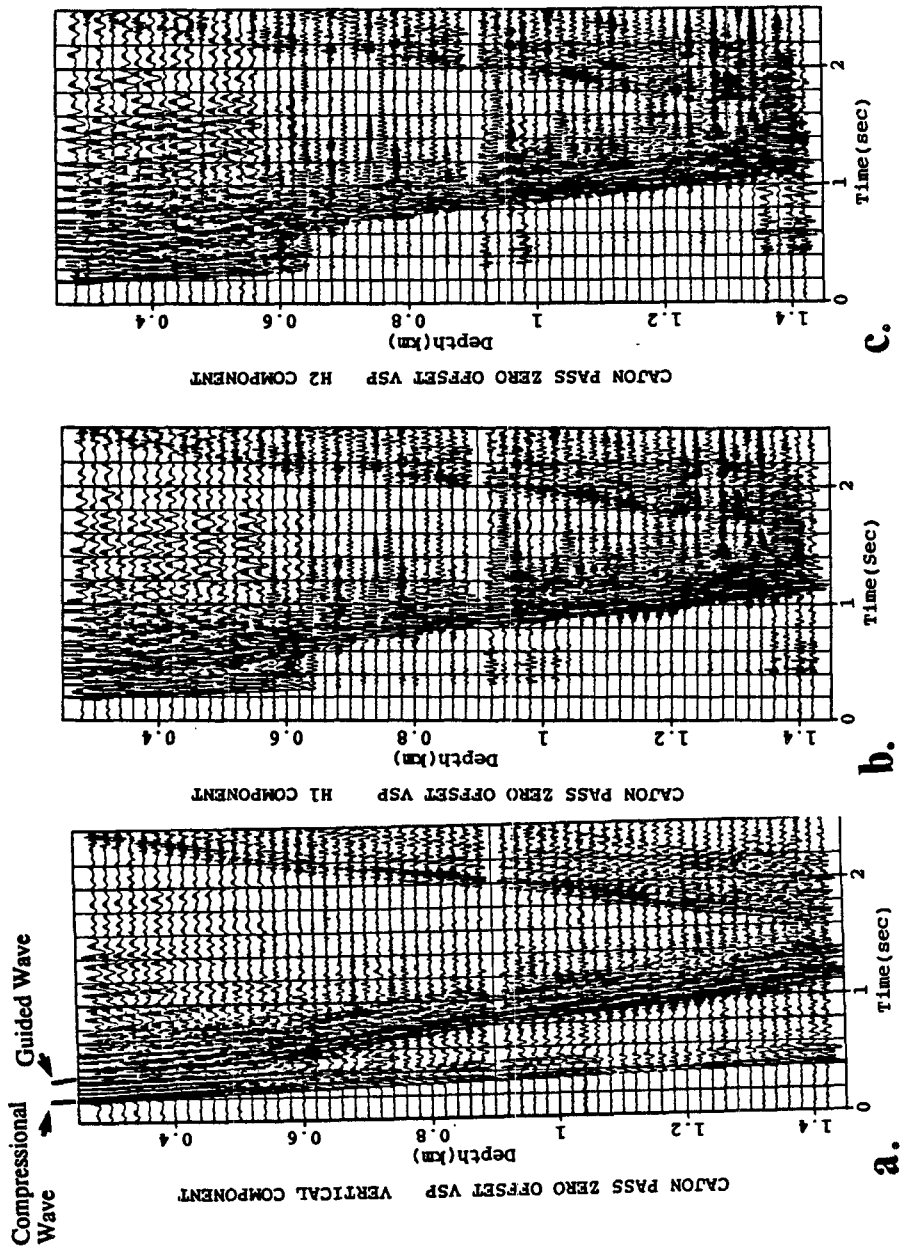
Figure 21. a) VSP profile of the vertical component for the zero offset data recorded in the upper section Cajon Pass well for the depth interval 300 m to 1420 m. These data were recorded using a gyroscope strung with the geophone sonde. The window limits around the compressional wave arrivals used in the analysis are indicated. b) the horizontal X and c) the horizontal Y component profiles for the zero offset data.

recorded with 10 m spacing and is shown in Figure 22. Gain value used are the same for each component. The compressional velocity is 3200 m/sec in the upper sedimentary section and 5500 m/sec in the lower section. The guided wave energy observed in the Cajon Pass data propagates at a velocity of 1715 m/sec. Again the velocity of this arrival is above that theoretically possible for a Stoneley mode but within the velocity range of the flexural mode. The borehole fluid at the time of logging was fresh water with a velocity of approximately 1500 m/s and the later mode is then higher than the fluid velocity. The irregularity of the onset of the compressional and guided wave energy is due source shifting required during the experiment to provide better ground contact and does not present a problem to the analysis of particle motion for a single shot and receiver pair.

Typical traces of the lower section of data are shown in Figure 23a from depth 1450 m. The onset of the compressional arrival is at 0.4 sec and the guided wave arrives at 1.1 sec. The maximum vertical amplitude is 11.7 over the window indicated in Figure 23a, the maximum H1 amplitude is 17.9 and the maximum H2 amplitude is 11.0. In examination of the Fourier response of the trace at 1450 meters the frequency response appears to be between 0 and 15 Hz for the three elements and the peaks are relatively well matched. For the data recorded at depth 1240 m the strong frequency peak at 25 Hz on the vertical component appears at 30 Hz on the horizontal components however the other higher frequency peaks are well matched. The three components amplitude spectra for depth 1450 m is shown to be well balanced in Figure 24.

As mentioned above the geophone was oriented for the upper 1120 meters of the recorded data. Both near offset (150 m) and 300 meter offset shots were recorded for each geophone position. Although substantial compressional wave energy is available in the zero offset data the compressional wave polarization azimuths were extremely variable between the redundant shots from the source pattern for each geophone position. This phenomena has been interpreted as the response of the compressional energy to the high degree of anisotropy in the granodiorite; this interpretation is supported by examination of the core. The far offset data were used to orient the tool where gyro data was unavailable. The gyro reading and the analyzed compressional wave particle motions for the far offset data generally show good agreement in source direction, particularly in the upper logged section (Rector, pers. comm.). Poor wavemode separation above depth 680 meters restricted the analysis of
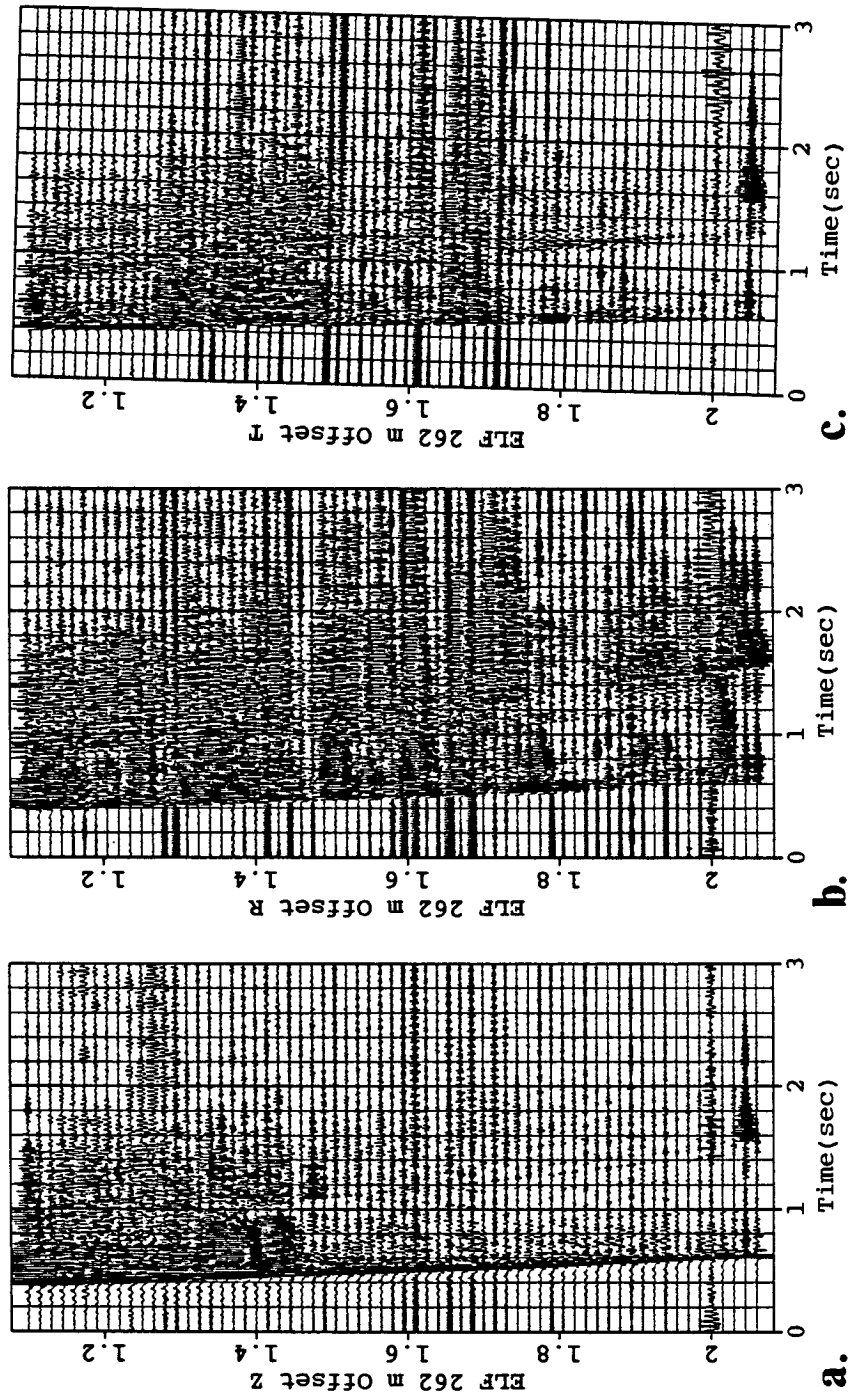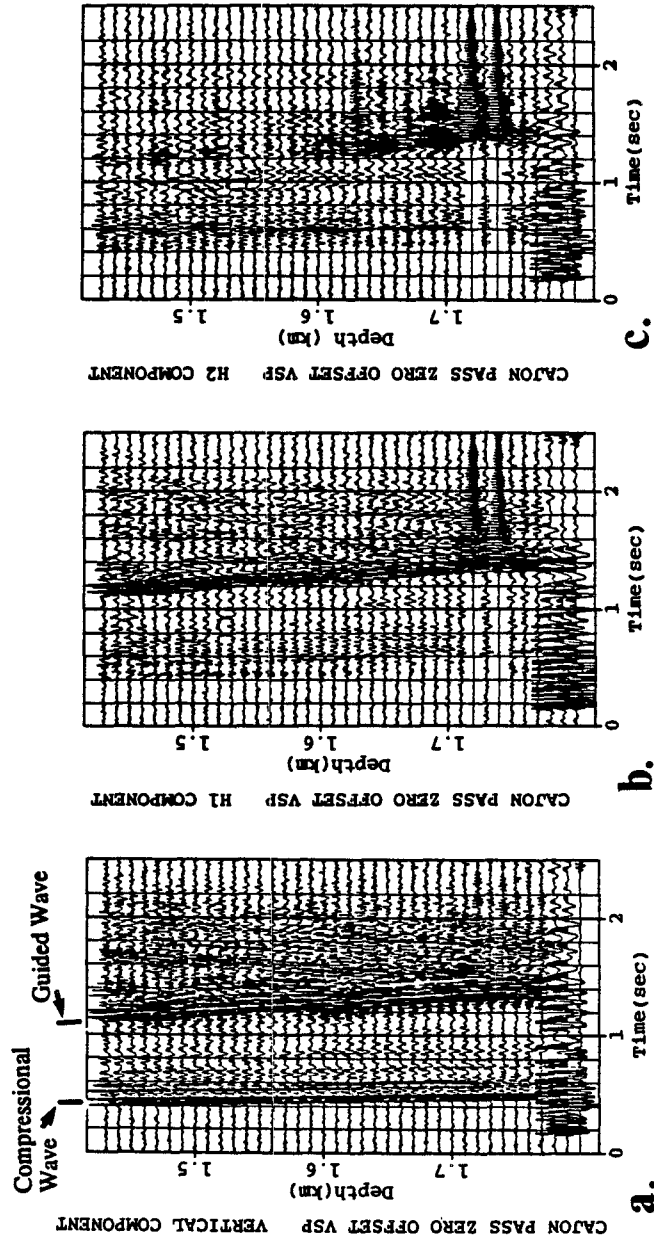
Figure 22. a) VSP profile of the vertical component for the zero offset data recorded in the lower section Cajon Pass well for the depth interval 1420 m to 1800 m. The window limits around the compressional wave arrivals used in the analysis are indicated. b) the horizontal X and c) the horizontal Y component profiles for the zero offset data.
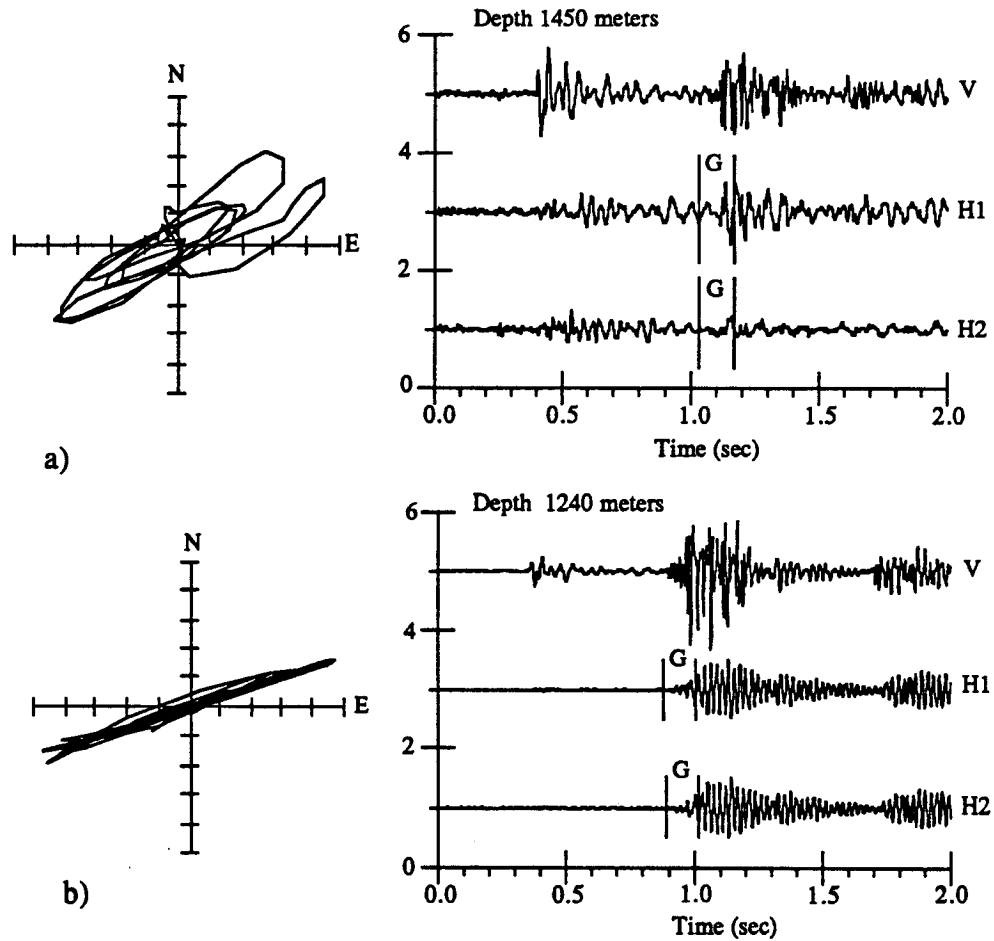
Figure 23. a) Times series and corresponding particle velocity plot corrected to north from depth 1450 m in the Cajon Pass well showing windowed guided wave arrival "G" on the horizontal X and Y components from 1.006 to 1.180 sec. This data is typical of that recorded with no gyroscope attached to the geophone sonde b) Times series and corresponding particle velocity plot corrected to north from depth 1240 m in the Cajon Pass well showing windowed guided wave arrival "G" on the horizontal X and Y components from 0.882 to 1.008 sec. This data is typical of that recorded while the gyroscope was attached to the geophone sonde.

Amplitude Spectrum

a.

Amplitude Spectrum

b.

Amplitude Spectrum

c.
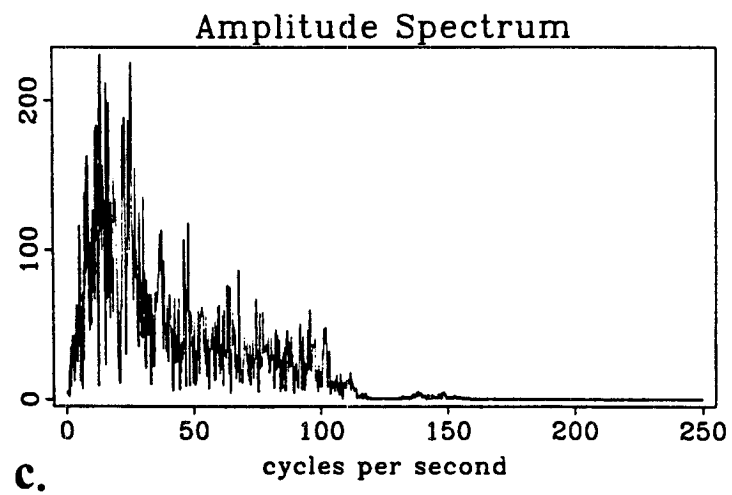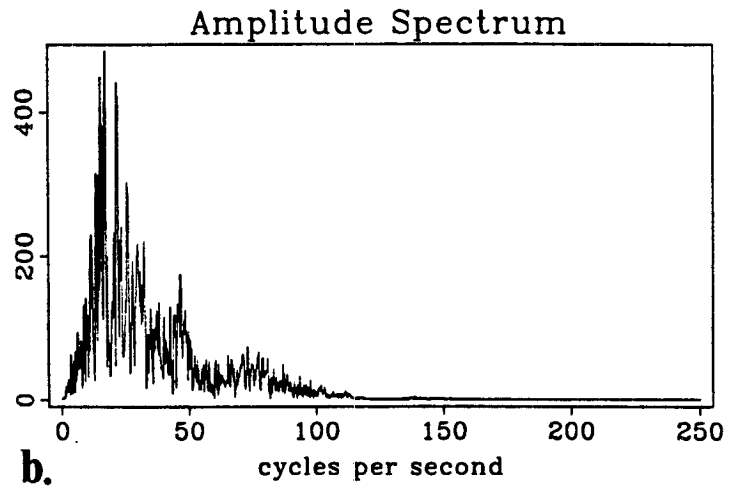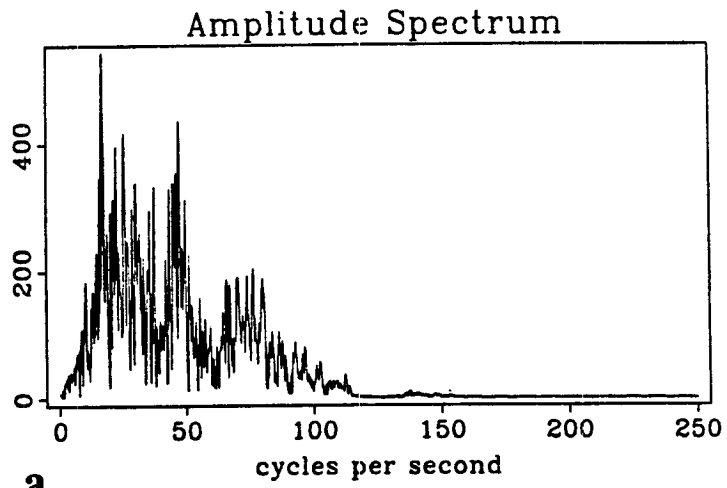
Figure 24. a) Amplitude spectra for the vertical b) H1 and c) H2 geophone elements for the time series at depth 1450 m in the Cajon Pass well.
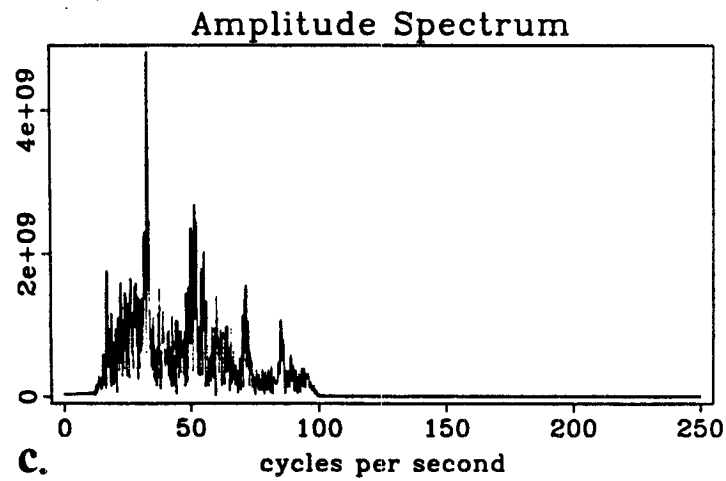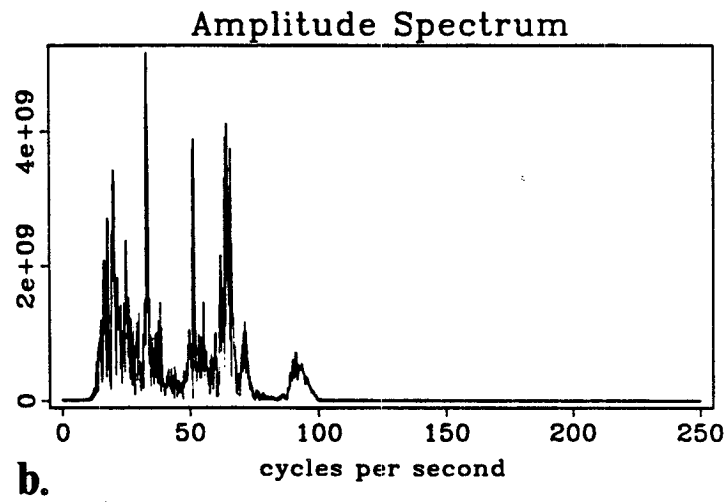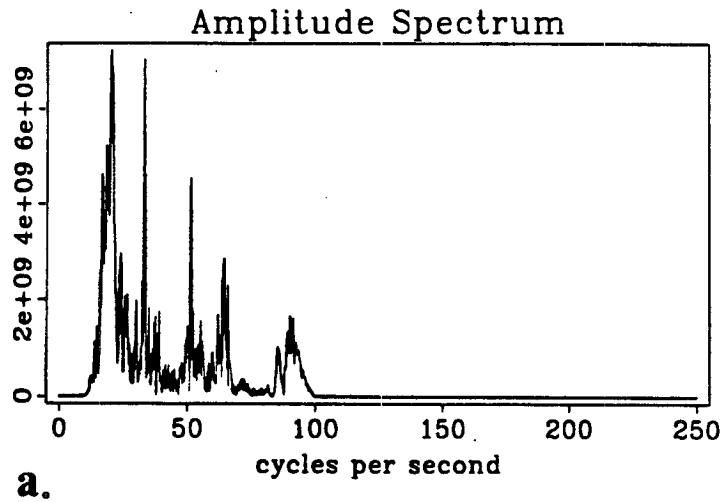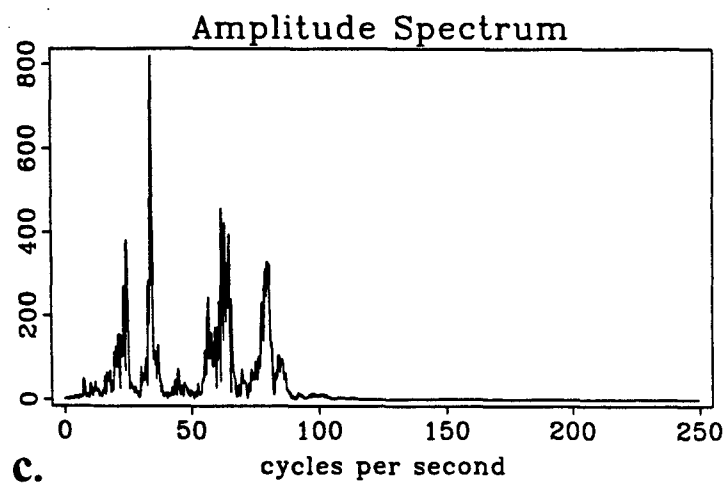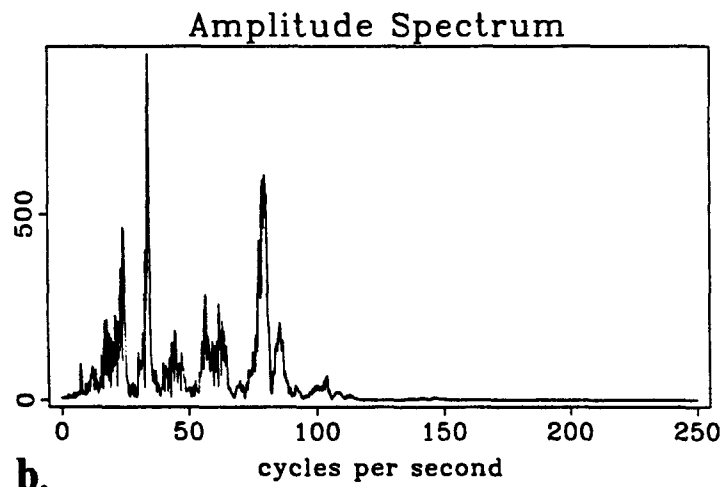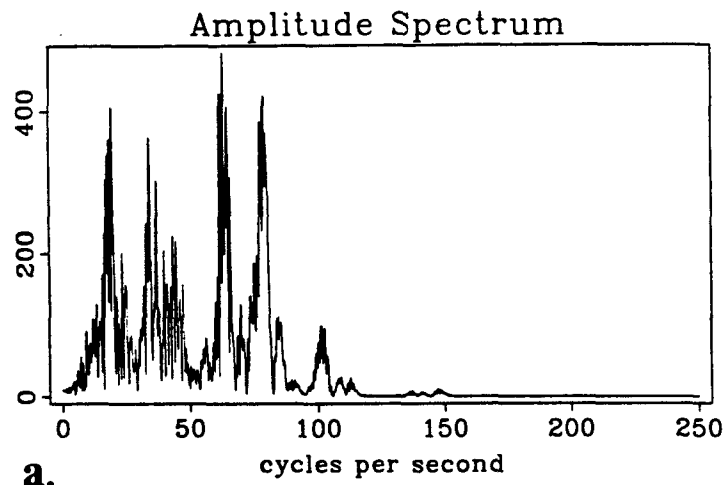
Figure 25. a) Amplitude spectra for the vertical b) H1 and c) H2 geophone elements for the time series at depth 1240 m in the Cajon Pass well.

the gyro oriented data to the 37 geophone positions between depths 1420 and 680 meters. The redundancy of the data at each geophone location provided a check for the polarization analysis for both compressional and guided waves. Unfortunately, the compressional wave polarizations below depth 1600 were very poorly oriented limiting the analysis of the non-gyro data to 19 traces between depths 1590 and 1420 meters. For the non-gyro records the data recorded between the geophone and all shot directions were generally in good agreement. However, for the gyro data, the the back, front and right shot positions were in good agreement but the data provided by the left shot was inconsistent with the others. The left shot gyro data were also poorly polarized in comparison with the other shot positions. The cause of the failure of one of these four shots to respond similarly to the geophone is not presently understood and the anomalous data were excluded from analysis. Other data excluded from the analysis include traces with low signal to noise ratio following the same criteria discussed above for other data sets.

A marked difference in the character of the guided wave particle motions between the gyro and non-gyro data was observed. Figure 23b shows a typical set of three component records and a hodogram plot of the windowed guided wave arrival, "G", from the gyro data in the lower set of plots. The non-gyro data, Figure 23a, exhibits a characteristic elliptical particle motion behavior while the gyro data shows very linear behavior. The waveforms for the gyro data show substantial ringing that is not present in the non-gyro data. This difference is interpreted as resonance due to the addition of the gyroscope which was attached rigidly to the geophone tool. The change in overall tool response caused by combining the tools apparently interfered with the recording performance of the transducers. The unfortunate consequence of measuring the location of the tool in this case is that it has effected the data.

The results of the analysis of the non-gyro data are shown in Figures 26 and 27. The distribution of polarization directions for the individual shots are shown as histograms in Figure 26 where the combined data give a mean direction of N50°E and standard deviation of 11°. The particle motion azimuths measured at each depth in the lower portion of the Cajon Pass well are plotted in collapsed view along with the principal stress trajectories for S_{Hmax} of N50°E in Figure 27. The stress state at the Cajon Pass drillsite indicates that S_{Hmax} is N73°E based on the analysis of wellbore breakouts (Shamir,et al., 1988) and hydrofracture experiments (Zoback and Healey,
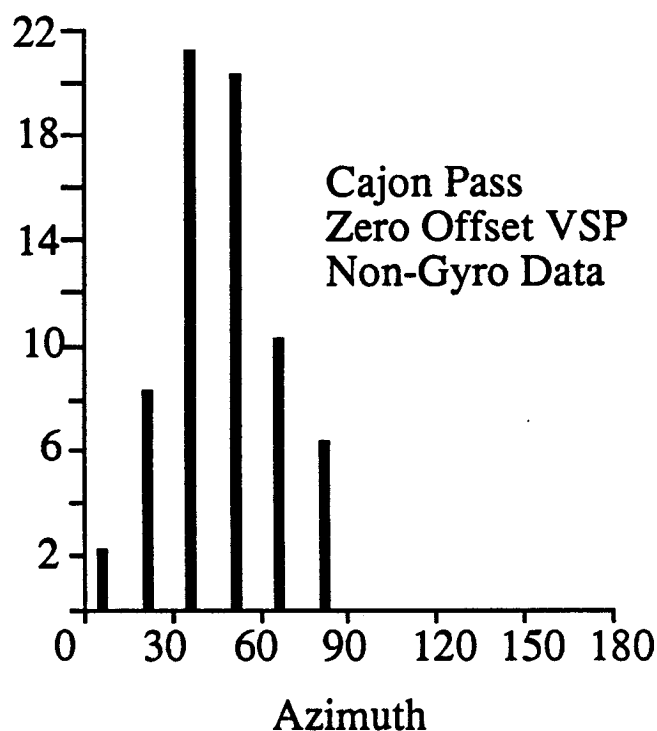
Figure 26. Histogram of the azimuth of guided wave particle motion for the non-gyro data from the four source shots recorded in the lower section of the Cajon Pass well . The combined data give a mean direction of N50°E.

1988). The results of this analysis of VSP data are consistent with an east-northeasterly direction of maximum horizontal principal stress.

The profiles in Figure 28 show the relative agreement between the guided wave polarization azimuths for each shot at the same geophone location. The four shots are fairly consistent at each depth and variations may be due to local inhomogeneities in the rock or that have caused the raypaths of the separate shots to differ. To examine the sensitivity of the guided wave polarization azimuths to variations in tool position, profiles of the guided wave polarization azimuth were plotted with a profile of the tool azimuth for each shot (Figure 29). Except for the apparent association of guided wave and tool azimuth for shots 1,2, and 4 at depth 1470 m the guided wave polarization and tool azimuths are uncorrelated. The association at 1470 m is possibly the result of a poorly oriented compressional wave azimuth.

Cajon Pass Zero Offset VSP
Shot #1

Cajon Pass Zero Offset VSP
Shot #2

Cajon Pass Zero Offset VSP
Shot #3

Cajon Pass Zero Offset VSP
Shot #4
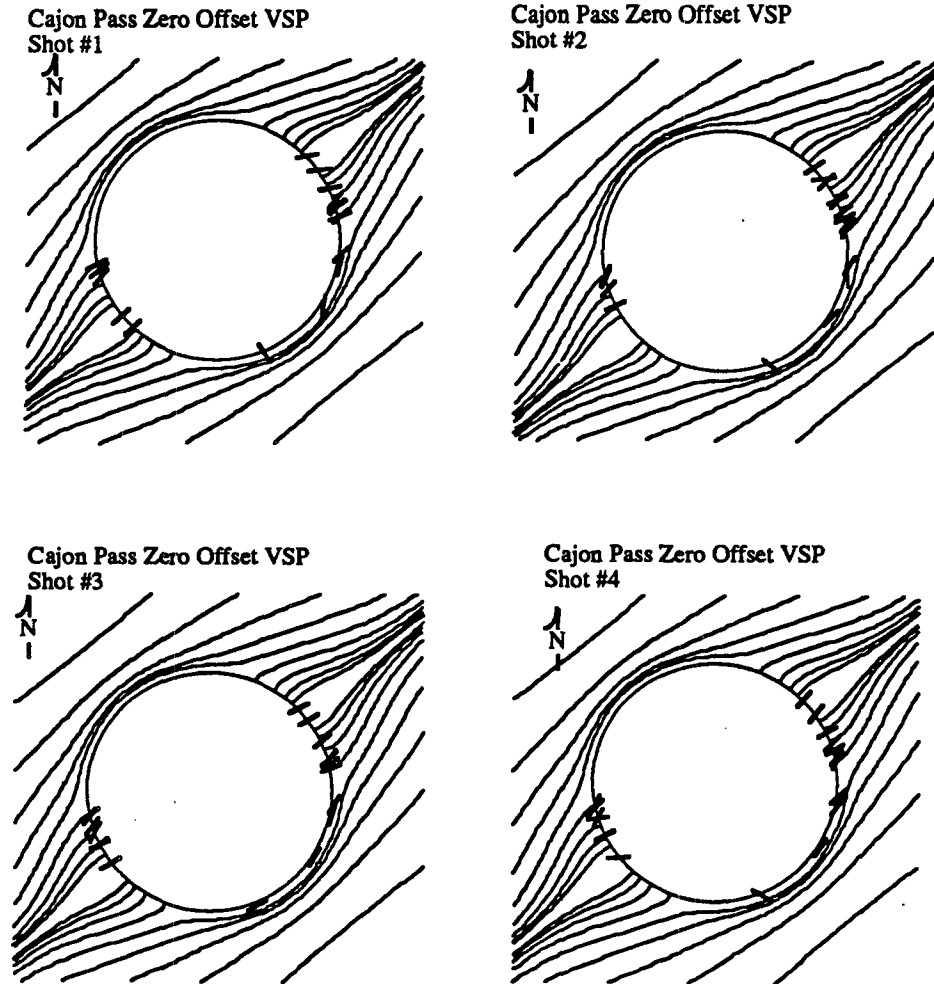
Figure 27. a) Orientation of the guided wave particle motion for the Cajon Pass data at multiple depths from each source in a collapsed view plotted with the the theoretical stress trajectories computed for S_{Hmax} at N50°E.
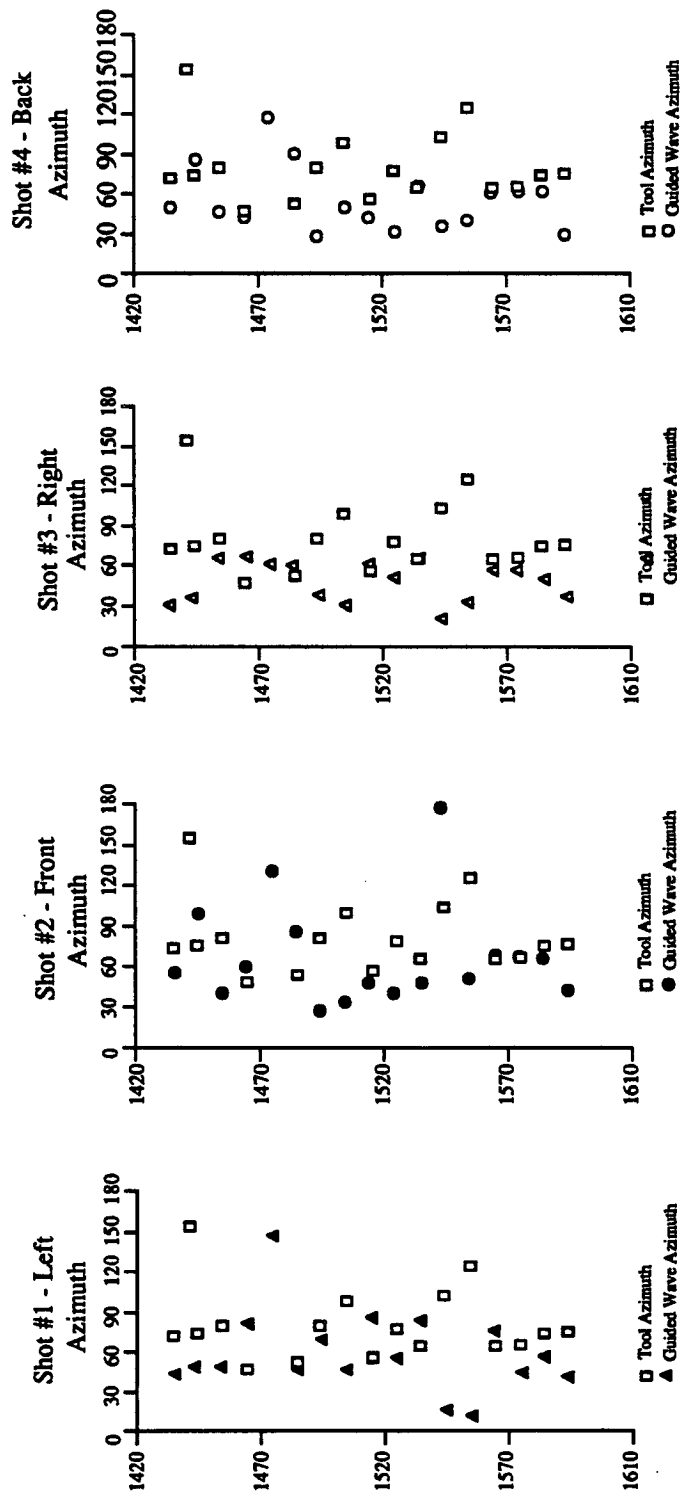
Figure 28. Depth profile of the polarization azimuths of the guided wave from the four separate shots in the Cajon Pass well at each geophone location.
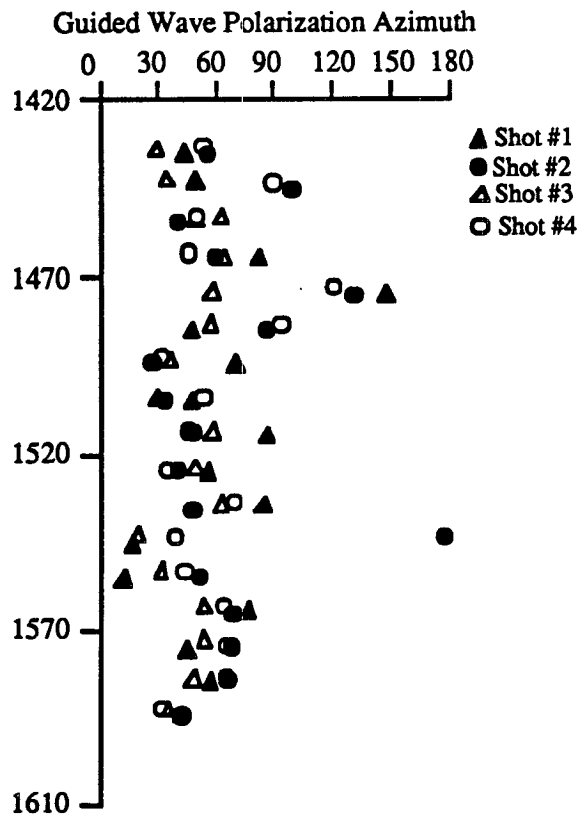
Figure 29. Depth profiles of the measured azimuths of the guided wave particle motion plotted with the determined tool azimuth.

The analysis of the data recorded with shot #1 of the ARIS[R] source in the upper section of the Cajon Pass well produced polarization directions that were inconsistent with depth and inconsistent with respect to the results obtained with the three remaining shots. The cause of these anomalous results is currently unknown. The results of the analysis of the gyro data for shots 2, 3, and 4 are shown in the histograms of Figure 29. Shot 2 data yield a mean polarization direction of 74° with a standard deviation of 16.9^o, shot 3 a mean direction of 77° with a standard deviation of 18° and shot 4 a mean direction of 64° with a standard deviation of 9°. Combined the mean direction is $N72^oE$. The discrepancy in the polarization directions between the gyro and non-gyro data are attributed to the bias of the gyro oriented data. Although the data from the upper section of the Cajon Pass well is

internally consistent this data may not represent the polarization direction that would have been measured without a gyroscope attached to the VSP sonde.
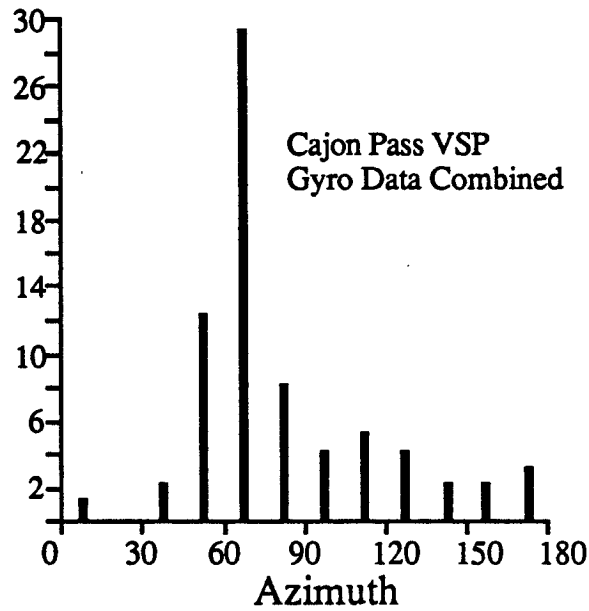
Figure 30. Histogram of the azimuth of guided wave particle motion for the gyro data from three of the four source shots recorded in the upper section of the Cajon Pass well . The combined data give a mean direction of N70°E.

INTERPRETATION

Discussion

The polarization of guided wave particle motion analyzed in three-component VSP data seems to be controlled by the direction of maximum horizontal stress. The variation in elastic properties as a function of azimuth around the borehole appears to control the displacement direction of the borehole guided wave. The argument of this hypothesis rests upon the recognition that VSP guided wave polarization behavior observed in field data is dominated by velocity anisotropy. Although the amplification of the far field stress at the borehole wall may give rise to stress-induced velocity anisotropy it has not been determined if the particle motion is controlled by intrinsic or stress-induced anisotropy or by a combined effect.

As mentioned above, determining which guided wave mode is recorded in a particular VSP experiment is difficult. Two guided wave modes that propagate within the recording frequency of the VSP are the Stoneley wave and the flexural wave. The symmetric Stoneley mode exhibits radial particle motion at all azimuths around a borehole in anisotropic material (Leveille and Seriff, 1988; Nicoletis et al., 1988). Radial particle motion was not observed in the data analyzed in this study. The borehole Stoneley wave is therefore not likely to exhibit the particle motion required to fit the particle motion behavior observed in these VSP data.

A preliminary finite element modal analysis of the behavior of the flexural mode has demonstrated that the flexural mode can show the particle motion behavior observed in VSP data. (Leveille and Seriff, pers com.). The results of modeling wave propagation in a cylindrical hole under horizontal transverse anisotropic conditions indicate that two flexural modes are excited, one parallel to each principal stress direction (Figure 31 from Leveille and Seriff, 1988). In the data analyzed in this study, only the flexural mode in the direction of maximum horizontal principal stress is observed. The effect of the far field stress is to introduce microcracks in a preferred direction resulting in a medium with a greater stiffness and lower attenuation in the direction of maximum principal stress and higher attenuation in the orthogonal direction (O'Connell, R.J. and Budiansky, B., 1979). In this model, flexural wave energy in the direction if S_{hmin} would be preferentially attenuated.
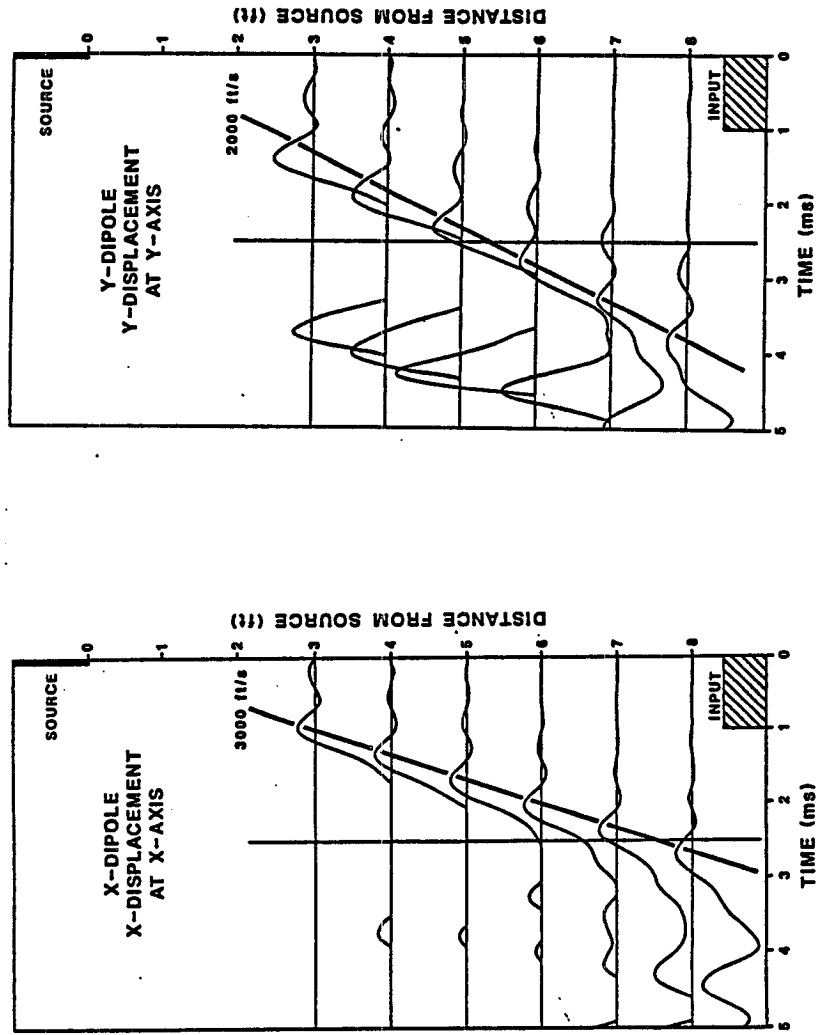
Figure 31. Results of the finite element modal analysis of the flexural wave traveling in horizontally transverse isotropic media where the flexural mode splits into two modes propagating in each of the principal stress directions (after Leveille and Seriff, 1988).

A full 3-D transient finite element model of the borehole flexural wave is required to determine if the observations in these analyses of VSP data can be explained as flexural wave behavior. There are two attributes of borehole guided waves that can provide a diagnostic tool for identifying flexural waves. The first is the propagation velocity of the guided wave mode and the second the relative amplitudes of the guided wave energy on the vertical and horizontal geophones. The velocities of the guided waves recorded in both data sets from in the Amoco Test well had velocities at approximately the fluid velocity. The guided wave velocities recorded in the Elf well and in the Cajon Pass well have at least one mode with velocities higher that that theoretically possible for the propagation of a borehole Stoneley wave and within the range of velocities possible for flexural waves.

For the data recorded at offset 12.2 m in the Amoco test well the horizontal to vertical amplitude ratio is approximately 1:1 however the second set of data recorded in this well has an amplitude ratio of 2:1. The data recorded in the ELF well have an horizontal to vertical ratio of 3.4:1 and that of the Cajon Pass well 1.5:1. Theoretical calculations of the radial to axial displacements in rock adjacent to a fluid filled borehole for the low frequency approximation of the borehole Stoneley mode in isotropic conditions indicate the the displacement ratios should be comparable (Cheng and Toksoz, 1984). In contrast, some of the data sets analyzed in this study have guided wave energy with horizontal to vertical amplitude ratios as high as 3.4:1. The observations of amplitude and velocity behavior as well as particle motion behavior anomalous to that theoretically predicted for borehole Stoneley waves provide evidence that the guided waves analyzed in this VSP data are the flexural modes.

This new approach to the measurement of in-situ stress has the limitations inherent to VSP data. Particle motion is a difficult wave propagation characteristic to analyze. Hodograms are very sensitive to local inhomogeneities in the rock and strongly effected by noise contamination. Data recorded at shallow depths often exhibits superimposed body and surface wave arrivals because of an insufficient time for mode separation. Interference from upgoing events will also mask the true particle motion path. These data, as well as extremely noisy or poorly coupled traces, must be excluded from analysis.

The time window used to generate the hodogram must be carefully selected. The choice of window position and length is somewhat a matter of interpretation and several analysis windows may need to be tested to produce a reliable hodogram

(Hardage, 1983). In this study, both the compressional and guided wave arrivals were windowed at three increasing time windows and the resultant polarization angles compared for consistency. The time intervals of 50, 100 and 200 ms were compared in both data sets recorded in the Amoco well and time windows of 20 40 and 80 ms were compared in the data recorded in the ELF well. Wherever agreement was not achieved between any two of the three windows, the trace was considered poorly oriented and was excluded from the analysis. It is noteworthy, however, that virtually all of the poorly oriented traces were those that show low signal-to-noise ratio in the time series.

Potentially, the most significant source of error in the analysis of polarization angles may be tool resonance. The position of the horizontal transducers on the VSP tool, one parallel to the plane of the locking arm and the other orthogonal to that plane, may cause a preferential direction of displacement. If the recorded signal were solely the result of equal amounts of particle motion on the radial and transverse components the resultant motion would be at 45⁰ to the tangent of the borehole at that tool position (L. Nicoletis, pers. com). In order to check this effect on the data analyzed in this study the distribution of the angle formed with the tangent to the borehole and the polarization of the guided wave particle motion was evaluated. The data recorded in the Amoco well and the Elf data show this angle to be completely uncorrelated with no peak at 45⁰ (Figure 32). A similar analysis of the Cajon Pass data again shows no correlation peak at 45⁰ for either the gyro (Figure 33) or the non-gyro (Figure 34) data sets. Another check for potential tool effects is to examine the quality the linear polarization of the compressional mode. Variation from a true linear particle motion path for compressional wave first motion would be indicative of the magnitude of tool resonance in the geophone records. The optimum VSP geometry for the generation of guided waves is a source close to the wellhead. However, strong compressional wave energy is also essential because tool orientation is required to reference the guided wave polarization to its compass azimuth. The ELF data analyzed in this study meets these criteria having two shots for each receiver depth, one at zero offset and one with a far offset. In order to compare amplitude information between depth shots it is also necessary to have a monitor geophone at zero offset to provide a normalization factor.

Amoco 12.2 Meter Offset VSP

a)

Amoco 48.8 Meter Offset VSP

b)

ELF Zero Offset VSP

c)
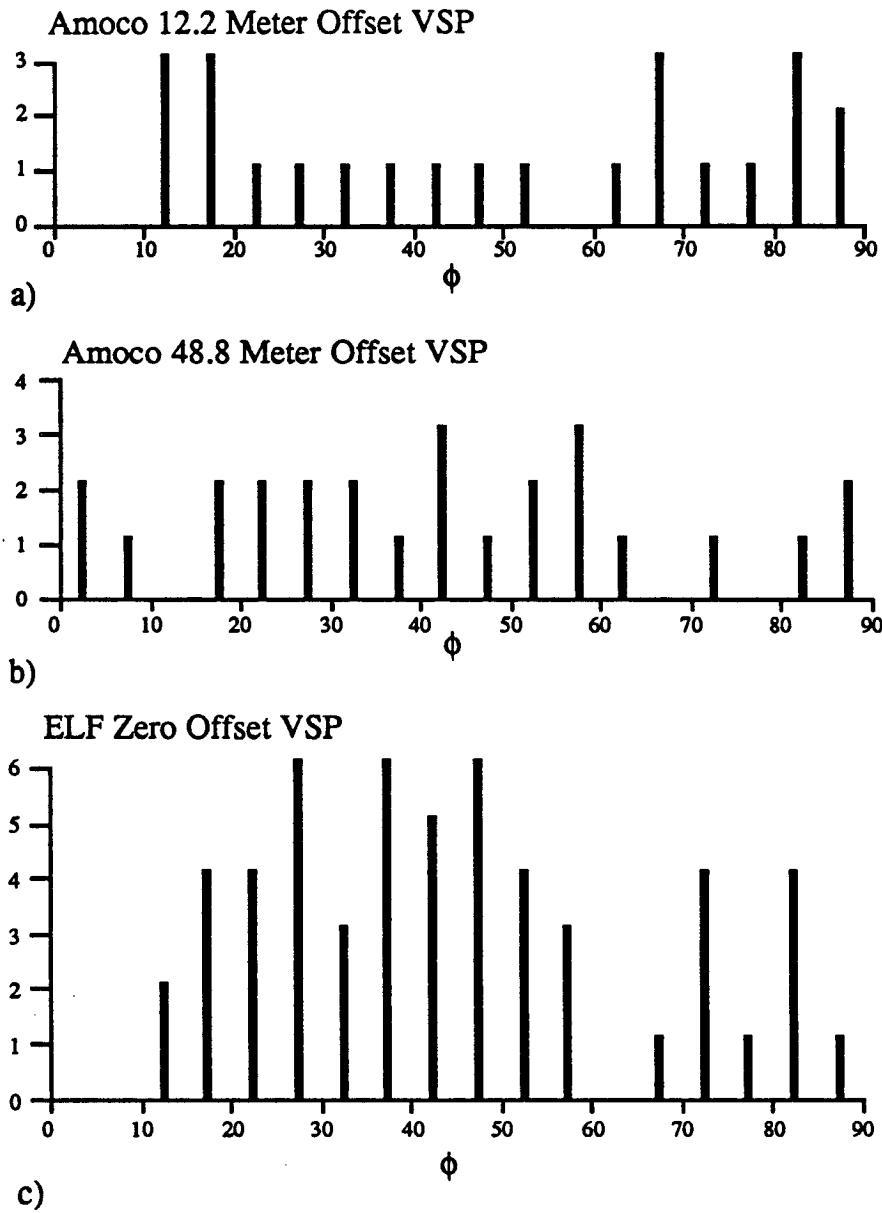
Figure 32. Distribution of angle φ measured from the measured azimuth of the guided wave particle motion to the tangent to the borehole at the corresponding tool location for a) the Amoco 12.2 m offset data b) the Amoco 48.8 m offset data and c) the Elf data.
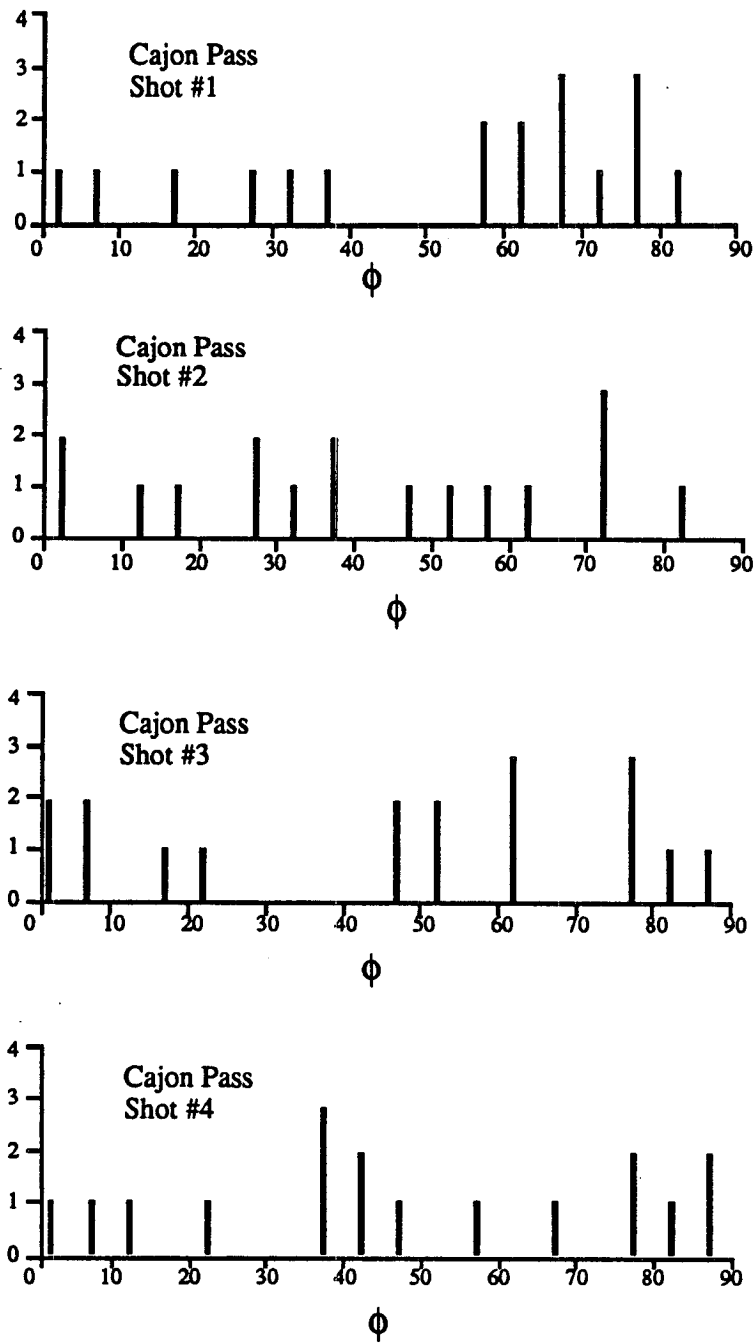
Figure 33. Distribution of angle φ measured from the measured azimuth of the guided wave particle motion to the tangent to the borehole at the corresponding tool location for the four source shots from the lower section of the Cajon Pass data.
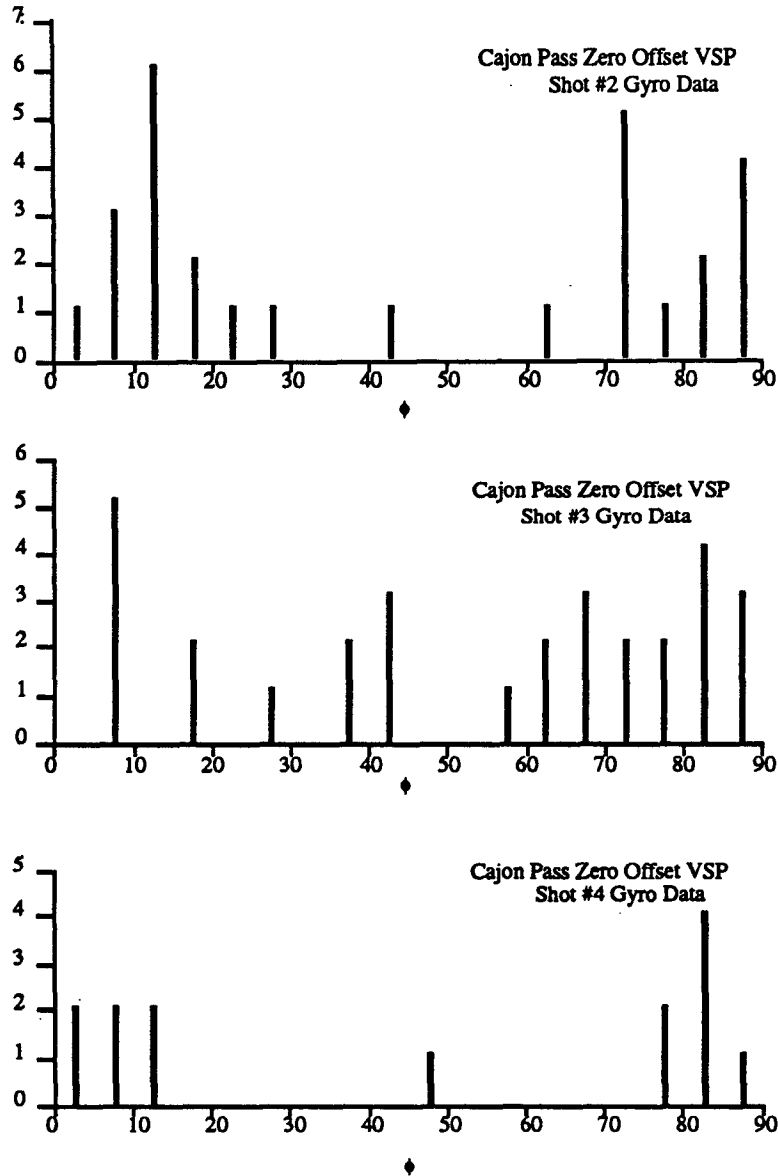
Figure 34. Distribution of angle ϕ measured from the measured azimuth of the guided wave particle motion to the tangent to the borehole at the corresponding tool location for three of the four source shots from the upper section of the Cajon Pass data.

It has been demonstrated that at each geophone location the particle motion is generally polarized in the direction of local maximum horizontal compression (Figures 12c,f, 20c, and 27). Inspection of the particle velocity plots at different depths for the data sets show that the particle motion is not linear motion in the horizontal plane (Figure 35) but, in fact the particle motion describes an approximately elliptical path in
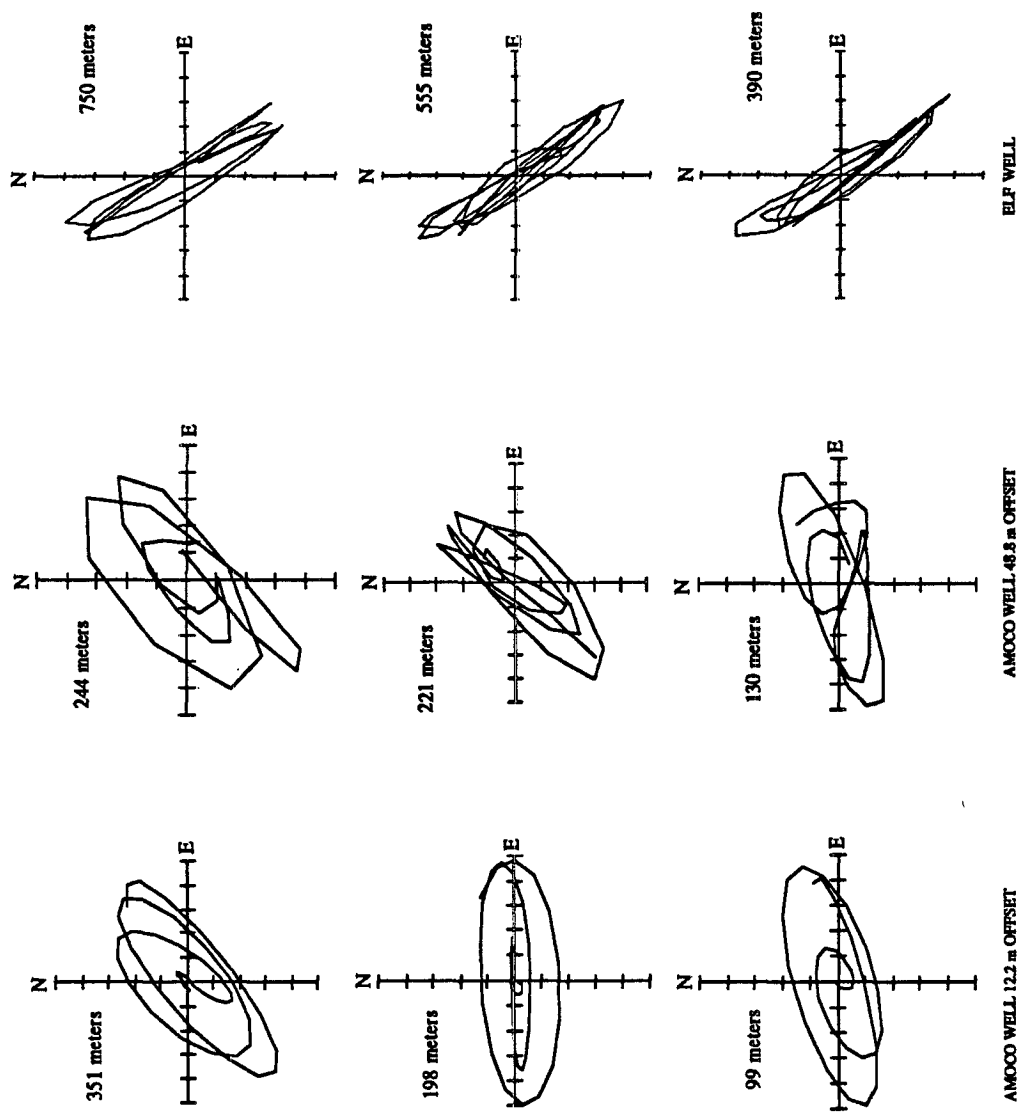
Figure 35. Aspect ratio of guided wave particle motion at three different depths plotted from three of the data sets analyzed. Particle motion in the horizontal plane has been oriented with north.

the horizontal plane as predicted by the preliminary numerical analysis mentioned above. The aspect ratios of these ellipses are similar for each of the multiple depth shots for a given data set. What is the cause of this consistent pattern observed in the data? The repetition of the observed particle motion behavior at different depths and in different experiments suggests that it is the result of intrinsic rock anisotropy probably induced by the regional stress field but possibly also reflecting the stress concentration around the borehole. Relating the magnitude of the U_r and U_θ components of particle motion observed in the VSP guided waves to the magnitude of the horizontal stresses will involve the solution of the displacement field for anisotropic materials.

Conclusions

The orientation of the principal horizontal stresses was determined from the polarization of the VSP guided wave particle motion. Two sets of data recorded using different shot geometries and instrumentation recorded in the same test well produce identical guided wave polarization directions both before and after the hole was cased. These directions are in agreement with the stress regime at the well site. Two additional sets of data recorded with zero offset and far offset geometry also corroborates the concept of the stress dependence of the guided wave particle motion. It is suggested that stress-induced velocity anisotropy in the rock adjacent to the borehole appears to cause antisymmetric flexural guided wave modes to be polarized in the direction of maximum horizontal principal stress. Thus, analysis of the horizontal particle motion of borehole guided waves appears to represent a new method for determining the orientation of horizontal principal stresses.

Based on the theory of guided wave behavior in acoustic boreholes (Roever, et al., 1974) and on the results of laboratory analysis of stress-induced anisotropy in materials (Nur 1969, 1971; Nur and Simmons 1969; Stesky, 1985) the anomalous particle motion behavior observed in this study can be explained as the response to stress-induced anisotropic conditions. Support for the effects of anisotropy on the propagation of guided waves includes recent finite element modeling of borehole flexural waves (Leveille and Seriff, pers. com.) and analogous particle motion studies using surface wave polarizations from teleseismic data (Crampin, 1977).

Certainly more VSP data from a variety of regions need to be analyzed by this method and techniques to improve the accuracy of the measurement of polarization angles need to be explored. The determination of stress magnitude utilizing borehole guided waves is an important target for future work. Studies of the phase velocity and frequency content of the guided waves may reveal the 3-D dispersion pattern of these modes and provide information related to the effective moduli of the material. In addition, the significance of the consistency of the horizontal amplitude ratios and their relationship to the ambient stress ratio warrants further study. Finally, a full 3D, transient, finite element model could be used to determine the propagation characteristics of the borehole flexural wave in anisotropic media.

APPENDIX A

BHTV DATA ACQUISITION AND ANALYSIS SYSTEM DOCUMENTATION

INTRODUCTION TO THE SYSTEM

The digital BHTV analysis system consists of two sets of programs, the first for data acquisition, and the second for data display and analysis. These routines are written in the C programming language and are implemented on Masscomp 5600 and 5500 series computers. The concepts that provide the basis for these programs are contained in the main body of this thesis. The documentation for each program includes a summary of its application to BHTV data and a description of input parameters. Samples of the execution of the programs are provided and samples of the output graphics are referenced to the preceding text where appropriate.

All digitized data are pre-processed to determine the ranges of amplitude and travel time values, to filter noise, and to correct for geometric effects before data can be displayed and interpreted. A data editor has been designed for this task. The different display routines share a common library of functions that control operations general to all routines such as read/write, graphics set up, and standard graphics displays. The data acquisition routines also share a common library of general routines for clock initialization, control of data acquisition parameters such as digitization delay and window length, etc. Data acquisition is controlled by two programmable clocks, one set to initiate at the source firing and the other to initiate after a user specified delay.

The format used for BHTV data is binary where each amplitude and travel time pair is stored in two bytes. The first 9 bits contain the amplitude value (ranging between 0 and 512) and the left 7 bits the travel time value (ranging between 0 and 256). A header is attached to the beginning of each data file. The basic header is generated at the time of data acquisition and the header information is augmented during pre-processing with the editor. Header values may be changed during editing or at any other time by a header editing facility.

DATA ACQUISITION SOFTWARE

DIGIT

Routine DIGIT is used to initially establish the parameters for digitizing a particular data set. The variability of borehole size and condition requires that the analog settings on the Simplec BHTV board be adjusted in conjunction with the ADC clock settings of delay and window length in order to capture only he reflected signal while digitizing. DIGIT digitizes a short section of data without reducing it to travel time and amplitude so that the raw digitized reflection waveform can be inspected and settings can be checked empirically before digitizing a data set. DIGIT creates a data file "raw_data" containing successive pulses of data which can be examined with routine SHOW_RAW.

Input parameters:

Ddelay: The time in μsec after the source firing to delay the second clock

Window: The window length in μsec used to sample the reflected pulse

Threshold: The background level of the signal in amplitude units (0 to 512). Only signal levels above this threshold will be used in the binary search for the peak amplitude

Sample program execution:

Enter gate delay in μsec: 65
Enter window length: 100
Enter threshold <4>:   10
Setting up A/D
Buffer = 289456

.
.

bytes written = xxxxxxx.

SHOW_RAW

Routine SHOW_RAW is a data preview facility used to display the output from DIGIT. SHOW_RAW prints the 100 values captured by the ADC for each pulse in a 5X20 matrix so the quality of the data can be examined. The digitized waveform should represent a square wave where initial constant low values have a sudden break to a constant high value. The user can check the file randomly entering any pulse number to examine.

Sample program execution:

Enter raw data file name: raw_data
Enter pulse number to show (0 to exit):   500

SAMPLE
    Routine SAMPLE is used to digitizes a small section (about 5 meters) of
analog BHTV data reducing the digitized waveforms to travel time and amplitude
values. SAMPLE should be used only after the parameters of delay, window length
and threshold have been determined using DIGIT and SHOW_RAW. SAMPLE
creates an image file called "packed_data". "packed_data" must be moved to a
different file name before SAMPLE is run again or it will be overwritten. After the
data acquisition is complete the user is prompted for information about the data and
data acquisition settings.

    Input Parameters:
        Ddelay: The time in μsec after the source firing to delay the second
            clock
        Window: The window length in μsec used to sample the reflected
            pulse
        Threshold: The background level of the signal in amplitude units (0 to
            512). Only signal levels above this threshold will be used in
            the binary search for the peak amplitude

    Sample program execution:
        Enter gate delay in μsec: 65
        Enter window length: 100
        Enter threshold <4>:   10
        Setting up A/D
        Buffer = 289456
            .
            .
        bytes written = xxxxxxx.
        Enter well name: DOSECC #1
        Enter well location: Cajon Pass, California
        Enter magnetic declination at site in degrees east of north: 15
        Enter starting depth: 2000
        Enter ending depth: 1000
        Are depths in feet or meters: meters
        Enter borehole fluid velocity in m/sec: 1500
        Tool used to record data was 1-Large Tool 2-Small Tool: 1
        High frequency (1) or low frequency (2) transducer?:   1
        Do you know the calibration? yes
            Enter calibration in μsec: 9.04
        If tool was in marker mode enter degrees to correct to north (enter
            0 if none):   0
        Enter borehole deviation (enter 0 if unknown):   0
The header will be printed and program execution ends.

TBHTV

       Routine TBHTV digitizes about 25 meters of analog BHTV data reducing input to travel time and amplitude values. This routine is used to acquire large depth sections of data and is the main data acquisition program. TBHTV should be used only after the parameters of delay, window length and threshold have been determined using DIGIT and SHOW_RAW. TBHTV creates an image file called "packed_data". "packed_data" must be moved to a different file name before TBHTV is run again or it will be overwritten. After the data acquisition is complete the user is prompted for information about the data and data acquisition settings.

      Input Parameters:

              Ddelay: The time in μsec after the source firing to delay the second clock

              Window: The window length in μsec used to sample the reflected pulse

              Threshold: The background level of the signal in amplitude units (0 to 512). Only signal levels above this threshold will be used in the binary search for the peak amplitude

      Sample program execution:

              Enter gate delay in μsec: 65
              Enter window length: 100
              Enter threshold <4>:   10
              Setting up A/D
              Buffer = 289456

                  .
                  .
                  .

              bytes written = xxxxxxx.
              Enter well name: DOSECC #1
              Enter well location: Cajon Pass, California
              Enter magnetic declination at site in degrees east of north: 15
              Enter starting depth: 2000
               Enter ending depth: 1000
               Are depths in feet or meters: meters
              Enter borehole fluid velocity in m/sec: 1500
              Tool used to record data was 1-Large Tool 2-Small Tool: 1
              High frequency (1) or low frequency (2) transducer?: 1
              Do you know the calibration? yes
                    Enter calibration in μsec: 9.04
              If tool was in marker mode enter degrees to correct to north (enter 0 if none): 0
              Enter borehole deviation (enter 0 if unknown): 0
    The header will be printed and program execution ends.

LOOK

Routine look is used to examine data during the process of digitization with routines SAMPLE or TBHTV. It can also be used to look at unedited data files where the execution of SAMPLE or TBHTV was interrupted by ^C. In other words, with LOOK you can examine a file only before a header has been written.

Sample Program execution:
Display which file?:   packed_data
Enter greatest depth of interest (0 for bottom depth): 0
First scan has xx sample.
Okay? Type 0 *** Type 1 to adjust: 0
LOOK will then display depth profiles of both travel time and amplitude values in the standard 360° view.

EDITOR

Program "editor" is used to visually edit unwanted scan lines and to correct data for noise and off-center tool effects. The editor also establishes the cut off values for histogram equalization. It augments the initial file header with additional information about the data. The user has the option to view or not view the data. With the view option data are plotted in 360° view with depth and the mouse (button #1) is used to select the top and bottom of any data interval the user would like to delete. Mouse button #2 is used to move to the next screen of data and button #3 is used to end the visual editing and to initiate correcting and rewriting the data. The user has the option to median filter and/or correct the geometry for off center tool effects.

Sample Program execution:
Display which file?:   packed_data
Enter greatest depth of interest (0 for bottom depth): 0
Would you like to see the data? yes
First scan has xx sample.
Okay? Type 0 *** Type 1 to adjust
The EDITOR will then plot a panel of data and issue the prompt:
Use the mouse to edit each screen full of data.
Use button #1 to select the lower and upper section to delete
Use button #2 to move on to the next panel of data
Use button #3 to write the data into a new file.
Once button #3 is used the routine returns:
Figuring array initial_byte....:
Then header it the printed and the EDITOR issues the prompt:
Would you like to change a variable: yes
Enter variable name enter 0 when done: Mag Dec
Enter new values of Mag Dec: 16
Would you like to median filter the data? yes
Correct geometry? yes
Is borehole circular or elliptical? circular
Writing data please wait....
End of edit

DATA DISPLAY AND ANALYSIS SOFTWARE

DRAW

    Routine DRAW displays one large panel of all the data pulses per scanline.
The default display is borehole diameter, use the -a option to plot amplitude displays.
A prompts then allows the user to hard copying and/or advancing to the next screen of
data.

    Sample Program execution:

        Display which file?:   packed_data

        Enter greatest depth of interest (0 for bottom depth): 0

        White for missing pulses?: yes (inverts black to white for plotting on
            white background)

        Enter 0 for linear scale 1 for equalized scale: 0

        First scan has xx sample.

        Okay? Type 0 *** Type 1 to adjust: 0

    Routine DRAW will then draw a panel of data and issue the prompt:

        Hardcopy? no

        Enter 1 to plot next panel 0 to quit: 1

DRAWBOTH

    Routine DRAWBOTH displays two 360° panels of amplitude and borehole
diameter side by side with depth. A prompt the allows the user to hardcopy and/or
advancing to the next screen of data.

    Sample Program execution:

        Display which file?:   packed_data

        Enter greatest depth of interest (0 for bottom depth): 0

        White for missing pulses?: yes (inverts black to white for plotting on
            white background)

        Enter 0 for linear scale 1 for equalized scale: 0

        First scan has xx sample.

        Okay? Type 0 *** Type 1 to adjust: 0

    Routine drawboth will then plot two panels, travel time in the right and
amplitude in the left and issue the prompt:

        Hardcopy? no

        Enter 1 to plot next panel 0 to quit: 1

DRAWTWO

　　　　Routine DRAWTWO displays two different data sets (amplitude is -a option or borehole diameter is default) side by side with depth. Prompts allow hard copying and/or advancing to the next screen of data.

　　　　Sample Program execution:

　　　　　　　　Display which file?:　　packed_data
　　　　　　　　Enter greatest depth of interest (0 for bottom depth): 0
　　　　　　　　Display which file?:　　packed_data
　　　　　　　　Enter greatest depth of interest (0 for bottom depth): 0
　　　　　　　　White for missing pulses?: yes (inverts black to white for plotting on
　　　　　　　　　　　　white background)
　　　　　　　　Enter 0 for linear scale 1 for equalized scale:　1
　　　　　　　　First scan has xx sample.
　　　　　　　　Okay? Type 0 *** Type 1 to adjust

Routine DRAWTWO will draw the two different data files and issue the prompt:

　　　　　　　　Hardcopy? no
　　　　　　　　Enter 1 to plot next panel 0 to quit

Routine DRAWTWO was used to generate Figure 8 on page 13.

3D

Routine 3D displays data in right panel (amplitude is -a option or borehole diameter is default) with depth. User may enter a scale to override the default scale as well as vary the x and y dimensions (delta_x and delta_y) of the cylindrical projection to achieve the best view of the feature. Use button #1 to select position in data file to begin drawing a cylindrical projection of data. The user has the option to color modulate the surface of the cylinder with the amplitude values. The rotation angle of the projected can be varied as can the position in the data to project.

Input Parameters:

Scale: Default scale is 100/max_tt+delay, user may choose a different scale

delta_x: horizontal exaggeration

delta_y: vertical exaggeration

Sample Program execution:

Display which file?:   packed_data

Enter greatest depth of interest (0 for bottom depth): 0

Enter scale?: yes

Enter desired scale: 1.5

Enter delta x and delta y? yes

delta_x and delta_y are: 2.0 1.5

White for missing pulses? yes (inverts black to white for plotting on white background)

Color modulate cylindrical projection with amplitude values? yes (plots amplitude as color in correct position on cylindrical projection)

Enter number of full scans at top: 8

First scan has xx samples.

Okay? Type 0 *** Type 1 to adjust

3D will then draw data in the right panel and issue the prompt:

Use mouse to select start of 1 meter section to plot.

Use button #1 to select, button #2 to quit and button #3 to clear text

Enter rotation in degrees: 90

3D will draw a cylindrical projection of the selected interval and user can continue selecting data section to project and varying the rotation angle.

Routine 3D was used to generate Figure 5 on page 8.

POLAR

Routine POLAR displays data in right panel (amplitude is -a option or borehole diameter is default) with depth. Use button #1 to select scan line position in data file to begin drawing a polar cross section of the data.

Sample Program execution:

Display which file?:   packed_data

Enter greatest depth of interest (0 for bottom depth): 0

White for missing pulses? (inverts black to white for plotting on white background)

Enter 0 for linear scale 1 for equalized scale: 1

First scan has xx sample.

Okay? Type 0 *** Type 1 to adjust

Routine POLAR then plots a panel of data and issues the prompts:

Use button #1 to select the scan line to plot

POLAR draws a polar cross section of a single scan of data with compass markings for orientation. The user may continue to select scans to plot in polar cross section.

FLATVIEW

Routine FLATVIEW displays data in right panel (amplitude -a option) or borehole diameter (default) with depth. Use button #1 to select the center position in data file of a flat isometric view of the borehole topography. User is prompted for delta x and delta y which scale the horizontal and vertical dimensions.

Input parameters

delta_x: Horizontal exaggeration for plot

delta_y: Vertical exaggeration for plot

Sample Program execution:

Display which file?:   packed_data

Enter greatest depth of interest (0 for bottom depth): 0

White for missing pulses? yes (inverts black to white for plotting on white background)

First scan has xx sample.

Okay? Type 0 *** Type 1 to adjust: 0

Routine FLATVIEW then plots a panel of data and issues the prompt:

Use the button #1 to pick the center of the plot area.

Use button #2 to quit

Use button #3 to make a hardcopy

One the coordinates of the plot are selected the routine issues the prompt:

Enter delta_x and delta_y: 1.5 2.0

An isometric perspective view is plotted and the user may then select another area to plot and other scaling factors.
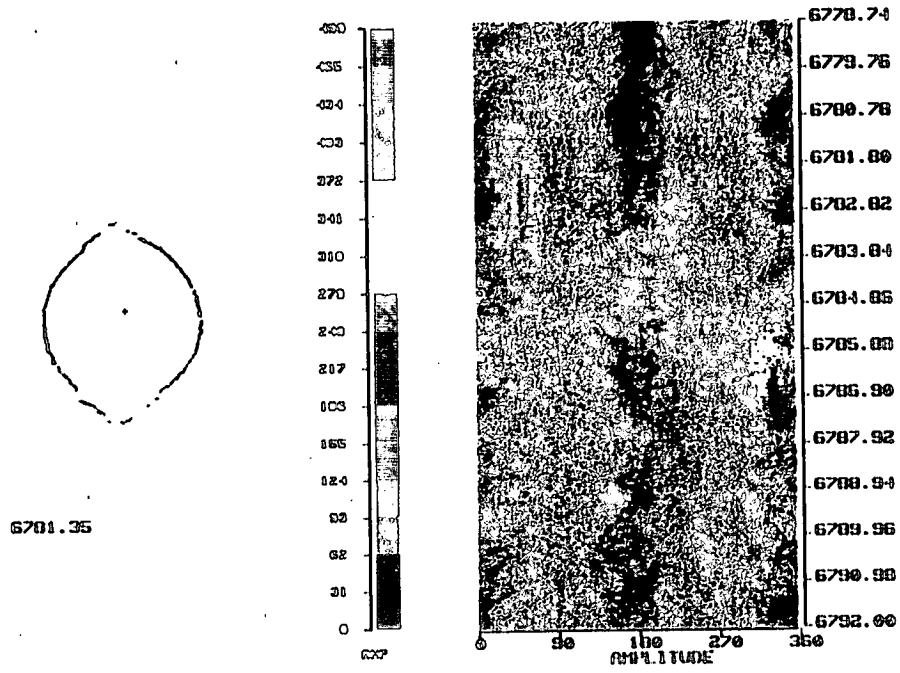
Figure A1. Sample output of the program POLAR from data recorded in the Cajon Pass well.
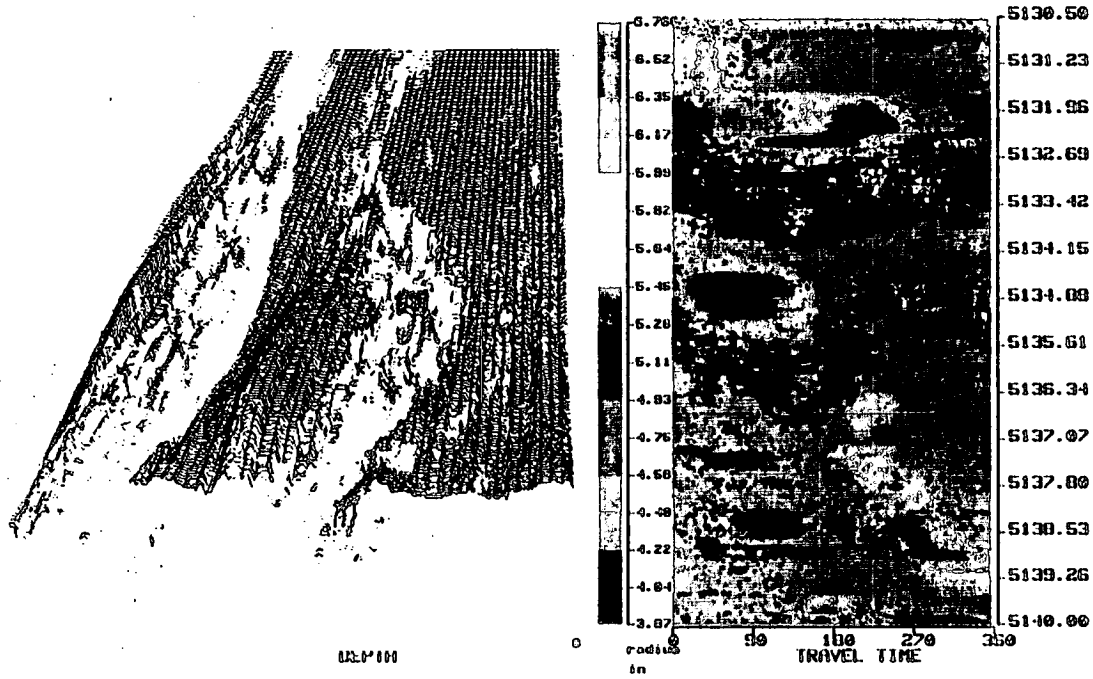
Figure A2. Sample output from the program FLATVIEW from data recorded over a fracture zone in the Auburn Geothermal well.

DATA ANALYSIS SOFTWARE

SHAPE
Routine SHAPE is used to performs a detailed analysis of borehole shape over user specified intervals of the borehole wall. Data are displayed in the right panel (amplitude is -a option or borehole diameter is default) with depth. User is may skip the current panel of data. Successive scanlines are plotted in polar cross section in the left panel. Use buttons #1 and #2 to click and drag through a breakout angles and button #3 to write the selected angles to disk. If you want to make a hardcopy answer no to the "Write to disk?" prompt and you will be prompted with "Do you want to make a hard copy?". If you answer no you may also repick any breakout angle until you are satisfied with you interpretation. These prompts will cycle until you answer yes to "write to disk?" and the next scanlines will be displayed. Shape creates an ascii data file of depth azimuth and width of breakouts.

Sample Program execution:
    Display which file?:   packed_data
    Enter greatest depth of interest (0 for bottom depth): 0
    Enter number of scan lines to superimpose (10 maximum): 5
    Enter output file name for depth/ azimuths: shape.out
    White for missing pulses: yes (inverts black to white for plotting on
        white background)
    Color modulate polar cross sections with amplitude values: yes
    First scan has xx sample.
    Okay? Type 0 *** Type 1 to adjust: 0

Routine SHAPE then plots a panel of data and issues the prompt:
    Skip this panel? no

6 polar cross sections of superimposed scans are then plotted in the left panel and the routine waits for the user to pick the breakout width with the mouse. (hold down button #1 and drag across the breakout angle then release the button). Once all of the breakouts displayed are picked use button #3 to activate the prompt:
    Write to disk (y) or (n) : yes (picked azimuths and widths are written
                                         to disk)

The next series of polar projections are then plotted.

Routine SHAPE was used to plot Figure 19 page 27.

APERTURE

        Routine APERTURE is used to measure fracture orientation and apparent aperture. Data are displayed in right panel (amplitude is -a option or borehole diameter is default) with depth. Use button #1 to select the peak and trough of the sinusoidal shape of the fracture. The measurement of the amplitude and phase of the sinusoid determined the orientation of the fracture plane. The fracture aperture can be measured by answering yes to the prompt "Measure fracture aperture?". The plotting scale can be magnified to enhance the fracture topography until the optimum scale is found. Using button #1 click and drag over the fracture width. Aperture creates an ascii file of fracture orientation and aperture with depth.

        Sample Program execution:

                Display which file?:   packed_data
                Enter greatest depth of interest (0 for bottom depth): 0
                White for missing pulses? yes (inverts black to white for plotting on
                        white background)
                Enter output file name for depth/fracture data: fracture.out
                First scan has xx sample.
                Okay? Type 0 *** Type 1 to adjust

Routine APERTURE then plots a panel of data and issues the prompt:

                Click peak then trough of sinusoid amplitude with button #1 or
                use button #2 to continue to next panel of data.

If the phase and amplitude of a fracture are selected the routine issues the prompt:

                Evaluate fracture aperture? yes (User draws cross sections across the
                        fracture (up to 7 sections) and clicks button #3 when finished.

The routine then issues the prompt:

                Enter scale for plotting cross sections, type 0 when finished:

Cross section will be drawn in the left panel and the routine issues the prompt:

                Pick apertures with button #1, use button #3 to write to disk.

Use mouse holding down button #1 across the fracture gap and release at the
                other side. A red line will be drawn across the fracture selected
                fracture interval.

User may continue to measure fracture in this panel of data or move on to the
                next panel.

Routine APERTURE was used to plot Figure 23 page 33.

CALIPER

Routine CALIPER is used to create "logs" of BHTV data. Data are displayed in right panel (amplitude is -a option or borehole diameter is default) with depth. An ellipse is fit to each scan (each depth) of borehole radius data to determine the major and minor axes, and the eccentricity and orientation of the ellipse. The borehole volume is computed and a value of the reflectivity is determined for each scan. The representative reflectivity is computed from a histogram of amplitude values. The user selects the upper cutoff of amplitude values used in the computation of the histogram in order to get a representative reflectivity of the intact rock. The user has the option to view the fit to an ellipse to determine how well the algorithm is working, to view the data in "log" profile form, or not to view the data but to process the data in "batch" mode. Two "filters" are specified to set the permissible variation in neighboring travel time values that define valid data to be used for the fit. The orientation filter is usually a larger value than the caliper filter so the algorithm can use the high travel times over breakout intervals to orient the ellipse. To find the correct aspect ration of the intact borehole however the caliper filter parameter should be relatively small. Caliper creates an ascii multiplex data file of depth, major axis minor axis, eccentricity, orientation angle, volume and reflectivity.

Sample Program execution:

Display which file?:   packed_data
Enter greatest depth of interest (0 for bottom depth): 0
View polar cross sections to verify the fit to an ellipse (2) or
process data (1): 1

Do you want to see the data? yes
Enter percent ellipticity below which ellipse
    orientations will not be plotted
Enter scaling factor for profiles
White for missing pulses? (inverts black to white for plotting
    on white background)
Average number of top amplitude bins for reflectivity log:
Enter output file name for caliper/amplitude data:
Enter filter for orientation: 5
Enter filter for caliper: 10
First scan has xx sample.
Okay? Type 0 *** Type 1 to adjust: 0

Routine CALIPER then plot scans of data in the right column and corresponding profiles of the a and b axes of the elliptical fit, the percent eccentricity, the orientation of the ellipse, the computed volume and the reflectivity.

If the answer to the View polar cross sections prompt is 2 the
    following sequence of prompts must be answered:
        Enter filter for orientation: 5
        Enter filter for caliper: 10
        First scan has xx sample.

Okay? Type 0 *** Type 1 to adjust: 0

In this case routine CALIPER will plot polar cross sections of the data at 5
scan intervals with the fit to an ellipse superimposed in red. The major and
minor axes of the ellipse are also displayed. After each plot the routine issues
the prompt:
New filters? — The user may vary the filter parameters to
improve the fit

3DVIEW

Routine 3DVIEW plots data in three 3-D cylindrical projections over a one meter depth interval where each view is rotated 120° to show the entire 360° image. Successive cylindrical projections are plotted and the user can specify the start azimuth of the plots. The depth location of features and a quality factor are selected using button #1. 3DVIEW creates an ascii file of feature depth and qualifier.

Input Parameters:

Scale: Default scale is 100/max_tt+delay, user may choose
a different scale
delta_x: horizontal exaggeration
delta_y: vertical exaggeration

Sample Program execution:

Display which file?:   packed_data
Enter greatest depth of interest (0 for bottom depth): 0
Enter scale?: yes
Enter desired scale: 1.5
Enter delta x and delta y? yes
delta_x and delta_y are: 2.0 1.5
White for missing pulses? yes (inverts black to white for plotting on white background)
Color modulate cylindrical projection with amplitude values? yes (plots amplitude as color in correct position on cylindrical projection)
Enter number of full scans at top: 8
Enter output file name for feature info: aperture.out
Constant rotation angle? yes (uses same rotation for successive plots)
Enter starting rotation angle: 90
First scan has xx sample.
Okay? Type 0 *** Type 1 to adjust: 0

3DVIEW will then plot 3 cylindrical projections of about 1 meter of data at 120° azimuths and issue the prompt:

Click button #1 to pick feature depth, click button #2 to hardcopy or continue

If a feature is selected the routine issues the prompt:

Enter fracture quality code: 1

User may continue to plot successive 1 meter intervals of data or quit by answering the prompt:.

Next panel?

Routine 3DVIEW was used to plot Figure 22 page 31.

QARL

Routine QARL is used to collect reflectivity data with depth. Data is displayed in the right panel and in the left panel is a profile of the representative value of the reflectivity for that scanline. This routine performs a histogram of the reflectivity values for each scan. The user is prompted for the number of reflectivity histogram bins (from highest bin value to lowest) to include in an average value for the reflectivity. This technique is used to provide a average value of intact rock and exclude effects of fractures, breakouts etc.

Sample Program execution:
Display which file?:   new_data
Enter greatest depth of interest (0 for bottom depth): 0
Enter output file name: qarl.out
First scan has xx sample.
Okay? Type 0 *** Type 1 to adjust: 0

Routine QARL will then plot a panel of data and issues the prompt:
Number of top amplitude bins to average, 0 to stop plotting: 300
A profile of the representative amplitude value with depth will be drawn in the left panel and the routine issues the prompt:
Enter 1 to plot the next panel 0 to quit.

Routine QARL was used to plot Figure 28 page 40.

<div align="center">

UTILITY ROUTINES

</div>

RDATA

Routine RDATA is used to print header and data values of a file for inspection.

Sample Program execution:
Display which file?:   new_data
Enter greatest depth of interest (0 for bottom depth): 0
First scan has xx sample.
Okay? Type 0 *** Type 1 to adjust: 0
Enter number of bytes to skip ahead: 1000

HEDIT

Routine HEDIT is used to edit only the header of a data file. Header file parameters will be listed and user may type in the parameter name to be changed and then change its value. Data is rewritten to the same file.

Sample Program execution:
Display which file?:   new_data
Enter greatest depth of interest (0 for bottom depth): 0
The header is printed and HEDIT issues the prompt:
Would you like to change a variable: yes
Enter variable name, type 0 when finished: Mag Dec
Enter new values of Mag Dec: 16

CONVERT

Routine CONVERT is used to convert old format files to the new BHTV format. The user will be prompted for information about the data location and digitization settings.

Sample Program execution:

Convert which file?:   old_data
Enter greatest depth of interest (0 for bottom depth): 0
First scan has xx sample.
Okay? Type 0 *** Type 1 to adjust: 0
Enter well name: DOSECC #1
Enter well location: Cajon Pass, California
Enter magnetic declination at site in degrees east of north: 15
Enter starting depth: 2000
Enter ending depth: 1000
Are depths in feet or meters: meters
Enter borehole fluid velocity in m/sec: 1500
Tool used to record data was 1-Large Tool 2-Small Tool: 1
High frequency (1) or low frequency (2) transducer?:   1
Do you know the calibration? yes
            Enter calibration in μsec: 9.04
If tool was in marker mode enter degrees to correct to north (enter
        0 if none):   0
Enter borehole deviation (enter 0 if unknown):   0

Routine CONVERT will then print the header and issue the prompt:

Would you like to change a variable: yes
        Enter variable name: Mag Dec
        Enter new values of Mag Dec: 16
Writing data...please wait.
End of convert.

BIBLIOGRAPHY

Aldrich, M.J. and Laughlin, A.W., A model for the tectonic development of the Southeastern Colorado Plateau Boundary, J.Geophys. Res., 89,10207 - 10218,1984.

Aldrich, M.J., Chapin, C.E. and Laughlin, A.W., Stress history and tectonic development of the Rio Grande rift, New Mexico, J. Geophys. Res., 91, 6199-6211, 1986.

Anderson, E.M., The dynamics of faulting and dyke formation with applications in Britain, 2nd ed. Oliver and Boyd, Edinburgh, 1951.

Angelier, J., Determination of the mean principal directions of stress for a given fault population: Tectonophysics, 56, T17-26, 1979.

Ankeny, L.A., Braile, L.W., and Olsen, K.H., 1986, Upper crustal structure beneath the Jemez Mountains volcanic field, New Mexico, determined by three dimensional simultaneous inversion of seismic refraction and earthquake data, J. Geophys. Res., 91, 6188-6198.

Balsley, J.R. and Buddington, A.F. Magnetic susceptibility anisotropy and fabric of some Adirondak granites and orthogneisses, Am. Journ. Sci., Bradley Vol., 258-A, 6-20, 1960.

Barton, C.A., Zoback, M.D. and Burns, K.L., In-situ stress orientation and magnitude at the Fenton Geothermal site, New Mexico, determined from wellbore breakouts, Geophy., Res. Let, 15, 467-470, 1988.

Barton, C.A. and Moos D., Analysis of macroscopic fractures in the Cajon Pass Scientific Drillhole over the interval 1829 - 2115 meters, Geophy. Res. Let., in press, 1988.

Barton, C.A, Moos, D. and Blangy, J.P., Analysis of full waveform acoustic logging data at ODP site 642 — Outer Voring Plateau, Volume 104, Part B — Norwegian Sea, Proceedings of the Ocean Drilling Program, Texas A&M University, 1988.

Bell, J.S. and and Gough D.I., Northeast-southwest compressive stress in Alberta: Evidence from oil wells. Earth Planet. Sci. Lett., 45, 475-482, 1979.

Birch, F., The velocity of compressional waves in rocks to 10 kbars, Part I, J.Geophy.Res., 65, 1083-1102, 1960.

Birch, F., The velocity of compressional waves in rocks to 10 kbars, Part I, J.Geophy.Res., 66, 2199-2228, 1960.

Biot, M. A., Propagation of elastic waves in a cylindrical borehole containing a fluid, J. Appl. Phys., 23, 997-1005, 1952.

Brace, W.F., 1965. Relation of elastic properties of rocks to fabric. Journ. of Geophy. Res., 70, 5657 - 5667.

Brace, W.F., Permeability of crystalline and argillaceous rocks, Int. J. Rock Mech. Min. Sci. & Geomech. Abstr., 17, 241-251, 1980.

Brace, W.F. and Kohlstedt, D.L., Limits on lithospheric stress imposed by laboratory experiments, J. Geophy. Res., 85, B11, 6248-6252, 1980.

Brown, L.L. and Golombek, M.P., Tectonic rotations within the Rio Grande Rift: Evidence from paleomagnetic studies, Journ. Geophy. Res., 90, 790-802, 1985.

Brune, J. N., Surface waves and crustal structure, in The Earth's Crust and Upper Mantle, Geophys. Monograph, 13, 230-242, A.G.U., Washington, D.C., 1969.

Burnes, D.R., Cheng, C.H., Schmitt, D.P. and Toksoz, M.N., Permeability estimation from full waveform acoustic logging data, The Log Analyst, 29, 112-122, 1988.

Burnes, K., Reconstruction of the stress field at Fenton Hill, in Workshop on recent research in the Valles Caldera, edited by G. Heiken, Los Alamos National Laboratory, Los Alamos, New Mexico, 1984.

Byerlee, J.D., 1978. Friction of rocks. Pure and Applied Geoph.,116, 615-626.

Byerly, P., The earthquake of July 6, 1934: amplitudes and first motion, Bull. Seis. Soc. Am, 28, 1-13, 1938. .sp Carmichael, R. S. (ed.), Handbook of physical properties of rocks,CRC Press, Boca Raton, Florida., 193, 1982.

Castleman, K.R., Digital image processing, Prentice Hall, Inc., Englewood Cliffs, N.J., 1984.

Chapin, C.E., and Cather, S.M., Eocene tectonics and sedimentation in the Colorado Plateau-Rocky Mountain area, in Relations of the Tectonics to ore deposits in the Southern Cordillera, edited by W. R. Dickenson and W. D. Payne, Ariz., Geol. Soc. Dig., 14, 173-198, 1981.

Cordell, L., Regional geophysical setting of the Rio Grande Rift, Geol. Soc. Am. Bull., 89, 1073-1090, 1978.

Coyle, B. and Zoback, M.D., In-situ permeability and fluid pressure measurement in the Cajon Pass Research Well, (this volume), 1988.

Cheng, C. H. and M. N. Toksoz, Generation, propagation and analysis of tube waves in a borehole, in Vertical Seismic Profiling, Part B, Advanced Concepts, (M. N. Toksoz and R. R. Stewart ed.), Geophysical Press, 276-287, 1984.

Crampin S., Distinctive particle motion of surface waves as a diagnostic of anisotropic layering, Geophy. J. Roy. Astr. Soc., 40, 177-186, 1975.

Crampin, S., A review of the effects of anisotropic layering on the propagation of seismic waves, Geophy. J. Roy. Astr. Soc, 49, 9-27, 1977.

Crampin, S., Seismic-wave propagation through a cracked solid: polarization as a possible dilatancy diagnostic, Geophy. J. Roy. Astr. Soc., 53, 467-496, 1978.

Crampin, S., Shear wave polarizations: A plea for three component recording, Abst, Soc. Exp. Geophy. 53rd Annual Meeting, Las Vegas, Nevada, S-12.7, 1983.

Crampin, S. and D. W. King, Evidence for anisotropy in the upper mantle beneath Eurasia from the polarization of higher mode seismic surface waves, Geophy. J. Roy. Astr. Soc., 49, 59-85, 1977.

Crampin, S. Distinctive particle motion of surface waves as a diagnostic of anisotropic layering, Geophys. J. R. Astr. Soc., 40, 177-186, 1975.

Crampin, S. The dispersion of surface waves in multilayered anisotropic media, Geophy. J. Roy. Astr. Soc., 21, 387-402, 1970.

Crampin, S., R. McGonie and D. Bamford, Estimating crack parameters from observations of P-wave velocity anisotropy, Geophysics, 45, 345-360, 1980.

Dey, T.N., State of stress in a hot dry rock reservoir at Fenton Hill, NM, EOS, 67, 1206, 1986.

DiSiena, J. P., J. E. Gaiser and D. Corrigan, Horizontal components and shear wave analysis of three-component VSP data, Vertical Seismic Profiling, Part B: Advanced Concepts, (Toksoz, M. N. and Stewart, R. R. ed.), Geophy. Press., 177-188, 1984.

Doell, R.R., Dalrymple, G.B., Smith, R.L. and Bailey, R.A., Paleomagnetism, potassium-argon ages, and geology of rhyolites and associated rocks of the Valles caldera, New Mexico, Geol. Soc. Am. Mem. 116, 211-248, 1968.

Eaton, G.P., 1979, A plate-tectonic model for late Cenozoic crustal spreading in the Western United States, in Rio Grande Rift: Tectonics and Magmatism, Riecker, R.E. ed., 7-32, A.G.U., Washington, D.C.

Ekren, E.B., Rogers, C.L., Anderson, R.E., and Orkild, P.P., 1968, Age of Basin and Range normal faults in Nevada Test Site and Nellis Air Force Range, Nevada, Nevada Test Site, Ecked, E.B. ed., Mem. Geol. Soc. Am., 110, 247-250.

Ekstrum, M.P., Dahan, C.A., Chen, M.Y., Lloyd, P.M., Rossi, D.J., Formation imaging with microelectrical scanning arrays, The Log Analyst, 28, 294-306,1987.

Eldholm, O., J. Thiede, E. Taylor, C. Barton, U. Bleil, K. Bjorklund, P. Ciesielski, A. Despariries, D. Donally, C. Froget, R. Goll, R. Henrich, E. Jansen, L. Krissek, K. Kvenvolden, A. LeHuray, D. Love, P. Lysne, T. McDonald, P. Pudie, L. Osterman, L. Parson, J. Phillips, A. Pittenger, G. Ovale, G. Schoenharting and L. Viereck, Volume 104, Part A — Initial Report, Norwegian Sea, Proceedings of the Ocean Drilling Program, Texas A&M University, 1987.

Engelder, T., Is there a genetic relationship between selected regional joints and contemporary stress within the lithosphere of North America?, Tectonophysics, 1, 161-177, 1982.

Fehler, M., House, L., and Kaieda, H., Seismic monitoring of hydraulic fracturing, 27th U.S. Symposium on Rock Mechanics, Univ. of Alabama, 606-613, 1986.

Froidevaux, C., Tectonic stress in France; in-situ measurements with a flat jack, in Proceedings of Conference IX, Magnitude of deviatoric stress in the Earth's crust and upper mantle, (Evernden, J.F., convener), U.S. Geol. Surv., Open-file Rep., No. 80-625, 434-443, 1980.

Gaiser, J. E., R. W. Ward and J. P. DiSiena, Three component vertical seismic profiles: Velocity anisotropy estimates from P wave particle motion, Vertical Seismic Profiling, Part B: Advanced Concepts (M. N. Toksoz and R. R. Stewart eds.), Geophy. Press., 189-204, 1984.

Gal'perin, E. I., Vertical Seismic Profiling, Moscow, Nedra, English Trans. S.E.G., Spec. Pub. #12, Tulsa,Ok,1971.

Georgi, D. T., Geometrical aspects of borehole televiewer images. SPWLA Logging Symposium Transactions, 1-C, 1985.

Gladwin, M.T. and F. D. Stacy, Ultrasonic pulse velocity as a rock stress sensor, Tectonophysics, 21, 39-45, 1973.

Goldberg, D.S., Gant, W.T., Seigfried, R.W. and Castagna, J.P., Processing and interpretation of sonic waveforms: a case study, SEG 54th Ann. Symposium, (trans), 28-31, 1984.

Golombek, M.P., Geology, structure, and tectonics of the Pajarito fault zone in the Espanola basin of the Rio Grande Rift, New Mexico, Geol. Soc. Am. Bul., 94, 192 - 205. 1983.

Gough, D.I. and Bell, J.S.,Stress orientations from oil well fractures in Alberta and Texas, Can. Journ. Earth Sci., 18, 1358-1370, 1981.

Haimson, B. C. and Doe, T.W., State of stress, permeability and fractures in the Precambrian granite of northern Illinois, Journ. Geophy. Res., 88, 7355-7371, 1983.

Hardage, B. A., Vertical Seismic Profiling, Part A: Principles, Geophy. Press, London, 1983.

Hardin, E.L., Cheng, C.H. , Paillet, F.L. and Mendelson, J.D., Fracture characterization by means of attenuation and generation of tube waves in fractured crystalline rock at Mirror Lake, New Hampshire, J. Geophys. Res., 92, 7989-8006, 1987.

Herin, E., Regional variations in P-wave velocity in the upper mantle beneath North America, *in* The Earth's Crust and Upper Mantle, Geophys. Mon., 13, 242-246, A.G.U., Washington, D.C., 1969.

Hickman, S.H., Healy, J.H. and Zoback, M.D., In situ stress, natural fracture distribution, and borehole elongation in the Auburn geothermal well, Auburn, New York, J.Geophys. Res., 90, 5497-5512,1985.

Hinz, K. and Schepers, R., SABIS - The digital version of the borehole televiewer, Eighth European Formation Evaluation Symposium, 1985.

Hubbard, M.K. and Willis, D.C., Mechanics of hydraulic fracturing, Trans. AIME, 210, 153-163, 1957.

Jaeger, J.C. and Cook, N.G.W., Fundamental of rock mechanics,2nd ed., Methuen and Co., London ,1979.

Jones, T. D. and A. Nur, Seismic velocity and anisotropy in mylonites and the reflectivity of deep crustal fault zones, Geology, 10, 260,263, 1982.

Kharaka,Y., Fluid chemistry in the Cajon Pass Scientific Drillhole, Geoph, Res. Lett., (in press), 1988.

King, M. S., M. R. Stauffer and B. I. Pandit, Quality of rock masses by acoustic borehole logging, Proc. 3rd Int. Congress. I.A.E.G., Sec. IV, 156-164, 1978.

Kirsch, G., Die Theorie der Elastizitaet und die Beduerfnisse der Festigkeitslehre. Zeitschrift VDI, 29, 797-807, 1898.

Lachenbruch A. and Sass J., The stress heat flow paradox and thermal measurements at Cajon Pass, Geophy. Res. Lett, (in press), 1988.

Leveille, J.P. and Seriff, A.J., Borehole-wave particle motion in anisotropic formations, Journ. Geophy. Res., in press, 1988.

Liu, H., Sembera,E., Westerlund, R., Fletcher, J., Reasenberg, P., and Agnew, D., Tidal variation of seismic travel times in a Massachusetts granite quarry, Geoph. Res. Let., 12, 243-246, 1985.

Lysne, P., Determination of borehole shape by inversion of televiewer data, The Log Analyst, xx, 64-71, 1986.

Malin, P. E. and P. C. Leary, Seismic velocity stress sensitivity of the crust near Palmdale, California, EOS, 62, 967, 1981.

Mardia, K.V., Statistics of directional data, Department of Mathematical Statistics, The University, Hull, England, Academic Press, London, 1972.

Marquardt, D.W., An algorithm for least-squares estimation of non-linear parameters, SIAM, 11, 431-441, 1963.

Mastin, L., An analysis of stress-induced elongation of boreholes at depth, master's thesis, Stanford University, 1984.

McEvilly, T. V., Central U.S. crust upper mantle structure from Love and Rayleigh wave phase velocity inversions, Bull. Seis. Soc. Am., 54, 1997-2015, 1964.

Moos, D. and M. D. Zoback, In-situ studies of velocity in fractured crystalline rocks, J. Geophy. Res., 88, 2345-2358, 1983.

Murphy, H.D. Lawton, R.G., Tester, J.W., Potter, R.M., Brown, D.M. and Aamodt, R.L., Preliminary assessment of a geothermal energy reservoir formed by hydraulic fracturing. Soc. of Pet. Eng 51 Annual Meeting, New Orleans, 1976.

Newmann, F., An analysis of the S-wave, Bull. Seis. Soc. Am., 20, 15-32, 1930.

Nicoletis, L., Bamberger, A., Quiblier, J., Joly, P., and Kern, M., Hole geometry and anisotropy effects on tube-wave propagation: a quasi static study, Geophysics, in press, 1988.

Nur, A., Effects of stress and fluid inclusions on wave propagation in rock, Ph.D. Thesis, M.I.T., Cambridge, MA., 1969.

Nur, A., Effects of stress on velocity anisotropy in rocks with cracks, J. Geophy. Res., 76, 2022-2034, 1971.

Nur, A. and G. Simmons, Stress-induced velocity anisotropy in rock: An experimental study, J. Geophy. Res., 74, 6667-6674, 1969a. .

Nur, A. and G. Simmons, The effect of saturation on velocity in low porosity rocks, Earth Planet. Sci. Lett., 7, 183-193, 1969b.

Nur, A. and Byerlee, J., An exact effective stress law for elastic deformation of rock with fluids, J. Geophy. Res., 76, 6414-6419, 1971.

O'Connell, R.J. and Budiansky, B., Seismic velocities in dry and saturated cracked solids, J. Geophy. Res., 79, 5412-5426, 1979

Olsen, K.H., Braile, L.W., Stewart, J.N., Daudt, C.R., Keller, G.R., Ankeny, L.A. and Wolf, J.J., Jemez mountains volcanic field, New Mexico: Time term interpretation of the CARDEX seismic experiment and comparison with bouguer gravity, J. Geophys.Res., 91, 6175-6187, 1986.

Paillet , F.L., Acoustic characterization of fracture permeability at Chalk River, Ontario, Canadian Geotech. Jour., 20,468-476, 1983.

Paillet, F. L. Acoustic propagation in the vicinity of fractures which intersect a fluid filled borehole, SPWLA, 21st Ann. Log. Symp., Paper D., 1980.

Paillet, F. L. and White J. E., Acoustic modes of propagation in the borehole and their relationship to rock properties: Geophysics, 47, 8, 1215-1228, 1982.

Plumb, R.A. and Cox, J.W., Deep crustal stress directions in North America from borehole elongation, EOS, 65, 1984.

Reasenberg, P. and K. Aki, A precise, continuous measurement of seismic velocity for monitoring in situ stress, J. Geophy. Res., 79, 399-406, 1974.

Rector, J.W. III, Acquisition and preliminary analysis of oriented multi-component multioffset VSP data: DOSECC Cajon Pass deep scientific drillhole, Geophy. Res. Let., Special Issue (in press), 1988.

Richards, J.A., Remote sensing digital image analysis, Springer-Verlag, New York, 1986.

Roever, W.L., Rosenbaum, J.H., and Vining, T.F., Acoustic waves from an impulsive source in a fluid-filled borehole. J. Acoustic Soc. Am., 55, 1144-1157, 1974.

Rosenbaum, J.H., Synthetic microseismograms: logging in porous formations, Geophysics, 39,14-32, 1974.

Rubel, H.J., Schepers, R., and Schmitz, D., High resolution televiewer logs from sedimentary formations, 10th European SPWLA Symp., Aberdeen, Scotland, 1986.

Schoenberg, M., Marzetta, T., Aron, J. and Porter, R.P., Space time dependence of acoustic waves in a borehole. Acoust. Soc. Am., 70, 5, 1496-1507, 1981.

Seeberger, D.A. and Zoback, M.D., The distribution of natural fractures and joints at depth in crystalline rock, Journ. Geoph. Res., 87, 5517-5534, 1982.

Shamir, G. , Zoback, M.D., and Barton, C.A., In-situ stress orientation near the San Andreas fault: Preliminary results to 2.1 km depth from the Cajon Pass Scientific Drillhole, Geophy. Res. Lett., (in press), 1988.

Sibson, R.H., A note on fault reactivation, J. Struct. Geology, 7, 6, 751-754, 1985.

Sleep, N.H., Kroeger, G., Stein, S., Canadian passive margin stress field inferred from seismicity, Journ. Geopy. Res., in press, 1988.

Smith, R.L. and Bailey, R.A., The Bandelier tuff - a study of ash flow cycles from zoned magma chambers, Bull. Volcanol., 29, 83-104, 1966.

Sjogren, B., A. Ofsthus and J. Sandberg, Seismic classification of rock mass qualities, Geophys. Prosp., 27, 409-442, 1979.

Solomon, S. C., Seismic wave attenuation and partial melting in the upper mantle of North America, J. Geophy. Res., 77, 1483-1502, 1972.

Stein, S., Cloetingh, S., Sleep, N.H., Wortel, R., Passive margin earthquakes, stresses and rheology, Journ. Geophys. Res., in press, 1988.

Stesky, R. M., Compressional and shear velocities of dry and saturated jointed rock: A laboratory study, Geopyhs. J. Roy. Astr. Soc., 83, 239-262, 1985.

Stephanson, O., G. Lande and A. Bodare, A seismic study of shallow jointed rock, Int. Rock Mech. Min. Sci. Geomech. Abst., 16, 319-327, 1979.

Stephen, R.A., Seismic anisotropy observed in the upper oceanic crust. Geophys. Res. Let. 8, 865, 1981.

Stephen, R.A., Borehole seismic experiments and the structure of the upper oceanic crust. in Vertical Seismic Profiling, Part B, Advanced Concepts, (M. N. Toksoz and R. R. Stewart ed.), Geophysical Press, 351-374, 1984.

Stierman, D. J., J. H. Healey and R. L. Kovach, An in-situ velocity study: The Stone Canyon well, J. Geophys. Res., 84, 672-678, 1979.

Stierman, D. J. and R. L. Kovach, Pressure induced velocity gradient: an alternative to a Pg refractor in the Gabila Range, central California, Bull. Seis. Soc. Am., 69, 397-415, 1979.

Walsh, J. B., The effect of cracks on the compressibility of rock, J. Geophy., Res., 70, 381-389, 1965.

White, J. E., Elastic waves along a cylindrical bore, Geophysics, 27, 327-333, 1962.

White, J. E., Motion product seismograms, Geophysics, 29, 288-298, 1964.

Wright,L., Late Cenozoic fault patterns and stress fields in the Great Basin and westward displacement of the Sierra Nevada block: Geology, 4, 489-494, 1976.

Zemanek,J., Glenn, E.E., Norton, L.J. and Caldwell, R.L.,Formation evaluation by inspection with the borehole televiewer. Geophysics, 35, 254-269, 1970.

Zoback, M.D., Silver, L.T., Henyey, T., Thatcher, W., The Cajon Pass scientific drilling experiment: Overview of Phase I, Geophy. Res. Let., Special Issue (in press), 1988.

Zoback, M.D. and J. Healey, Hydraulic fracturing stress measurements in the Cajon Pass scientific drillhole to 2 km depth, Geoph. Res. Let., (in press), 1988.

Zoback, M.D., Mastin, L., Barton, C.A., In-situ stress measurements in deep drillholes using hydraulic fracturing, wellbore breakouts, and Stoneley wave polarization, in Proceedings of the International Symposium on Rock Stress Measurements, Stockholm, 289-300, 1986.

Zoback, M.D., Moos, D., Mastin, L., Anderson, R.N., Wellbore breakouts and in-situ stress, J. Geophys. Res., 90, 5523-5530, 1985.

Zoback, M.D. and Healey, J.H., Friction, faulting, and in-situ stress. Annales Geophysicae, 2, 689-698, 1984.

Zoback, M.L. and Zoback, M.D., State of stress in the conterminous United States,Journ. Geophys. Res., 85, 6113-6156, 1980.

Zoback, M.L., and Thompson, G.A., 1978, Basin and Range rifting in northern Nevada: Clues from a mid-Miocene rift and its subsequent offsets, Geology, 6, 111-116.

Zoback, M.D. and Moos, D., In-situ stress, natural fracture and sonic measurements in the Moodus, Connecticut scientific research well, report prepared for Woodword-Clyde Consultants, Wayne, N.J., 1988.

Zoback, M.L. and Zoback, M.D., Tectonic stress field of the continental United States. In: Geophysical framework of the Continental United States, edited by L. Pakiser,and W. Mooney, GSA Memoir, 1987.